DEVELOPMENT OF A NOVEL POLYMERIC OSMOTICALLY TRIGGERED DELAYED RELEASE VACCINE DELIVERY DEVICE

KERR DOUGLAS GORDON SAMSON

Submitted for the degree of Doctor of Philosophy

Heriot-Watt University

School of Engineering and Physical Sciences

April 2020

The copyright in this thesis is owned by the author. Any quotation from the thesis or use of any of the information contained in it must acknowledge this thesis as the source of the quotation or information.

ABSTRACT

In this work, a delayed release osmotically triggered delivery device was developed that was able to release a payload after a delay of approximately 21 days in a consistent and reproducible manner. The device was constructed out of a flexible polycaprolactone photo-cured network, which expelled up to 21.5 % of its total payload after burst, enabling close to bolus-like release profile. Characterisation of the factors that control the delay of release was also performed, with evidence demonstrating that it was advantageous to adjust material permeability and device wall thickness over manipulation of the osmogent concentration, in order to maintain burst reproducibility. The photo-cured polycaprolactone network was shown to be degradable under simulated physiological conditions, and there was no evidence of cytotoxicity after 11 days of direct contact with primary dermal fibroblasts. This study provides strong evidence to support further development of flexible biomaterials with the aim of continuing improvement of the device burst characteristics in order to provide the greatest chance of the devices succeeding with *in-vivo* vaccine booster delivery. Additionally, a polycaprolactone-based stereolithography resin was developed that retains a degree of semi-crystallinity, thus providing significantly improved toughness while retaining biocompatibility. Benzyl alcohol was shown to be a more suitable diluent than dioxane for the formulation of PCL macromer photo-curable resins. An improved automated dip-coat-curing machine for the production of the device tubular part was also constructed.

DEDICATION

This thesis is dedicated to my parents: Ian and Sandra.

ACKNOWLEDGEMENTS

A huge thank you to my supervisor, Dr Ferry Melchels, for all his support and guidance over the years. I've had a great time working with you, and I look forward to continuing our work together with the SAVE project! Likewise, a big thanks to Alberto Di Bartolo who was the other PhD student in the group when I started. Your wise words, observations, ideas, and support were of great value throughout my PhD, but particularly so during the crucial early stages when I was rather useless! I will also thank the more recent arrivals to the group, Andrew McCormack and Aisling McGuigan, despite highlighting how old and boring I am. I look forward to seeing you both progress through your own PhDs.

Other notable mentions include Kyriakos Michail, Ameya Vaidya and Dean Crawford, whom I must thank for the wildly varied 'interesting' conversations we had while all procrastinating in the office. I will thank my squash partner Ewa Guźniczak, for trying to keep me fit while providing expert advice of all kinds, and often bursting my lungs from laughing about stuff. I must thank my flatmate Hanna Buist who often had to put up with living with a grumpy Kerr when things weren't going well, or when I was just stressed out. Thanks for your support, particularly during my write up and preparation for my viva. It was good to have your company (and home baking!) throughout the COVID19 lockdown. I'd like to thank the many IB3 colleagues and friends who also helped and provided social support along the way. I wish you all the utmost success in each of your respective careers. To Dr Tim Dargaville, Mariah Sarwat, Jongryul Park, Eleonore Bolle, and Raquel Sánchez Díaz at QUT for including me into the group like one of your own and your contributions in various manners to my work and wellbeing. I'll now emphasise some specific contributions: Jongryul, for the assistance in optimising the recovering the small PCL crosslinker macromer; Eleonore, for the help in planning/designing the cytotox work and ultimately performing the experiments on my behalf due to the strict H&S requirements; Mariah, who took on the time-consuming (and likely rather boring!) task of performing all the sampling of the experiment I left behind which generated the raw data used to make Chapter 8. Thanks to all the others at QUT/IHBI for the fun BBQs, parties, beach trips and hikes! Thank you to my friends from high school and undergrad; in particular Fraser Watt, my ice hockey and pub buddy.

Finally, I'd like to thank my family network who have provided encouragement and support not just during this PhD, but always. I hope we can celebrate together soon under more normal circumstances.

Research Thesis Submission

Please note this form should be bound into the submitted thesis.

Name:	Kerr Douglas Gordon Samson		
School:	EPS		
Version: *(i.e. First, Resubmission, Final)*	Final	Degree Sought:	Doctor of Philosophy

Declaration

In accordance with the appropriate regulations I hereby submit my thesis and I declare that:

1. The thesis embodies the results of my own work and has been composed by myself
2. Where appropriate, I have made acknowledgement of the work of others
3. The thesis is the correct version for submission and is the same version as any electronic versions submitted*.
4. My thesis for the award referred to, deposited in the Heriot-Watt University Library, should be made available for loan or photocopying and be available via the Institutional Repository, subject to such conditions as the Librarian may require
5. I understand that as a student of the University I am required to abide by the Regulations of the University and to conform to its discipline.
6. I confirm that the thesis has been verified against plagiarism via an approved plagiarism detection application e.g. Turnitin.

ONLY for submissions including published works

Please note you are only required to complete the Inclusion of Published Works Form (page 2) if your thesis contains published works)

7. Where the thesis contains published outputs under Regulation 6 (9.1.2) or Regulation 43 (9) these are accompanied by a critical review which accurately describes my contribution to the research and, for multi-author outputs, a signed declaration indicating the contribution of each author (complete)
8. Inclusion of published outputs under Regulation 6 (9.1.2) or Regulation 43 (9) shall not constitute plagiarism.

* *Please note that it is the responsibility of the candidate to ensure that the correct version of the thesis is submitted.*

Signature of Candidate:		Date:	03/07/2020

Submission

Submitted By *(name in capitals)*:	KERR DOUGLAS GORDON SAMSON
Signature of Individual Submitting:	
Date Submitted:	03/07/2020

For Completion in the Student Service Centre (SSC)

Limited Access	Requested	Yes		No		Approved	Yes		No	
E-thesis Submitted ***(mandatory for final theses)***										
Received in the SSC by *(name in capitals)*:						Date:				

Inclusion of Published Works

Please note you are only required to complete the Inclusion of Published Works Form if your thesis contains published works under Regulation 6 (9.1.2)

Declaration

This thesis contains one or more multi-author published works. In accordance with Regulation 6 (9.1.2) I hereby declare that the contributions of each author to these publications is as follows:

Citation details	e. g. Author 1 and Author 2, Title of paper, Title of Journal, X, XX-XX (20XX)
Author 1	Contribution....
Author 2	Contribution....
Signature:	
Date:	

Citation details	e. g. Author 1 and Author 2, Title of paper, Title of Journal, X, XX-XX (20XX)
Author 1	Contribution....
Author 2	Contribution....
Signature:	
Date:	

Citation details	e. g. Author 1 and Author 2, Title of paper, Title of Journal, X, XX-XX (20XX)
Author 1	Contribution....
Author 2	Contribution....
Signature:	
Date:	

Please included additional citations as required.

Contents

Chapter 1 – General introduction

1.1 Immunisation and vaccine delivery

Immunisation through the utilisation of vaccines is a pivotal component of modern healthcare systems, with availability of immunisation classed as a core component of the human right to health [1]. Licenced vaccines to prevent or control 25 different infections are available, and cover previously widespread diseases with high mortality rates, such as neonatal tetanus and tuberculosis [2]. The current standard for vaccine administration is injection via syringe and needle, with vaccines being administered via intramuscular, subcutaneous, or intradermal routes. For vaccines that require 'boosters', the bolus injectable approach requires the patient to receive further injections often weeks later in order to achieve reliable immunity. This need for multiple single bolus injections can have a negative effect on patient compliance, and creates logistical issues which are greatly exacerbated in developing countries [3]. Veterinary vaccination programmes can be very expensive, and in some cases unprofitable. The wage bill resulting from multiple visits by a veterinary team to deliver the initial and booster doses can be significantly more expensive than the combined total cost of all the doses [4]. Therefore, there is great interest in development of single administration vaccine (SAV) delivery devices or methods, not only to reduce costs but also to improve the efficacy of both human and animal vaccination programmes.

Development of new vaccine delivery technologies are recognised as an important part of the World Health Organisation's Global Vaccine Action Plan [2]. Development of non-injectable delivery routes such as oral and intranasal delivery have been attempted in order to address patient compliance [5]. Unfortunately, each new delivery route presents different problems to be overcome, such as mucosal membrane permeability or stability of antigenic material within gastrointestinal(GI) fluids when delivered using the oral route [6]. As such, only polio and rotavirus vaccines have licenced oral administration options [7], [8], and currently there is only a single intranasal vaccine on the market for influenza [9]. While these methods provide the advantage of not requiring injectables, progress on overcoming the harsh environment of the GI tract has not been swift, and they generally still require multiple administrations to achieve immunity.

Birrenbach and Speiser (1976) were the first to demonstrate evidence that novel controlled release forms of antigen delivery were effective at not only delivery of the

antigen to the immune system, but also the potential to increase the immune response against the associated antigen [10]. Shortly after, Preis and Langer (1979) proposed use of such controlled release technologies to simplify vaccination schedules, and went on to demonstrate the first sustained release vaccine delivery device in the form of an implantable degradable polymer/antigen pellet that was able to illicit prolonged antibody formation [11]. While these early delivery systems did not make it to the clinic due to their toxicity, they demonstrated a strong proof of concept which has driven the development of modern SAV systems [12]. The sustained interest in SAV approaches is due to their potential to eliminate the need for booster doses, and therefore could reduce the logistical costs and impact on point-of-care staff/facilities associated with repeat administrations. Furthermore, SAV systems have the ability to ensure the optimal time-delay between initial and future doses, resulting in better development of immunity against the desired pathogen. Similarly, use of a SAV system to deliver the doses of vaccine required in one appointment also eliminates the issue of patient non-compliance part of the way through a vaccination programme. The significance of the ability to immunise completely at first point of healthcare contact is highlighted by drop-out rates from vaccination programmes in developing countries. Such rates of individuals receiving the initial dose, but not returning for subsequent boosters, can reach 70 %. There are numerous potential reasons for these drop-out rates, with geographical and geopolitical issues such as difficulty in traveling to the clinic from isolated areas, areas experiencing war or political turmoil, or more personal reasons such as needle phobia, fear of side effects, or a general lack of faith in vaccination [13], [14]. Numerous SAV approach delivery platforms are currently being researched. Potential platforms include liposome vesicles, polymeric particles, inorganic nanoparticles, and self-exploding microcapsules [15]–[20]. While most of the systems listed above involve micro or nanoscale dispersions, an approach where the vaccine dose is stored within an osmotically active macroscale polymer implant was first published by Melchels *et al* [21].

Exploiting osmosis as the driving force for drug delivery is not a new concept, with initial designs such as the Rose-Nelson [22], where constant release was achieved through osmotic-induced swelling pushing drug through an orifice via a distended membrane, dating back to 1955. One of the main advantages of drug release from osmotic systems is that they are generally unaffected by the body's pH, presence of food or other physiological factors, resulting in excellent *in vitro to in vivo* bioequivalence [23]. However, osmotic systems are typically utilised in advanced oral delivery formats, rather

than implants. The elementary osmotic pump (EOP) developed by ALZA in 1974 as the OROS™ system was the first practical example of an osmotic pump-based drug release system for oral use. The original tablet consisted of an osmotic core containing the drug, surrounded by a semi-permeable membrane with a laser drilled orifice. Following ingestion, water is absorbed into the tablet, which dissolves the drug and swells the osmogent, resulting in the resulting solution being created and dispensed at the same rate as the water entering the tablet. The format has continued to be modernised with new generation devices based on the OROS™ concept being clinically approved for oral sustained-release of drug treatments across a wide range of therapeutic areas, including cardiology, endocrinology, urology, and neurology [23], [24]. Osmotic devices for delayed pulsatile release have been described where no orifice is made. Osmotic uptake generates a gradual increase in hydrostatic pressure within the device that operates the release trigger, which can be in the form of ejection of a plug, expansion of an orifice, or rupturing of a membrane allowing bolus release of drug [25]. Use of such devices for vaccine delivery has been suggested [26], and appropriate delay times have been shown for an injectable osmotic-implant system [27].

1.2 Device concept overview

The proposed device resembles a hollow tubular structure that is sealed at both open ends of the tube. The dimensions of the devices are proposed to be similar to the Implanon™ contraceptive device, approximately 30 mm long with an outer diameter of ~ 2 mm [28]. The internal space will contain the vaccine payload and an osmotically active solution (osmogent). The device will be implanted subdermally during the same appointment as the initial priming dose of vaccine. The capsule trigger method is depicted in the cartoon illustration shown in Figure 1.1.

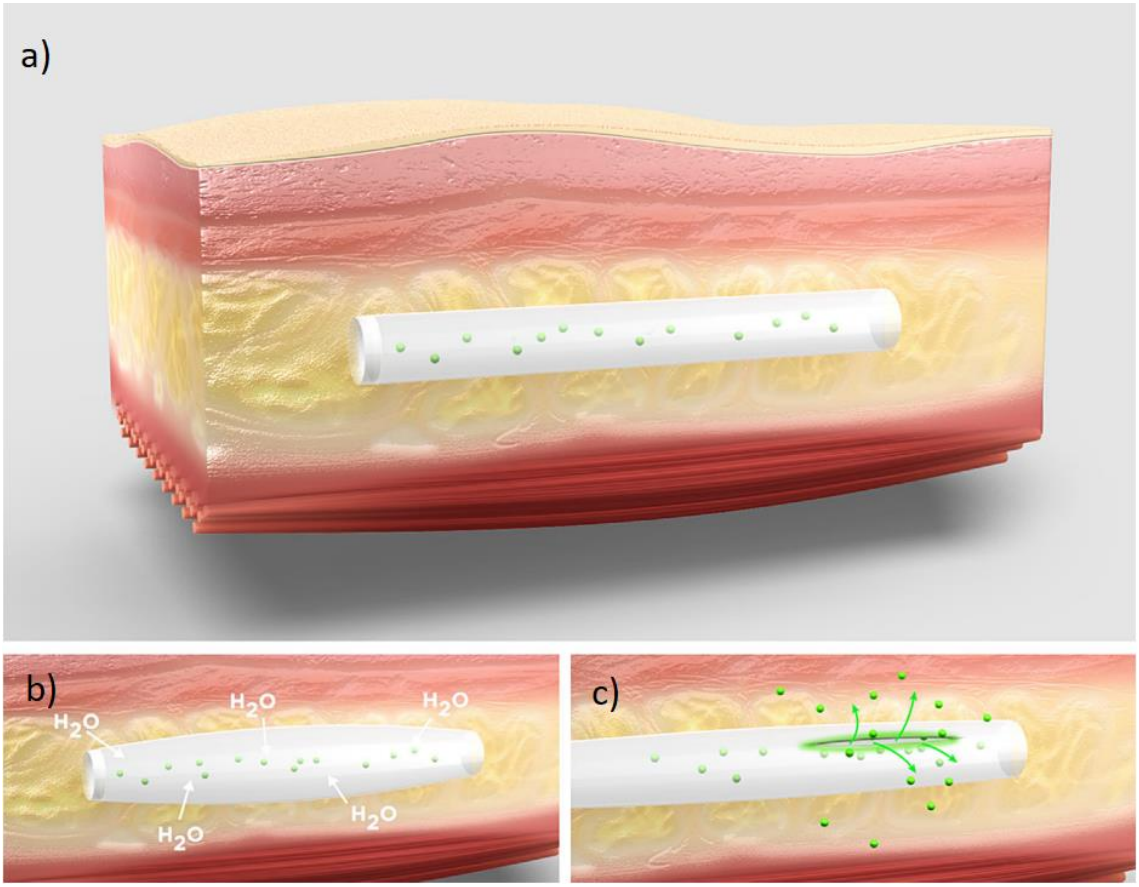

Figure 1.1:- a) schematic of a device implanted under the skin. b) osmosis-driven water uptake leads to an internal volume increase that swells the device. c) the internal hydrostatic pressure overcomes the burst strength of the device causing it to rupture, releasing the vaccine into the surrounding space. Images reproduced from Melchels et al [21].

The device walls function like a semi-permeable membrane; impermeable to the vaccine and osmogent, but permeable to water. The osmogent drives water uptake into the central compartment of the device at a rate dictated by primarily the material permeability, the osmogent concentration, and the device wall thickness. As the internal volume increases, and hydrostatic pressure rises, an increasing force is exerted on the walls of the devices. Ultimately, the increasing pressure will overcome the burst pressure of the devices and will burst, releasing the vaccine payload. Thus, the aforementioned characteristics also directly affect the delay to burst. The devices are constructed from a material capable of being biodegraded or bioresorbed after burst, eliminating the need for surgical removal. Similarly to orifice-based osmotic systems, it is expected that the osmotically driven devices will function independently of external factors [23], therefore presenting a reliable platform for vaccine delivery. Melchels *et al* demonstrated delayed burst release of a model dye from such devices, with an average delay of approximately 9 days. The authors also demonstrated that the delay time could be tailored through parameters relating to the capsule material, capsule geometry, and osmogent concentration [21].

1.3 Research motivation

The main motivation to this work was to develop and demonstrate a polymeric biomaterial device capable of storing and releasing a chosen payload in bulk after a reproducible and tunable delay period. The main shortcoming from Melchels *et al's* 1st generation devices was that at burst only a small pinhole was formed for payload to diffuse though, and so did not demonstrate the large bolus immediate-release desired. This work aimed to improve upon the 1st generation devices, by using a more flexible material which would burst in a manner more capable of immediate bolus dose release. This research would also deliver *in-vitro* evidence to support future *in-vivo* testing of such a device and its ability to deliver a vaccine to a live animal. Furthermore, this study would contribute to the material science field new photo-curable biomaterials suitable for the production of implantable biomedical devices that offer unique mechanical characteristics.

1.4 Aims and outline of the thesis

The aims of this thesis are:

- to develop new photo-crosslinkable resins (specifically based on polycaprolactone) that result in biocompatible, biodegradable materials, and can be processed by stereolithography.
- to characterise the resulting photo-crosslinked networks in an appropriate manner regarding general biomedical use, and also specifically regarding their suitability for developing novel vaccine delivery devices.
- to design, and manufacture prototype vaccine delivery devices produced from the developed resins and perform mechanical characterisation of the constructed devices.
- to perform *in vitro* osmotic burst testing of the crosslinked devices to demonstrate the capability of the devices to mimic the delayed bolus delivery of a booster injection, and compare them to 1st generation devices.

Chapter 2 contains a literature review covering the main themes and techniques that feature within this thesis. In particular, vaccine delivery systems, delivery systems for SAV, the fundamentals of osmotic-based drug release, structure-property relations for polymer networks, and how the devices could be manufactured, are reviewed.

Chapter 3 describes the preparation of functionalised poly(caprolactone)(PCL) macromonomers, the development of a method for the purification and recovery of low

(<1,500 g/mol) molecular weight PCL macromers, and the identification of a suitable non-reactive diluent for photo-curable resin formulations.

Chapter 4 describes the development of a series of PCL macromer-based photocurable resins and in particular a tough, degradable bimodal PCL network suitable for stereolithography 3D printing. The effect of molecular weight and distribution of chain length in polymer networks on mechanical properties and resin reactivity and 'green' part network development were investigated.

Chapter 5 presents the findings of *in-vitro* cytotoxicity assessments of our photo-crosslinked networks. Direct contact experiments were performed to evaluate any effect on the metabolic activity, and proliferation of human primary dermal fibroblasts cultured on the surfaces of the materials.

Chapter 6 describes the manufacture of the delivery devices through dip coating and stereolithography techniques. Characterisation of the wall thicknesses of the produced tubular parts is conducted by micro computerised tomography. Mechanical burst assessments are investigated as a method predicting osmotic burst behaviour, which is performed using universal testing apparatus.

Chapter 7 details the motivation behind the design and construction of a bespoke dip coating machine for the production of the tubular part of the delivery devices and details its construction and use. Evidence of tubes successfully produced using this machine is also shown.

Chapter 8 describes the *in-vitro* osmotic dye release study of prototype photo-cured vaccine delivery devices. Devices are compared with thermoplastic devices similar to those used in the initial concept paper [21] to investigate the effect of chemical/permanent crosslinking on the device's osmotic and burst behaviours. The rate of water uptake, delay to burst, release at the moment of burst, and total release are assessed and discussed.

Chapter 9 summarises the main findings of the work presented within this thesis, discusses and lays out recommendations for future work.

Chapter 2 – State of the art

2.1 Vaccine delivery systems

The hypodermic needle is the current gold standard of vaccine delivery technology due to offering a direct, low cost method, with instant verification of dose delivery. Bolus-dose injections have demonstrated an excellent efficacy profile over decades of use, despite limitations such as pain and needle phobia which can be detrimental to patient compliance. In some developing or 3rd world countries, vaccine coverage can be low due to failure in booster follow-up, or a lack of trained personnel or facilities [29]. Additionally, such follow-ups can be highly expensive in a veterinary setting. Thus, methods of delivering antigenic material in a controlled manner from a system that can be injected/implanted in a single appointment would be advantageous. Examples of the SAV methods in the literature are discussed below, as well as other novel vaccine delivery methods being proposed.

2.1.1 Polymer particles

Polymeric particles form the main focus for development of SAV systems [15], [30]. The concept typically involves encapsulation of antigen in a biodegradable polymer matrix. Release from such particles typically show either a continuous or pulsatile profile due to degradation erosion of the polymer. For continuous release particles, the profile is typically biphasic, while the pulsatile release particles show triphasic profiles [31]. The initial release stage of both variants is typically due to release of loosely bound antigenic material near the surfaces of the particles. For continuous release particles, this transitions into a period of zero-order release, while for pulsatile particles there is typically a lag-phase where minimal release occurs, followed by a significant burst release [30], [31]. A wide range of natural and synthetic polymers have been used to make vaccine delivery particles, such as poly (D,L-lactic-coglycolic acid)(PGLA), poly(lactic acid) (PLA), alginate, starch, and dextran [15], [32]–[34]. Most particle formulations developed feature the continuous release profile [35], [36]. However, there is currently no evidence from human clinical trials that demonstrate whether continuous release of antigenic material can achieve an equal level of immune system stimulation to typical pulsatile methods [30]. Some particle design considerations for pulsatile antigen release can contrast with those for continuous release methods. One such consideration is that the delayed release pulsatile particles must persist within the body for the desired time with minimal antigen release or loss. This is typically achieved through very low concentrations of antigen

payload, so that large barriers of polymer slow or prevent diffusion [37]. Additionally, the carrier particle should be immunologically inert to prevent recognition and premature clearance by the immune system prior to payload release [30]. One of the more recent examples of pulsatile microparticle antigen delivery was able to replicate 3 antigen pluses *in vitro* mimicking the kinetics of 3 bolus doses in a clinical setting. The PLGA particles from the same study were also able to approximately match antibody titre development over time, and peak antibody titres produced by 3 bolus vaccine injections [38]. While the feasibility of vaccine encapsulation within degradable polymers for SAVE purposes have been shown in many studies, particle systems are yet to show convincing utility in clinical trials [30]. A disadvantage of this approach is that mixing of the polymer with the antigenic material to produce the loaded particles typically involves harsh conditions, including high temperatures, organic solvents (methylene chloride), and freeze drying, all of which have been shown to affect antigen conformation [39]. Additionally, particle antigen-loading efficiencies are typically low, and the more desirable pulsatile-profile particles often fail to release the complete dose upon burst. This low efficiency also has a negative impact on projected cost of such an approach.

2.1.2 Liposome vesicles

Since the ability of antigen-laden liposomes to induce immune responses was first demonstrated by Gregoriadis and Allison [40], the field of liposomes and liposome-based vaccines has become one of the most widely researched vaccine development systems [16]. The field includes liposome-derived nanovesicles such as archaeosomes and virosomes. The liposome construct encapsulates the antigenic material payload within a bilayer phospholipid bilayer sphere, or can be incorporated into the membrane itself, or by surface attachment on the membrane [33]. Stability enhancing polymers (such as poly(ethylene glycol)(PEG), and charged membrane-associated adjuvants that affect how liposomes behave *in vivo* are also typical components. A key advantage of liposomes and their associated derivatives is their versatility through the adjustability of their physicochemical attributes, which enables them to be tailored for individual applications [15]. Typically changes in surface charge, membrane fluidity, overall size, and location of loaded antigen can significantly alter the vaccine delivery functionality of the liposome system. Subsequently, this customisability also introduces a significant degree of complexity. Liposome-based vaccines for hepatitis A (Epaxal®) [41] and influenza (Inflexal®) [42] have been approved for use in humans, however liposomal delivery systems still have some outstanding concerns. Many novel liposome systems feature

synthetic materials which may generate cytotoxic effects *in vivo*. Furthermore, most liposomal systems do not have long-term safety profiles in animal models, let alone human use [43]. Long term storage stability is also a concern, due to often being customised with functional materials that are environment sensitive. Manufacturing scale up of the multi-level liposomal modifications required is of practical difficulty, due to the number of complex steps required, and severe batch variation. Use of expensive materials to modify the liposomes may price any clinically successful liposome system out of the market. Additionally, like many areas of the drug development field [44], liposome vaccine delivery research suffers from prevalence of low reproducibility of published outcomes.

2.1.3 Self-exploding microcapsules

De Geest *et al's* microcapsule concept involves a degradable hydrogel core surrounded by a semi-permeable polyelectrolyte membrane [3], [45], [46]. Microcapsule have been explored previously for drug release, but typically involve an external trigger mechanism such as an electric field [47], IR light [48], or pH [49]. The payload-laden core was constructed from a crosslinked dextran-hydroxyethyl methacrylate (dex-HEMA) network. Degradability was incorporated by activating HEMA with 1,1'-carbonyldiimidazole (CDI), which following conjugation to dextran, results in formation of carbonate esters that are able to be hydrolysed under physiological conditions [20]. The outer semi-permeable membrane enables influx of water to the core, while retaining the core materials and payload within the microcapsule. The microcapsule releases the antigenic material through osmotic swelling and degradation of the hydrogel core so that it bursts through the membrane outer layer. The rate upon which the swelling occurs is regulated by crosslinking density of the dex-HEMA core. A release profile with separate pulsed waves of antigen release was theoretically possible by injecting populations of microcapsules with sets of dex-HEMA hydrogels with varied crosslinking densities. Unfortunately, the polyelectrolyte shell of the capsules was prone to infiltration and degradation by recruited inflammatory cells, which caused early rupture of the capsules and led to disruption of the desired controlled release profile of the payload [50]. The osmotically active microcapsules also possessed other limitations such as the burst times being highly sensitive to variations in size of the capsules, and potential redistribution throughout, or clearance from the body. Additionally, in the case of an adverse event, due to their size and distribution it would be impossible to remove the particles.

By removing the dex-HEMA osmotic core, an alternative approach of antigen presentation directly to dendritic cells was tested. An *in vitro* antigen presentation assay demonstrated that dendritic cells actively uptake the polyelectrolyte microcapsules, which then rupture within endolysomal vesicles where the antigen is released and processed. It was shown that the capsules could efficiently stimulate CD4 and CD8 T-cell proliferation by this method [51], [52].

2.1.4 Inorganic particles

Despite their low degradability, many inorganic micro- and nanoparticle-based vaccine systems have been researched due to the excellent level of control over their synthesis [53], [54]. Gold particles are highly stable and extensively modifiable enabling relatively straightforward antigen conjugation [55], [56]. Carbon particles are rapidly taken up by antigen-presenting cells and are capable of carrying multiple antigens simultaneously [57]. Mesoporous carbon spheres are being investigated as potential oral vaccination systems [58]. Calcium phosphate particles are a promising candidate for vaccine delivery systems as they are bioresorbable, non-toxic, and easily loaded with antigenic material [59]. Calcium phosphate was used as an adjuvant in a series of commercialised vaccines in France, but was replaced by aluminium salts in the 1980s, and later disregarded due to the success of the aluminium adjuvants [60]. It has been suggested in recent years that calcium phosphate may return to replace the aluminium adjuvants in current vaccines due to toxicity and side-effect concerns. Aluminium particles have been researched for use as antigen-carrying particles themselves. Studies shown that the aluminium particles are able to simultaneously act as the delivery system and adjuvant. However, it was also been shown that the antigenic material adsorbed by the aluminium can be bound so tightly that the protein structure of the antigen is altered, ultimately reducing vaccine efficacy.

2.1.5 Osmotic spherical capsules

Early work on spherical osmotic capsules were recently demonstrated as a potential delayed-release drug delivery system [61]. Biodegradable poly(lactic acid-co-glycolic acid)(PLGA) was used to construct the outer spherical shell with a radius of between 1.5 and 2.2 mm. The internal space contained a saturated salt solution of sodium chloride or lithium chloride, which were used as osmogents to drive water uptake into the capsule at a controlled rate, alongside a payload. The capsule function through an increase in hydrostatic pressure generated by the water influx, which eventually overcomes the tensile strength of the outer PLGA shell resulting in release of the payload. Therefore,

these spherical capsules operate in a highly similar manner to the tubular monolithic capsules described by Melchels *et al* [21] and those proposed within this thesis. Multiple spherical capsules would be employed to provide pulsatile release profiles over a series of time points. *In vitro* testing indicated that the delay time could be adjusted between approximately 1.5 – 17 days by changing the osmogent solution, capsule radius, and shell thickness. However, the current manufacturing process is laborious and uses organic solvents during encapsulation of the osmogent and payload, which may destroy the antigenic compound. Additionally, beyond the 10 day mark it was found that the capsule burst point deviated from predictions and was attributed to significant degradation of the PLGA shell.

2.1.6 Outer membrane vesicles

Outer membrane vesicles (OMVs) are naturally occurring, non-replicating vesicles derived from Gram-negative bacteria [62]. OMVs generally consist of bacterial phospholipids, lipopolysaccharides, outer membrane proteins and entrapped periplasmic components, depending on the host bacteria species, which give OMVs inherent immunostimulatory properties [63]. Desired antigenic material can be present either on the surface, inside the lumen of the vesicle or unbound in the contained solution. However, strong immune responses against the platform backbone have been reported, while other issues are due to the heterogeneity of the vesicle product populations, which introduces complications in processing during manufacture [62]. At present, two outer membrane vesicle vaccines (Bexsero [64] and Trumenba [65]) for meningitis B are licensed for human use and are delivered via intramuscular injection.

2.1.7 Other novel approaches to vaccine delivery

Plant and algae cells have been researched as oral vaccine delivery platforms due to the potential ease and low cost to vaccinate large populations [15], [66]. The tough cell walls are able to protect intracellular material from the harsh GI tract environments that often pose as a major complication for other oral delivery systems. The cell wall is able to be digested by microbes that colonise the intestines, releasing the antigenic payload [67].

Both plant-, and algae-based systems are subject to variance in the reliability of the immunogenic response generated due to the complexity and diversity of the gut microbiome [15]. Additionally, poor expression yields of antigenic material within transgenic cells is also a concern [66]. Separately, pollen grains have been investigated as an oral vaccine delivery platform due to the outer shell of the grain being shown to be

able to survive the harsh conditions of the stomach [68]. While systemic and mucosal responses could be generated from antigenic material within pollen grains [69], [70], a greater knowledge of the molecular mechanisms behind the internalisation and interactions of the pollen particle and immune cells is required. Microarray patches (MAP) consists of a cluster of tens to thousands of projections less than one millimetre in length attached to a backing that can be applied to the skin typically with finger pressure or an applicator. While a series of MAPs are in preclinical, and one in clinical stage trials, to date no microarray technology has been FDA-approved for the delivery of a vaccine [71]. Barriers to approval currently include skin irritation, confirmation of doses delivered, and compatibility of the antigenic material with the microneedle manufacturing process [15]. Another, drawback is that even if it is proven to be an effective approach it is difficult to identify a market due to the MAP approach likely to cost more than any existing product [71].

2.1.8 The monolithic capsule

The initial concept of the monolithic osmosis-driven delayed vaccine delivery device was first described by Melchels *et al* [21]. An overview of the device was shown in Section 1.2. The device uses water uptake as the delay mechanism and trigger to release a bolus booster dose of vaccine. Such a method offers a series of advantages when compared with microparticles and self-exploding microcapsules, shown in Table 2.1.

	Microparticles	Self-exploding microcapsules	Monolithic osmotic capsules
Tailoring delay time	+	-	++
Exposure of antigen to harsh conditions	-	+	+
Pulse-like delivery	-	+	++
Dependence on physiological factors	-	-	+
Sterilisation	-	-	+
Ease of administration	+	+	-
Removal if adverse reaction	-	-	+
Cost	-	-	++

Table 2.1:- Comparison of advantages and disadvantages of monolithic osmosis driven delayed burst release capsules compared to microparticles and self-exploding microcapsules for vaccine delivery. Reproduced from Melchels et al [21].

One of the main advantages of the monolithic capsule is that the device itself is developed and prepared independently from the payload, and so the devices could potentially be loaded with a variety of different payloads to suit different purposes without extensive redesigns or adjustments to loading. Due to the capsule being largely manufactured prior to filling with payload and osmogent, the antigenic payload will be exposed to minimal processing in comparison to those required (heat/organic solvents) for polymer microparticles. The main disadvantage of the monolithic capsule approach is the method of administration due to the size of the device. The capsule requires use of a large diameter needle to be implanted under the skin. However, a device with similar geometry marketed as Implanon™ contraceptive is currently being used successfully in women, where the application via a needle and plunger is performed by nurses and general practitioners without the need for specific training. Implanon is termed a "single rod subdermal implant", where the rod is 40 mm long with a diameter of 2 mm. Progestin etonogestrel is continuously released from the device through rate controlling membrane of ethylene vinyl acetate for up to 3 years. The Implanon device is not biodegradable, and therefore must be removed through an incision through which the device can be extracted using forceps. From large scale post marketing surveillance studies, Implanon has been found to be a highly effective drug delivery system with low complication incidence rates and severities [28], [72]–[75]. The device geometry, positioning, and implantation procedure have been demonstrated to be acceptable to patients, with the main insertion complication being local skin irritation which occurred in less than 5 % of women [28], [72], [75]. A disadvantage relating specifically to the osmotic capsules is the possibility of cell necrosis resulting from local hypertonicity after burst, due to release of the osmogent into the local tissue. This is expected to be transient however, as local isotonicity would be re-established. The osmotic delivery devices will be constructed from a biodegradable/bioresorbable material, thus eliminating the need for surgical removal as is required with Implanon.

A previous attempt at a monolithic delayed-burst delivery device was proposed by Barr and Thiel in 1992 [27]. The payload was integrated into a core of solidum starch glycolate, coated with a pH-sensitive Eudragit S 100 film. An outer coating of insoluble Eudragit NE30D mixed with hydroxypropyl-methylcellulose (HPMC) as pore former was applied. When introduced to an aqueous environment, the HPMC in the outer coat dissolved, allowing water to access the S 100 coating underneath, which dissolves at tissue pH. This allows water to penetrate and swell the inner core, completely rupturing the outer NE30D

membrane and releasing antigen payload. This device concept was last referred to within a review by Stubbe *et al* in 2004 [26], however no further literature on the device has been found.

This thesis aims to build upon the work by Melchels *et al* through the development of the next (2^{nd}) generation of osmosis-driven burst-release capsules.

2.2 Osmotic uptake and burst mechanics

2.2.1 Osmotic water uptake

A simplified one-dimensional process of osmotic water uptake into the internal compartment of the device can be described in terms of Fick's laws. The driving force behind the transport process which involves sorption, diffusion, and permeation is the concentration difference between the external and internal phases. An example of osmotic flux through a water-permeable polymer membrane (wall) is shown in Figure 2.1.

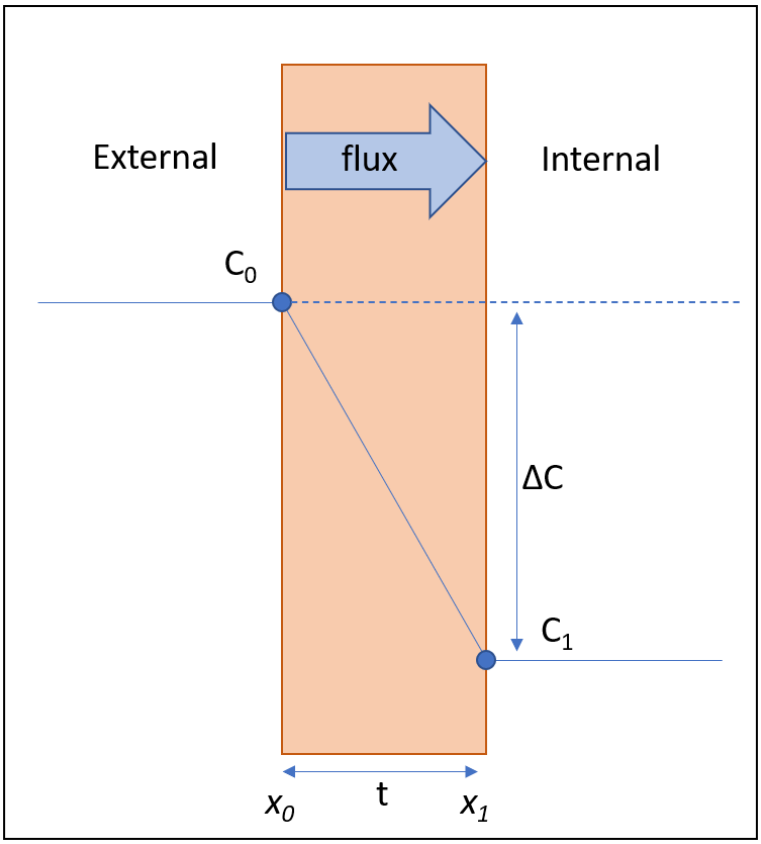

Figure 2.1:- Flux of water across a polymer wall of thickness t driven by the concentration gradient ΔC.

Fick's first law describes this process, where the rate of mass transfer or flux (J) is proportional to the concentration gradient ($\delta C/\delta x$), and the proportionality constant is the diffusion coefficient of the diffusing species through the polymer (D):

$$J = -D\frac{\partial C}{\partial x} \qquad \text{Equation 2-1}$$

Fick's first law is only applicable to diffusion in the steady state.

By integrating Fick's first law we attain a formula that can be used to approximate diffusivity through a membrane [76], shown in Equation 2-2, where, *t* is the thickness of the wall and C_2 and C_1 are respectively the concentration of water at the downstream and upstream polymer surfaces.:

$$J = -\frac{D(C_2 - C_1)}{t} \qquad \text{Equation 2-2}$$

We can introduce the sorption equilibrium parameter (*S*) into Equation 2-2, to form Equation 2-4, through the relationship in Equation 2-3. *S* is the constant of proportionality between pressure (*p*) and concentration (*C)*.

$$C = Sp \qquad \text{Equation 2-3}$$

$$J = -\frac{DS(C_2 - C_1)}{t} \qquad \text{Equation 2-4}$$

The diffusion coefficient (D) can be combined with the sorption equilibrium parameter (s) to get the final form of the equation:

$$Pw = DS \qquad \text{Equation 2-5}$$

$$J = -\frac{P_w(p_2 - p_1)}{t} \qquad \text{Equation 2-6}$$

Where *J* is the diffusion flux, P_w is the permeability of the polymer wall, and *p* represents the pressure on each side of the wall. Use of a polymer with different water uptake equilibria is a method of adjusting the burst delay time.

The osmotic pressure generated by the concentrated osmogent within the capsule can be calculated. The Van't Hoff equation (Equation 2-7) is only suitable for dilute mixtures, therefore the Granik *et al* theory and associated equation (Equation 2-8) [77] can be used:

$$\pi = RTC_2 \qquad \text{Equation 2-7}$$

$$\pi = \frac{RTm_2'V}{\left[1 + (1+V)\frac{m_2'}{m_1'}\right]} \qquad \text{Equation 2-8}$$

Where, R is the gas constant, T is the temperature in kelvin, C2 is the solute molar concentration, V is the volume of a solution of m2 moles of solute dissolved in 1 L of

solvent, and m'1 and m'2 are the solute molal concentrations of solute and solvent respectively. Through modulation of the loaded osmogent concentration, the osmotic pressure can be varied as a possible method of controlling the delay to burst, however it has been previously shown that lower osmotic pressures can introduce burst variance [21].

2.2.2 Burst mechanics

As translocated water driven by osmotic uptake fills the space within the device, an internal pressure is produced and exerts stress on the material comprising the cylinder walls in all directions. The device is considered a perfect, straight cylinder with homogenous wall thickness throughout, and the plugs/caps that seal the open ends are assumed to stay flat under load. Only the deformation of the tubular part is considered due to the capsule length being substantially larger than the diameter ($L >> D$). For simplicity, the device is considered a thin walled pressure vessel and therefore radial stress is assumed to be substantially smaller than circumferential stress and can be ignored.

The stress in the axial (σ_z) and circumferential (σ_θ) direction can be described by Barlow's formulae [78], where P is the internal hydrostatic pressure, t is the wall thickness, and r is the outer radius of the tubular part, respectively:

$$\sigma_z = \frac{Pr}{2t} \qquad \text{Equation 2-9}$$

$$\sigma_\theta = \frac{Pr}{t} \qquad \text{Equation 2-10}$$

As indicated by the denominator, the stress in the circumferential direction is twice as large as the stress in the axial direction, and therefore burst can be expected along the tubular part rather than the end caps.

By rearranging Equation 2-10 the pressure at which the tubular part will burst (P_{burst}) can be estimated from:

$$P_{burst} = \frac{2\,S_u\,t}{D} \qquad \text{Equation 2-11}$$

Where, S_u is the ultimate strength of the material, and D is the outer diameter of the device. From Equation 2-11, it can be shown that burst pressure decreases as diameter increases, making this another possible parameter to control the burst delay time with. Additionally, Melchels *et al* experimentally confirmed the linear correlation of burst pressure with wall

thickness for PCL tubes [21]. While the equations above are not utilised to model the device burst within this thesis, they provide a basis to what we expect and observe from device burst testing.

2.3 Polycaprolactone

2.3.1 Physiochemical properties and biomedical use

Polycaprolactone (PCL) is a semi-crystalline, biodegradable polymer with low glass transition (- 60 ^{o}C) and melting temperatures (~ 60 ^{o}C). The degree of crystallinity tends to increase with increasing molecular weight. PCL offers superior rheological and viscoelastic properties over other resorbable polymers, which make the material highly processable. The attractiveness of PCL for medical device development is aided by the presence of PCL-containing medical devices already FDA approved and CE Mark registered, which enables a faster route to market [79]. One such example is the slow degrading monofilament suture marketed under the name MONOCRYL® [80]. Other biomedical applications of PCL devices include degradable cardiovascular stents[81], [82], tissue scaffolds [83], nerve guidance conduits [84], contraceptive devices [85], and as a root canal filler in dentistry [86], [87].

2.3.2 PCL networks and stereolithography 3D printing

To enable network formation, PCL oligomers have been modified with functionalised end groups containing an unsaturated moiety such as an acrylate [88]–[90], methacrylate [91] or fumarate [92], [93] group to form macromers. To be photo-cured the macromers must be in the liquid state, which is achieved via heat or use of a diluent, and be mixed with a photo-initiator. To date, only photo-curing of low M_w PCL-macromers (300-6,000 g/mol) have been reported. The resulting networks have been amorphous, and demonstrate tougher mechanical properties as M_w increases [88], [91]. Elomaa *et al* was first to print a network with low M_w trifunctional PCL-macromers in the melt [91]. Green *et al*, more recently demonstrated printing of low M_w bi- and trifunctional PCL-macromers formulated into a resin using dioxane as a diluent [88]. Both studies performed *in vitro* cytotoxicity studies that indicate the photo-cured PCL networks are non-toxic and allow cells to proliferate. Furthermore, Green *et al* implanted thin film networks to the subretinal area of one eye in five pigs. One month after the surgery, none of the eyes showed evidence of intraocular inflammation, and all the retinas had reattached, with preservation of the retinal layers adjacent to the implant [88].

2.3.3 PCL degradation

Degradation of PCL *in vivo* proceeds through a two-stage degradation process. The first stage involves predominantly non-enzymatic hydrolytic cleavage of ester groups, while the second stage involves intracellular degradation of sub 3,000 M_w chains after uptake by macrophages, giant cells, and fibroblasts [94]. Due to the hydrophobicity of PCL, degradation both *in vivo* and *in vitro* can take between 2-4 years, depending on the initial molecular weight and crystallinity [79]. To study PCL degradation within more acceptable time frames, use of acidic or alkaline pH environments and/or temperature to accelerate the rate of degradation can be performed. Different variants of these accelerated methods are evaluated within a recent review by Bartnikowski *et al* [95]. Studies most commonly utilise alkaline solutions and elevated temperatures, which can bring degradation times of high molecular weight oligomer structures, or crosslinked networks, down to hours instead of years [96]–[98].

2.4 Biological evaluation of biomedical devices and their materials

2.4.1 Overview

Medical devices and the materials they are composed of need to be evaluated for their safety within the context of a biological risk management process. The guidance for the biological safety evaluation of medical devices is presented within the ISO 10993 standard framework [99]. By aiming for inherent safety by design (sometimes referred to as quality by design [QbD]), the risks should be controlled by eliminating or minimising them to the greatest extent possible. This applies not only to the finished product, but to the manufacturing process as well. *In vitro* cytotoxicity studies are the preferred primary evaluation method as they are fast, simple, and highly sensitive tests can that identify toxic components during early stage pilot studies which can then feedback into the manufacturing process [100]. Use of such tests at an early stage also minimises the use of animal models for preliminary testing [101]. The cytotoxic evaluation specific guidelines are presented within ISO 10993-5 [102].

2.4.2 Commonly used cytotoxicity assays

Cytotoxicity and cell viability assays typically fall into the following classifications based on their measurement types of end points, colourimetric, fluorometric, or luminometric.

Perhaps the most commonly used assay is the colourimetric MTT assay, which determines cell viability through reduction of the dye to a purple formazan product by the intracellular mitochondrial enzymes of viable cells. The degree of formazan production

is used to indicate the extent of cell viability. The main disadvantage of the MTT assay is the formazan product is water-insoluble and requires a 2nd step to solubilise the formazan into a solution so that the absorbance can be taken [103]. This disadvantage can be overcome through use of similar colourimetric assays such as XTT, MTS and the WSTs, where the converted dye product is water soluble, and therefore no solubilisation step is required. These assays are very similar, and feature negatively charged dyes that prevent penetration into the cell and are therefore used in conjunction with an intermediate electron acceptor which reduces the dye extracellularly or at the cell membrane. These assays are generally regarded as being less toxic than other assays that require intracellular dye reduction; however, the potentially toxic nature of the co-administered intermediate electron acceptor likely makes this advantage small [104]. Another colourimetric assay is the lactate dehydrogenase (LDH) assay. LDH enzyme is released from cells with damaged membranes, therefore as cell viability reduces, LDH concentration in the media will increase. Addition of a tetrazolium salt to the media initiates a coupled enzymatic reaction that ultimately results in production of a red formazan product. The absorbance of the solution can be quantified and used as an indicator of cell death. The major limitation of this assay is that serum and some other compounds have inherent LDH activity, and therefore can generate substantial background absorbance [103]. The resazurin reduction assays are a common example of fluorometric assays and are often synonymously referred to using the commercial trademark name Alamar Blue (AB). The AB assay functions through reduction of a cell permeable indicator resazurin to resorufin by viable cells [105]. AB is generally regarded as being more sensitive than the tetrazolium assays, providing there is no fluorescent interference from test compounds or sample materials [103]. The ATP assay is an example of a luminometric assay. The ATP assay is based on the oxidisation of luciferin to oxyluciferin, which is catalysed through the enzyme luciferase in the presence of Mg^{2+} ions and ATP. The catalysed reaction produces light (bioluminescence) that can be quantified using a plate reader. Due to the high sensitivity of the assay, the main limitation is the reproducibility of pipetting replicates rather than through the assay chemistry itself [103]. The above assays cover the more commonly used assays for cell viability and cytotoxicity estimation. It is important to note that each assay has its own set of advantages and disadvantages. However regardless of the assay method chosen, major factors such as a consistent cell population, determination and use of the optimal reagent

incubation times and concentrations, and ensuring interfering components are eliminated or kept to a minimum, are essential.

2.4.3 Requirements for the implantable medical device

The monolithic delivery capsule is classified as a long-term implantable device as the contact time of the device with surrounding issues will exceed 30 days, considering the estimated degradation time of the device. Devices within this category generally require a total of 11 endpoints of biological evaluation to be assessed, such as cytotoxicity, carcinogenicity, genotoxicity, irritation or intracutaneous reactivity, and implantation site effects. Information regarding the physical and chemical nature of the materials used in the device and its manufacture are also required. Assessment can be satisfied through the use of existing data, or presentation of a rationale for why a specific endpoint does not apply. In the case of novel materials that have not been previously used in similar medical device applications and where no toxicological data exists in the literature, specific endpoint testing is required. While the ISO guidelines do not stipulate that the device implanted must be biodegradable/bioresorbable, such a property is typically viewed as positive due to the elimination of the necessity to surgically remove a non-degradable device after it has performed the desired function. In the case of a degrading material/device, the degradation products require characterisation and biological evaluation with regards to the same endpoints are the bulk material or device.

2.5 Dip coating

Dip coating is a common bulk manufacturing process often used to produce coated fabrics and for adding friction materials or corrosion protection to metal tooling. In its most basic form, dip coating involves submerging a substrate in a solution and then lifting the substrate out from the solution, which causes a wet film to be deposited on the substrate surface. In industry, dip coating typically involves immersion of the desired part in thermoset polymer materials, which are baked on to the object. In biomedical research, dip coating can be used to deposit thin film coatings to fabricate biosensors, and tissue engineering implants [106], [107]. While appearing simplistic, the dip-coating process involves a complex combination of often counteracting factors, such as the immersion time, number of dipping cycles, solution composition, the speed of substrate removal from the vat, viscous drag from the liquid during removal, among many others [108].

2.6 Stereolithography 3D printing

2.6.1 Introduction to stereolithography

Stereolithography (STL) was the first additive manufacturing (AM) technology developed [109], [110]. STL technology falls under what is typically referred to as 3D printing, which is a blanket term encompassing all AM technologies. 3D printing technologies produce the final 3D object typically through the layer-by-layer creation and subsequent joining of cross-sectional slices in a repeated manner. The process of printing a part or model by 3D printing, including STL, can be summarised in a few steps. Firstly, a computer aided design (CAD) of the desired part created or obtained. The CAD file is then converted into a format that can be understood by the printer software/firmware. This file format is typically a ".stl" file. The print settings such as the layer thickness or speed of the printer mechanical movements are then chosen. Finally, the print is initiated, and the printer autonomously manufactures the part. Modern 3D printers are generally pre-optimised for a specific brand or set of materials, which when used together require little user input or supervision.

While sharing the generic manner of operation with other 3D printing techniques, in most other ways STL is quite different from other technologies. STL utilises spatially controlled light irradiation to cure a liquid photo-polymerisable resin into a solid. The resins are typically composed of highly reactive, low molecular weight monomers and/or polymers, reactive diluents, photo-initiators and photo-absorbers. The curing process occurs through photo-initiated radial polymerisation to produce a crosslinked thin layer, generally between 10 – 100 μm thick. The light source and build platform that the printed structure is built upon are computer controlled. The first layer pattern solidifies the resin and adheres to a build platform which is then moved by the desired layer thickness to make space for the next layer. Fresh resin flows into the space or recoats the build head ready for the next layer to be photo-cured. Each new layer crosslinks into the previous layer and is repeated many times, which ultimately generates one 3D highly crosslinked polymeric network. After completion of the print, excess resin is washed off of the printed part to obtain the 'as-fabricated' (or green) part. The green structure is usually only partly cured, and so post-curing is often performed to improve the mechanical properties of the parts.

STL printers come in two main orientations. The 'bottom-up' orientation was the original format when the apparatus was first designed. A cartoon diagram of this arrangement is shown in Figure 2.2.

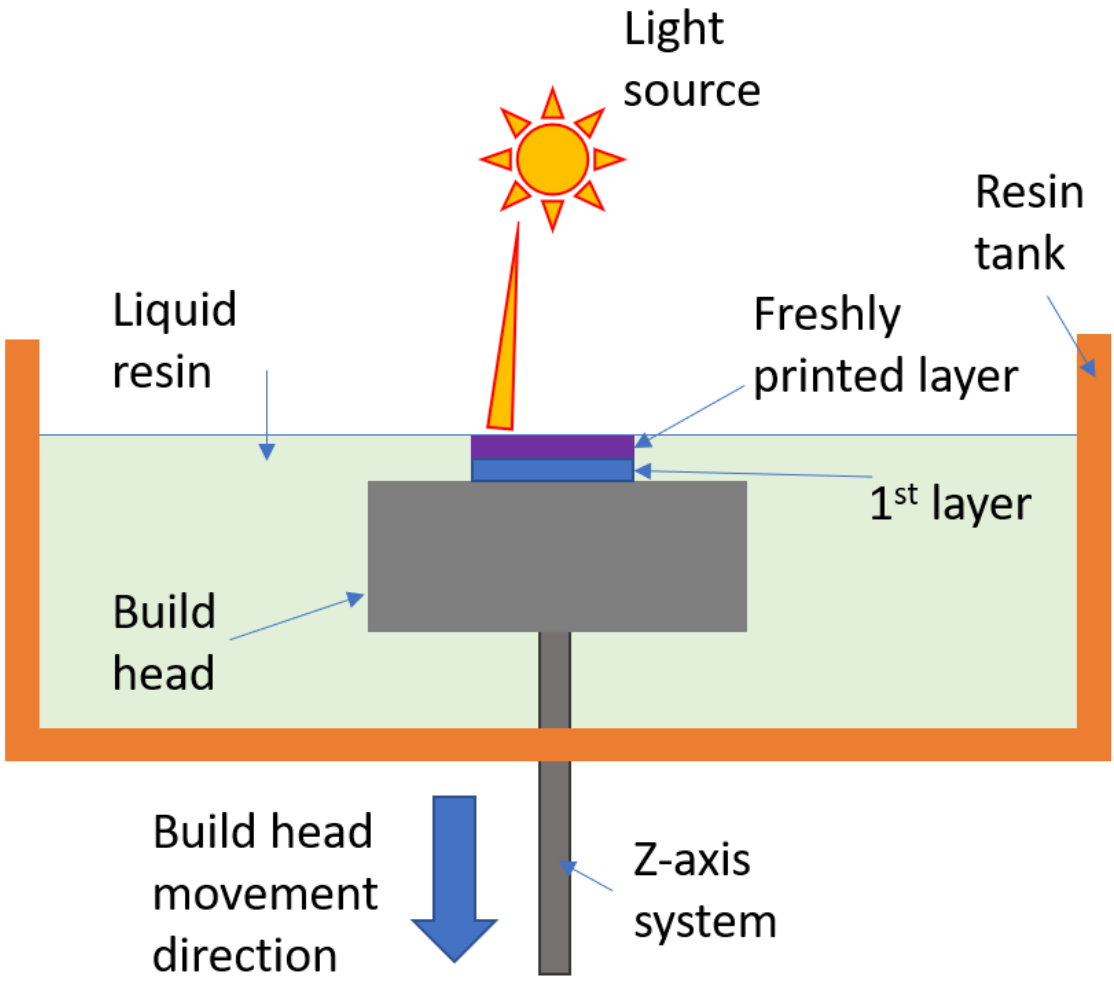

Figure 2.2:- A cartoon schematic of 'bottom-up' stereolithography printing.

The 'bottom-up' arrangement involves a build platform submerged within the vat of resin, where the surface of the build platform rests just below the resin surface. The light source above illuminates the remaining thin layer of resin between the resin surface and the build head surface. The build head is then retracted further into the resin vat, ready for the next thin layer to be illuminated and cured. This process is then repeated until the entire model is built. The alternative 'top-down' printing arrangement is shown in Figure 2.3.

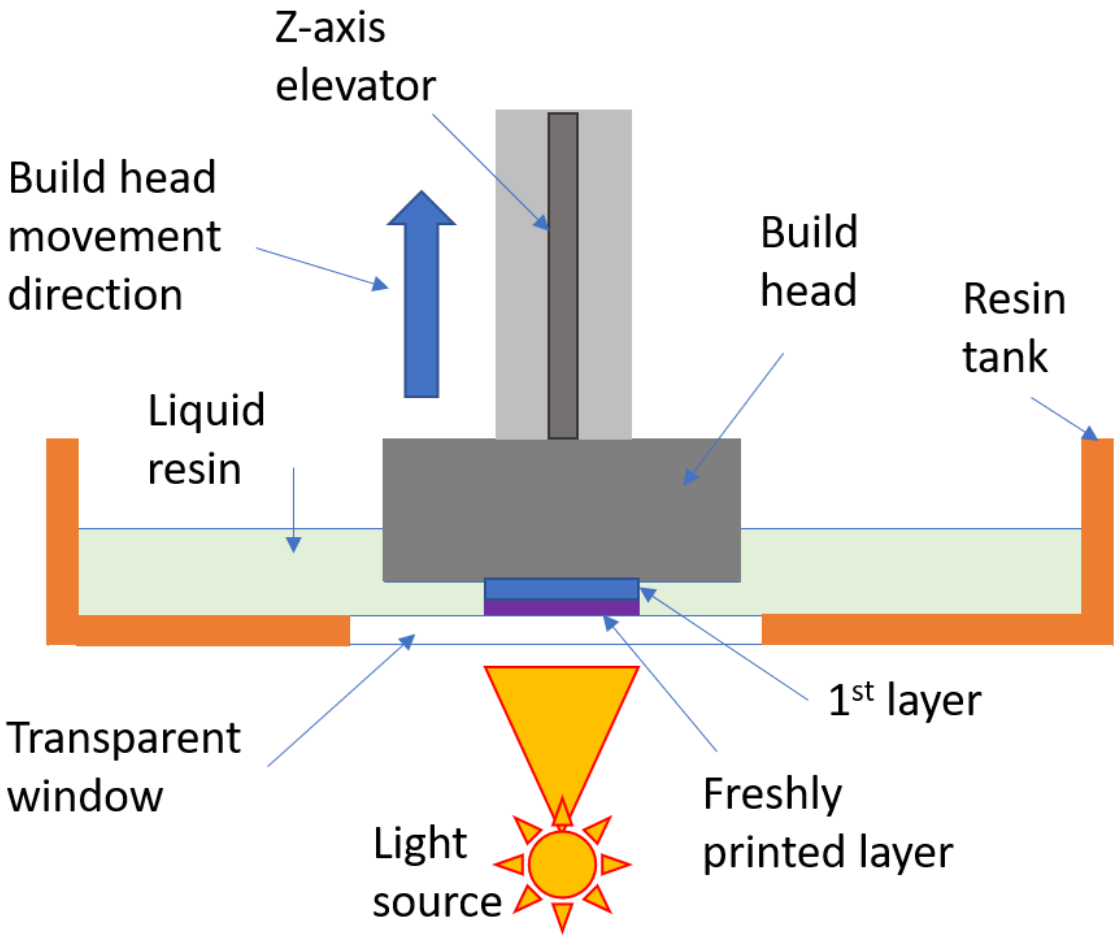

Figure 2.3:- Cartoon schematic of a 'top-down' stereolithography system.

The 'top-down' method involves light being illuminated through a transparent window on the bottom of the resin vat, while the build head rests within the liquid resin so that only a thin layer of resin is trapped between the platform surface and the inner window surface. This orientation is becoming more common on modern STL printers. While structures printed on 'top-down' STL printers are subjected to larger mechanical forces during the layer peeling stage between layers, the 'top-down' layout offers a series of advantages. In 'top-down' printing, smaller volumes of resin are required, the illuminated layer is not exposed to the atmosphere – so oxygen inhibition is limited, recoating of the structure is not required, and the surface being illuminated is always smooth.

The light source for STL printers was typically a laser system that sweeps the desired pattern for each layer. While still in common use in modern commercial STL printers, an alternative illumination method is becoming more prevalent in the form of digital light processing (DLP). With DLP technology, light is reflected off of a digital mirror device (DMD), which is composed of an array of up to several millions of mirrors that can be toggled on or off. Use of such a device enables projection of a complete layer at once. Build times are reduced in comparison to the laser-based systems, particularly if printing

large or multiple objects due to the elimination of the need for the laser to trace out and fill in each area desired. DLP layer completion times only depend on the layer thickness desired, and the associated exposure time required for that depth.

STL printers of all typical forms are considered as the most accurate form of 3D printing, due to their ability to form complex geometries with features detail sizes within the 100 µm range. One form of STL apparatus offers an even greater level of resolution by utilisation of two-photon polymerisation (2PP) technology, resulting in two-photon stereolithography (2PSL). 2PSL offers nanoscale accuracy (100 nm or better) but at a considerable increase in cost and large build times for macroscale objects.

2.6.2 Stereolithography layer thickness control

In STL, control of the layer thickness is one of the most critical parameters. Each resin formulation will possess different curing kinetics and will require different doses of light(energy) to generate a layer of a specific thickness. In DLP systems the dose of light is controlled by adjusting the power of the light source, or through adjusting the exposure time. For laser-based systems, the light source power and the scanning speed are the main variables for control of dose. To obtain successful prints with the desired level of detail, it is fundamental to have knowledge of the photo-curing behaviour relating to the combination of the resin and printer system in use. Characterisation of such behaviour is generally performed through use of a semi-empirical equation, which relates the thickness of a solidified layer (the cure depth, C_d in µm) to the light irradiation dose E (mJ/cm^2), and is shown in Equation 2-12.

$$C_d = D_p \, ln\left(\frac{E}{E_c}\right) \qquad \text{Equation 2-12}$$

The equation is used in combination with a semi-logarithmic plot of the determined cure depth versus the applied irradiation dose results in a linear relationship and is known as the Jacob's working curve [111]. The slope of the working curve is the penetration depth (D_p) of the resin for that light source wavelength. Since ln(1) = 0, the intercept of the working curve (i.e the value of E where $C_d = 0$) is the critical exposure (E_c) or gel point of the resin for that light source wavelength. Equation 2-12 is an adaptation of the Beer-Lambert equation, which describes the exponential decay of the intensity of light as it passes through a medium in which it is absorbed, therefore we can write:

$$I(z) = I_0 exp\left(\frac{-z}{D_p}\right) \qquad \text{Equation 2-13}$$

Where I(z) is the irradiance at a depth z in reference to the position in which the light enters the resin, where it takes the value I_0. An assumption is made that the degree of curing is directly proportional to the absorbed energy at that depth, meaning that initiation is deemed the limiting step of the polymerisation, and not propagation and termination. Therefore, Dp is the inverse of the absorption coefficient and works as the characteristic depth at which the light irradiance has decreased to 37 % of its initial value. Subsequently, this means that it can be considered that 4 D_p is a practical upper limit of printable layer thickness [112], as due to the exponential decay any further curing becomes extremely slow. Additionally, the value of D_p can be considered to be the lower printable thickness limit, because at this thickness the green part is strong enough to withstand the printing process. The most effective manner of adjusting D_p is through the resin formulation, specifically the photo-initiator and photo-absorber as they absorb the most light [113], [114]. While the kinetics of the different stages of the addition-type polymerisation (initiation, propagation-termination) of multi-vinyl monomers can be expressed mathematically [115], in practise the simpler equations described above more commonly used to good effect.

2.6.3 STL of biomaterials

The poor selection of degradable and biocompatible materials with varied mechanical properties to suit specific biomedical tasks is one of the biggest disadvantages of STL. However, considerable research into utilisation of polymeric materials already used for biomedical purposes in their bulk forms has been conducted, and largely driven by the tissue engineering community [116], [117]. As such, novel macromers from PCL [88], [91], poly(D, L-lactide)(PDLLA) [118]–[120], poly(trimethylene carbonate) (PTMC) [121]–[123], poly(ethylene glycol) (PEG) [124], poly(propylene fumarate) (PPF) [125] have been processed via STL. Essentially all of the above work produced tissue engineering scaffolds, although were of varied geometries and purpose. While STL has undoubtedly great potential for patient-specific biomedical applications, the clinical use of devices/implants produced from STL-compatible biomaterials is rare. Research tends to focus on temporary degradable polymer networks for biomedical purposes, but occasionally circumstances require a more permanent solution and use of non-degradable biomaterials can offer great benefits to the patient in specific circumstances. One such circumstance was a patient suffering from Van Buchem Disease, where hyperostosis of the skull can lead to increased pressure on the brain, had her entire cranium replaced with a poly(methylmethacrylate) STL printed patient specific implant in a world first

procedure. The part was produced by Anatomics Australia, with the surgical procedure performed at the University Medical Center Utrecht by Dr. Bon Verweij [126]. More common and less invasive uses of non-degradable STL printed materials are as patient specific dental surgical guides, and retainers [127].

Chapter 3 – Development of photocurable PCL-based resins

3.1 Introduction

In this chapter, we discuss the synthesis of the PCL macromonomers (macromers) used, and the assessment of solvents for formulating liquid resins.

Photo-crosslinkable polymer resins have been used in the preparation of biomaterials for various biomedical applications such as dentistry, tissue engineering, and development of drug delivery systems. To produce such resins, biomaterial oligomers are typically end-functionalised with reactive moieties, such as acrylate or methacrylate groups, capable of undergoing photo-initiated radical polymerisation to produce highly crosslinked polymeric networks. Due to the semi-crystalline nature of the PCL macromers use of a diluent or heat is required to generate a liquid resin suitable for photo-curing applications, including stereolithography. Previous work with PCL methacrylate macromers demonstrated that macromers of smaller than 1,500 g/mol were not able to be recovered from the reaction mixture precipitation in isopropanol method employed with macromers of higher molecular weight [91].

In this work, a method for the purification and recovery of <1,500 g/mol methacrylated PCL macromers was developed. Methacrylate end-functionalised PCL macromonomers (macromers) were produced with the intention of being used to formulate photo-curable resins that can generate bioresorbable networks suitable for implantation. Aiming for networks with stronger and more elastic mechanical behaviour than previously demonstrated in the literature, use of relatively high molecular weight linear PCL macromer was desired. The detailed rationale for use of the selection of macromers produced is presented in Chapter 4. Due to the macromers existing in a crystalline or waxy state at room temperature, a solvent was desired to formulate low viscosity liquid resins suitable for UV curing methods, including stereolithography printing.

The first objective is the synthesis and characterisation of PCL methacrylate macromers of various molecular weights with high degrees of functionalisation. As part of this objective, development of a reliable method for the purification and recovery of <1,500 g/mol PCL macromers will be performed. Secondly, an evaluation of solvents to determine the most suitable diluent for preparation of PCL macromer-laden liquid resins will be undertaken, where suitability will be determined by the ability of a solvent to dissolve the largest (10,000 g/mol) PCL macromer, possess low vapour pressure, and be of low-toxicity.

3.2 Materials and methods

3.2.1 Materials

Polycaprolactone (PCL) diol [M_n = 10,000 g/mol and M_n = 2, 000 g/mol], PCL triol [M_n = 900 g/mol], methacrylic anhydride (MAAh), sodium hydroxide pellets (NaOH) magnesium sulphate ($MgSO_4$), and trifluroacetic anhydride (TFAA) were acquired from Sigma Aldrich (UK); potassium carbonate (K_2CO_3), toluene, dichloromethane (DCM), and hexane were obtained from Fisher Scientific (UK). All chemicals were used as received.

3.2.2 Macromonomer synthesis

The PCL oligomers were reacted with MAAh to synthesise reactive macromers with methacrylate end groups. An excess of 50-100 mol% of MAAh per hydroxyl group was used. K_2CO_3 was used as a proton scavenger in the same molar quantity as the added MAAh. Methacrylation of both PCL oligomers was performed within a round bottom flask (RBF) with a PTFE stirring bar, at 130 ^oC under a nitrogen (N_2) atmosphere. Methacrylation of the 900 g/mol PCL was performed in the melt with no further solvents required. Due to the increased viscosity of the 10,000 g/mol PCL oligomer, small quantities of anhydrous toluene were added until smooth stirring at circa 150 rpm was achieved and maintained. Upon development of a well-mixed solution, MAAh was added in full with the K_2CO_3 added slowly to avoid foaming, and the N_2 atmosphere re-established. The degree of functionalisation (DF) was monitored over the course (4-8 hours) of the reaction using proton-nuclear magnetic resonance spectroscopy (^{1}H-NMR, $CDCL_3$, Bruker AVIII 300 MHz). Prior to addition of MAAh, a ^{1}H-NMR sample was taken of the reaction mixture to determine the initial integral of the peak at ~3.65 ppm attributed to the penultimate methylene group adjacent to the hydroxyl termini of the oligomers. Subsequent spectral peak integrals for that reaction were normalised to one another by keeping the integral of the peak associated with methylene groups at ~2.3 ppm constant. To confirm the nature of the protons, the oligomers were reacted with trifluroacetic anhydride (TFAA). The progression of the methacrylation reaction was observed by monitoring the disappearance of the peak at ~3.65 ppm, with the reaction continued until the peak was completely abolished, indicating 100 % DF.

3.2.3 Precipitation and purification of macromers

The 10,000 g/mol and 2,000 g/mol PCL macromer reaction mixtures were precipitated in cold (-80 ^oC) hexane under stirring. The precipitated mass (fine powder) was filtered off,

and the filtrate discarded. The filtered mass was left to dry within the conical filters overnight, before being transferred to a large surface area glass dish to encourage further evaporation of any remaining solvent. After a steady mass was obtained, the final product was vacuum-sealed into bags and stored in a freezer (-20 ^{o}C).

The 900 g/mol PCL macromer reaction mixture was poured into hexane under stirring. The macromer forms a low viscosity wax at the bottom of the beaker. The beaker contents were mixed vigorously, and allowed to settle before decanting off the upper phase. This was repeated several times until a clear upper phase was achieved. After the final decanting step is performed, the remaining wax was transferred to a separation funnel. Further hexane washes are then performed, recycling the waxy phase, while discarding the hexane phase. The wax was then transferred to suitable centrifugation containers and mixed with DCM and a 2 M NaOH solution in a 1:1:6 volume ratio. Containers were briefly shaken prior to loading into the centrifuge (Beckman Coulter, Allegra X-12R). Samples were then subjected to 2,000 G for 5 minutes at 25 ^{o}C. The upper aqueous phase was decanted/pipetted off and discarded, and the containers topped up with water, shaken and returned to the centrifuge. This was repeated until a clear aqueous phase was achieved. The final aqueous phase was discarded and the DCM/macromer phases from each container were poured into a beaker and mixed with $MgSO_4$ to scavenge any remaining water. After successful removal of water, the $MgSO_4$ was filtered off, leaving a clear DCM/macromer solution, which was transferred to an RBF. The RBF was moved to a rotary evaporator, where the DCM was boiled off leaving behind the waxy macromer. The macromer was melted and poured into falcon tubes and stored away from heat and light.

3.2.4 Solvent evaluation for formulation of photo-curable resins

A selection of solvents known in the literature to dissolve HMW PCL were evaluated as suitable candidates. Potential solvents were assessed in terms of vapour pressure, reported toxicity, and the ability to dissolve quantities of 10 kg/mol macromer. Vapour pressures of the solvents were taken from the U.S National Library of Medicine database PubChem, or from appropriate literature if no value was listed. The International Council for Harmonisation of Technical Requirements for Pharmaceuticals for Human Use (ICH) guidelines were referred to for data regarding reported toxicity and residual solvent limits. If no data was recorded on the ICH databases, the European Chemicals Agency (ECHA) database and the literature were searched for toxicological data. Following acceptable vapour pressure and toxicity levels, solvents were purchased for macromer solubility

testing. Increments of 0.25g were added to 1 mL of each solvent. Each time macromer was added, the solution was heated to 50 ^{o}C for 30 mins, before being maintained at 25 ^{o}C overnight. If the solution was a single phase, flowable, and showed no signs of precipitation, it was deemed a soluble concentration of macromer. This was repeated until precipitation of the macromer occurred, showing that the solubility limit had been breached. The largest mass of macromer able to be added without precipitation occurring was regarded as the maximum soluble concentration of macromer.

3.3 Results

3.3.1 PCL macromers

The 1H-NMR spectrum and associated proton identification for the PCL oligomers are shown in Figure 3.1, using the 10,000 g/mol oligomer as an example.

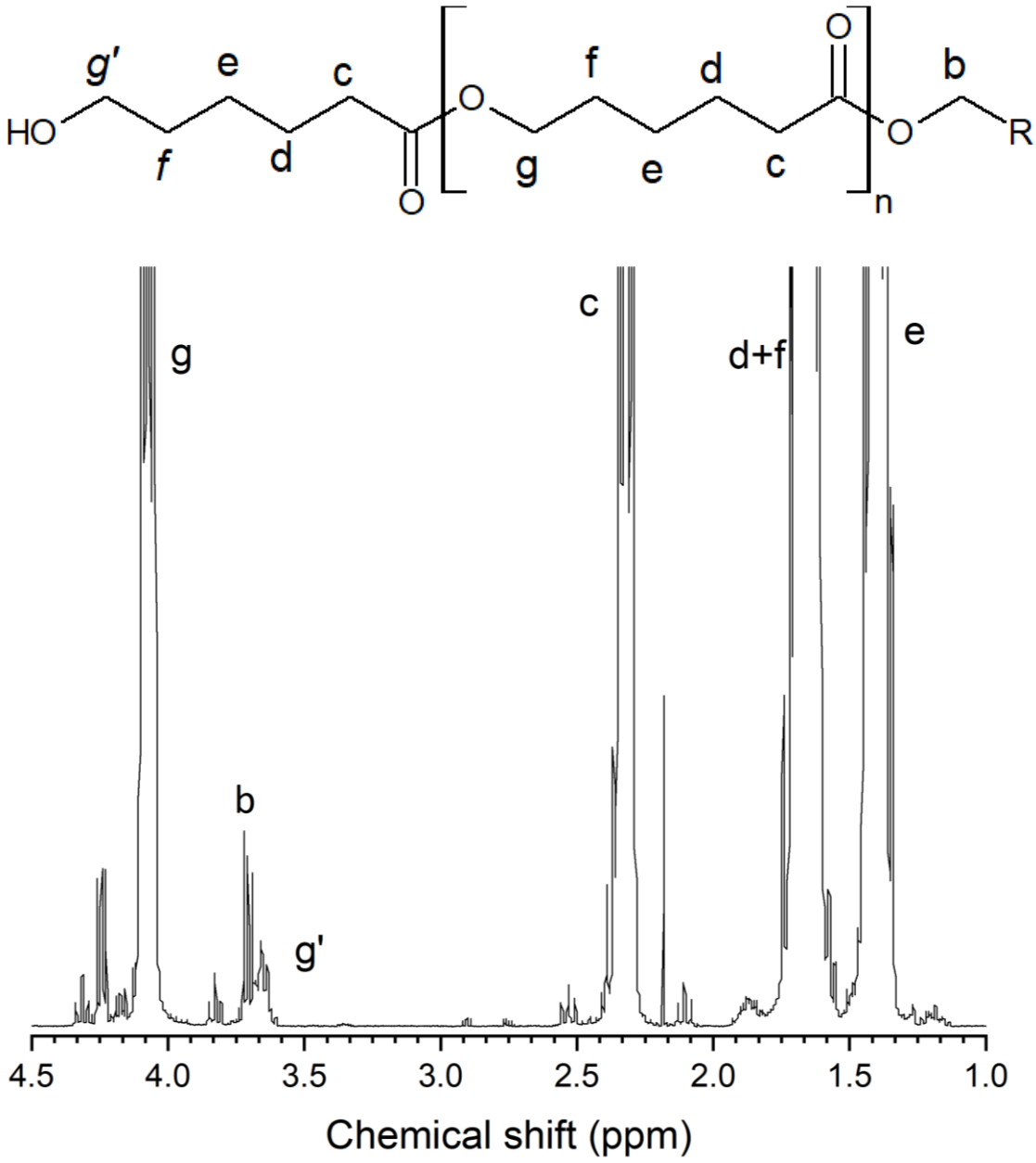

Figure 3.1:- The nomenclature and ^{1}H-NMR spectra of the 10 kg/mol oligomer. b represents the initiator residue, while R is the symmetry axis. The g'peak associated with the penultimate CH_2 methylene group adjacent to the terminal OH hydroxyl group was used to monitor the methacrylation reaction and determine DF.

Spectra of the 10 kg/mol oligomer, TFAA reacted oligomer, and methacrylated macromer, are shown in Figure 3.2. Nomenclature for the vinylic protons on the methacrylate end unit is also shown.

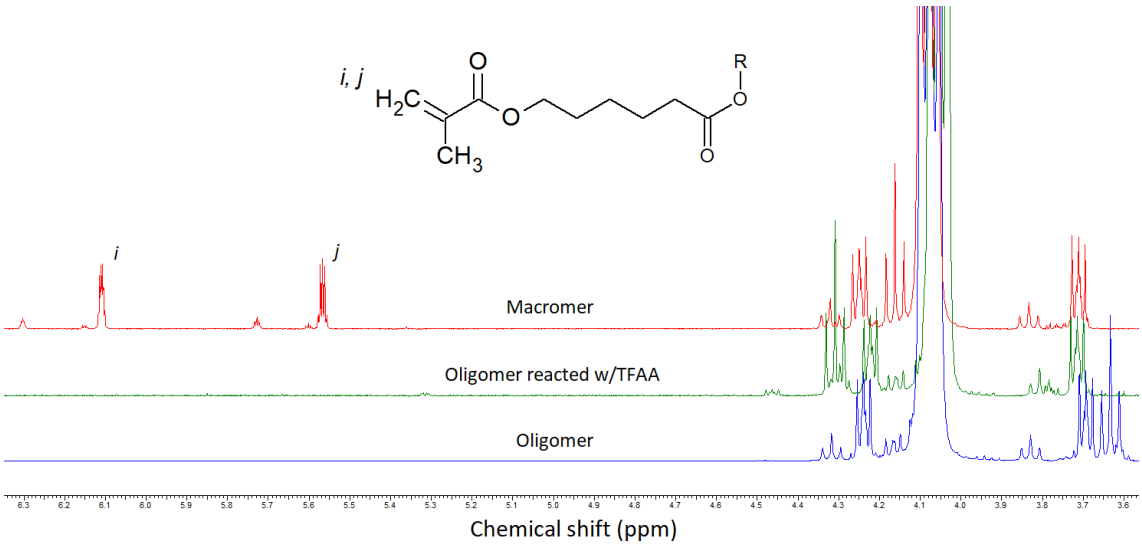

Figure 3.2:- ^{1}H-NMR spectra of the 10 kg/mol oligomer (blue), TFAA reacted oligomer (green), and macromer (red). The g' peak at 3.65 ppm in the oligomer trace, is not present in the TFAA or macromer spectra. The macromer spectra shows the methacrylate end-group vinyl carbons at 5.57 and 6.11 ppm. Here, R represents the rest of the molecule.

Reacting the oligomer with TFAA results in a shift of approximately +0.8 ppm of the g' peak associated with the penultimate methylene groups adjacent to the hydroxyl termini. The completed methacrylation reaction results in a similar shift of g' to the left (4.18 ppm) of the g peak at ~4.00 ppm. The macromer spectra also features the development of new peaks at 5.57, and 6.11 ppm (i and j) corresponding to the vinylic protons of the methacrylate end groups as well as peak k at ~ 2.00 ppm attributed to the methyl group. The summation of the integrals of these peaks closely matches the initial g' integral from the original oligomer ^{1}H-NMR indicating the absence of side reactions on the hydroxyl termini. By comparing the oligomer and macromer spectra, it can be seen that the g' peak in the macromer data is completely abolished at 3.65 ppm, indicating essentially 100 % DF.

Addition of each methacrylate unit adds 68 g/mol to the theoretical M_n of the oligomer. The oligomer starting molecular weight and final fully functionalised macromer molecular weights are shown in Table 3.1, alongside the nomenclature to which the macromer units will be referred.

Oligomer M_n (g/mol)	Theoretical macromer M_n (g/mol)	Macromer label	Functionality (oligo/macromer)
900	1,104	0.9k-3MA	triol/trimethacrylate
2,000	2,136	2k-2MA	diol/dimethacrylate
10,000	10,136	10k-2MA	diol/dimethacrylate

Table 3.1:- Oligomer molecular weights as described by manufacturer, with associated theoretical macromer molecular weights after methacrylation. The assigned macromer shorthand label and functionality is also shown.

The macromer labels take a condensed form of the original oligomer M_n, combined with their functionality, where MA is shorthand for methacrylate and the number indicates the number of end termini.

Over the course of the project, various batches of macromers were produced. Prepared macromer batches and their DF and recovery yields are shown in Table 3.2.

Exp. No.	Oligomer M_n	DF (%)	Yield (%)
EXP045	900	100*	17^+
EXP045v2		97	30^+
EXP048		98	31^+
KS840.9k		100*	n.d
Aus/Jongryul		100*	71
KS 18/4/19		100*	n.d
EXP008 - 2k	2,000	95	85
EXP024		100*	n.d
KS 22/1/19		100*	n.d
EXP010	10,000	100*	n.d
EXP024		100*	n.d
EXP037		100*	91
EXP052		100*	82
KS8410k		100*	n.d
Aus/xin		100*	n.d

*Table 3.2:- Degree of functionalisation and yield of macromer products from batches produced from oligomers of various molecular weights. Experiments are grouped per oligomer. * indicates g' peak was completely undetectable, n.d = not determined, $^+$indicates that purification method was still under development.*

With 10,000 g/mol oligomer, methacrylation was typically complete within 4 hours, with the g' peak completely abolished. Recovery of the 10,000 g/mol oligomer derived macromer resulted in reliable yields of >80 %. Methacrylation of the 2,000 g/mol oligomer generally took approximately 5 hours to reach completion. The recovery yield of the 2,000 g/mol macromer was only calculated for one reaction batch, but in that instance was 85 %. The 900 g/mol triol oligomer needed the longest time to reach 100 % DF, typically taking up to 6 hours to abolish g'. Recovery yields for the 900 g/mol macromer were poor for the early batches that were recovered through primarily liquid/liquid extraction (indicated by $^{+}$). Later batches that were precipitated into cold hexane resulted in higher yields closer to 70 %. The 10k-2MA product was a white fine powder, while the 2k-2MA product was more coarse and waxy, often forming clumps. The 0.9k-3MA product exists as a moderate viscosity wax, and is pourable (although slow moving) and able to be handled with positive displacement pipettes.

3.3.2 Solvent selection for the preparation of photo-sensitive resins

The search for suitable solvents for our PCL macromers was primarily directed by the extensive list of chemicals assessed by their ability to solubilise 14 kg/mol PCL oligomers by Bordes *et al* [128]. From this database, 27 potential solvents were found, however 21 of them were immediately disregarded due to severe toxicity or high volatility. Acceptable solvent toxicity status was defined through the solvent being ICH class 3, evidence of current use in products for biomedical purposes, and/or other evidence of minor/acute local toxicity. The 21 eliminated solvents along with the reason is shown in Table 3.3.

Solvent/Chemical name	Exclusion reason
Morpholine	Banned (UK and EU) fruit waxing component. Exceptional fire hazard. Capable of severe eye damage. Corrosive.
Chloroform	ICH Class 2 - 60ppm limit. CNS depressant
Benzene	ICH Class 1 - 2ppm limit. Carcinogenic
Methylene chloride	ICH Class 2 - 600ppm limit. Carcinogenic (ECHA)
Dimethyl sulfide	Highly irritant to skin, B_p = 37 ^oC, V_p = ~500 mmHg at 25 ^oC. "Disagreeable odor".
Acetyl chloride	Corrosive to metals and tissue. V_p = ~287 mmHg; flash point 4-5 ^oC.
Tetrahydrofuran	ICH Class 2 - 720ppm limit. Carcinogenic.
Furan	Carcinogen. B_p = 31 ^oC. V_p = ~600 mmHg.
Pyridine	ICH Class 2 - 200ppm limit.
2,2,2-Trifluoroethanol	Highly toxic to multiple organ systems
Trifluroacetic acid	Strong acid, highly exothermic.
1,2-Dichlorobenzene	Irritant. 50ppm per 8 h limit
1,2-Dichloroethane	Toxic. ICH Class 1 - 5ppm limit.
2-Chloroethanol	Highly toxic via inhalation and skin absorption
Methyl formate	B_p = 32 ^oC. V_p = ~585 mmHg. Respiratory irritation.
1,4-dioxane	ICH Class 2 – 380 ppm limit. Group 2B carcinogen
Aniline	Toxic, carcinogenic, mutagenic
Toluene	ICH Class 2 - 890ppm limit
o-Xylene	ICH Class 2 - 2170ppm limit. Suspected teratogen.
3-Pentanone	nervous and organ system damage
Nitrobenzene	highly toxic, CNS damage, easily absorbed through skin

Table 3.3:- Eliminated solvents with a description of the reason.

The vapour pressure (V_p), and maximum soluble concentration of the 10 kg/mol macromer of the remaining solvents, are shown in Table 3.4. Vapour pressure was evaluated on the basis that the lowest pressure at 25 ^oC was most desirable, with the vapour pressure of water (~23 mmHg at 25 ^oC) being the upper maximum acceptable limit. An additional 5 solvents that were already in use by the group for photo-curable resin formulation of other macromers are also shown. These were propylene carbonate, diethylene glycol, ethyl benzoate, diethylene glycol diethyl ether and butyl lactate,

Solvent	V_p (mm Hg)	Max conc. (g/mL)
Acetophenone	0.40	1.00
Benzaldehyde	1.27	0.75
Benzyl alcohol	0.09	1.50
Methyl salicylate	0.03	0.75
Propylene carbonate	0.05	n.s
Diethylene glycol	<0.01	n.s
Ethyl benzoate	0.27	0.5
Diethylene glycol diethyl ether	0.52	n.s
Butyl lactate	0.4	n.s

Table 3.4:- Lists the vapour pressures, maximum soluble 10 kg/mol PCL- macromer concentrations of the tested solvents.

Benzyl alcohol achieved the greatest concentration of dissolved macromer, and also possesses one of the lowest vapour pressures of all the tested solvents. Acetophenone, benzaldehyde, methyl salicylate, and ethyl benzoate were able to dissolve the PCL macromer but at a lower concentration than that of benzyl alcohol. Propylene carbonate, diethylene glycol, diethylene glycol diethyl ether and butyl lactate were not able to solubilise the lowest concentration (0.25 g/mL) of macromer. None of the solvents listed in Table 3.4 are currently listed in the latest ICH residual solvent guidelines (ICH Q3C R6), and only 5 were listed in the ECHA Council on classification, labelling, and packaging of substances and mixtures (CLP) legislation databases. Essentially all the solvents listed demonstrate acute/minor skin irritation and/or eye irritation.

3.4 Discussion

3.4.1 Summary

PCL oligomers of 10,000, 2,000, and 900 g/mol M_n were successfully functionalised with methacrylate end groups. Macromers of all molecular weights were shown to be of essentially 100 % DF, by the absence of the g' peak at 3.65 ppm and the establishment of peaks typical of methacrylate-functionalised oligomers. A new method for the purification of low (sub 1500 g/mol) molecular weight PCL macromers was demonstrated. During the evaluation of potential solvents benzyl alcohol was found to be most effective at solubilising the 10 kg/mol PCL macromer, while also possessing a low vapour pressure of 0.09 mmHg at 25 ^{o}C, and acceptable toxicological profile with multiple current examples of use in/with medicinal products and procedures.

3.4.2 Recovery of PCL macromers

PCL macromers of <1,500 g/mol have been shown to be difficult to recover from the reaction mixture using methods that work well for higher molecular weight macromers, such as precipitation in isopropanol [91]. Initial attempts to develop a method for the recovery of such macromers involved repeated liquid/liquid extractions steps between the macromer dissolved in DCM and distilled water to remove excess anhydride and methacrylic acid side product. Such methods resulted in yields of between 17-31 % (shown in Table 3.2), which was deemed unacceptable. Further literature searches found that it had been shown that acrylated PCL macromers down to 900 g/mol could be successfully recovered from precipitation in hexane [129]. The method detailed in 3.2.3 incorporates recovery of the 1,104 g/mol waxy macromer from hexane precipitation and removal of non-hexane soluble methacrylic acid using liquid/liquid extraction. The yield from this improved method was calculated to be 71 %. However, this method is also labour intensive in comparison to relatively simple precipitate and filtration methods.

The 2,000, and 10,000 g/mol macromers were easily recovered though precipitation into cold hexane, followed by filtration to obtain the solid product. Recovery yields were typically >80 %, and did not present a particular efficiency issue, leading to exact determination of the yield not being performed.

3.4.3 Benzyl alcohol for resin formulation

From Bordes' list, acetophenone, anisole, benzaldehyde, benzyl alcohol, and methyl salicylate were determined to possess acceptable vapour pressures, and toxicology. However, anisole was found to be prohibitively expensive and was not pursued further. Of the solvents currently in use with other macromers in the lab, only ethyl benzoate demonstrated any ability to solubilise the 10 kg/mol PCL macromer. Benzyl alcohol was found to be able to solubilise the greatest concentration of macromer, with a maximum soluble concentration of 1.5 g/mL. This value was 0.5 g/mL greater than the joint second highest maximum soluble concentration demonstrated by acetic acid and acetophenone. Benzyl alcohol also offers a very low vapour pressure of 0.09 mmHg at 25 ^{o}C, which makes it attractive for open vat stereolithography. Benzyl alcohol is not currently classified under ICH residual solvent guidelines, however it is often used as an excipient in medicinal products that are administered intramuscularly, or intravenously, as well as being used in topical preparations [130]. Outside of medicine, benzyl alcohol sees use as a flavouring substance in the food industry (up to 400 mg/kg) and in the cosmetics industry as a fragrance component, preservative, solvent and viscosity-reducing agent. It

is also a natural constituent in some edible fruits (~ 5 mg/kg) and teas (up to 30 mg/kg). *In vivo* toxicology assessments in rodents did not show compound-related adverse effects at dose levels up to 200 mg/kg by weight in mice, and 400 mg/kg by weight in rats when administered intravenously [131]. While dose- and time-dependant benzyl alcohol cytotoxicity has been observed with retinal pigment epithelial cells [132], [133], tests with other cell types are not present in the literature. Considering the photo-cured networks will be extracted and dried as a standard procedure to remove the solvent used to formulate the resin, it is expected that if any solvent would remain, that it would be in residual quantities and therefore pose a minimal risk of adverse toxic effects. However, the risk of adverse effects can be reduced further by using a solvent that has been demonstrated to display low toxicity. Benzyl alcohol fulfils the desired criteria by demonstrating the highest soluble concentration of macromer, one of the lowest vapour pressures, and low toxicity.

In the present literature, dioxane is the most commonly used non-reactive diluent in for formulating photo-curable resins of low molecular weight (<2,000 g/mol) PCL macromers [88], [90], [97], [134]. Dioxane was one of the solvents eliminated from this study due to being an ICH class 2 solvent with a very low pharmaceutical product residual solvent concentration limit of 380 ppm. It is also regarded as a class 2B carcinogen by the International Agency for Research on Cancer (IARC). The database from Bordes *et al* regards benzyl alcohol within the same PCL oligomer solubility bracket as dioxane. With respect to the findings within this chapter, benzyl alcohol should be strongly considered as an alternative solvent featuring lower toxicity and lower vapour pressure.

3.4.4 Conclusions

PCL macromers of 10,000, 2,000 and 900 g/mol molecular weights with 100 % degree of functionalities have been synthesised. A method for the purification and recovery of <1,500 g/mol PCL macromers was developed, and may offer a cleaner product and higher recovery yields. A series of solvents were evaluated in regards to suitability for solubilising the macromers as liquid resins. Benzyl alcohol was determined to be able to solubilise the greatest quantity of 10,000 g/mol macromer, while possessing a low vapour pressure, and being of low-toxicity. Therefore, benzyl alcohol will be used as the solvent of choice in the subsequent chapters of this thesis for the formulation of photo-curable PCL resins. Additionally, it is suggested that benzyl alcohol should replace dioxane as the solvent/diluent of choice for PCL-based photo-curable resin formulations due to being less toxic and having a lower vapour pressure.

Chapter 4 – Bimodal networks for stereolithography and network characterisation

4.1 Introduction

3D printing is a diverse field that offers highly versatile manufacturing suitable for numerous materials and applications, including polymeric biomedical implants [135], [136]. Digitally designed structures can be 3D printed reproducibly, while easily facilitating design iterations during prototyping. Stereolithography (SL) techniques (especially twin photon polymerisation [2PP]) offer superior accuracy and resolution to any other 3D printing techniques [137]–[139]. In SL techniques, spatially controlled light exposure photo-polymerises a liquid resin into a chemically cross-linked solid in a layer-by-layer fashion. SL resins are typically composed of low molecular weight multifunctional monomers or oligomers, which either are already liquids, or combined with reactive or non-reactive solvents to produce a liquid resin. Such compositions provide excellent reactivity, but result in materials that are brittle, which is a common trait of amorphous polymer networks [137], [140]. The number of stereolithography resins suitable for biomedical applications is limited, with biodegradable or bioresorbable resins suitable for implantation being even rarer [141], [142].

Polycaprolactone (PCL) is a promising resorbable polymer platform for biomedical applications. PCL is a hydrophobic, semi-crystalline polymer, with a low melting point (~60 ^{o}C) and glass transition (-60 ^{o}C) [79], [143]. Most notably, PCL possesses a slower rate of degradation over other typical resorbable-polymer counterparts, which naturally lends itself to long-term implantable medical devices [79]. Printing of PCL structures have previously been demonstrated using mainly FDM, and SLS techniques, and to a lesser extent, SL [144], [145]. Elomaa *et al* were first to prepare tissue engineering scaffolds composed of PCL using a DLP printer. The PCL macromers used were trifunctional (three-armed) and had a molecular weight of 1500 g/mol, and were processed in the melt at a temperature of 43-46 ^{o}C [91]. More recently, Green *et al* demonstrated DLP printing of dumbbell-like structures from a 1250 g/mol bifunctional and 300 g/mol trifunctional PCL macromers at room temperature by using dioxane to formulate a liquid resin [88]. The structures printed by both groups are amorphous and rubbery, with tensile strengths a full magnitude lower than that of non-crosslinked 45,000 g/mol PCL.

Based on working examples from the development of tough cross-linkable poly(trimethylene carbonate) networks, similar improvements of PCL networks could potentially be achieved through utilisation of macromers with higher molecular weights than previously demonstrated [146]. However, high molecular weight macromers typically are solids at room temperature, and therefore require diluent to form a liquid resin suitable for SL. Use of large quantities of diluent introduces new complications with structures during the printing process being more fragile than solvent free resins, which can result in partial or complete delamination and detachment of subsequent layers [147]. Early investigations into unimodal and bimodal poly(dimethyl siloxane) (PDMS) networks demonstrated that large improvements in maximal tensile strength, elongation at break, and toughness can be achieved by varying the distribution of network chain lengths through preparation of bimodal networks from a mixture of short- and long-chain molecules [148]–[152]. This approach was utilised by Bochove *et al* to produce bimodal PTMC networks via SL that displayed greatly improved mechanical properties over the unimodal networks [153].

Photo-curable resins containing linear PCL macromers with higher (~10,000 g/mol) molecular weights and crystallinity are expected to enable production of networks with tougher mechanical properties than those previous demonstrated. We hypothesise that due to utilisation of higher molecular weight macromers, the resins will be less reactive due to the lower concentration of reactive C=C bonds and will suffer from poor mechanical properties in the green state during printing. To combat the lower reactivity, bimodal resins will be formulated that include smaller multifunctional crosslinkers alongside the larger linear macromer to raise the concentration of available C=C bonds, and therefore resin reactivity. Pentaerythritol tetraacrylate will be used as a crosslinker, however we hypothesise that networks containing the tetraacrylate will be non-degradable, and therefore a small three-armed PCL macromer will be tested in an attempt to maintain degradability. For comparison, a unimodal resin with linear 2,000 g/mol PCL macromers will be formulated to contain the same concentration of C=C bonds as the bimodal PCL resin. We hypothesise that the bimodal resin will demonstrate greater reactivity and mechanical properties than the C=C matched unimodal resin, despite a similar average length between crosslinks.

4.2 Materials and methods

4.2.1 Materials

10k-2MA, 2k-2MA, and 0.9k-3MA macromers were synthesised and purified as discussed in Chapter 3. 45,000 g/mol M_n PCL, diphenyl(2,4,6-trimethylbenzoyl)phosphine oxide, 2,5-Bis(5-tert-butyl-benzoxazol-2-yl)thiophene, hydroquinone and pentaerythritol tetraacrylate were obtained from Sigma Aldrich (UK). Benzyl alchol was obtained from Alfa Aesar (UK). Formlabs flexible (FL Flex) resin was purchased from an authorised UK formlabs vendor GoPrint3D.co.uk. Kudo3D Black DLP resin was acquired from Kudo3D (USA) (discontinued). Verowhiteplus PolyJet resin was obtained from Stratasys (USA).

4.2.2 Resin formulation

The required amount of macromer was weighed and added to a suitably sized wide neck RBF. The required amount of diluent (BnOH) was added, while being magnetically stirred and a gentle heat of 35-40 ^oC applied. The mixture was kept under heat and stirring until the macromer was completely dissolved. The required amount of photoinitiator (TPO), UV-absorber (BBOT), and inhibitor (HQ) were weighed out, added to the flask, and stirred until completely dissolved. The flask was typically covered in aluminium foil to avoid exposure to ambient light. A composition was deemed different if any component or component concentration was changed. Photo-curable resins were utilised in the injection moulding of samples for mechanical, degradation and cytotoxicity characterisation, as well as directly within stereolithography apparatus.

The core resin formulations used to make injection moulded photo-cured networks utilised within this Chapter are shown in Table 4.1.

Resin/network name	Resin Formulation component (% wt)				
	10k-2MA	0.9k-3MA	PTOL-4A	2k-2MA	BnOH
xPCL10k	45	x	x	x	55
xPCL2k	x	x	x	46.8	53.2
xPCL10k0.9k	30	15	x	x	55
xPCL10k+4A	30	x	15	x	55

Table 4.1:- List of resin formulations for injection moulding used within Chapter 4. The photoinitiator was added relative to the total weight of macromer and diluent, with all the above resins featuring 3 % wt of TPO.

Any adjustments to the resin formulations above, such as change of photo-initiator content, or addition of photo absorber, or inhibitor will be detailed in the relevant results section. Formulations were largely dictated by solubility. In particular, the xPCL10k resin contains as much 10,000 g/mol macromer as possible without precipitating or forming a highly viscous liquid which would make printing and moulding difficult. The xPCL10k+4A resin formulation was determined by replacing 10,000 g/mol macromer with PTOL-4A until a suitable reactivity was achieved for printing. The xPCL10k0.9k formulation follows a similar logic, however it was felt that reducing the content of the 10,000 g/mol macromer further would negatively affect mechanical toughness. The xPCL2k resin was used as a unimodal comparison to the bimodal xPCL10k0.9k and was therefore formulated to contain the same double bond content as the xPCL10k0.9k resin. The importance of the double bond content on reactivity and mechanical properties is explored later in this chapter.

4.2.3 Tensile sample preparation

Custom mould inserts to create ASTM D638 type IV dumbbells with scaled geometry to fit our modular system were produced. Details of the dumbbell geometry are shown in Figure 4.1. The absence of dust or other contaminant material from within the mould was checked during assembly of the mould systems.

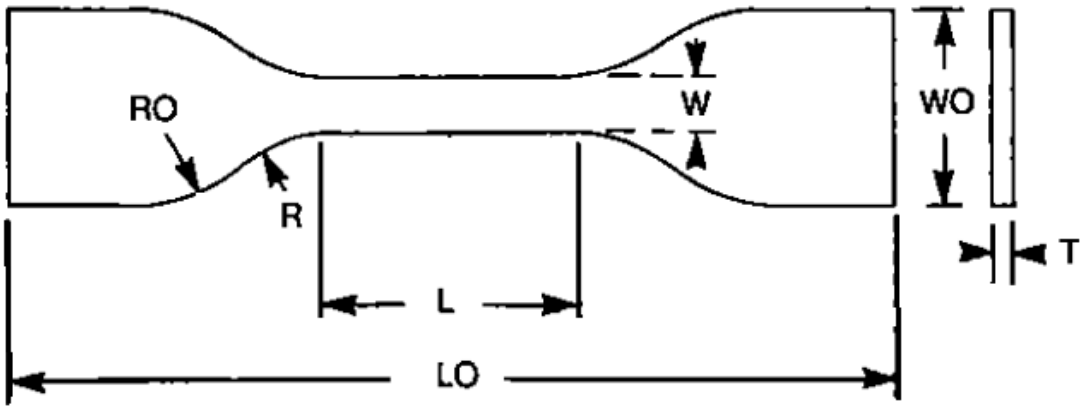

	Properties						
	W	L	T	WO	LO	R	RO
Dimensions (mm)	5	22	2	13	72	8.6	15.3

Figure 4.1:- Schematic of dumbbell shape above, with target dimensions shown in the table below. W = width of narrow section; L = length of narrow section; T = overall thickness; WO = overall width; LO overall length; R = radius of inner fillet; RO = radius of outer fillet. Schematic is an edited version from ASTM 638b.

Resins for injection mould-curing were formulated with the absence of UV-absorber to ensure light was able to fully penetrate the depth of the resin in the mould. Resin of the

desired formulation was injected into the mould using a luer lock syringe fitted with a 14 Gauge adhesive dispensing tip. The moulds were then moved to a UV crosslinker oven (VWR International, UVP CL-1000, 365 nm) and irradiated for the 90 mins, removed from the mould and flipped over and irradiated on the other face for another 30 mins. Post-cured networks were weighed, placed within cellulose thimbles, and then extracted with isopropanol (Fisher Scientific, UK) using Soxhlet apparatus for at least 96 hours. The extracted networks were left to dry in their thimbles while in any excess isopropanol. When dry, samples were placed on a smooth flat PTFE sheet (RS Components Ltd., opaque fluoroplastics sheet 3 mm thick) and placed in an oven at 80 ^{o}C (SciQuip, SQ-4845). Samples were periodically removed from the oven and weighed until a steady mass was obtained. Dried samples were stored flat in sealed bags until use.

For the non-crosslinkable 45kg/mol PCL, tensile dumbbells with the same geometry as the crosslinked specimens were generated by melt compressing moulding. The apparatus consisted of a manually operated hydraulic press with two electrically heated plates (top and bottom) as the compression surfaces. The dumbbell moulds were machined into a steel plate. DuPont Kapton™ film was positioned underneath the steel mould, and the vacant mould spaces filled with excess polymer pellets. Another sheet of Kapton™ film was placed on top, so that now both open sides of the moulds were between the film. The film/mould sandwich was placed on a solid steel plate, and positioned on the lower plate of the hydraulic press. A further solid steel plate was gently balanced on top of the upper film layer of the mould. The heating controls of the press surfaces was set at 120 ^{o}C, and the upper surface of the press lowered to be close, but not touching, the upper steel plate of the mould sandwich. The heat from the surfaces slowly melts the PCL pellets, floating the upper steel mould plate on molten polymer and allowing some trapped air to escape. Once the upper steel plate rested on the mould, a series of compression, holding, and partial relief steps, increasing in force each time, were performed to help expel any further trapped air. After no bubbles were noticed in the excess polymer material along the mould edges during compression of the mould, a final compression force of 15 tons was held, while the heating was turned off and the press and mould allowed to cool. Once cold enough to touch, the compression force was released, and the mould sandwich moved under running cold water. The Kapton™ film was peeled away carefully, and excess polymer material removed from the steel mould plate by scalpel and bladed screwdriver. The dumbbells were then pushed out of the mould, and trimmed of any further excess

material before being cooled on the lab bench. Dumbbells were inspected for air bubbles and were reprocessed or excluded if they were found to have air bubbles present.

4.2.4 Universal testing apparatus setup and procedure

Tensile testing of dumbbell samples was performed using a universal testing system (Instron chassis No.: 5567), fitted with a 500 N load cell and side-action grips. An extension rate of 5 mm/min was used. All samples were tested at room temperature and humidity. Starting distance between grips was 30 mm. Raw data was exported from Instron Bluehill 2 software and processed in Microsoft Excel and OriginLab OriginPro 2018b.

4.2.5 DSC and degradation sample preparation

Disc shaped samples of a diameter of 5 mm and thickness 1.6 mm were produced using injection moulding and UV curing in a similar fashion to the dumbbell tensile specimens. Disk specimens were subjected to the same curing, extraction and drying regime as the dumbbells described in 4.2.3. For evaluation of degradation, the disk specimens were used in their full form, while for DSC the appropriate mass was cut from the disk and loaded into the pans.

4.2.6 DSC methodology

Differential scanning calorimetry (DSC) was performed using a Netzsch DSC 214, with aluminium pans and pierced lids. The calorimetry was performed under a nitrogen flow. Samples of oligomers, macromers, and photo-cured networks with a target mass of 10 mg were used, with the exact weight measured for each run. Samples were stabilised at -20 ^{o}C before performing a heating ramp at 5 ^{o}C/min to 100 ^{o}C. The samples were then cooled back to -20 ^{o}C at a rate of 10 ^{o}C/min and held for 5 mins, prior to a second identical heating ramp. The data was analysed using Netzsch Proteus Analysis, with melting and crystallisation peaks determined using the peak tool, and their associated enthalpies calculated with respect to temperature using the integration tool.

4.2.7 Autodesk EMBER DLP printer features and calibration

Ember is an open source stereolithography printer that is no longer in production or supported by Autodesk. It features a 405 nm centred LED light source, which produces an irradiance of 22.5 mW/cm^2. Light is reflected 90 degrees off a digital mirror device (Texas Instruments DLP4500 .45 WXGA) with a XY plane resolution of 50x50 µm and projected through a glass window. Model files are processed using Autodesk's

proprietary software Print Studio, which packages the print settings and model slices into a .zip file which is sent to the printer by USB or Ethernet connection. The available XY plane print area is 64x40 mm with a maximal Z-axis height of 134 mm. Resin is contained within a tray constructed of polypropylene, with a PDMS window for the light to shine through. The Z-axis stepper motor provides a minimum step increment of 10 µm. The build head has an anodized aluminium print surface. The head is attached to the frame via a ball and socket, which enables multi-axial adjustment. The beginning of each new print job involves a largely manual calibration of the build head. Here the print head is lowered into the resin to the starting height above the PDMS window stipulated by the print settings. The user must orientate and lock the build head, after which the printer will carry out the rest of the print instructions automatically. The printer features a relatively unique layer peeling method, where the tray rotates around an arc, peeling laterally, followed by upwards movement of the build head. This in theory reduces the suction force seen with other peeling techniques that involve only Z-axis movements alone, but introduces its own unique problems. The peeling should be aided by the oxygen buffer provided by the PDMS window to reduce the risk of jamming during peeling.

4.2.8 EMBER: working curve

The build head was removed from the EMBER printer. Resin was dispensed on to an approximately 1 mm thick microscope slide and positioned within the resin tray over the PDMS window. A print job was created that would expose a 10 mm^2 square for every layer, with each layer being able to be assigned a different exposure time. After each layer, the cured material was removed from the slide and replaced with a fresh slide and resin. The cured material belonging to each printer layer was measured for its thickness (Mitutoyo Dial Thickness Gauge 7301) and the process was repeated multiple times for each exposure time. The average thickness for a given exposure time was plotted against the irradiated maximal dose (time · power), and logarithmic fitting was performed to obtain the equation for the working curve.

4.2.9 EMBER: stereolithography printing

Models for printing were created using Autodesk AutoCAD, or Autodesk Fusion 360, and exported as .stl files. Initial print settings were estimated from the working curve data for that particular resin composition. A small waffle-like structure, with an outer rectangular shape of 5x9 mm and 1 mm^2 square pore/channels through its entire Z-height (5 mm), was preferred as the initial test print model, due to its simple geometry and the

pores providing areas for early feedback regarding resolution. During the initial printability tests, the window was checked by eye after each layer had printed and peeled to ensure the layer had adhered to the build head. If print failure was detected, the print was cancelled, print settings changed, and then reinitiated with the new settings. Persistent issues usually resulted in appropriate changes to the resin composition. Once suitable printing settings were identified, the printer could be operated with less user input, and other print geometries could be printed successfully. For complex structures with features overhanging the base area, or without at least one flat face, supports were added through PrintStudio. Print settings shall be detailed in the appropriate results sections.

After printing, models were post-cured in the UV box while still attached to the print head surface. Post-cure times varied depending on the resin composition used. Post-cured models were cut from their supports with fine bladed pliers or detached from the build head using a thin bladed spatula. Printed models were then extracted using Soxhlet apparatus and dried as previously described in 4.2.3.

4.2.10 UV-rheometry

UV-rheometry was performed on an Anton Paar MCR302 rheometer, which featured a quartz lower plate that allowed light from a 365 nm LED mounted underneath to shine through and illuminate the sample area. Additionally, use of a Peltier hood provided fine temperature control, and protected the sample from ambient light. The LED was powered by an external laboratory power pack, set at an output of 3.1 V and 0.33 A, which resulted in an irradiance of 1.54 mW/cm^2 at the sample contact surface of the quartz plate. Irradiance measurements were performed using a Solar Light PMA2100 data-logging radiometer coupled with a MA2180-440-40 (S/N: 22535) sensor. With this setup, the sample was irradiated uniformly while being subjected to constant oscillatory small amplitude stress. A parallel plate of 15 mm diameter was used as the upper geometry. A gap size of 0.1 mm was maintained. All measurements were performed at a controlled temperature of 25 ^oC. Resin gelling behaviour was monitored throughout a time sweep where constant oscillations were applied at a fixed frequency of 40 rad/s with a target strain of 0.3 %, which was in the linear viscoelastic region of the materials. Rheological measurements were performed in duplicate. The gel point is considered to reside at the time where the storage (G') and loss moduli (G") are equal providing G' is increasing over several orders of magnitude.

4.2.11 Autoclave degradation method

Accelerated degradation of our materials and photo-cured networks were performed within an Astell ASB 270 BTO autoclave. A modified 5-stage sterilisation cycle was used, with a target temperature and pressure of 120 ^{o}C and 2.25 bar respectively. The stages involved are, an intermediate temperature and pressure-building phase, a temperature ramp to sterilisation temperature, the sterilisation stage, a cooling stage, and lastly, a drying stage. For simplicity, we regard only the length of the sterilisation stage as our period of degradation. The length of time the sterilisation stage lasted could be adjusted from 1 second to 4.25 hours. For periods longer than 4.25 hours, multiple cycles were performed on the same sample(s). Disk shaped samples were each weighed, and immersed separately in small glass vials containing 4 mL of 1 M NaOH solution. The collection of vials was placed within a large glass beaker and positioned in the centre of the autoclave. After the autoclave cycle was performed, the vials were inspected and any remaining mass noted and weighed. This is performed until no retrievable mass was available. In the absence of recoverable mass, autoclave cycles were continued until no gel fragments or other indicators of residual sample material could be seen. A material or network was regarded as fully degraded when the solution was completely clear at room temperature.

4.2.12 RBF boiling degradation method

Accelerated degradation was also performed by immersing samples within boiling 1 M NaOH within an RBF. A 50 mL RBF was placed within a suitably sized thermal block on a hotplate stirrer. Approximately 30 mL of 1 M NaOH solution was poured into the RBF, and a water condenser fitted. Prior to sample addition, the NaOH solution was brought to boil. Disk shaped samples were weighed prior to immersion. The disks were removed at various time points, re-weighed and then returned to the RBF. This is performed until no retrievable mass was available. In the absence of recoverable mass, boiling was continued until no gel fragments or other indicators of residual sample material could be seen. A material or network was regarded as fully degraded when the solution was completely clear at room temperature. The evaluation criteria in the absence of measurable mass, and in terms of degradability were identical to the autoclave method above.

4.3 Results

4.3.1 Tensile testing

Mechanical properties such as the Young's modulus, ultimate strength, elongation at break, toughness, and yield stress of the materials were determined. The stiffness was determined from the stress gradient over the initial 0.3 mm of elongation (i.e. 1% of the initial grip-to-grip distance). Yield stress was obtained by calculating the peak stress value over the first 7.5 mm of elongation, with the exception of the xPCL10k+4A group, which did not show a peak. Instead the yield appeared as a gradual gradient transition, and so the point of yield was estimated from the interaction between two trendlines, the first of which was determined from the first 0.6 mm of elongation, and the second from between 4-10 mm of elongation. Toughness was calculated from the area under the curve of the sample profile. Ultimate strength, and elongation at break was defined as the stress or elongation, respectively, at which sample break occurred. Representative tensile profiles from each material group are displayed in Figure 4.2. Average properties for each material group are shown in Table 4.2. Each group typically contained 10-15 individual samples, with the exception of the FL Flex group that contained 4 samples.

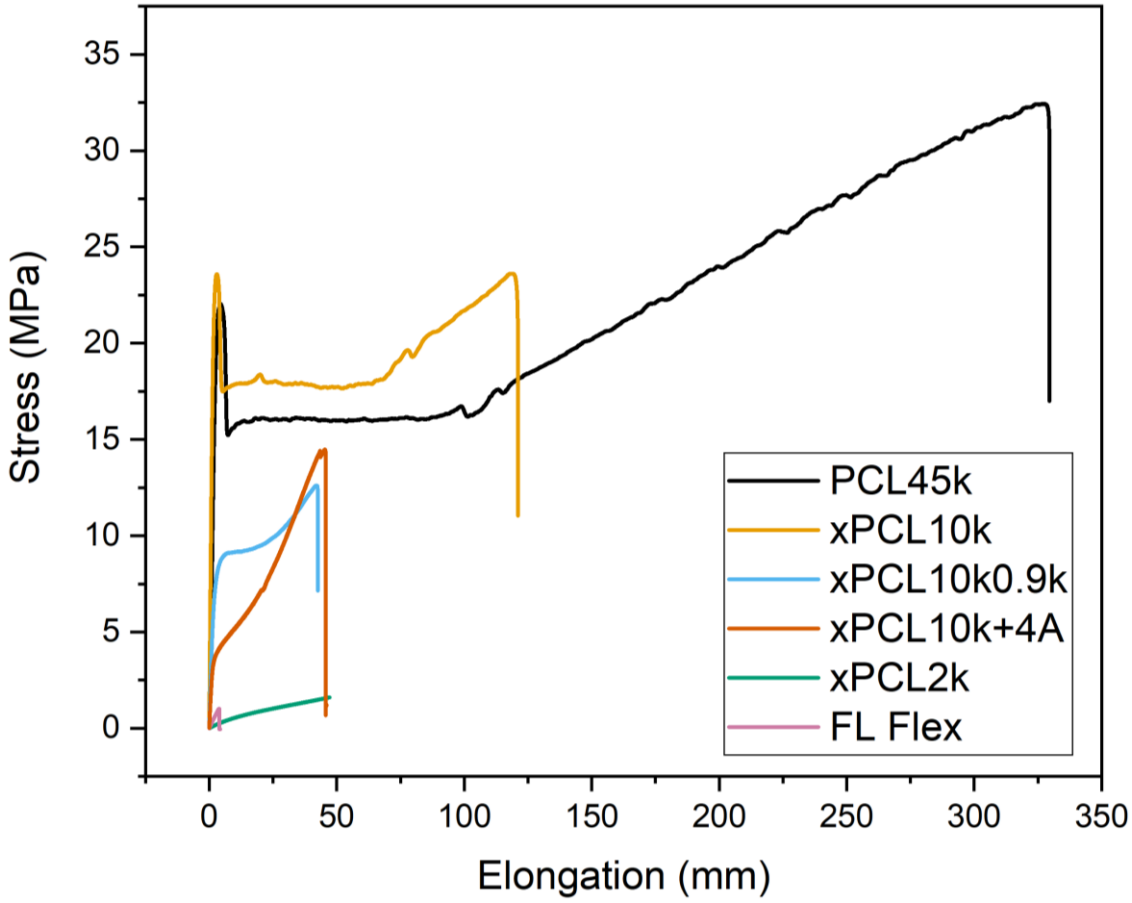

Figure 4.2:- Representative tensile profiles of all investigated material groups, with inclusion of a commercial flexible resin (FL Flex) for comparison. PCL45k is non-crosslinked PCL polymer. xPCL refers to photocured PCL materials, where xPCL10k is comprised of only 10,000g/mol macromers. xPCL10k0.9k, and xPCL10k+4A indicate the inclusion of another crosslinking component, where the 0.9k refers to a 900 g/mol PCL macromer, and the +4A refers to PTOL-4A. Samples are dumbbell shaped. Initial grip-to-grip distance was 30 mm. One sample of each group is shown out of a population size of at least 15 samples (n = >15), with the exception of PCL45k where n=10, and FL flex where n = 4. Extension rate was 5 mm/min. Samples were extended until break.

Name	Stiffness (MPa/mm)	Ultimate strength (MPa)	Elongation at break (mm)	Toughness (J/cm^3)	Yield stress (MPa)
PCL45k	15.84 ± 0.50	31.4 ± 2.6	308 ± 45	174 ± 22	22 ± 0.7
xPCL10k	15.62 ± 0.38	23.9 ± 2.9	112.9 ± 24	79 ± 17	24 ± 1.2
xPCL10k0.9k	4.70 ± 0.47	12.6 ± 1.5	42.9 ± 6	14 ± 3	9 ± 1.0
xPCL10k+4A	2.92 ± 0.19	14.0 ± 0.7	43.9 ± 3	11.4 ± 1.3	3 ± 0.4
xPCL2k	0.09 ± 0.01	2.3 ± 0.5	67 ± 9	2.89 ± 0.9	n/a
FL Flex	0.37 ± 0.01	1.08 ± 0.05	4.9 ± 0.45	0.04 ± 0.01	n/a

Table 4.2:- List of key mechanical properties determined from tensile testing for each material composition. PCL45k is non-crosslinked PCL polymer. xPCL refers to photocured PCL materials, where xPCL10k is comprised of only 10,000g/mol macromers. xPCL10k0.9k, and xPCL10k+4A indicate the inclusion of another crosslinking component, where the 0.9k refers to a 900 g/mol PCL macromer, and the +4A refers to PTOL-4A. Samples are dumbbell shaped. Initial grip-to-grip distance was 30 mm. Each group average was calculated from a population size of at least 15 samples (n = >15), with the exception of PCL45k where n=10, and FL flex where n = 4. Extension rate was 5 mm/min. Samples were extended until break. Values are shown as average ± SD.

It was observed during testing that the PCL45k, xPCL10k and xPCL10k0.9k materials displayed stable necking after yielding until break. The non-cross-linked PCL45k material displays substantial toughness, largely attributed to a high stress and elongation at break, and an extensive strain-hardening phase. The xPCL10k cross-linked material displays an initial profile and Young's modulus that is highly similar to the PCL45k material but possesses shorter cold drawing and strain-hardening stages, and stress/elongation at break. The xPCL10k0.9k profile shows similarities to the xPCL10k material, but with approximately half the stress and elongation values throughout. Additionally, the xPCL10k0.9k network does not display the large peak-like yield point that the PCL45k and xPCL10k materials shown, and instead smoothly transitions between elastic and plastic deformation regions. The xPCL10k+4A material shows a similarly smooth transition but yields at a lower stress. The xPCL10k+4A strain hardens significantly, with slightly greater ultimate stress and elongation at break that the xPCL10k0.9k material. This combination results in the xPCL10k+4A material being marginally less tough than the xPCL10k0.9k. The xPCL2k material profile displays no yield point and breaks at a similar elongation to the xPCL10k0.9k group but at substantially lower stress. The FL Flex dumbbells break after only small amounts of elongation with low ultimate strength.

4.3.2 Thermoanalytical investigation of photo-cured networks

DSC was performed to determine the melting temperatures ($T_{m(n)}$) and enthalpies ($\Delta H_{m(n)}$) from both heating ramps, and the crystallisation temperature (T_c) and enthalpy (ΔH_c) from the cooling ramp, for each oligomer, macromer, and photo-cured network composition. The positions ($T_{m(1)}$) and enthalpies ($\Delta H_{m(1)}$) of the macromers and networks are representative of the thermal history of the materials resulting from our synthesis and manufacturing processes. Oligomer $T_{m(1)}$ and $\Delta H_{m(1)}$ are representative of the thermal history from the manufacturer's synthesis, transport, and storage processes. The value of $\Delta H_{m(1)}$ can be inferred as proportional to the sample crystallinity. Sample T_c positions and ΔH_c enthalpies are highly dependent on the cooling rate and temperature used during the DSC cycle, and as such directly affect the following $T_{m(2)}$ and $\Delta H_{m(2)}$ values.

The melting and crystallisation temperatures and enthalpies of the oligomers, macromers, and networks are listed in Table 4.3. Example DSC traces of the 2 kg/mol oligomer, macromer and network are shown in comparison to the xPCL10k0.9k network within Figure 4.3.

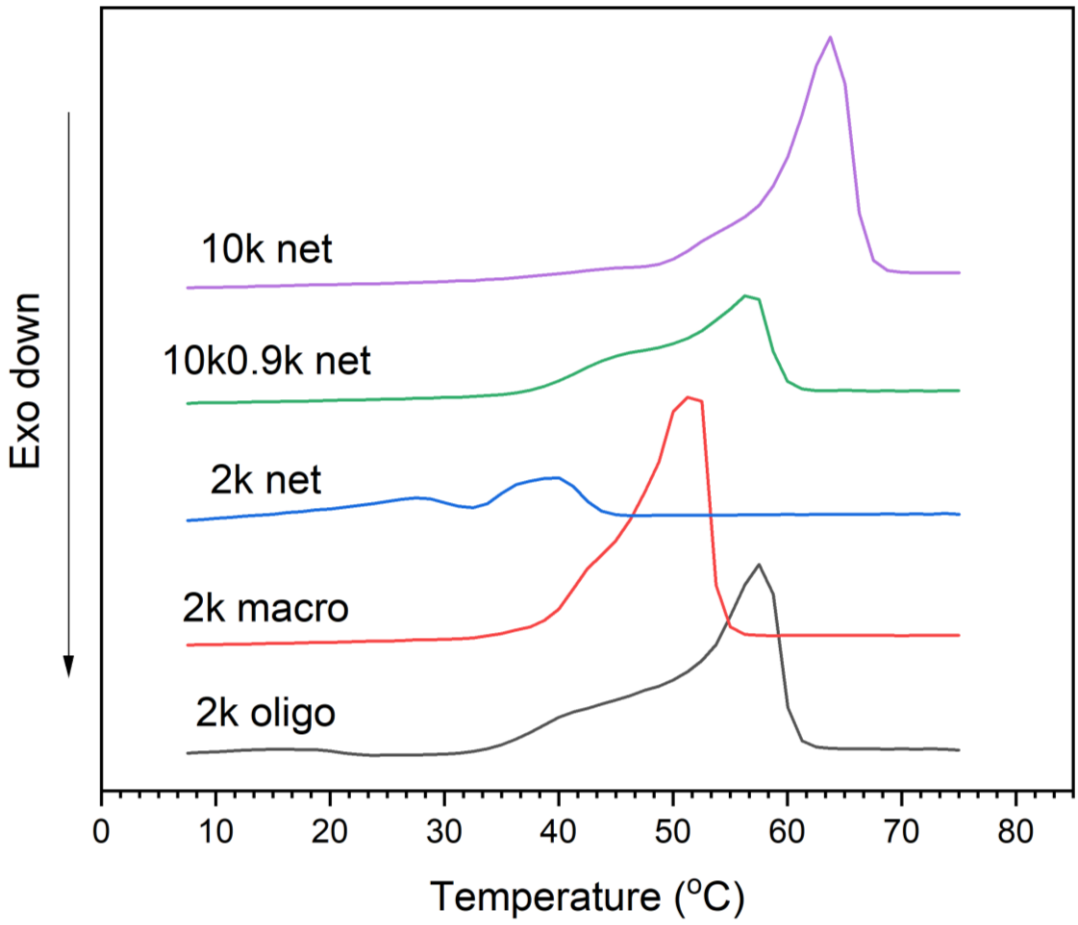

Figure 4.3:- DSC traces displaying the 1st melting peaks ($T_{m(1)}$) of the 2 kg/mol (2k) PCL oligomer (black), macromer (red), and network (blue), the bimodal xPCL10k0.9k network (green), and the xPCL10k (10k) network (pink). The xPCL10k0.9k network is composed of both 10,000 (10k) and 900 g/mol (0.9k) macromer units. (n=1) Traces are offset for clarity.

Sample backbone composition	$T_{m\,(1)}$ °C			$\Delta H_{m\,(1)}$ (uV/mg)			$T_{m\,(2)}$ °C			$\Delta H_{m\,(2)}$ (uV/mg)			T_c °C			ΔH_c (uV/mg)		
	Olig	Mac	Net	Olig	Mac	Net	Olig	Mac	Net	Olig	Mac	Net	Olig	Mac	Net	Olig	Mac	Net
45k	67			280			61			197			27			-203		
10k	67	60	64	318	335	262	57	57	59	256	239	205	26	34	28	-247	-247	-212
2k	58	52	40	280	302	67	45/51	42/50	30	239	219	28	22	18	n/a	-234	-220	n/a
0.9k	38	34		109	77		29	20		131	86		-21	-7		-5	-60	
10k0.9k			57			167			54			118			-4			-75
10k+4A			52			23			n/a			n/a			n/a			n/a

Table 4.3:- List of values for melting temperature (T_m), melting enthalpy (ΔH_m), crystallisation temperature (T_c) and crystallisation enthalpy (ΔH_c) for each oligomer (Olig), macromer (Mac), and network (Net). 10k0.9k, and 10k+4A indicate a bimodal network with the inclusion of another crosslinking component alongside the main 10,000 g/mol (10k) PCL backbone, where the 0.9k refers to a 900 g/mol (0.9k) PCL macromer, and the +4A refers to PTOL-4A. The number in the brackets of the T_m and ΔH_m headers indicate the 1st or 2nd heating ramp the values have been acquired from. T_c and ΔH_c were determined from the cooling ramp between the heating ramps. "xx/xx" indicates the presence of a clear twin peak and represents the positions of both of these peaks individually. (n=1)

The $\Delta H_{m(1)}$ of the 10k and 2k macromers were higher than their equivalent oligomers, while the 0.9k oligomer and macromer show the opposite trend. However, the difference in $\Delta H_{m(1)}$ between oligomer and macromer forms of the same backbone composition is small. The $\Delta H_{m(1)}$ of the crosslinked networks were lower than their equivalent oligomers and macromers. The networks can be arranged in order of the largest $\Delta H_{m(1)}$, where xPCL10k > xPCL10k0.9k > xPCL2k > xPCL10k+4A. When comparing the crystallinity retained by the crosslinked networks against the non-crosslinked PCL45k, the xPCL10k, xPCL10k0.9k, xPCL2k, and xPCL10k+4A networks retain 94, 60, 24, and 8% crystallinity, respectively. Macromers typically possess a $T_{m(1)}$ lower than their non-functionalised oligomers. $T_{m(2)}$ peak positions are generally at lower temperatures than their $T_{m(1)}$ values for all materials. Associated $\Delta H_{m(2)}$ are also typically lower than $\Delta H_{m(1)}$ values for all materials except 0.9k where an increase is observed. An exothermic crystallisation peak is present for all oligomer/macromer materials, and the 10k and bimodal networks during the cooling ramp. For the linear oligomers, macromers, and 10k network, the magnitudes of $\Delta H_{m(2)}$ and ΔH_c are highly similar. The xPCL2k and xPCL10k+4A network samples exhibited no T_c peak. The xPCL10k+4A material displays no thermal signature after the initial heating ramp. The PTOL-4A monomers demonstrated no noticeable thermal signature.

4.3.3 The working curve

Working curves of each resin formulation were generated for use as a tool to aid resin formulation, but also for the selection of initial print settings. The Jacobs working curve is a semi-logarithmic plot of cure depth (C_d in μm) versus light irradiation dose (E in mJ/cm^2) used to describe the fundamental variables associated with stereolithography such as, the depth penetration (D_p) of light, and the critical dose (E_c) to gelation [111]. Generation of a working curve should result in a linear relationship, which can be described by Equation Equation 4-1:

$$C_d = D_p \ln \frac{E}{E_c} \qquad \text{Equation 4-1}$$

The gradient of the slope of the working curve trendline is the depth penetration of the resin at that UV source wavelength. The x-intercept of the trendline corresponds to the critical dose required for the resin to reach the gel point. The critical dose can be converted into the critical irradiation time by dividing the E_c by the irradiance of the UV source, which for EMBER is 22.5 mW/cm^2 or 22.5 mJ/cm^2 per second. The lowest possible exposure time to generate a crosslinked layer with sufficient strength to survive

manipulation is defined as t_{min}. The working curves of uni- and bimodal resins tested alongside a commercial resin (PR-48) are shown in Figure 4.4, and the values of D_p, t_c, and t_{min} shown in Table 4.4.

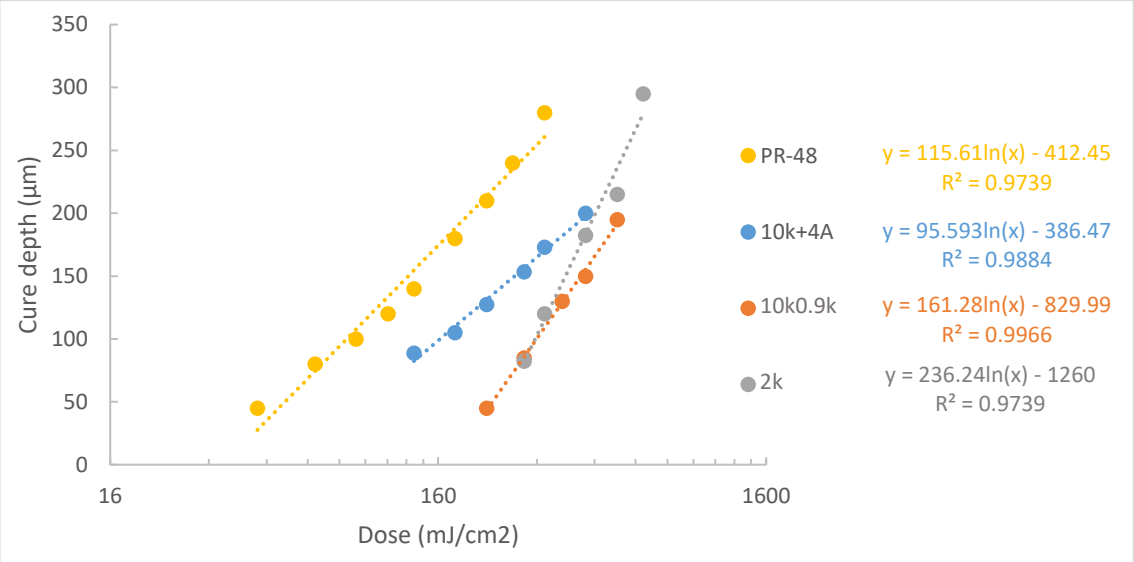

Figure 4.4:- Working curves of PCL-macromer-based resins compared with a commercial resin (PR-48) on the Autodesk EMBER DLP 3D printer. 2k is comprised of only 2,000g/mol PCL macromers. 10k0.9k, and 10k+4A indicate the inclusion of another crosslinking component, where the 0.9k refers to a 900 g/mol PCL macromer, and the +4A refers to PTOL-4A. Trendline formulae shown in figure legend for each.

Resin name	Resin functionality C=C conc. (mM)	Resin properties		
		D_p (µm)	t_c (s)	t_{min} (s)
PR-48	5,310	116	0.16	2
xPCL10k+4A	1,760	96	2.5	6
xPCL10k0.9k	467	161	7.6	10
xPCL2k	438	236	9.2	13
xPCL10k	89	n/a	~120 [a]	n/a

Table 4.4:- Lists the resin depth penetration (D_p), critical time to gelation (t_c), and minimum time to form a viable layer (t_{min}) determined from the performing the working curves on the printer. PR-48 is a highly reactive commercial resin. xPCL refers to photocured PCL materials, xPCL10k is comprised of only 10,000g/mol macromers. xPCL10k0.9k, and xPCL10k+4A indicate the inclusion of another crosslinking component, where the 0.9k refers to a 900 g/mol PCL macromer, and the +4A refers to PTOL-4A. [a] Gel point estimated from working curve attempts.

PR-48 demonstrates substantially greater reactivity than the PCL-based macromer resins, which can be seen from very low values of t_c (0.16 s) and t_{min} (2 s). Both bimodal PCL-based resins (xPCL10k+4A and xPCL10k0.9k) are more reactive than the unimodal xPCL2k resin, demonstrated by lower values of t_c and t_{min}. In particular, considering the similar C=C bond concentration within the xPCL10k0.9k and xPCL2k formulations, the

bimodal xPCL10k0.9k resin indicates a clear reactive advantage. This trend in reactivity was also shown from the UV-rheometry results in 4.3.4. The D_p of the xPCL10k+4A and PR-48 formulations are very similar, with the xPCL10k0.9k and xPCL2k resins D_p being approximately 50 and 100 μm deeper, respectively. A working curve of the xPCL10k only resin (listed in Table 4.1) was also attempted, but required extremely long exposure times of greater than 120 s (> 2700 mJ/cm^2), which were tacky gels that were difficult to handle and measure.

4.3.4 UV rheometry determination of the critical time

To further evaluate the reactivity of the different resin formulations, UV rheometry was performed. Referring back to Table 4.1, the xPCL2k, xPCL10k, and xPCL10k0.9k resins contained 5 wt% of TPO, with macromer/diluent composition remaining as shown. Each resin composition was repeated in triplicate, with the average critical time (t_c), maximal storage modulus (G'_{max}), and time to 95 % maximum storage modulus (t_{plat}) determined. The G'/G'' crossover while G' is displaying an exponential increase was used to determine the t_c. For comparative purposes, the average critical times of three commercial photo-curable materials were also determined. Representative rheological profiles of the resins during UV curing are shown in Figure 4.5, and the average t_c, G'_{max}, t_{plat} listed in Table 4.5.

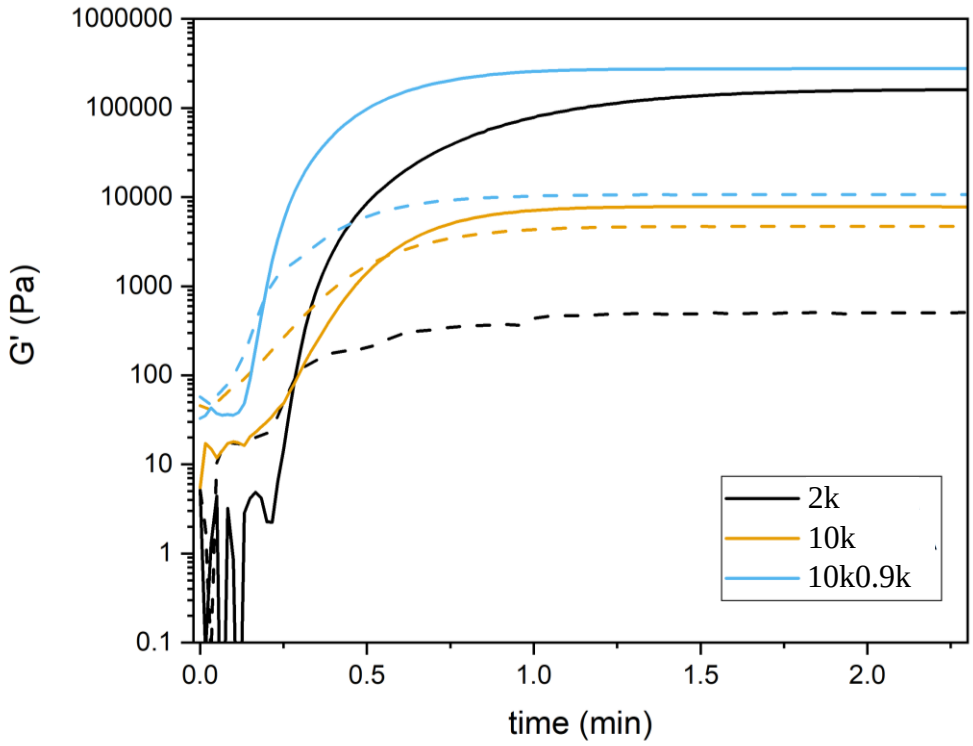

Figure 4.5:- Representative rheological profiles of sample G' and G''. Sample resin groups are comprised of PCL macromers of various molecular weights. 2k refers to PCL macromers of 2,000 g/mol, with 10k being macromers of 10,000 g/mol. The 10k0.9k formulation contains both 10,000 g/mol and 900 g/mol macromer units. The critical time to gelation can be determined from the crossover of the moduli, where G' has become larger than G''. UV curing begins at t = 0. One representative set of traces for each group is shown from n=3.

Resin	C=C (mM)	t_c (s)	G'$_{max}$ (MPa)	t_{plat} (s)
xPCL10k0.9k	467	11.2 ± 0.6	275.1 ± 7.2	73 ± 1
xPCL2k	438	17	159.9 ± 2.5	106 ± 15
xPCL10k	89	34 ± 0.6	8.1 ± 0.2	82 ± 4

Table 4.5:- Average critical time (t_c), maximal storage modulus (G'$_{max}$), and time to G' plateau (t_{plat}) for each resin composition determined from UV rheometry.. Sample resin groups are comprised of PCL macromers of various molecular weights. xPCL2k refers to PCL macromers of 2,000 g/mol, with xPCL10k being macromers of 10,000 g/mol. The xPCL10k0.9k formulation contains both 10,000 g/mol and 900 g/mol macromer units. n=3.

The xPCL10k material featuring the lowest C=C concentration, demonstrated the largest t_c of 34 s. The xPCL2k and xPCL10k0.9k resins with higher C=C concentrations featured substantially shorter t_cs of 17 and 11 s, respectively. The commercial resins demonstrated very quick t_cs of sub-five seconds. Kudo3D black DLP resin had a t_c of 2 s, while the Formlabs flexible (v1) had a t_c of 3.6 s. The verowhite Polyjet 3D printing material returned a t_c of 2.6 s. The xPCL10k0.9k resin had the highest G' Max, followed by the xPCL2k, then the xPCL10k resins. The xPCL10k0.9k resin was also the quickest to reach t_{plat}, followed by xPCL10k, and finally xPCL2k resins.

4.3.5 Stereolithography 3D printing

SL printing of the xPCL10k+4A formulation was performed. The xPCL10k+4A core resin within Table 4.1 contained the same quantities of macromer and diluent, but contained 5 wt% TPO, 0.2 wt% BBOT, and 0.1 wt% HQ, relative to the total macromer-diluent weight. The layer exposure times used for the xPCL10k+4A resin were split into 3 groups, an individual first layer of 20 s, a set of 10 burn in layers at 13 s, and the remaining model layers at 8 s. The peel rotation was set to the slowest speed of 1 rpm for the entire printing process. A series of structures were printed, including 70 % porosity gyroid tissue scaffolds, square-based pyramids, and Voronoi D towers. Images of the printed objects were taken using a DinoLite microscope-camera, and are shown in Figure 4.6.

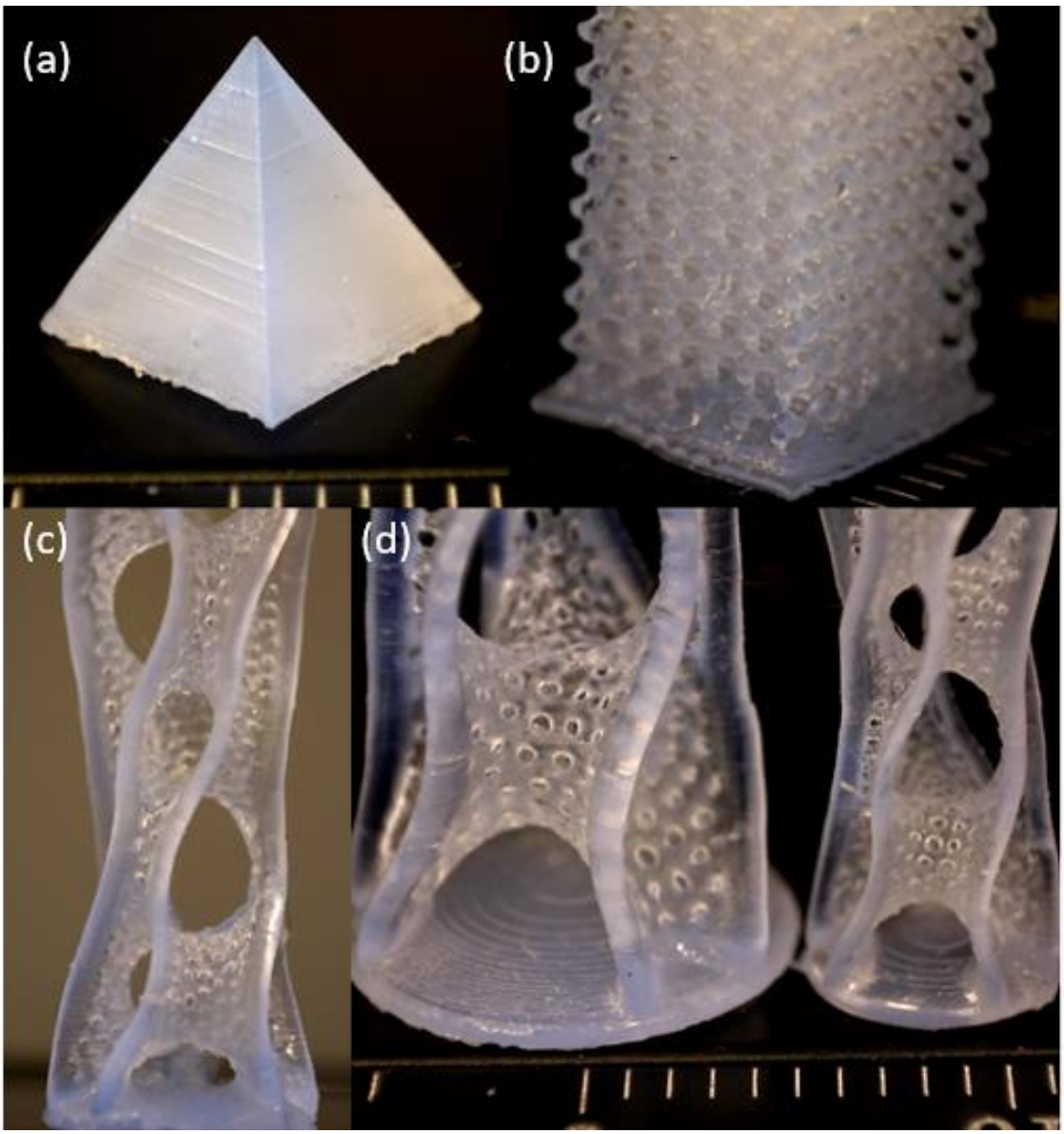

Figure 4.6:- DinoLite microscope camera images of (a) 1cm^2 square based pyramid, (b) 70 % porosity gyroid tissue scaffold, (c) and (d) Voronoi D towers (two different sizes). All models were printed on EMBER using the xPCL10k+4A (PCL 10,000 g/mol macromer and PTOL-4A) formulation. Line markings in (a), (b) and (d) are 1 mm apart.

Models produced from the xPCL10k+4A resin were generally well-formed. The initial layers tended to have slightly poorer resolution due to the overexposure required for good attachment. Slight damage was also caused by the bladed spatula used to remove the models from the build head surface, as can be seen most evidently by the bases of the pyramid and gyroid models.

Printing of the xPCL10k0.9k was also attempted. Unfortunately, prior to completion of the first 11 layers, the models typically tore around the trailing edge in reference to the peel direction. An example of this tearing is shown in Figure 4.7, from attempts at printing the square-based pyramid model. Print settings for this particular attempt were an

individual first layer of 120 s, a set of 10 burn-in layers at 80 s, and the remaining model layers at 60 s. Detachment or damage occurred during the burn-in layers.

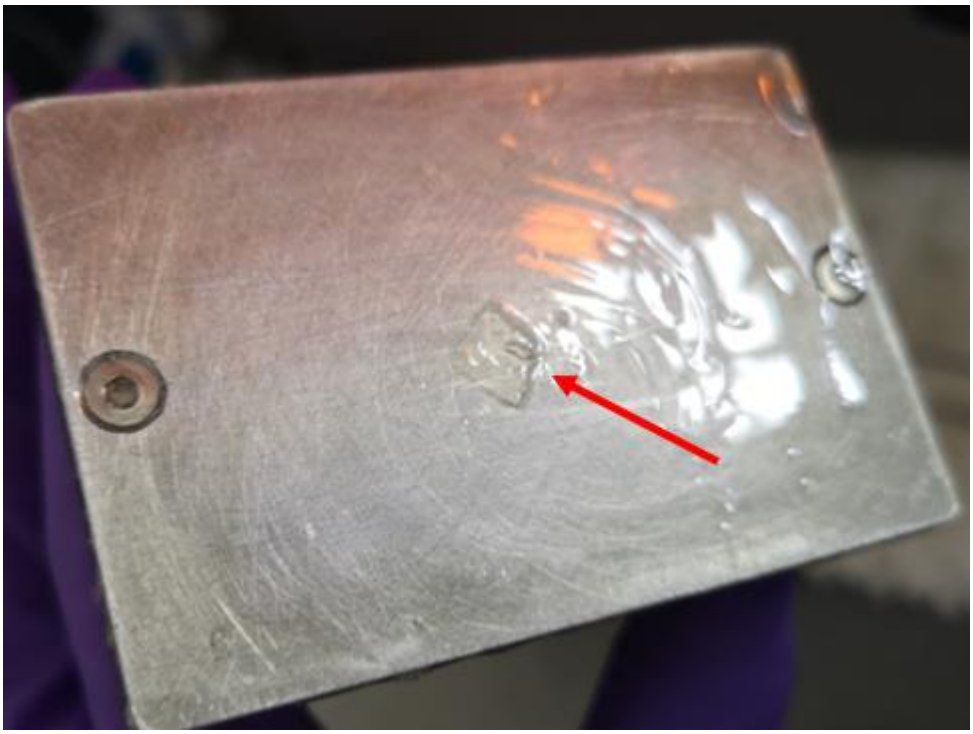

Figure 4.7:- Photograph showing the damaged model on the build head surface during the initial burn-in layers, while attempting to print with the xPCL10k0.9k (PCL 10,000 g/mol and 900 g/mol macromers) resin. Damage can be seen to the right edge (arrow indicating), with debris on the surface where the next layer should attach.

Similar delamination/tearing of printed layers was noticed with other model geometries too, such as the waffle-like cuboid, which was typically used for print setting optimisation. Over the course of the next few layers, the damaged/delaminated area would grow until new layers no longer adhered to the model. Debris from the damaged area often was dragged within the print area during peeling, compounding difficulties for attachment of the next layers. Various print exposure times were tested, as well as different positioning and rotation of the model in attempts to improve survivability, but none achieved any meaningful improvement.

4.3.6 Degradation: pressurised

Degradation samples were weighed after each autoclave sterilisation cycle to establish mass profiles for each material type. The average wet mass (only superficial fluid removed) at each time point was determined from triplicate samples. The mass profiles during accelerated degradation are shown in Figure 4.8, and the approximate rate of mass loss, and time to complete degradation for each network presented in Table 4.6.

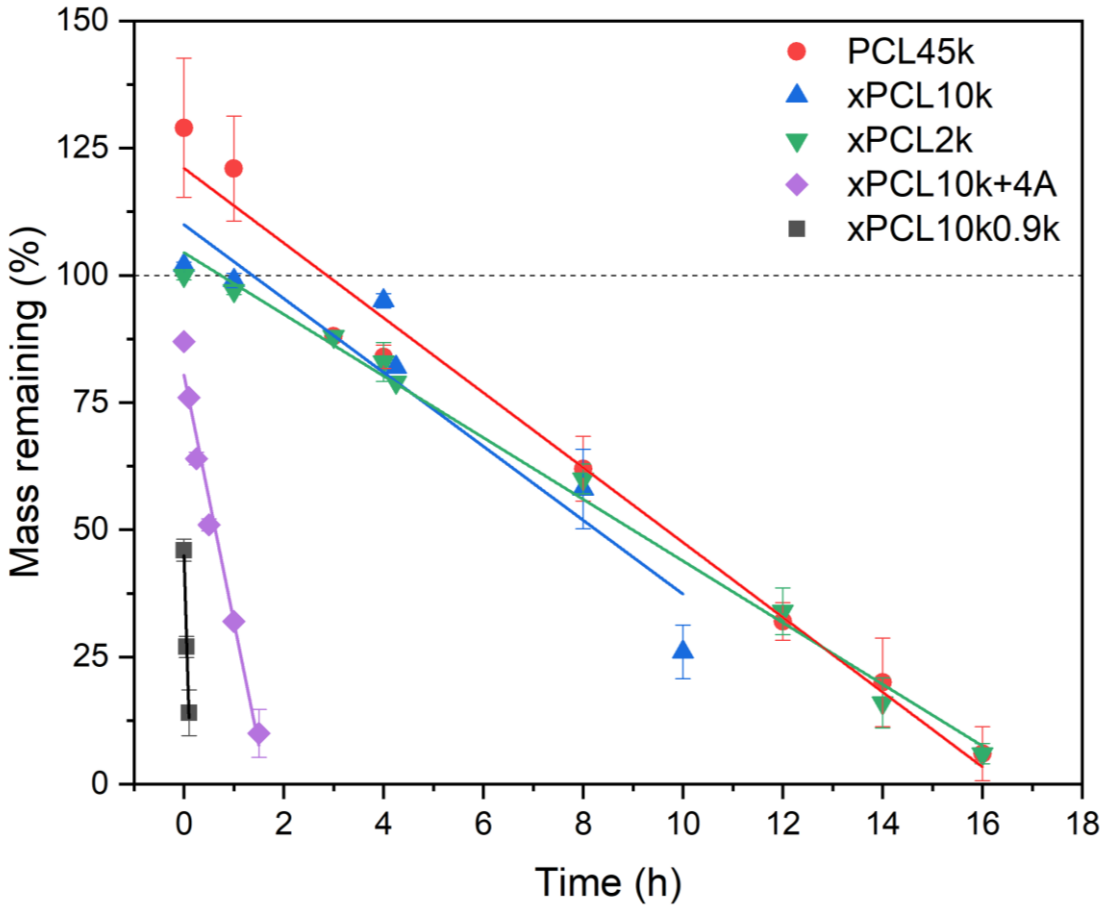

Figure 4.8:- Average mass of non-crosslinked, and crosslinked networks during accelerated degradation. PCL45k is non-crosslinked PCL polymer. xPCL refers to photocured PCL materials, xPCL10k is comprised of only 10,000g/mol macromers. xPCL10k0.9k, and xPCL10k+4A indicate the inclusion of another crosslinking component, where the 0.9k refers to a 900 g/mol PCL macromer, and the +4A refers to PTOL-4A. Average is calculated from the mass of 3 individual discs (n=3). Error bars represent SD. Dashed reference line indicates starting mass (100%).

Network label	Mass loss rate (% per hour)	Extrapolated time to m = 0 (h)	Approximate time to clear solution (h)
PCL45k	7.4	13.6	18
xPCL10k	8.5	11.8	14
xPCL2k	6.1	16.5	20
xPCL10k+4A	48.6	2.1	2
xPCL10k0.9k	324.8	0.3	0.5

Table 4.6:- Rate of mass loss, extrapolated time to complete mass loss, and the experimentally determined approximate length of time required to obtain a clear solution. PCL45k is non-crosslinked PCL polymer. xPCL refers to photocured PCL materials, where xPCL10k is comprised of only 10,000g/mol macromers. xPCL10k0.9k, and xPCL10k+4A indicate the inclusion of another crosslinking component, where the 0.9k refers to a 900 g/mol PCL macromer, and the +4A refers to PTOL-4A.Values determined from the trendlines fitted to the averages of n=3 samples of each group.

All tested samples fully degrade within 20 hours. Bimodal xPCL10k0.9k and xPCL10k-4A materials rapidly lose mass, with complete degradation occuring within 0.5, and 2 hours respectively. The xPCL10k0.9k The PCL45k non-crosslinked material appears to increase in mass prior to steady mass loss. The PCL45k discs melt during the autoclave cycle and reform into polymer spheres after the cooling stage. The profiles of the xPCL10k and xPCL2k materials start very similarly, but the xPCL10k nework degradation settles at a steeper rate and degrades quickest out of the 3 unimodal materials, while the xPCL2k material ultimately becomes the slowest material to fully degrade. The xPCL10k networks fragment and no longer resemble disks beyond the 8 hour mark, The xPCL10k+4A and xPCL2k disks appeared thinner as degradation time increased, while retaining their circular cross-sectional shape until no measureable mass was found. Due to the rapid degradation of the xPCL10k0.9k networks the disks disintegrate after 15 mins and form a cloudy solution, which becomes a clear solution at the 30 min time point.

4.3.7 Degradation: atmospheric

Degradation of samples from xPCL10k0.9k, and xPCL10k resin formulations were tested alongside xPCL10k+4A networks that contained different amounts of the PTOL-4A (4A). The overall sum of macromer content always equates to 45 wt% of the total resin weight, therefore quantities of PTOL-4A replace a wt% of 10k-2MA macromer; 4A concentrations of 5, 10, and 15 wt% were tested. The mass profiles during degradation are shown in Figure 4.9, and the approximate rates of mass loss and times to complete degradation indicated in Table 4.7.

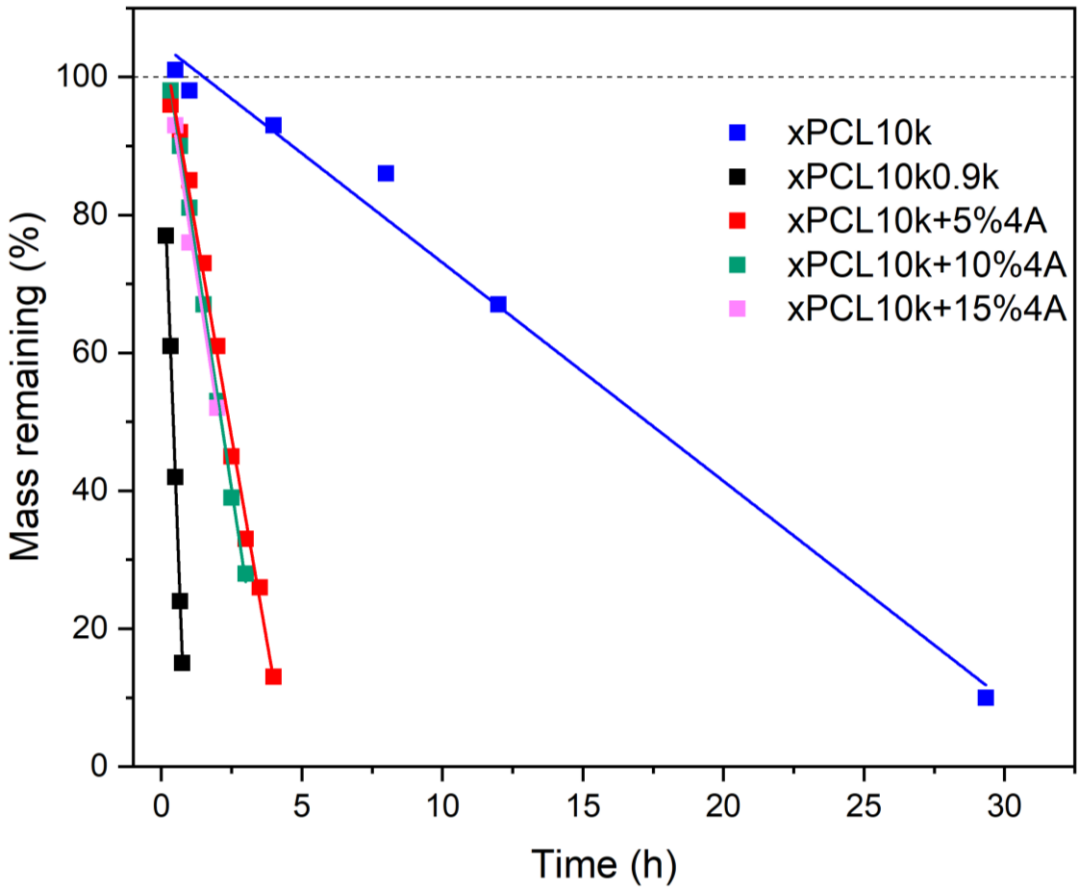

Figure 4.9:- Degradation profiles of photo-cured networks during boiling in 1M NaOH in a RBF. PCL45k is non-crosslinked PCL polymer. xPCL refers to photocured PCL materials, xPCL10k is comprised of only 10,000g/mol macromers. xPCL10k0.9k, and xPCL10k+4A indicate the inclusion of another crosslinking component, where the 0.9k refers to a 900 g/mol PCL macromer, and the +4A refers to PTOL-4A. Each data series follows the mass loss of the same disc specimen until no measurable mass remained. (n=1). Dashed reference line indicates starting mass (100%).

Network label	Mass loss rate (% per hour)	Extrapolated time to m = 0 (h)	Approximate time to clear solution (h)
xPCL10k	3.2	31.4	48
xPCL10k0.9k	108.0	0.9	5
xPCL10k+5%4A	23.5	4.3	n/e
xPCL10k+10%4A	27.0	3.7	n/e
xPCL10k+15%4A	27.2	3.7	5.5

Table 4.7:- Extrapolated time to complete mass loss and the experimentally determined approximate time required for a clear solution. PCL45k is non-crosslinked PCL polymer. xPCL refers to photocured PCL materials, where xPCL10k is comprised of only 10,000g/mol macromers. xPCL10k0.9k, and xPCL10k+4A indicate the inclusion of another crosslinking component, where the 0.9k refers to a 900 g/mol PCL macromer, and the +4A refers to PTOL-4A. "n/e" = not evaluated. (n=1) . Values determined from the trendlines fitted to samples of each group.

The rate of mass loss is fastest for the xPCL10k0.9k disks, while slowest for the xPCL10k group. The PTOL-4A containing networks degrade relatively quickly, with the amount of PTOL-4A appearing to make little difference to the degradation rate.

4.4 Discussion

4.4.1 Summary

To prepare degradable PCL structures by stereolithography, a bimodal resin composed of 10k-2MA and PTOL-4A macromers and benzyl alcohol non-reactive diluent, was prepared. Tough degradable semi-crystalline structures of various geometries were printed via SL using the bimodal PCL10k+4A photo-curable resin. Networks of unimodal and bimodal macromer resin compositions were also produced by injection moulding and UV curing. The tensile, thermo-mechanical, and degradation properties of the networks were investigated. It was demonstrated that the bimodal networks offered greater strength, toughness, and faster degradation over unimodal PCL networks of comparable reactive group concentration. Unimodal xPCL10k networks demonstrated superior toughness to the bimodal networks but were not printable.

4.4.2 Network thermo-mechanical properties

The mechanical properties of polymer materials are highly dependent on the method of processing, sample crystallinity, degree of crosslinking (if any), and the molecular weight(s) [154], [155]. The mechanical properties of the materials were assessed through tensile experiments, while the material crystallinity was determined by DSC. All the photo-cured networks are semi-crystalline in nature, containing between 8.2 – 93.6 % of the crystallinity associated with non-crosslinked PCL45k. Samples with a greater extent of crystallinity, demonstrated greater network toughness during tensile testing. Interestingly, the bimodal xPCL10k0.9k networks retained over double the crystallinity of their xPCL2k counterparts and were more than 10x tougher. The other bimodal network, xPCL10k+4A, returned the lowest retention of crystallinity, which is likely due to the PTOL-4A units being unable to crystallise, combined with lower overall network crystallinity from denser crosslinking.

The tensile data for the xPCL2k material appears in good agreement to the tensile behaviour of linear 1250 g/mol PCL diacrylate (PCLDA) studied by Green *et al* [88]. Both materials have a Young's modulus of approximately 3 MPa, and show a similar elastomeric-like tensile profile, with the xPCL2k networks being tougher as a result of greater ultimate elongation and stress. Previously reported ultimate tensile strengths of approximately 45,000 g/mol M_w PCL processed by compression moulding range between 16 – 21.6 MPa, with Young's moduli ranging between 251.9 and 400 MPa [156]–[158]. PCL45k material tested in this study demonstrated a greater ultimate tensile strength of

31 ± 2.6 MPa, with a stiffness of 15.84 ± 0.50 MPa/mm. These values are expected to be partially inflated due to the dumbbell specimen shape having a non-homogeneous cross-section between the grips, as opposed to standard rectangular tensile specimens, and so the values appear to be within the expected range. At this time, literature concerning crosslinked networks of PCL macromers close to 10,000 g/mol could not be found. Therefore, the xPCL10k networks appear to be the first demonstration of networks produced by photo-crosslinking PCL macromers of greater molecular weight than 2000 g/mol (bifunctional) [129], and 6000 g/mol (trifunctional) [91]. Flexible bimodal PTMC-based photo-curable networks were demonstrated by Bochove *et al*, which appear to be the only other current example of bimodal stereolithography networks. The resins were composed of various ratios of 700 and 10300 g/mol tri-methacrylate macromers and solubilised with propylene carbonate. Following extraction and drying, the bimodal networks of the compositions shown demonstrated 3-4x the toughness of the unimodal networks from each of the macromers individually. Comparing the most similar bimodal PTMC network (in terms of large:small macromer ratio) to our xPCL10k0.9k, the overall network toughnesses are very similar (PTMC700/10300 (31/69) = 15.52 ± 3.92 J/cm^3, xPCL10k0.9k = 14 ± 3 J/cm^3. The tensile profiles are considerably different however, with the PTMC bimodal network profile representative of a highly elastic material, with toughness being a feature of its high elongation at break (531 %) despite its low ultimate stress (5.4 MPa) [153]. In previous investigations with PDMS elastomeric networks, increases in both elongation and stress at break were observed from the bimodal networks, over the unimodal networks of each component [150]. The bimodal PTMC networks performed differently, with their increases in toughness being derived from an increase in only one factor (elongation or stress). The bimodal PCL-based materials also appear to perform differently from both the PDMS and PTMC bimodal networks. The xPCL10k0.9k networks show a decrease in both elongation and stress at break when compared with a unimodal network of xPCL10k. It is anticipated that the reduction in overall toughness of the bimodal xPCL10k0.9k network is largely attributed to the reduced crystallinity regained in comparison to the xPCL10k network. While we did not produce networks purely from 0.9k-3MA, based on similarly sized tri-functional PCL macromers from Elomaa *et al* [91], we can assume that such networks would possess low toughness. Considering this, and the low ultimate stress and toughness of the xPCL2k materials of similar crosslinking density, the xPCL10k0.9k networks offer a significant improvement in mechanical properties.

Overall, our results do suggest that use of larger linear molecular weight macromers has potential to substantially increase the toughness of PCL-based networks. Bimodal formulations utilising a combination of large linear macromers with small multi-functional macromers would likely be useful to maintain an adequate level of reactivity, and structural integrity during printing.

4.4.3 Reactivity and the development of mechanical properties during curing

The reactivity of the xPCL10k0.9k, xPCL10k, and xPCL2k resins were investigated by dynamic UV rheology and through the Jacobs working curve. Both methodologies demonstrate through the time to gelation (t_c), that the bimodal xPCL10k0.9k formulation is more reactive than the unimodal xPCL2k resin, and with the xPCL10k resin consistently the least reactive. From rheological measurements, the bimodal xPCL10k0.9k resin was approximately 3x faster to gelation than xPCL10k, and 1.5x faster than xPCL2k. The gel point during photo-rheology was determined to occur at the G'/G" crossover, accompanied by an exponential increase in G' over several orders of magnitude. The scattering of G' and G", especially from the xPCL2k resin, during the early stages of curing are ignored, and are likely related to the low viscosity of the resin and/or inertial effects from the top geometry. While this method has been shown to have a dependence on frequency for some materials by Winters [159], for many other material systems the G'/G" crossover has been demonstrated to be a reasonable indicator of gelation [160]–[163].

Evaluation of a new photo-curable resin via the Jacobs working curve has become a standard procedure, and is particularly useful due to the information gained regarding the depth penetration, cure depth at a specific exposure, and curing speed through gel point dose and the time to gel point. For fast curing resins, information from the Jacobs working curve is largely sufficient for effective translation to stereolithography due to their rapid increase in mechanical strength as a direct result of quick double bond conversion. For formulations composed of comparatively large macromers with lower crosslinking density potential, more time is needed after establishment of gelation to develop such mechanical strength. Therefore, the information gained from the Jacobs working curve alone is not sufficient to suggest, in a reliable manner, the printability of these slower, less densely crosslinked formulations. Use of rheology to determine the gel point and provide an insight into the development of the mechanical properties during the curing stage was first demonstrated by Khan *et al* [164]. More recently, photo-rheology combined with simultaneous real-time near infrared spectroscopy was used to relate

curing speed, mechanical properties, and double bond conversion of a resin sample simultaneously in order to aid resin optimisation [165]. The photo-rheology in this work was performed with a 365 nm UV LED as no 405 nm variant was readily available, which makes direct comparison to the EMBER-derived exposure doses not possible. Additionally, it was not possible to monitor the curing process with simultaneous Fourier-transform infrared spectroscopy (FTIR); therefore, no measurement of double bond conversion was taken either. Despite this, the dynamic rheology measurements were still useful in their own right. The rheological measurements confirmed resin reactivity trends seen from the Jacob's working curves, and provided an insight into post-gelation development of mechanical properties during curing. The storage modulus is an indication of the material's ability to store deformation energy in an elastic manner, and is directly related to the degree of crosslinking [165], [166]. Networks produced from resins with higher concentrations of reactive groups did demonstrate greater G'_{max} values, shown in Table 4.5, as would be anticipated. The bimodal xPCL10k0.9k material possessed the highest G'_{max} value, indicating that it may offer the greatest print survivability compared with the xPCL2k and xPCL10k formulations, based on its greater crosslinking degree [165]. Ideally, future dynamic rheology with a 405 nm light source and monitoring of double bond conversion with FTIR would enable better crossover with the Jacobs working curve data, which in turn should enable a more complete resin characterisation, and assist in optimising formulations as described by Hofstetter *et al* [165]. It should be noted that rheology on the xPCL2k formulation shown in Figure 4.5 and Table 4.5, was performed in triplicate, despite the t_c determined from the G'/G" crossover being a singular value. In the other two rheology runs, the initial pre-exposure G' signal appears artificially high in comparison to the G' curve from the other sample, and do not cross their G" curves rendering determination of t_c via this method not possible. Interestingly, the profiles of G' after 0.5 mins, and the G" profiles over the entire time course are identical to the sample that did feature a valid G'/G" crossover. The rheometer appeared to struggle to maintain a precise measurement of G' and G" during the initial liquid resin state, indicating that this particular formulation would likely have benefited from a larger diameter upper plate or a smaller gap size. Due to the small errors (± 0.6 s) in calculated t_c between repeated measurements of the other materials, it seems reasonable to expect that the singular 17 s t_c remains valid and will be subject to a similar degree of error.

4.4.4 Stereolithography fabrication of tough semi-crystalline structures

Several structures were printed on the EMBER printer using the PCL-based xPCL10k+4A resin formulation, as shown in Figure 4.6. Printing using the xPCL10k+4A formulation was reliable and repeatable between batches of resin. From tensile tests, the xPCL10k+4A resin possesses significantly tougher mechanical properties to previous PCL-based materials that are capable of printing via stereolithography. Amorphous PCL structures printed in the melt via SL by Elomaa *et al* were of low toughness, with an ultimate stress at break of 2.55 ± 0.5 MPa, and an elongation at break of 19.5 ± 0.5 %, or the equivalent of approximately 10 mm [91]. Green *et al* used a non-reactive diluent in the form of dioxane to formulate a series of 1:1 (w:w) low molecular weight PCL-macromer/dioxane resins capable of being printed at room temperature by SL. The acrylated macromer molecular weights ranged between 300-1250 g/mol, and were either bi- or tri-functional. Amorphous networks were produced from these resins, with all of the networks demonstrating < 1 MPa stress and < 40 % strain at break. The 1250 g/mol diacrylate formulation possessed the greatest toughness at 0.15 ± 0.02 J/cm^3 [88]. Our xPCL10k+4A resin exhibits an ultimate stress of 14.0 ± 0.7, an elongation at break of 43.9 ± 3 (equivalent to approximately 147 %), and a toughness of 11.4 ± 1.3 J/cm^3. Photo-cured parts produced from the xPCL10k+4A formulation retained approximately 8 % of the crystallinity associated with parts moulded from 45,000 g/mol non-crosslinked PCL. As such, we believe that this is the first demonstration of a tough semi-crystalline PCL-based stereolithography resin.

4.4.5 Advantages of bimodal photo-cured networks

The main advantage of the bimodal networks from a stereolithography point of view is their greatly improved reactivity, while retaining a degree of the mechanical properties offered by the larger macromer unit. The xPCL10k resin, while resulting in networks with excellent toughness when injection moulded and UV cured, was limited by its ability to be solubilised in large enough quantities to offset its low mole content of reactive groups, and as such required long exposure times to form viable layers. The resulting cured layers possessed poor mechanical properties in the solvated state, which frequently resulted in jamming and layer/model damage (shown in Figure 4.7) or detachment during printing attempts. With the substitution of 15 wt% of 10k-2MA with PTOL-4A to form the xPCL10k+4A resin, the curing behaviour changed vastly. The xPCL10k+4A resin was able to form layers with sufficient strength to survive the printing method, possessing a working curve t_c of over 48x lower than the xPCL10k only resin. Similarly, the

xPCL10k0.9k resin, which features substitution of 15% 10k-2MA with 0.9k-3MA, also demonstrated a sharp reduction in working curve t_c of approximately 16x when compared with the xPCL10k resin. However, the xPCL10k0.9k resin appears to be more fragile than the xPCL10k+4A during printing, demonstrated by frequent print failures. Substitution of a portion of the 10kg/mol bi-functional macromer with the smaller, multi-functional macromers results in a reduction in network toughness. Although, the toughness of the bimodal resins are still significantly higher than typical stereolithography resins [167]–[169]. The bimodal networks also offer substantially faster rates of degradation over the unimodal networks and oligomers of all compositions.

4.4.6 Network degradability

In this study, the xPCL10k and xPCL2k networks degrade at a similar rate to non-crosslinked PCL45k material, taking between 14 and 20 hours using the autoclave method to produce a clear solution. Both bimodal network compositions degrade rapidly, with the xPCL10k0.9k and xPCL10k+4A networks producing clear solutions within 0.5, and 2 hours. The ~20 ^{o}C higher incubation temperature gained from the autoclave enabled further acceleration of the degradation process over the typical boiling method in a flask at atmospheric pressure. The increase in degradation temperature from the autoclave affected the network degradation rates during the linear-like state to different extents depending on the network composition, with the xPCL10k0.9k network being approximately 3x faster, and the xPCL10k+4A degradation rate being ~1.8x faster than the RBF method. There appears to be no obvious correlation to average molecular weight, cross-link density, or initial degree of crystallinity in the networks for this behaviour.

Previous work comparing the degradation rates of non-crosslinked and crosslinked films of PCL noted that the network films degraded faster than the non-crosslinked films. Hoglund *et al* attributed this to the lower degree of crystallinity within the network films facilitating a greater rate of hydrolysis through easier migration of water into the material [170]. Another study reached the same conclusion when investigating the effect of crystallinity and degradation rate for melt blends of PCL with various wt% of poly(glycerol-succinate)(PGS). Samples with a higher content of PGS possessed reduced crystallinity, and demonstrated an increased sample degradation rate [171]. In contrast, due to the degradation temperatures surpassing the melting temperatures of all the materials, it would be expected that no crystallinity remains, and that the differences in rates of degradation between samples degraded using the same method therefore arise from factors other than crystallinity. Chain molecular weight for the PCL45k oligomer,

or the molecular weight between crosslinks for the xPCL2k and 10k networks, appear not to significantly influence the rate of degradation under these conditions, with rates being within a few %/h of each other. Introduction of either 0.9k-3MA or PTOL-4A crosslinkers drastically increase the degradation rate compared with the unimodal oligomer, and networks. However, the mechanism for this phenomenon is not clear.

Due to the elimination of sample crystallinity, it is important to note that the order in which samples fully degrade via these methods may not be the same order that they would degrade in via more physiologically related degradation methods. Therefore, it is recommended that the accelerated degradation methods used within this Chapter are most suitable for rapidly determining whether a network is entirely degradable, and to produce degradation products for analysis or toxicology purposes.

4.4.7 Stereolithography challenges

A drawback of the DLP stereolithography approach is the layer separation methods used to peel the printed layer from the optical window, which often result in the layers or structures being subjected to high mechanical forces during the printing cycle. Printing difficulties with low functionality or high molecular weight macromers during attempts to produce networks with improved mechanical properties, has been reported for multiple biopolymer formulations [91], [147], [172]. Resins with the highest macromer molecular weights possessed the lowest molar concentrations of reactive groups and required the greatest amount of diluent. The diluent-laden structures generated from such resins during printing were of low crosslinking density and demonstrated fragility.

In this work, the xPCL10k and xPCL10k0.9k formulations are composed of predominantly diluent, which led to the production of weak structures during printing. When combined with the rough printer movements during layer peeling, these highly solvated layers were easily damaged, preventing successful printing. Ideally, the resin formulations would contain a greater quantity of reactive components, which in our case only consists of the combination of macromers, with the BnOH not being incorporated into the network. Commercial open vat stereolithography resins often contain reactive diluents combined with the main backbone monomers to formulate a resin that consists completely of reactive network forming components, such as Autodesk's PR48 [173]. Other formulations can be composed of monomers that are liquid at room temperate, therefore not requiring any diluent at all. Such formulations offer quick curing times and sufficient network strength during printing, such that print failures will mainly occur from attempting to print highly complex structures with insufficient supporting sub-structure.

Unfortunately, all the resins were formulated essentially at the maximum soluble macromer concentration in BnOH. Due to the PCL macromers being crystalline, dissolution is thermodynamically less favourable. A solvent with a greater capacity for, in particular, the 10k-2MA macromer may enable formulation of a resin that produces structures of greater strength during printing. Potentially lowering the molecular weight of the large linear macromer, perhaps to 6 – 8 kg/mol could be considered. This would increase solubility and concentration of reactive groups simultaneously, while retaining a degree of the mechanical properties shown by the 10 kg/mol macromer. Alternatively, a heated resin tank would increase solubility, enabling the resin to contain a greater proportion of macromer at saturation that may be sufficient to strengthen the network during printing. Regarding printer technology, utilisation of a different printer that features a gentler peeling system that the EMBER may help improve printability of existing resin formulations. However, it was not possible to find a printer on the current market that is fully open source and has a substantially improved peeling system over the EMBER system.

4.5 Conclusions

In this work, a bimodal PCL and PTOL-4A photo-curable liquid resin was developed and used to print a series of structures of ranging complexity. The resulting networks were semi-crystalline, and offered substantially tougher mechanical properties to previous SL printed PCL networks. A series of photo-cured uni- and bimodal networks were prepared from a variety of bi- and tri-functional PCL macromers of various molecular weights, and were characterised in terms of their reactivity, printability, crystallinity, tensile properties, and degradability. It was confirmed that unimodal networks produced from greater molecular weights of macromer, possessed greater crystallinity and mechanical toughness than those composed of lower molecular weight macromers. Networks composed of purely 10,000 g/mol were shown to be exceptionally tough, but offered poor printability, due to low reactivity and inadequate mechanical properties in the solvated state during printing. Bimodal networks composed from 10,000 g/mol macromer and either 0.9k-3MA PCL or PTOL-4A, demonstrated good reactivity, and maintained a portion of the toughness shown by the 10,000 g/mol networks, while being vastly tougher than 2,000 g/mol macromer networks of similar crosslinking potential. Under accelerated conditions, the bimodal networks degraded faster than the unimodal networks, with all networks completely degraded within 20 h. As far as we have found, the networks demonstrated here offer superior toughness to any previously photo-cured PCL networks in the current

literature. Additionally, we propose benzyl alcohol as a suitable solvent for PCL-macromer SL resin formulations for printing at ambient temperatures. The PCL and PTOL-4A resin provides a new tough material option for biomaterial stereolithography.

Chapter 5– Network cytotoxicity evaluation

5.1 Introduction

This chapter evaluates the *in vitro* cytotoxicity of photo-crosslinked networks produced from the polycaprolactone-based photo-curable resins developed in Chapter 4.

The proposed vaccine delivery implant is to be constructed from PCL-based macromers crosslinked together to form a solid network. PCL is a well-studied resorbable polymer, and is a commonly used material in tissue engineering and other biomedical fields. It is largely accepted that PCL is able to constitute an intrinsically biocompatible system when interacting with various cell types and tissues [174]–[177]. The term "biocompatibility" has historically had numerous definitions, but is currently defined as "the ability of a material to perform with an appropriate host response in a specific application" [178], which takes into account the interactivity between the material and the host. Evaluation of *in vitro* cytotoxicity is the first step in assessing the suitability of new materials for biomedical purposes. Similarly with many other polymeric biomaterials, while the compatibility of non-crosslinked PCL is well studied, evidence to support the compatibility of networks derived from end-functionalised PCL macromers is not well documented. Of the studies that have been performed on crosslinked PCL networks, the results have been shown to be positive, with cell proliferation appearing equivalent or only slightly poorer than tissue culture polystyrene [90], [179]. Similar testing of photo-crosslinked PDLLA networks demonstrated cell proliferation equivalent to high molecular weight (HMW) polymer and tissue culture polystyrene controls by 11 days of culture [120]. Photo-crosslinked PTMC networks also appeared to show good cell proliferation, however no comparisons to controls were made [122]. Overall, the evidence suggests that crosslinked networks derived from biomaterials will perform similarly to their non-crosslinked HMW counterparts in short-term *in vitro* studies.

As per international standards, new medical devices and their constituent materials must be evaluated in a manner that reduces the risk of harm to the patient/animal as much as possible. Such investigations typically consist of both *in vitro* and *in vivo* testing to provide sufficient information [180]. For the purposes of toxicity testing under ISO 10993, medical devices are characterised by their nature of contact to the body and their contact duration. For an implantable vaccine delivery device of the nature that is proposed within this thesis, the device would be classed as an implant device and falls into duration category "C" (Permanent [>30 days]). For implantable medical devices in this category,

the necessary requirements to be satisfied are extensive. Such necessary testing areas include cytotoxicity, sensitisation, irritation, acute systemic toxicity, subacute/subchronic toxicity, genotoxicity, carcinogenicity and local effects after implantation [99]. Naturally, a comprehensive analysis of all the above areas for a material/device would take significant time and financial backing. For early stage development, it is generally preferred to perform initial *in vitro* pilot evaluations into the more general areas, such as cytotoxicity. Cytotoxicity evaluations are favoured due to being simple, fast, having high sensitivity, and save animals from testing by replacing *in vivo* testing at early stages [101]. The *in vitro* cytotoxicity assessments within this chapter use dermal fibroblasts as the subject cell type. This cell type was chosen due to fibroblasts being abundant in the sub-cutaneous region the device would be implanted, being a widely studied and utilised cell type for *in vitro* studies of this type, and also due to the group having extensive knowledge and experience in working with these cells. Additionally, due to the short-term nature of my travel scholarship, a cell type was required that already had ethical and health and safety approval.

In this chapter, direct contact evaluations were performed by culturing fibroblasts on photo-cured PCL networks for up to 11 days. The WST-1 assay was used to indicate cell viability. WST-1 is a tetrazolium colourimetric assay, which therefore develops a colour in response to the degree of metabolic activity of viable cells as the tetrazolium is reduced to formazan, enabling measurement of viability via spectrophotometer. The WST-1 tetrazolium salt is reduced non-enzymatically to water soluble formazans by NAD(P)H, in the presence of intermediate electron acceptors. The reduction of the WST-1 tetrazolium occurs at the cell surface, rather than intracellularly [181]–[183], thus WST-1 reduction is actually a measurement of net extracellular membrane redox activity. The extent of the colour change is proportional to this net metabolic activity, which in turn can theoretically be proportional to the number of viable cells present [104]. For visualising the cells and their morphology, dual staining of fixed cells with DAPI and TRITC-phalloidin was performed. DAPI is a cell permeable, fluorescent dye that binds to the minor groove of double-stranded DNA, which enables staining the nuclei of fixed and permeabilised cells [184]. DAPI has excitation/emission wavelengths of 358/461 nm. TRITC-phalloidin is a fluorescently labelled phallotoxin cyclic peptide that interacts with polymeric actin, producing a stabilising effect that cause the actin filaments to resist depolymerisation and assembly [185], [186]. The conjugated TRITC label provides a

red-orange fluorescence, with an excitation at 540 nm and emission at 565 nm. DAPI and phalloidin are commonly used together, where DAPI aids assessment of cell density, while phalloidin enables characterisation of cell morphology indicated through the arrangement of cytoskeletal actin filaments [187]–[189].

The following sample groups were investigated: non-crosslinked 45 kg/mol PCL (PCL45k), photo-cured bimodal networks produced using the xPCL10k0.9k formulation (xPCL), and glass coverslips. The inert glass coverslips were used as a non-polymeric positive control. With non-crosslinked PCL being well characterised as non-cytotoxic and performing similarly to tissue culture plastics, the PCL45k was used as a polymeric positive control. The experimental groups consisted of 3 variants of the xPCL networks. Extracted networks, non-extracted networks, and benzyl alcohol (BnOH) swollen networks were used. The extraction process for the extracted networks is expected to remove the leachables required as part of the photo-curable resin formulations such as unreacted photo-initiator and macromers, as well as residual BnOH. Of these, TPO is the only well studied component and has been shown to be cytotoxic to a variety of cell types [190]. While BnOH has been shown to be cytotoxic to cell types localised in the eye [132], [133], the solvent is in frequent use in skin-applied cosmetics and as a vehicle for parenteral drug delivery and is therefore expected to be less toxic to skin localised cell types. Unreacted macromers have been shown to have cytotoxic effects [191], [192]. If extraction is performed correctly, the potentially toxic leachables should be removed; therefore, the extracted networks are expected to perform similarly to the PCL45k. The rationale behind investigating the non-extracted and swollen networks comes from the work of developing the vaccine delivery devices (detailed later in Chapter 6). Our current method of sealing the devices involves injection of ~10-15 μL of resin into the open ends after filling with payload, which is then cured with UV. Extraction of the sealed devices to remove leachables from the small quantities of resin at the end caps would lead to solvent exchange between the internal payload solution and the isopropanol used in the extraction process, and is therefore not feasible. Therefore, small quantities of potentially toxic leachables will remain in the non-extracted end caps. The non-extracted sample group aim to replicate this scenario. The BnOH swollen sample groups are intended to assess the toxicity specifically related to leaching of the solvent.

5.2 Materials and sample preparation

Glass disc coverslips of 5 mm diameter were purchased from Thomas Scientific (USA). 10k-2MA, and 0.9k-3MA macromers were synthesised and purified as discussed in

Chapter 3. Other photo-curable resin components such as photo-initiators were purchased and used as discussed in Chapter 4. xPCL10k0.9k disc samples for toxicity testing were produced in the same manner, and from the same resin formulations, as discs used for degradation studies described in Chapter 4. For the purposes of this chapter, only the xPCL10k0.9k composition of photo-cured network is investigated and shall be referred to using the shorter abbreviation "xPCL". Non-crosslinked PCL45k discs were punched from sheets of polymer produced by melt compression moulding, also detailed in Chapter 4.

In addition to the extracted and dried crosslinked networks, non-extracted and BnOH swollen xPCL networks were also assessed. The not-extracted group is comprised of discs formed by the photo-crosslinking procedure, but excluded from the extraction procedure to leave networks that still contain potentially non-crosslinked macromer, BnOH and unused TPO. The swollen group is composed of extracted and dried networks that were bathed in fresh BnOH after the ethanol washes, in an attempt to investigate any effect of BnOH separately from potential TPO residues. The swollen group were rinsed with PBS and soaked in media overnight as described for the other disc groups in 5.3.3.

5.3 Preparation and evaluation of primary fibroblasts

5.3.1 Materials

Human dermal fibroblasts were isolated from split thickness biopsies from consenting patients undergoing abdominoplasty surgery and breast reduction surgery [193]. Ethical approval for human skin collection was obtained from the Queensland University of Technology Research Ethics Committee (1300000063) and the Uniting Healthcare / St Andrew's Hospital Ethics Committee (0346). Trypsin, Collagenase-A, Dulbecco's Modified Eagle's Medium (DMEM), foetal calf serum (FCS), penicillin, streptomycin, L-glutamine, and tetramethylrhodaminyl-conjugated phalloidin (TRITC Phalloidin) and phosphate buffered saline were acquired from Invitrogen (Australia). 4'6- diamidino–2–phenylindole (DAPI) was acquired from Life Technologies (USA). Phosphate buffered saline (PBS) tablets, cell proliferation reagent WST-1, Triton X-100, bovine serum albumin (BSA), were purchased from Sigma Aldrich (Australia). Paraformaldehyde was purchased from ProSciTech (Australia).

5.3.2 Initial culture protocol

To allow separation of the dermis and epidermis, enzyme digestion was performed in 0.125% trypsin at 4 ^{o}C overnight. The dermis was then comminuted and incubated in 0.05% collagenase-A in DMEM at 37 ^{o}C and 5% CO_2 for 48 hours to allow harvesting of the fibroblasts. The resulting solution was centrifuged at 212 g for 10 minutes prior to resuspension and subsequent culture of the cells in fibroblasts growth medium, which consisted of DMEM supplemented with 10% FCS, 50 U/mL penicillin, 50 µg/ml of streptomycin and 2 mM L-glutamine. All cells were used at passage 5.

5.3.3 Sample sterilisation

Samples for cell culture were sterilised by immersion in 80% ethanol for 60 minutes and dried in a laminar flow cabinet. Following 3 washes in PBS, samples were placed in fibroblasts growth medium overnight and were deemed ready for use the following morning.

5.3.4 Cell viability assessment

Samples for cell proliferation experiments were 5 mm in diameter and placed in a 96 well plate. Isolated fibroblasts, $5x10^3$ in 10 µL, were seeded onto the samples and allowed to attach for 1 hour, prior to addition of 150 µL fibroblast growth medium. Medium was replaced every 2-3 days. Cellular proliferation on the samples was studied at 1, 4 and 11 days using WST-1. Upon reaching day 1, 4, and 11, three samples per experimental group were transferred into a 48 well plate, 200 µL of fresh medium was added along with 20 µL of WST-1 reagent. Samples were incubated in the dark for 2 hours. The supernatant was then transferred into a 96 well plate and readings taken on a plate reader (BioRad xMark Microplate Spetrophotometer) at 450 nm with the reference wavelength set to 650 nm. The average of triplicate blank well (growth media only) absorbances were deducted from the sample absorbance values at each time point. The coverslip group absorbances were regarded as indicating 100 % cell viability. All sample group values were expressed as a percent of relative metabolic activity vs. the coverslip controls.

5.3.5 Cell proliferation and morphology on the disc surface

Samples (12 mm in diameter) to study cellular morphology were seeded with $1.2x10^4$ fibroblasts in 10 µL, within a 24 well plate and allowed to attach for 1 hour, prior to addition of 1.5 mL of fibroblast growth medium. Medium was replaced every 2-3 days. Cellular density and morphology on the samples was studied at 1, 4 and 11 days using confocal laser scanning microscopy (CLSM). Upon reaching the time points, the samples

for CLSM were rinsed in PBS supplemented with calcium and magnesium, and fixed in 4% PFA for one hour at room temperature. Samples were then incubated in 0.2% (v/v) Triton X-100 in PBS for 5 minutes, prior to incubation for 10 minutes in 1% BSA/PBS (w/v) blocking solution. Samples were fluorescently labelled by placing them in a working solution containing blocking solution, 0.8 U/mL TRITC Phalloidin, and 5 µg/mL DAPI. Samples were incubated in working solution for 45 minutes on a shaker and protected from light. Stained samples were stored in the dark at 4 ^{o}C immersed in PBS until use. Samples were washed 3 times in PBS between each step above. Samples were imaged on an epi-fluorescent microscope (Nikon, Eclipse Tis).

5.4 Cytotoxicity: primary dermal fibroblasts

5.4.1 WST-1 viability assessment

The WST-1 assay was performed on triplicate samples of each disc group after 1, 4 and 11 days of cell culturing. Three variants of the bimodal xPCL formulation discs (extracted, swollen, and not-extracted) were tested alongside discs composed of glass, and non-crosslinked PCL45k. The relative metabolic activity in reference to the glass positive control group is shown in Figure 5.1.

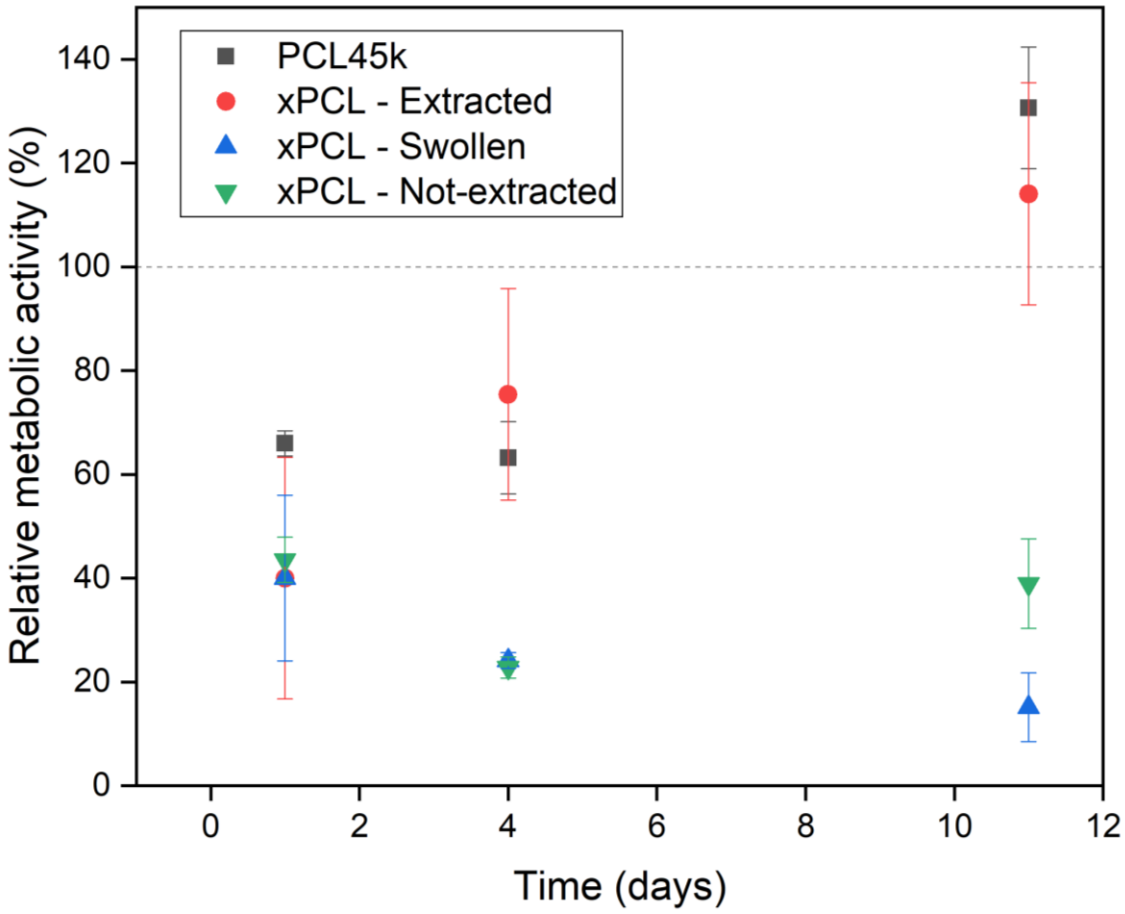

Figure 5.1:- WST-1 assay determined average metabolic activity over 14 days of culturing in relation to control group (glass discs). Data represents an average of triplicate samples ± SD.

Over the course of the experiment, the average absorbance (and therefore overall fibroblast metabolic activity) associated with the glass positive control group cultures approximately doubles, indicating sustained cell viability accompanied by cell proliferation during the 11-day incubation. The average relative metabolic activities of the fibroblasts on the PCL45k, xPCL extracted, swollen and non-extracted groups in relation to the control group were 66 ± 2, 40 ± 23, 40 ± 16, 43 ± 4 % at day 1, 64 ± 7, 75 ± 7, 24 ± 2, 23 ± 2 % at day 4, and 130 ± 12, 114 ± 21, 15 ± 7, 39 ± 9 at day 11, respectively.

Initially, all experimental disc groups show reduced cell viability in relation to the control group. The xPCL extracted group average viability appears to climb steadily, matching the control group by around approximately day 8/9, and surpassing the control group at day 11. While the non-crosslinked PCL45k reaches a similar endpoint by day 11, but appears to indicate a slight decrease in average viability at day 4. The swollen and non-extracted networks both start at approximately the same level of viability at day 1, but viability reduces almost by half at day 4. By day 11, the swollen networks continue to

show decreased cell viability, while some recovery of viability appears to be occurring for the not-extracted group.

5.4.2 DAPI/phalloidin proliferation and morphology assessment

Fibroblasts on the surfaces of the glass, PCL45k and extracted xPCL discs were fixed and stained on days 1, 4 and 11 of the experiment. Representative microscope images of each disc group at the three time points is shown in Figure 5.2.

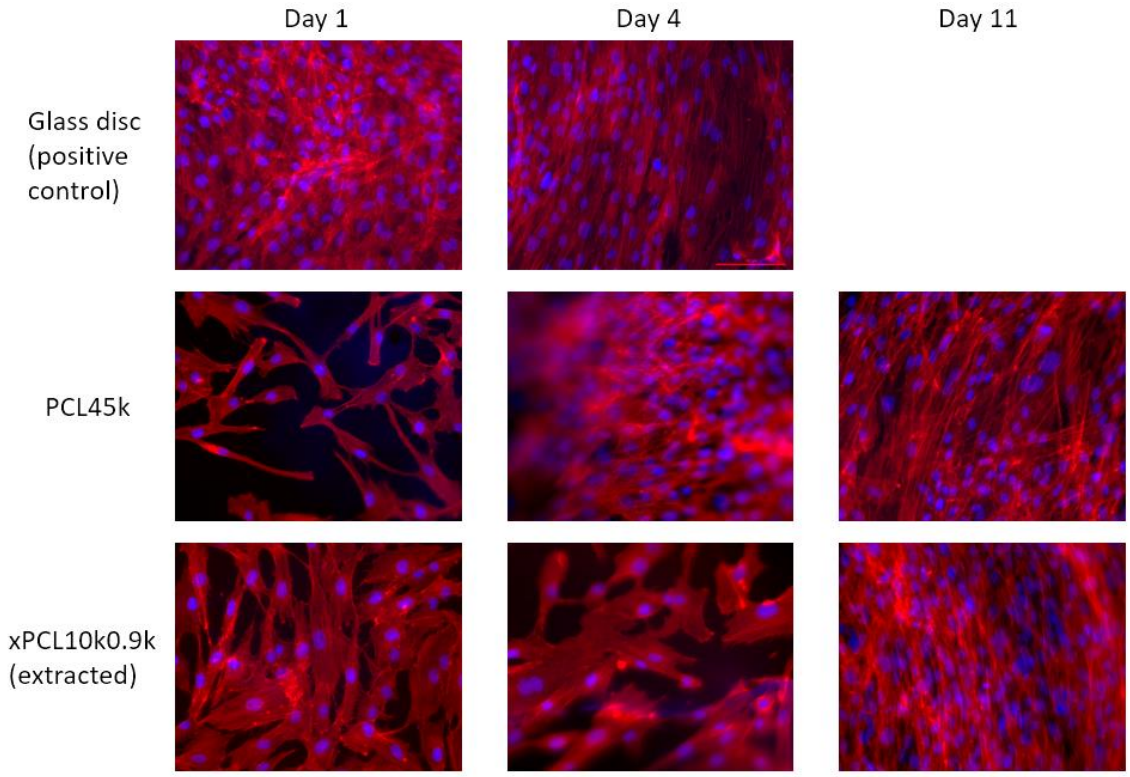

Figure 5.2:- Microscope images of DAPI/phalloidin-stained fibroblasts cultured on top of glass, PCL45k, and extracted xPCL discs, after 1, 4 and 11 days of culturing. Magnification 20x.

Cell nuclei are stained blue by the DAPI, while the TRITC-phalloidin stains the actin filaments yellow/green. During merging of the DAPI and phalloidin images, the phalloidin channel was assigned to a different colour, in this case red, which enhances the contrast. The glass positive control disc shows a substantially larger population of cells present on the surface at day 1 than the other discs, but the actin filaments appear unordered. By day 4, a similarly high population of cells is apparent on the glass disc, but the fibroblasts are now highly ordered and confluent, displaying a pattern of cells side-by-side with actin filaments arranged vertically. Unfortunately, the day 11 glass disc sample was damaged during processing and was unable to be imaged. The PCL45k and xPCL samples show much fewer fibroblasts present on the disc surface at day 1, and additionally appear to show a different morphology. By day 4 the fibroblasts on the PCL45k sample appear to have reached a similar density level to the day 1 glass disc

population, also showing the same unordered arrangement of actin filaments. The fibroblasts on the PCL45k discs at day 11, are displaying an ordered pattern arrangement of actin filaments and appear confluent. The xPCL image shows a similar trend to that seen in the PCL45k images, with an initially low cell density at day 1 progressing to a confluent, dense population by day 11. The fibroblasts on the xPCL disc at day 4 appears to be proliferating slower than the fibroblasts on the PCL45k disc, based on the lower cell density in the day 4 images.

5.5 Discussion

5.5.1 Summary

Cell metabolic activity of the primary dermal fibroblasts cultured on the glass, PCL45k, and extracted xPCL disks increases over the course of the experiment; however, the PCL materials both show a brief lag period in the few days after initial seeding. The net metabolic activity of primary dermal fibroblasts cultured on PCL45k and xPCL discs matches or exceeds the glass coverslip positive control by day 11. Fluorescent imaging supports the view that the increase in net metabolic activity is due to an increasing number of viable, metabolically active cells being present on the disc surfaces, with increases in cell densities being shown. xPCL discs that were swollen in BnOH or not-extracted after curing show low or static levels of cell metabolic activity.

5.5.2 Crosslinked networks and cell metabolism

Over the 11 day experiment, the primary fibroblast net metabolism on the extracted xPCL discs increases from approximately 40 % to 114 % in relation to fibroblast net metabolism on the glass control discs. In conjunction, the cell density visibly increases over the 11 day period, with the fibroblasts on the xPCL disc appearing confluent.

This combination of results suggests that the rise in net metabolic activity measured through the WST-1 assay is likely due to the proliferation and growth of viable cells, which would indicate that the crosslinked networks are not cytotoxic under these conditions. Such findings are in agreement with previous literature that investigated the cytotoxicity of photo-crosslinked PCL networks using similar methods. Elomaa *et al* evaluated the compatibility of human umbilical-vein endothelial cells (HUVECs) cultured on photo-crosslinked PCL films using an MTT assay. The optical density (proportional to metabolic activity and the number of living cells) increased at every time point within 7 days of culturing. The signal for the PCL network was only slightly behind the tissue plastic control. Therefore, it was deemed that the networks showed good

cytocompatibility. In the same study, mouse mesenchymal cells were also cultured on the networks, and monitored by measuring the double stranded DNA (dsDNA) content. It was shown that the dsDNA concentration tripled in the PCL network group, indicating that the cells proliferated well on the networks over 14 days of culturing [179]. A study by Kweon *et al* assessed the interaction between networks derived from 2,000 g/mol PCL diacrylate macromers and human MG-63 osteoblasts. It was shown that the osteoblasts did attach and proliferate on the crosslinked PCL scaffolds; however, their proliferation index was lower than the culture plastic control. The authors attributed this to poor cell attachment due to lack of suitable matrix, rather than a cytotoxic effect [90].

The swollen and non-extracted networks however, are potentially cytotoxic. Net metabolism associated with fibroblasts cultured on the swollen and non-extracted disc surfaces almost halved between day 1 and day 4, before the cells on the non-extracted discs appear to partially recover to day 1 metabolism levels. The cells cultured on the swollen discs however, continued to fall to 15 % of the glass control by day 11. The swollen and not-extracted xPCL disc variants were not imaged, so the cytostatic or decreasing net metabolism values cannot be cross-referenced. It would be expected that imaging of these disc variants would show low cell densities based on the low net metabolic activity indicated by WST-1, and/or potentially cell debris [194] from non-viable cells. The WST-1 measurements of the non-extracted and BnOH swollen groups appear to demonstrate that one or more components are toxic. The non-extracted group will contain BnOH, TPO photo-initiator, and potentially free macromers that were not included into the network. Due to being derived from extracted networks, the BnOH swollen group should only contain BnOH. The overall low WST-1 signal from the BnOH swollen disks may suggest that BnOH itself is cytotoxic. While BnOH has been shown to be cytotoxic to human retinal pigment epithelial cells in a dose dependant manner [132], [133], investigations into the cytotoxicity of other cell types are not present in the literature at this time. It is possible that the swollen networks adsorb lower quantities of proteins from the culture media during the sample preparation phase, therefore leading to poorer initial cell attachment, and subsequently lower metabolic activity thereafter due to the presence of less fibroblasts in comparison to other groups. As such, the toxicity of BnOH on the fibroblasts is not fully proven here. Type I photo-initiators such as TPO, have been shown to display concentration dependant cytotoxic effects in human oral keratinocytes and V79 (Chinese hamster lung fibroblasts) cells [190]. Further work specifically investigating the extent and nature of toxicity from unreacted macromer,

BnOH, and TPO individually is required. The current data suggests that our method of vaccine delivery device sealing using un-extracted resin is likely unsuitable due to the evidence of cytotoxicity. The concentrations of the toxic components will be higher within the non-extracted and BnOH swollen groups that what would be present within the small volumes of unextracted resin used to cap the devices. Future work regarding the dose dependency of the cytotoxic effects of TPO and BnOH would provide more appropriate information before disregarding the current sealing/capping methodology.

5.5.3 Crosslinked networks and cell morphology

Primary dermal fibroblasts cultured on the xPCL material surfaces initially (days 1 and 4) exhibited a less elongated and more spread morphology, than the fibroblasts cultured on the glass discs. Fibroblasts on the PCL45k discs at day 1 demonstrated similar morphology to those cultured on the xPCL material. This spread morphology appears consistent with various human fibroblasts cultured in low cell densities on different 2D surfaces and materials [195], [196]. As the cell density increases on the PCL45k and xPCL materials, the fibroblasts appear to adopt a heavily elongated and narrow morphology, which appears to be highly ordered. Initial cell morphology of fibroblasts on the glass disc show this elongated and narrow morphology too, but appear unordered with respect to each other. At day 4 the fibroblasts on the glass disc form a similar linear ordered pattern seen from fibroblasts cultured on the PCL45k/xPCL(extracted) discs at later culturing stages. These nematic homogeneous populations of elongated, spindle-shaped cells are typical of well-established confluent fibroblast populations [197]–[199]. With the fibroblasts proliferating and adopting their expected morphology, it would appear that the extracted xPCL discs are not causing the fibroblasts to deviate from their normal behaviour.

5.5.4 Cell attachment

All the PCL-based disc groups start the experiment with a lower net metabolic activity, and primary fibroblast density than the glass control. This is potentially caused by the cell seeding methodology and/or poor or slow cell surface attachment at the start of the experiment. It is widely reported that polymeric materials, such as PCL, used in medical applications often require surface modifications or treatments to improve cell adhesion and general biocompatibility [200]–[202]. PCL tissue scaffolds produced by Wang *et al* were demonstrated to retain only 30 % of the Human adipose-derived stem cells (ADSC) seeded. ADSC attachment was improved to approximately 50 % by NaOH surface

erosion treatment and embedding of pristine graphene nano-particles [203]. Similar results were obtained by Recek *et al*, where plain PCL surfaces were the least suitable environment for HUVEC adhesion, while NH_3 or O_2 plasma treated PCL surfaces enabled strong HUVEC adhesion [204]. While poor initial cell adhesion presents a consistency issue between discs or disc groups for the purposes of the WST-1 and DAPI/phalloidin assays, in the case of the vaccine delivery device, the adherence or growth of cells on the device surface is not an aim. It is expected that preventing or reducing cell (specifically macrophage) adherence to the device would actually be advantageous by reducing the extent of the foreign body response and hindering fibrous encapsulation [205]. Considering this, modifications to the surface of the materials to promote cell adherence are not regarded as being within the scope of this project. In terms of improving the reproducibility and consistency of cell seeding on the discs for cytotoxic evaluation, future testing could consider investigating a few changes to the methodology.

It is suspected that the two-stage seeding method used where a high concentration of cells in a small volume is directly added to the disc and then topped up with growth media after a period of time (as described in 5.3.4 and 5.3.5), may have an unintended flush-effect. This effect may be displacing non-adherent cells due to the forces from addition of a relatively large volume through the pipette into the well. Perhaps suspending the same number of cells in the total well volume of growth medium and adding this to the well in one action would allow the cells to settle without further fluid currents potentially washing them off the surface. While this may lead to a lower initial cell density on the disc from cells settling on the well plate surface itself, it should be more consistent between replicates and between disc groups than the current method. Another consideration may be to perform a prolonged disc incubation step with the FCS-containing growth medium to allow potentially greater quantities of attachment promoting proteins, such as vitronectin and fibronectin, to become adsorbed on the material surface, which may aid initial fibroblast attachment [206], [207]. Assessments would have to be conducted to determine whether lack of anchor proteins is a substantial contributing factor to our variation in initial cell attachment.

5.5.5 Future considerations

While we have demonstrated that our extracted photo-cured materials perform similarly to PCL oligomers during direct contact *in vitro* cytotoxicity assessments with a fibroblast monoculture, looking ahead to other important factors such as the nature of the inflammatory response to the implant is key to further device development. Generally,

implantation of an object will cause injury to local tissue, initiating inflammatory, wound healing, and other foreign body responses [208]. However, it is possible to alleviate or mitigate aspects of the body's response through the material(s) used[209], and also the size and shape of the implanted object [210].

The foreign body response (FBR) initiates a complicated signalling cascade, involving various cell types such as neutrophils, macrophages, and fibroblasts among others [208], [211]. The main purpose of the FBR is to contain or wall off the "foreign object" from local tissues. Initial injury begins the deposition of proteins at the materials surface and recruitment of neutrophils as part of the acute inflammatory response [208]. This can progress to chronic inflammation marked by the presence of monocytes and lymphocytes. Migrating monocytes can differentiate into macrophages which release inflammatory mediating agents such as oxygen free radicals, other reactive oxygen intermediates, degradative enzymes, and acids to attack the material [208], [212]. Additionally, the macrophages attempt to phagocytose it but will be unable to digest or phagocytose the implant. This leads to the macrophages undergoing fusion in an attempt to improve their efficiency, forming multinucleated giant cells, known as foreign body giant cells (FBGCs). It is thought that FBGCs generate signals to recruit fibroblasts to arrive at the injury site, which synthesise and deposit collagen [213]. The combination of FBGCs and fibroblasts develops granulation tissue which effectively isolates the implant from the rest of the body via a fibrous capsule [214]. The histology of the produced granulation tissue or fibrous capsule can vary significantly, with differences in thickness, extent of packing, and vasculature. In particular, the packing and vasculature aspects can affect diffusion of even small molecules [215] through the fibrous capsule, with tightly packed fibrous capsules restricting diffusion, while granular, well vascularised capsules offering greater permeability [216].

Due to the FBRs complexity, it is best assessed within a suitable *in vivo* host model. For subcutaneous implantation, use of rodent models is typical, however suffer from poor translation to human trials [217]. Use of primates as a more physiologically relevant host model is preferred for long term *in vivo* studies, but their use is limited by strict ethical guidelines [209], [210]. Due to this, co-culture *in vitro* models have been developed to evaluate the FBR to materials. For example, it has been shown that in *in vitro* fibroblast/macrophage co-culture models can be a viable and useful tool to predict *in vivo* response to polymer implants [218], [219]. Other options include *ex vivo* which has the advantage of containing all the cell types found in skin [220]. However, the *in vitro*

approach is simpler, cheaper, and without the need to be processed within hours following collection and avoids the high donor-to-donor variability of explants [221], [222]. As such, well-constructed *in vitro* studies can continue to provide relevant information about the more complex *in vivo* environment an implanted capsule would operate in.

Photo-initiated crosslinked networks are formed through the polymerisation of the end groups via an addition type reaction. The carbon-carbon chains that result from these addition polymerisation reactions are referred to as kinetic chains. While it is generally accepted that the main polymeric backbone of networks constructed from such degradable biomaterials will degrade and show low toxicity, the leftover kinetic chains are typically insoluble and of variable molecular weight, and therefore may accumulate in the body [223], [224]. Various studies have been performed with the aim of characterising and/or controlling the kinetic chain lengths [225]–[227], but few proceed to perform cytotoxicity evaluations on the produced kinetic chains themselves. Jansen *et al* demonstrated a method of controlling the kinetic chain length of PDLLA-MA networks and performed an XTT assay with fibroblasts, which suggested that extracts of the PDLLA network were not cytotoxic [228]. Similar findings were suggested by Wang *et al*, where the degradation products of crosslinked poly(propylene fumarate)(PPF) networks were added to 4 cell lines, with no change in metabolic activity or morphology observed compared with a non-cytotoxic control [229]. However, this appears contradictory to earlier work on the degradation products of crosslinked PPF networks by Timmer *et al* [230]. At the time of writing, literature regarding the cytotoxic evaluation of degradation products from photo-crosslinked PCL networks was not found. Due to the overarching aim to use the degradable photo-crosslinked PCL networks to construct an implantable device, work should be performed to assess the potential cytotoxicity of the degradation products, with a particular focus on the kinetic chains.

5.6 Conclusions

Primary dermal fibroblasts cultured on the crosslinked PCL networks that have been extracted and dried, appear to constitute a biocompatible system. The net metabolic activity of the primary fibroblasts cultured on the crosslinked and extracted PCL networks was shown to approximately match or exceed the glass positive control and the non-crosslinked PCL group after 11 days of culture. Moreover, culturing the fibroblasts on the PCL45k and xPCL extracted disc surfaces does not appear to adversely affect cell morphology, with the fibroblasts adopting their typical spindle morphology at

confluency. The PCL discs all displayed an initial lag phase with lower cell density and metabolism after day 1 of culture, compared with the control group, which appears to be at least partly due to poor cell adherence to the disc surfaces. Not-extracted and BnOH swollen photo-cured networks indicate a potential cytostatic or cytotoxic effect and require further evaluation to determine the root cause. Further investigation into the cytotoxicity of network degradation products, including the kinetic chains, is of high importance prior to proceeding to *in vivo* characterisation. The results within this chapter indicate that the extracted crosslinked networks perform similarly to HMW PCL, and demonstrate a minimal degree of cytotoxicity under these culture conditions.

Chapter 6– Device manufacture

In this chapter, the development of the methods for device manufacture and initial assessment of the prototype devices will be discussed.

6.1 Introduction

Thermoplastic non-crosslinked PCL devices were shown to be viable delayed release devices, but upon burst released only small amounts of the contents, rendering them highly inefficient [21], [231]. Previous work with PDMS devices by Dunker suggested that flexible networks could enable greater instantaneous release at burst. While the PDMS devices demonstrated the concept well during mechanical testing, due to their non-degradability and significant leaking issues during *in vitro* osmotic burst testing this material was not pursed further [232]. Investigation of devices constructed from degradable flexible crosslinked-PCL materials will be performed to assess whether such photo-cured materials can provide the combination of flexibility and degradability desired for the delayed release vaccine delivery implant.

We hypothesise that use of the xPCL10k0.9k formulation (characterised in previous chapters) will swell to a greater extent than thermoplastic PCL materials and burst releasing a greater amount of content, as desired. Use of a dip coating machine will enable production of tubes with consistent wall thicknesses, which is a key parameter that influences the osmotic uptake, burst pressure, and therefore the delay-to-burst of the tubes. We hypothesise that mechanical burst testing of the tubes will verify the greater ability of the xPCL tubes to flex, and swell over the PCL counterparts, and provide a demonstration of the xPCL tubes greater extent of burst release. Within this Chapter, use of dip coating and stereolithography methods to manufacture the tubular part of non-crosslinked PCL and xPCL devices will be assessed. Dip coated tubes of both material types will be characterised and compared in terms of the wall thickness distributions and mechanical burst behaviour. The effect of capping methods on the mechanical burst characteristics for xPCL devices will be investigated. PCL tubes will undergo a preliminary osmotic burst site evaluation, with detailed investigation of the osmotic burst behaviour of devices composed of both materials is reserved for Chapter 8.

6.2 Materials

Medical grade polycaprolactone PURASORB® PCL was purchased from Corbion (The Netherlands). Chloroform was purchased from Sigma Aldrich (Australia). Macromers

from Chapter 3 were used to formulate a liquid resin as was performed in Chapter 4 and Chapter 5. For dip coating, the crosslinked material formulation used was the xPCL10k0.9k formulation, while for stereolithography printing the xPCL10k+4A formulation was used. The details regarding the compositions of both formulations are listed in in Table 4.1 of Chapter 4.

Here, the non-crosslinkable PURASORB® PCL will be referred to as PCL, while the crosslinked xPCL10k0.9k material will be referred to as xPCL.

6.3 Methods

6.3.1 Dip coating

Dip coating of PCL and xPCL was performed on a custom-built automatic dip coating apparatus. The PCL material was dissolved in chloroform to produce a solution that contained 15 % w/v of PCL. The xPCL was used as formulated. The apparatus, shown in Figure 6.1, features a movable stage with a vat of resin attached, and a motor that rotates a shaft connected to a 2 mm diameter rod. The machine is controlled through G-code scripts interpreted via Mach 3 CNC software.

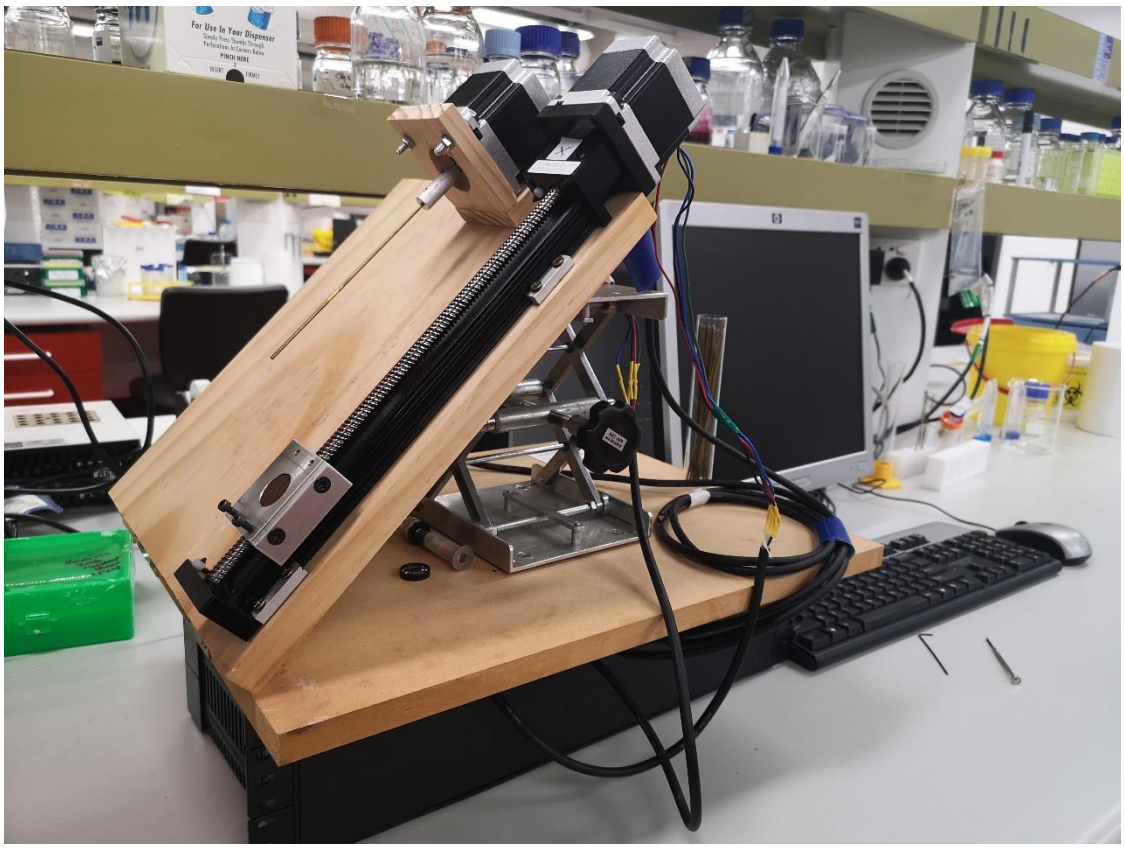

Figure 6.1:- Mark 1 auto dip coater. The stage on the linear ball screw rail moves up and down control the depth and speed of dipping or removal. The rod is fitted directly to a separate motor shaft via an aluminium shaft coupler. Note resin container is not attached to the stage in this image.

The rod acts as the substrate upon which material is deposited. Dip coating of both materials involves a repeated dip cycle that consists of 4 stages. The first stage is the raising of the vat, which coats the rod. The second stage is a holding step while the rod is submerged. The third step features the lowering of the vat, so that the coated rod is open to air. The fourth and final stage is another hold step. Throughout all stages the rod is kept rotating. These 4 stages are repeated 4 times for the PCL material and 3 times for the xPCL material. While the overall layout of the dip cycles is highly similar, the specific settings for each stage and final processing is different for each material type.

The PCL material setup maintains a rod rotation of approximately 10 rpm and features short residence times during the 2nd stage hold step, which decrease with each dip from 6, 3.5, 2.5 to 2 s. The fourth stage of each cycle enables evaporation of chloroform to allow deposition of the PCL to the rod. The length of this evaporation step was maintained at 3 mins for all dips. The complete G-code file for this procedure is listed in Appendix B. After the dip coating cycle was completed, the PCL coated rods were prepared for annealing to improve the surface quality of the deposited material. The rods were positioned vertically into a block of Teflon, and placed within an oven at 70 ^{o}C. Annealing in the oven was performed for 1 hour, after which the Teflon block and samples were removed and allowed to cool on the benchtop.

For the crosslinkable material, a UV (365 nm) light source (OmniCure® S2000) was positioned in a manner so that the emitted light covered the entirety of the coated rod. The arrangement of the dip coater and UV source is shown in Figure 6.2.

The dip coating cycles listed above were determined from some initial preliminary testing runs using knowledge gained from previous work [231], [232] as a starting point. The number of dips for a particular formulation was determined by measuring the wall thickness of a tube produced with a calliper. The target wall thickness was 200 µm. If the tube was thicker than the target the number of dips was reduced and *vice versa*.

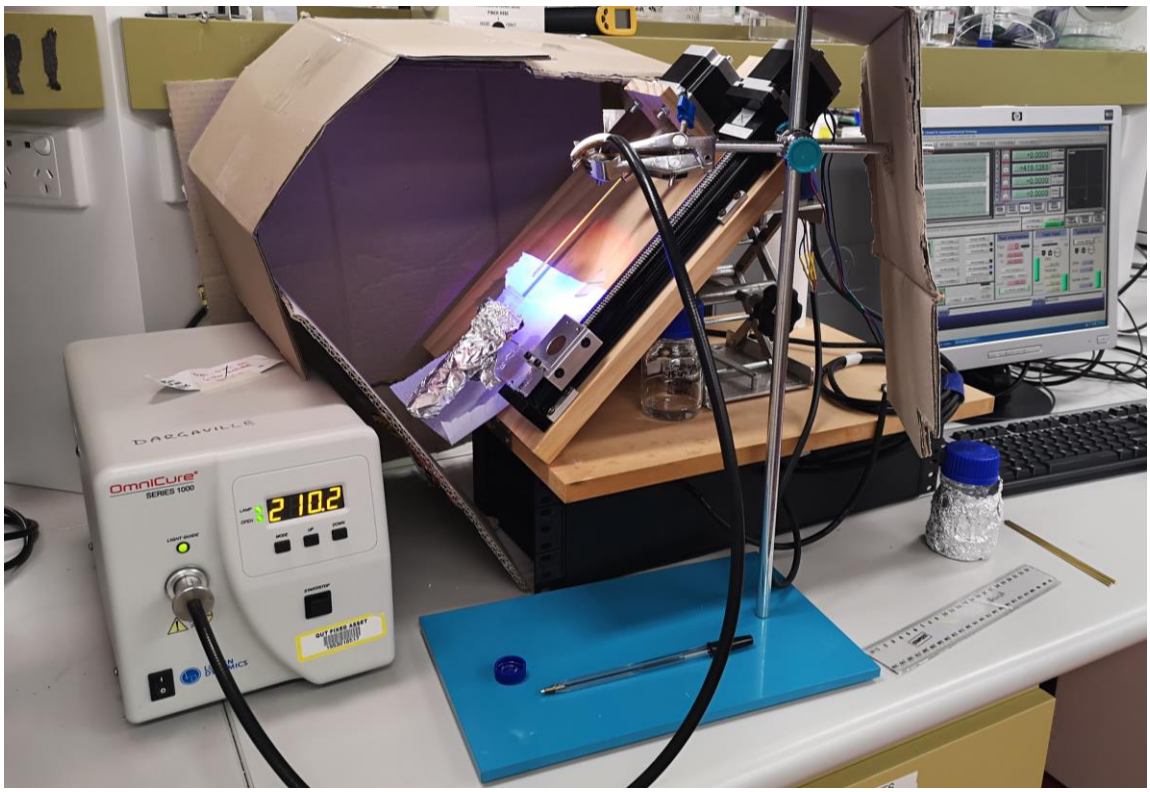

Figure 6.2:- Mark 1 dip coater with OmniCure UV system positioned for photo-crosslinking of xPCl tubes.

The UV source was manually turned on and off for the curing stages of the xPCL material dip cycle. Instead of facilitating evaporation, the final hold step of each cycle was the curing stage, where the UV source was enabled for 7 mins. The last curing stage time was doubled to 14 mins. After removal of the rod from the dip coater, the rod was placed within a Teflon block and positioned within a UV crosslinker for 1 hour of post-curing.

After completion of the annealing or post-cure stages, the coated rods of both material types were submerged in ethanol to facilitate swelling and easier removal from the rod. Approximately 5 mm was cut from the top and bottom ends of the tube, as these regions tended to be thicker (bottom) or thinner (top) due to gravity and material flow. The remaining central portion was cut into 30 mm lengths where the wall thicknesses appeared most homogeneous and defect free. Typically, 1 or 2 viable 30 mm long tubes could be cut from a single dipped rod. The g-code for producing the xPCL tubes is shown in Appendix B.

The xPCL tubes require Soxhlet extraction to remove all resin components not part of the photo-cured network. Extraction with IPA was performed for 3 days. Extracted tubes were dried in an oven at 80 ^{o}C until a steady weight was reached.

6.3.2 Stereolithography

The xPCL10k+4A resin formulation that was used to print the various structures in Chapter 4, was also used to print the tubular parts of the devices on the EMBER stereolithography printer. Print settings and exposure times were the same as detailed in Chapter 4 4.3.5.

6.3.3 Assessment of wall thicknesses

A SCANCO μCT 50 micro-computed tomography (microCT) scanner was used to determine the wall thicknesses of dip coated tubes. Tubes were positioned vertically within the sample holder, and scanned in 3.4 μm voxels, at 45 kVp, 200 μA, and using an integration time of 1.2 s. Tubular samples either were scanned along the majority of their length, or were scanned in 3 particular zones at the top, centre and bottom of the sample. These regions are in reference to the position of the material on the rod during dip coating, with the top being the region furthest from the resin vat, and the bottom being the end of the rod that is first to come in contact with the resin during dipping. Each zone consisted of 250 slices. For tubes that were scanned over the majority of their length, at total of 7060 slices were analysed covering 24 mm, with the 3 mm at each end (30 mm long tube) not scanned. Slices were exported as .TIF files for measurement within ImageJ. A batch processing measurement script (shown in Appendix B) was produced, which measures the wall thickness of a ring slice at 1^{o} intervals around the circumference of the ring. The measurements were then exported and analysed within Excel.

6.3.4 Thermoplastic PCL device sealing

The PCL tubes were sealed using a thermal welding technique, where a plug of PCL is melted and fused with the open end of the tubular part. A custom sealing device was used to position the PCL tubes and plugs during the process. A design render of the device is shown in Figure 6.3.

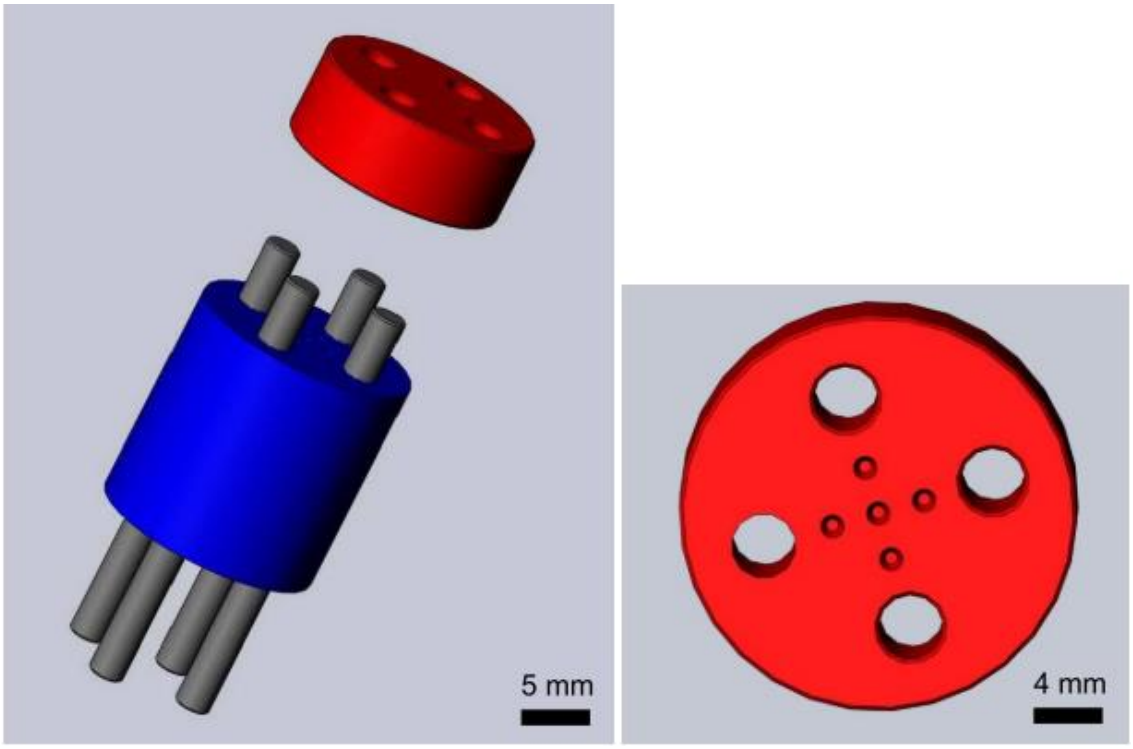

Figure 6.3:- The custom made sealing device. The blue are red components are blocks of copper machined to accommodate the tubes and caps. Alignment between the main body (blue) and heat transfer block (red) is maintained by the 4 grey rods fixed within the main body. Image reproduced from [232].

This device had been made and used previously as part of the proof of concept work [21], [232]. The sealing device consists of a copper main body where the tubes are positioned, while also functioning as a heat sink, and a removable copper top section that transfers heat to the tube and plug. The main body has 5 channels drilled through its entire length with a diameter of 3 mm. The channels are threaded for approximately half their length, where grub screws enable height adjustment for each channel individually. The top heat block features 5 cone indentations aligned with the channels within the main body, which aid heat transfer around the plug and the end of the tube, while also shaping the polymer melt. An example of one end of a PCL tube sealed using this device is shown in Figure 6.4.

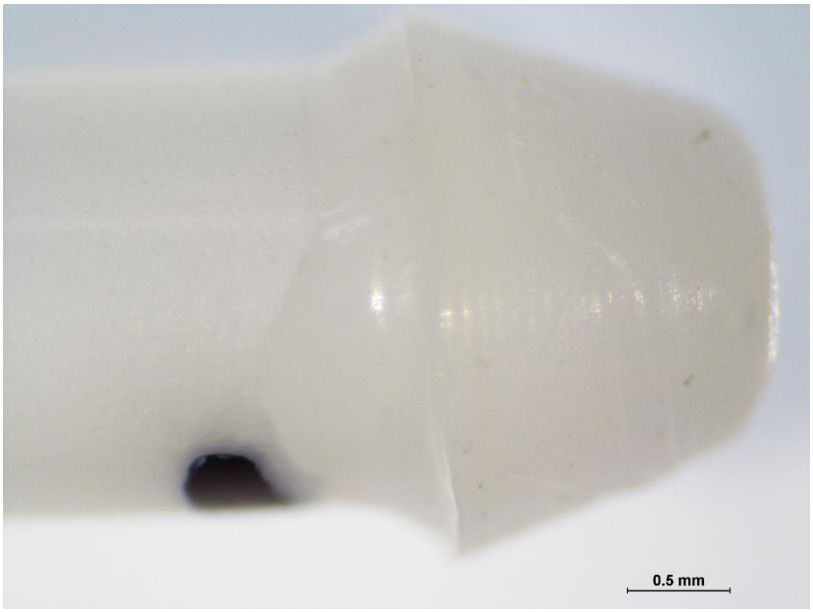

Figure 6.4:- Example of a sealed PCL tube end. The melted plug is shaped and folded down over the end of the tube.

PCL plugs 3 mm long and 2 mm diameter were punched from a block of PCL using a 2 mm biopsy punch. A plug was inserted exactly 1.5 mm into the open end of the tube. The tube outer surface is marked with a pen 2.5 mm from the tip of the plug, which is used to make the height consistent between tubes within the main body of the device. The tube is then positioned within the main body and the grub screw adjusted so that the pen mark is visible. The top heat block was placed indentation side face down on a hot plate set at 100 ^{o}C for no less than 5 mins. The hot top block was placed onto the main body and held firmly for 20 s, and then the entire unit is held under running cold water until cold to touch. The top block was then carefully removed as the fused tube/caps typically adhered to it. The stuck tubes were gently agitated to detach them from the top block.

If the tube was being used for osmotic burst testing, after one side was sealed a filling step was performed before repeating the sealing process for the remaining open end. The filling process is described in Chapter 8 8.2.2. Tubes for mechanical burst testing were only sealed on one side, and were therefore ready for use after one side was successfully sealed.

6.3.5 Photo-crosslinked device sealing

Different sealing methods were used with the xPCL tubes to determine the most suitable method for future studies. The following methods were used: 1) Injection of 15 μL of xPCL10k0.9k resin into the open end, followed by 10 mins of curing using the Omnicure UV source. 2) Injection of 15 μL of medical grade cyanoacrylate glue and left to solidify overnight. 3) Injection of 10 μL of cyanoacrylate glue, and insertion of a 3 mm long, 2

mm diameter PCL plug with 4 μL of glue dispensed around the barrel of the plug, then being left of cure overnight. Similarly to the PCL tubes, the xPCL tubes for osmotic release studies require filling after sealing of the first end, followed by sealing of the remaining end, while tubes for mechanical testing only require a single end to be sealed. Examples of tubes sealed using each of the capping techniques are shown in Figure 6.5.

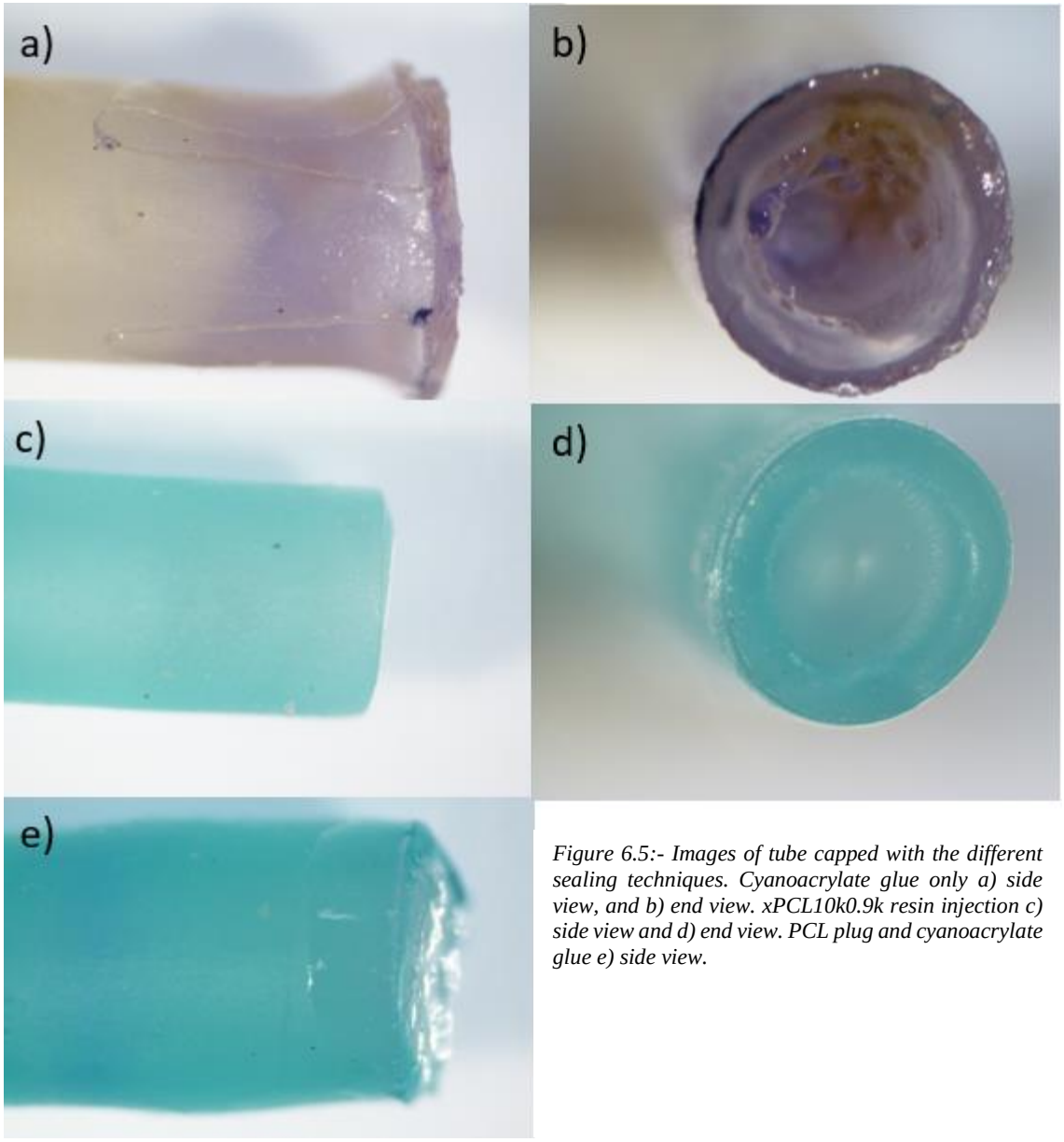

Figure 6.5:- Images of tube capped with the different sealing techniques. Cyanoacrylate glue only a) side view, and b) end view. xPCL10k0.9k resin injection c) side view and d) end view. PCL plug and cyanoacrylate glue e) side view.

6.3.6 Mechanical burst pressure testing

The burst pressure of the tubular parts was assessed using a custom syringe-holding setup and an Instron 5567 universal mechanical tester. Images of the setup are shown in Figure

6.6 , where a) shows the general setup, b) shows a close up of the syringe in the mount, and c) shows a tube mounting arrangement.

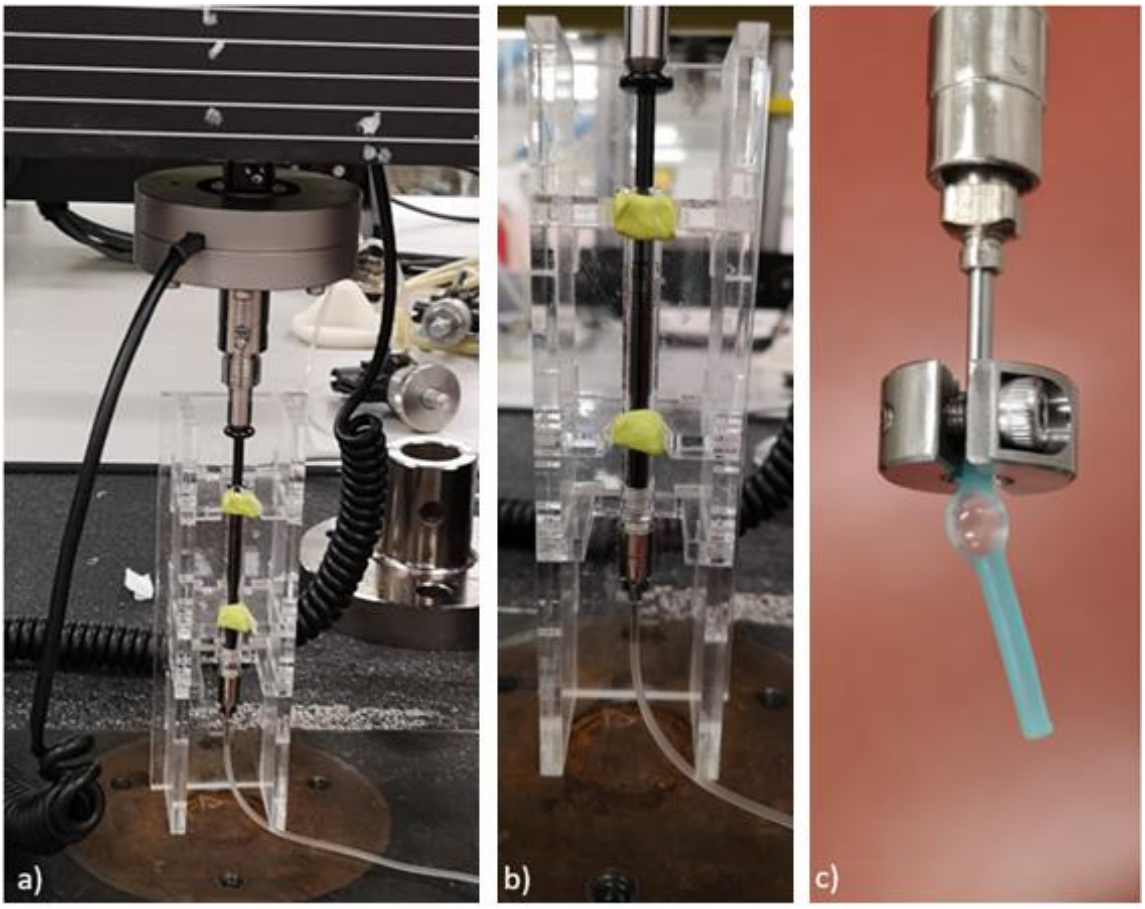

Figure 6.6:- Mechanical burst pressure testing setup. a) Shows the whole setup, b) the syringe mounted in the holder being depressed, c) an example of a tube mounted to the needle. Note that images a) and b) show the setup connected to a catheter rather than a tube from this study.

A vertical mount for a 1 mL glass syringe was laser cut from acrylic. The tube to be tested was sealed/plugged on only one of the open ends. The remaining open end was mounted on to a blunt 14-gauge stainless steel needle, which had two 2 mm inner diameter O-rings pre-mounted. The O-rings were rolled over the mounted portion of the tube. A small clamshell clamp was placed over the O-rings and tightened to help hold the tube in place and form a good hermetic seal. The mounted tube and needle were submerged in water, and syringe was filled with water. The needle/tube arrangement was mounted to the syringe underwater to prevent air bubbles. The syringe and mounted needle/tube was then placed in the syringe holder and centred under the crosshead of the Instron chassis. The Instron chassis was fitted with a 500 N load cell, which had a small piece of billet aluminium attached so there was a flat surface for depressing the syringe plunger. The syringe plunger was depressed at a rate of 5mm/min during the burst experiments and was continued until briefly after the burst event. Burst was detected by ejection of water, a sharp drop in force reported, and sometimes an audible crack or pop. Average force

due to friction was determined over 3 runs using the syringe filled with water and with the needle mounted, but without any tube attached. Sample force curves had the average friction force curve subtracted. The hydrostatic pressure exerted on the samples was determined by dividing the force measured by the syringe plunger's surface area (16.6 mm^2). It was calculated that to displace 1000 μL of water, 60 mm of travel was required. Using this, the volume required to burst a tube was calculated from the distance travelled by the crosshead. The burst sites of tubes were also imaged under a microscope.

6.3.7 Osmotic burst site investigations

PCL tubes were filled with 4 M glucose and dye solution and sealed prior to being submerged in 15 ml of 1x PBS solution within a screw top glass vial. The vials were placed in an oven at 37 ^oC until bursts were identified by release of the blue dye into the PBS solution. Burst devices were removed, wiped of superficial solution, before the burst site being investigated under a microscope (Zeiss Stemi 2000-C with axio cam 105 camera).

6.4 Results

6.4.1 Tubular part wall thickness

One tube from each of the material groups was selected at random and scanned over the majority of their lengths. The distribution profiles of the data obtained from the tubes scanned in their entirety are shown in Figure 6.7. The average, minimum, and maximum thicknesses determined for each material type are shown in table Table 6.1.

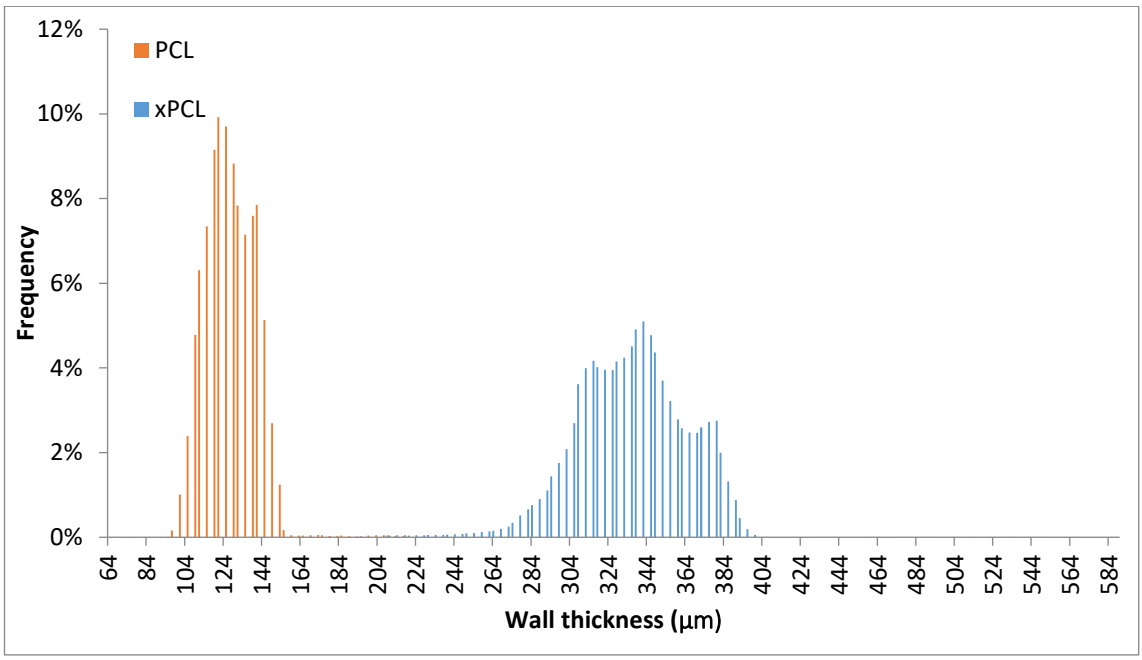

Figure 6.7:- Histograms of the PCL and xPCL full tube scans. Bin size is 2 μm increments. The number of counts within each bin is expressed as a percentage of the total number of counts. Both groups feature 2,541,600 measurements each determined from a single tube.

Tube material	Average thickness ± SD (μm)	Min thickness (μm)	Max thickness (μm)
PCL	127 ± 13	64	243
xPCL	335 ± 29	196	588

Table 6.1:- Average, mimimum, and maximum thicknesses determined from the complete tube scans of one PCL and one xPCL tube. Each average and standard deviation is determined from, 2,541,600 measurements on slices from a single tube.

The wall-thickness distribution profiles from Figure 6.7 show two distinct populations, and that the xPCL devices are thicker and more variable than the PCL devices. The PCL histogram distribution appears to be gaussian. Considering only 95 % of the data points centred around the mean of the full tube scans we can determine that the PCL tube thicknesses range predominantly between 102-148 μm, while the xPCL range over 282-384 μm. Comparing the full tube scan data in Table 6.1, the xPCL tube is approximately 2.6x thicker (335 μm) on average than the PCL tube (127 μm).

The average, minimum, and maximum wall thicknesses determined from the regional tube scans are shown in

Tube material	Tube number and region	Average thickness ± SD (µm)	Min thickness (µm)	Max thickness (µm)
PCL	1 Top	201 ± 22	125	250
	1 Centre	219 ± 25	132	264
	1 Bottom	201 ± 39	108	277
	2 Top	118 ± 7	61	159
	2 Centre	123 ± 10	64	142
	2 Bottom	116 ± 11	64	135
	3 Top	197 ± 16	136	233
	3 Centre	117 ± 11	64	135
	3 Bottom	192 ± 25	105	240
xPCL	1 Top	335 ± 7	318	358
	1 Centre	410 ± 11	382	436
	1 Bottom	411 ± 17	368	473
	2 Top	298 ± 7	264	345
	2 Centre	328 ± 11	294	432
	2 Bottom	344 ± 5	314	362
	3 Top	293 ± 5	257	307
	3 Centre	333 ± 7	297	351
	3 Bottom	344 ± 9	304	368

Table 6.2.

Table 6.2:- Lists the average, minimum, and maximum wall thicknesses measured from the microCT images using the ImageJ script. For each sub-section scan, the average and standard deviation is determined from 90,720 measurements.

The sub-region scans for the PCL 1 and 2 tubes appear to show a trend where the average thickness of the top and bottom regions appear similar and thinner than the centre portions. While PCL tube 3 bottom and top regions are similar, the centre region is thinner. The xPCL tubes appear to show a trend of increasing thickness from top to bottom.

6.4.2 Mechanical burst characterisation

The friction forces were found to vary as the plunger was depressed over a distance of 40 mm (equivalent to dispensing of 0.67 mL), as shown in Figure 6.8.

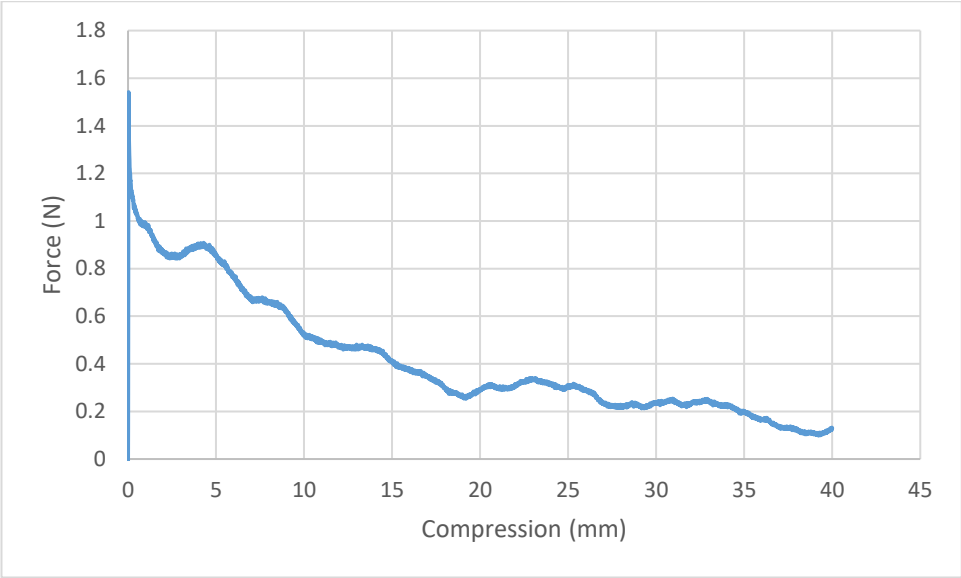

Figure 6.8:- The average friction force generated from expelling water from the syringe through the blunt needle with no tube attached. (n=3).

As the crosshead makes contact with the plunger, the force required to maintain crosshead speed briefly spikes before gradually declining as compression continues. The average friction forces were deducted from the forces recorded for each tube specimen tested prior to the calculation of pressure. No tubes required plunger compression of more than 20 mm and therefore the data above covers the entire friction range required.

Burst pressure testing was performed on 5 PCL, 2 xPCL – Glue, 2 xPCL Plug + Glue, and 1 xPCL - Resin device. The yield point was defined as the point of peak pressure where burst does not occur. The burst moment was identified by expulsion of water from the tube, accompanied by a rapid drop in pressure. Representative burst profiles from each group are shown in Figure 6.9. The average pressure and volume displaced at yield and burst is shown in Table 6.3.

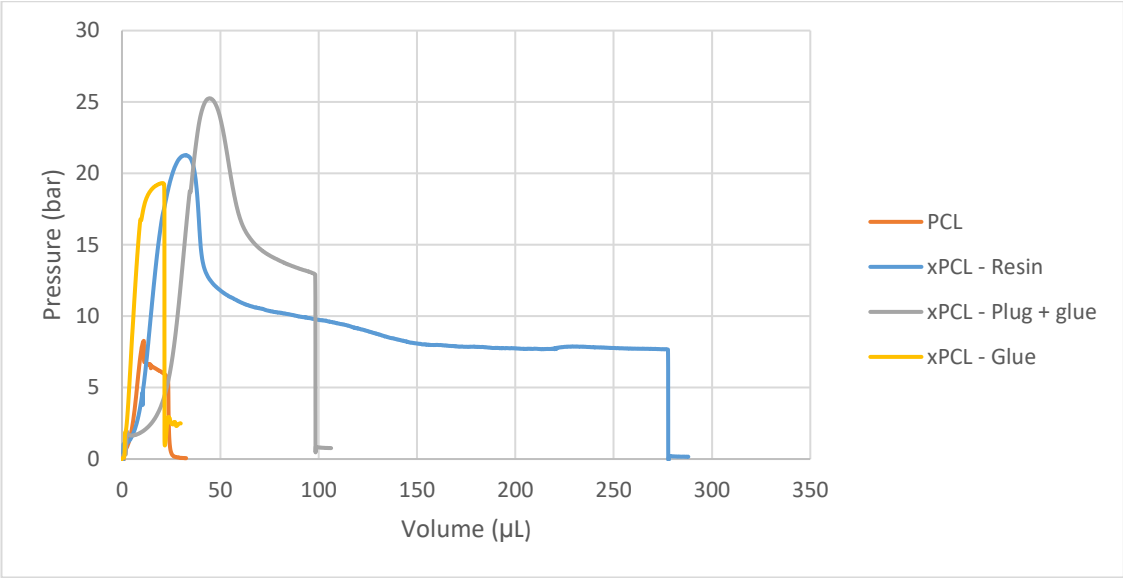

Figure 6.9:- Representative burst pressure profiles of PCL and xPCL tubes featuring each of the three xPCL tube capping techniques.

Tube/cap composition	Yield at:		Burst at:	
	Pressure (bar)	Volume (µL)	Pressure (bar)	Volume (µL)
PCL	7.4 ± 1.4	11.6 ± 1.4	5.3 ± 0.4	22.3 ± 1.4
xPCL – Resin	21.3	32.2	7.7	277.2
xPCL – Plug + Glue	24.5 ± 0.2	44.1 ± 0.7	13.2 ± 0.7	89.3 ± 9.2
xPCL – Glue	n/a	n/a	19.6 ± 0.9	19.2 ± 2.5

Table 6.3:- The average pressure and displaced volume at yield and burst for PCL and xPCL tubes determined by mechanical burst testing. PCL n=5. All xPCL groups n=2, except xPCL- Resin where n=1.

With exception of the xPCL – Glue tubes, all displayed bursts along the tubular part and feature a 2-stage profile, as shown in Figure 6.9. The 1st stage involves the building of pressure prior until peaking followed by a steep decline in pressure, which is accompanied by visible localised material deformation, generally in the form of a bulge at a position on the tubular part. The 2nd stage features growth of this deformation zone during a period of gradual pressure decline until burst. From visual observation, the deformation areas were largest for the xPCL Resin device, followed by the xPCL Plug + Glue devices, and finally the PCL devices. The extent of deformation coincides with the magnitude of the volume of water required to burst each device type. When the PCL devices burst, a narrow jet of water was forcefully, but briefly, expelled from the area of deformation. The xPCL Resin and Plug + Glue devices burst akin to bursting of a water filled balloon, with water being explosively released in no specific direction. The xPCL Glue tubes burst in a single

phase as the pressure peaks, with a small volume of water ejected from around the cap or through the cap itself.

Images of representative mechanical burst sites from PCL and xPCL tubes are shown in Figure 6.10.

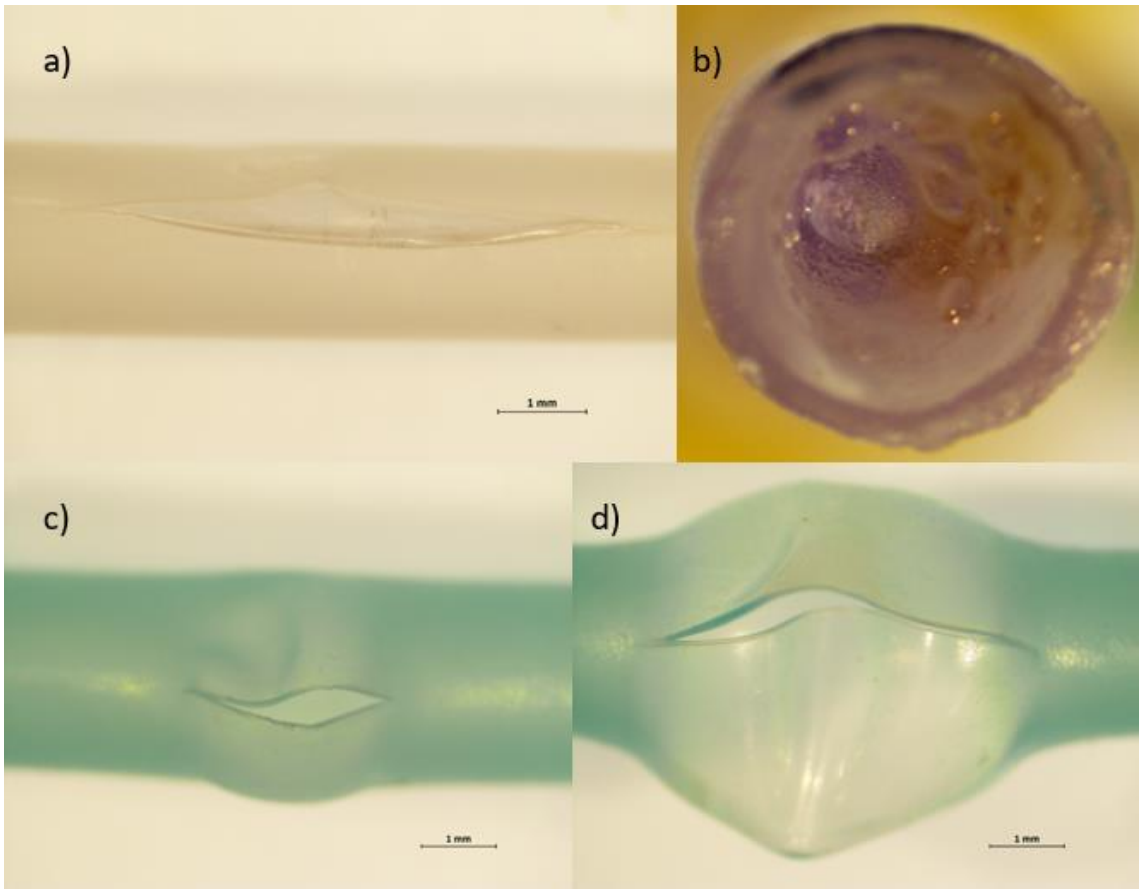

Figure 6.10:- Representative burst sites from mechanical burst testing of a a) PCL device, b) xPCL cyanoacrylate glue sealed device, c) xPCL plug and glue device, and d) xPCL sealed with resin device. Scale bars indicate 1 mm.

The PCL tubes (a) feature what looks like a large (5.8 mm long) fissure, positioned longitudinally on the tubular part. However, this large deformation is deceptive, with only a small pinhole in the centre of the deformed zone forming a channel through the device wall. While it was observed that the xPCL – Glue devices (b) burst from the cap region, it was not possible to detect the nature of the burst site via microscope. The xPCL plug and glue devices (c) displayed a clear bulbous deformation (estimated diameter ~3 mm) with a gaping longitudinal tear approximately 2.5 mm in length. The xPCL resin sealed device displayed a larger zone of deformation (estimated diameter ~5 mm), combined with a longer tear of approximately 5 mm.

6.4.3 PCL tube osmotic burst sites

Microscope images of the PCL device burst sites were taken following osmotic experiments. Out of 8 devices tested, 5 demonstrated bursts along the tubular section, while the remaining 3 devices featured bursts around the sealed cap regions. Images from devices that burst along the tubular part reveal that small pinholes are formed at burst allowing flux of dye into the surrounding solution. An example of such pinhole bursts are shown in Figure 6.11.

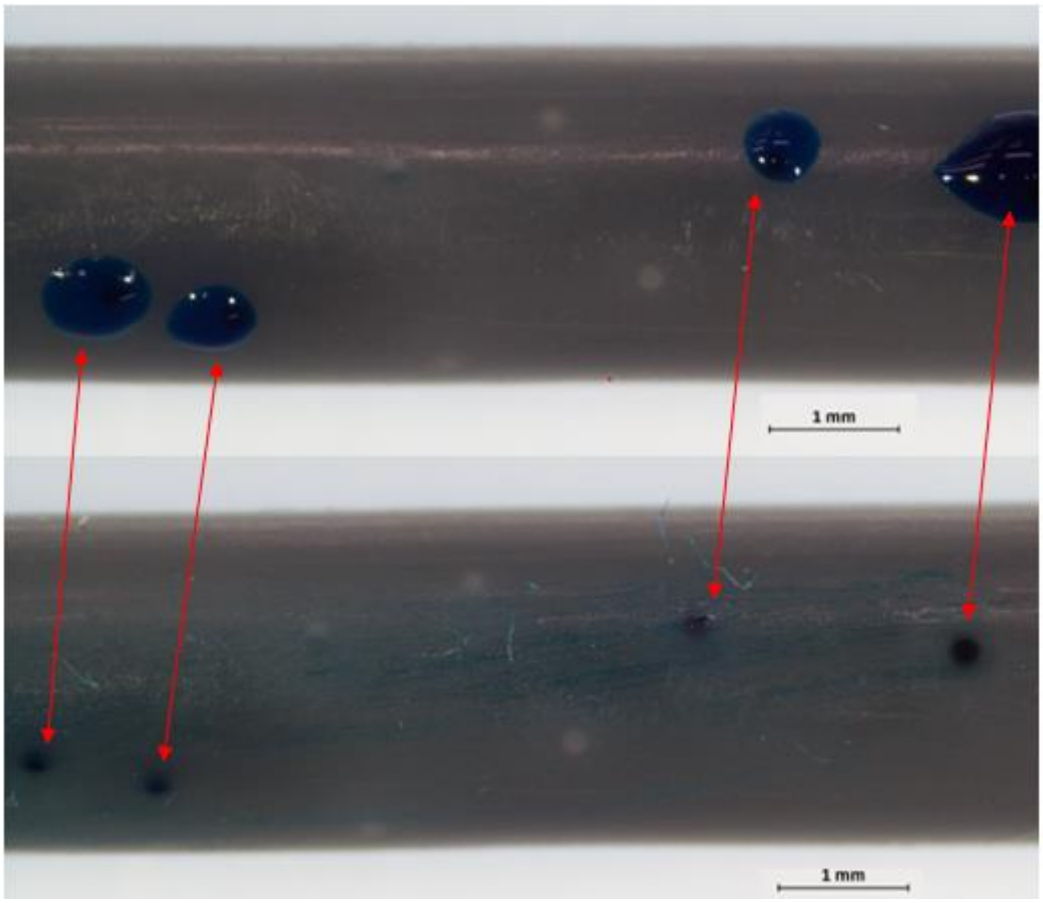

Figure 6.11:- Osmotic burst induced pinholes on the tubular part of a PCL device. Upper images shows the tube squeezed between fingers to enable easy identification of burst sites, while in the lower image the dye is wiped away to show the size and shape of the burst sites. Scale bars indicate 1 mm.

Multiple pinholes were found on all 5 of the devices that were noticed to burst along the tubular part. The burst sites appear significantly different to those found after mechanical burst testing.

Of the 3 devices that burst around or directly through the cap, 2 are considered to be caused by defects generated during the capping procedure, and are shown in Figure 6.12.

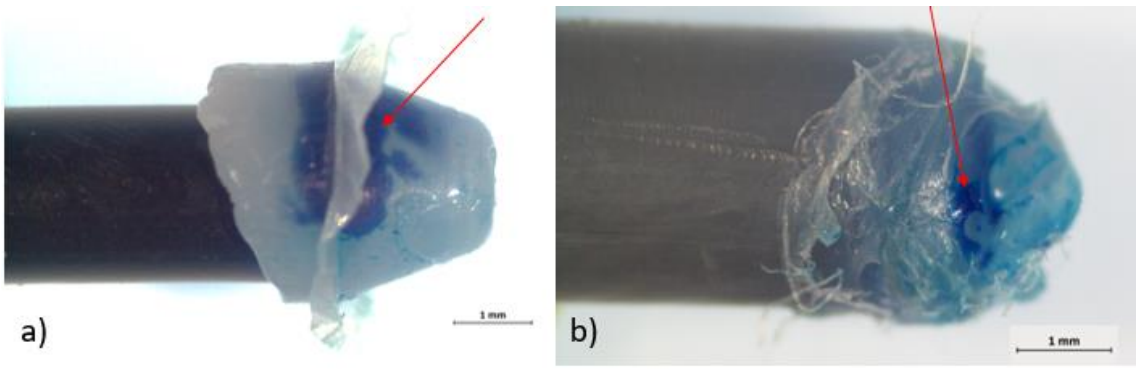

Figure 6.12:- PCL devices with burst sites inside the cap. Both appear to be from defects. The cap in image a) featured a large hollow space, potentially from an air bubble trapped in the molten polymer during capping. The cap in right image b) appears severely damaged, possibly from attempted removal from the sealing device before the polymer had fully cooled and re-solidified. The red arrows indicate the hole or channel from which the dye flows.

The cap of the device in Figure 6.12 a) featured a hollow space within the cap, rather than being solid throughout. A small channel was present at the outer surface of the hollow space through which dye was able to travel. The cap in device b) is malformed with a narrow channel through the cap that enables premature leaking of dye into the surrounding solution.

The final device burst between the edge of the cap and the tubular part, as shown in Figure 6.13.

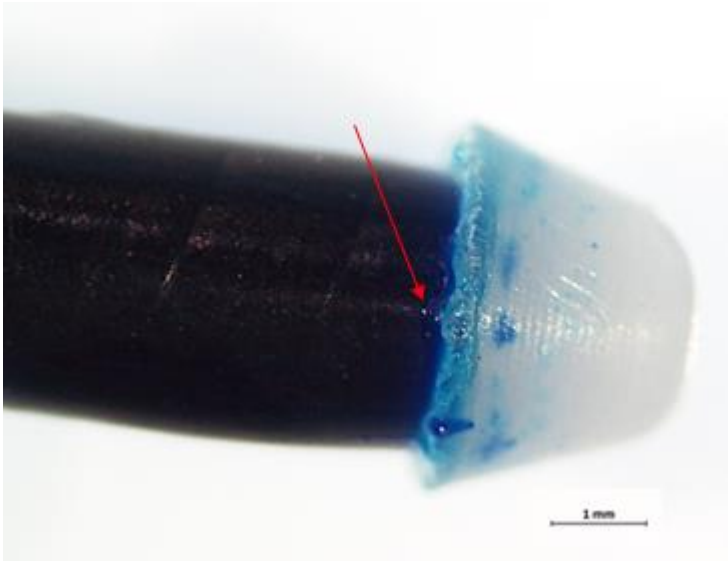

Figure 6.13:- PCL device with burst site at the interface between the end of the tube and skirt of the plug/cap. Red arrow indicates position of the burst site.

It is difficult to determine whether this was due to a defect introduced during capping or if it is an unfortunately positioned viable burst on the tubular part.

6.4.4 Stereolithography printing of devices

Production of devices was performing using stereolithography using the xPCL10k+4A resin. For the first attempt a printing tubular devices using the EMBER printer, 3 30 mm long 2.4 mm overall diameter (200 μm wall thickness) tubes were positioned vertically on the build head directly without supports. The freshly printed tubes are shown in Figure 6.14.

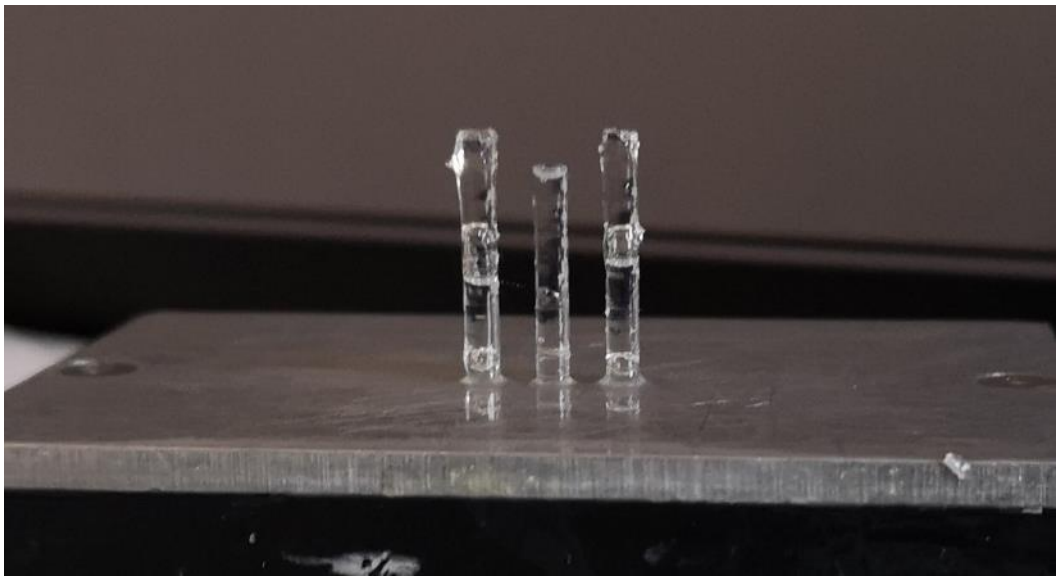

Figure 6.14:- Vertically positioned tubes printed by stereolithography. Resin and air can be seen through the transparent walls while the material is still solvent-laden. The centre tube can be seen to be shorter than the tubes either side of it.

The print process proceeds without issue until the tubes reach approximately >15 mm in length. During the rotating peel process after this milestone, the tubes begin flexing and struggle to remain completely straight. The middle tube in Figure 6.14 did not return properly for the next layer to be added, which then left debris on the build window, which disrupted further layers. The print was stopped after this point to prevent potential damage to the other tubes also. Aside from this flexing issue, the tubes were well formed and without defects.

In a second attempt, 4 tubes were placed at the tips of an ‘X’ shaped central support in order to provide greater resistance to flex during peeling. Photographs of the printed layout is shown in Figure 6.15.

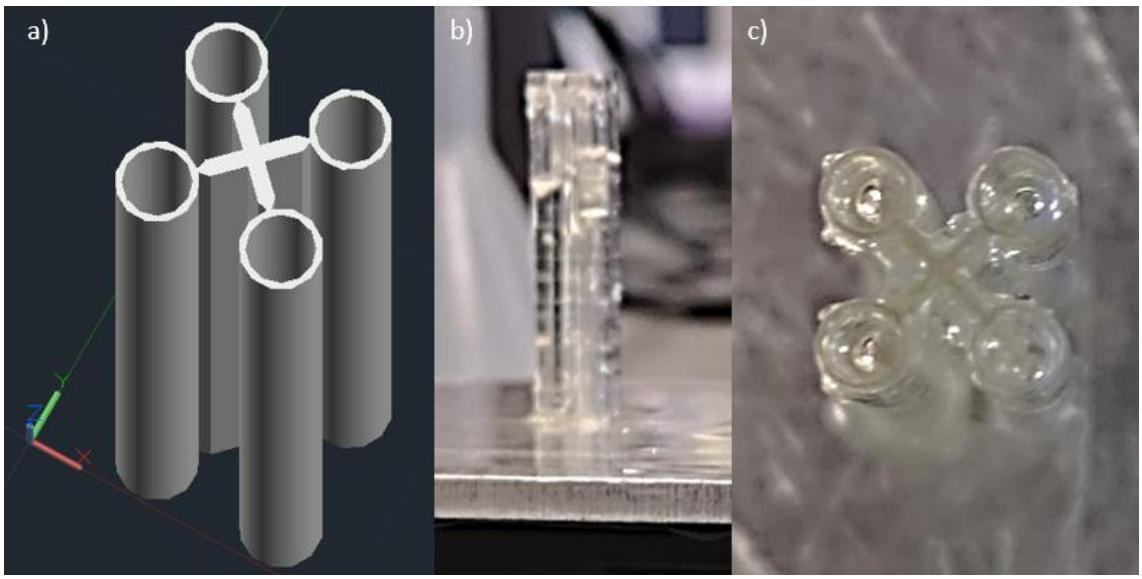

Figure 6.15:- a) CAD design of the tubes and support structure. b) side view and c) top view of the printed model. Again resin is held within the internal space through capillary forces, and is washed out prior to post-curing.

This print layout worked well, with the print completing with all tubes at full length without defect.

Typical supported layouts were also investigated. Within the print software, the tube model was positioned at 45^{o} with one open end 1.5 mm above the surface of the build head. This allowed a series of supports to be added along the length of the tube. The first attempt of this layout failed as shown in Figure 6.16.

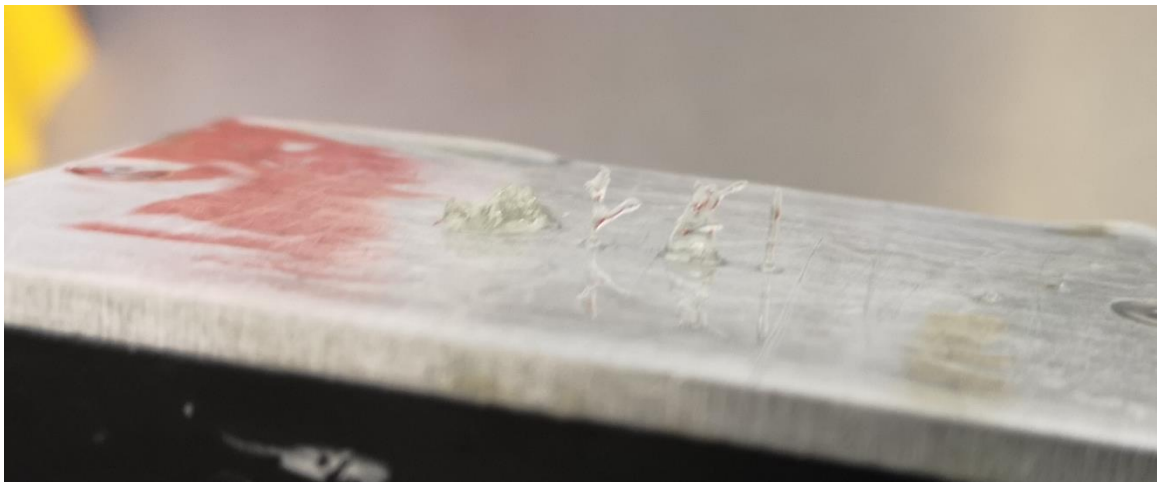

Figure 6.16:- Failed attempt at a tilted tube printed with typical stereolithography support structures. A blob of supports and collapsed initial layers of tube can be seen to the left side, with support 'trees' having been printed well but without the tube to link up with.

The support density was not high enough during the critical initial layers of the lowest portion of the tube. Another attempt was made featuring greatly increased support density and at a reduced tilt angle. The printed tube is shown in Figure 6.17.

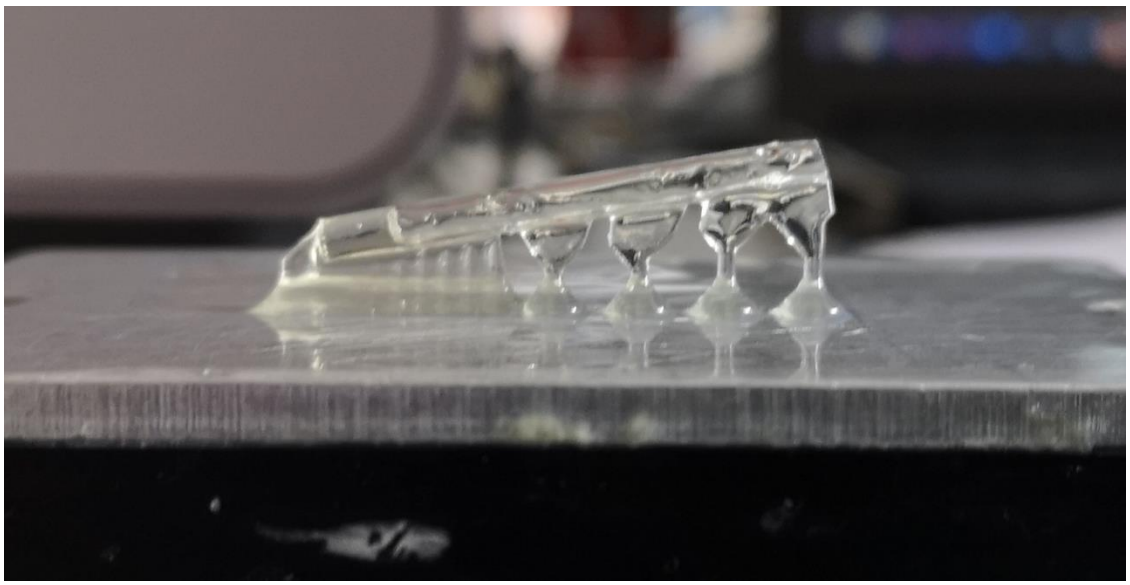

Figure 6.17:- Increasing the support density and a more gentle overall tilt angle on the tube led to a successful print. The support structure underneath the lowest part of the tube are so close together that it essentially generates a single solid supporting piece along the initial length of the tube. Resin held in by capillary forces can be seen towards the left-most (lower) open end.

This print layout could be printed successfully with the tube being printed in full length and without defect.

6.5 Discussion

6.5.1 Summary

Viable osmotic devices were able to be produced easily using automated dip coating apparatus. Tubular devices were able to be printed via stereolithography, but were susceptible to damage during post-print processing. Mechanical bursting of xPCL devices sealed with resin or a cap and glue technique lead to explosive-like bursting, releasing water in an immediate manner from a zone of local deformation. Such devices also require a greater displacement of water to burst than PCL or xPCL devices sealed with glue alone. The xPCL device sealed with resin required over 10x more water to be displaced to burst, than the PCL devices. Images of the burst sites confirm what was witnessed during mechanical burst testing. From these preliminary tests it appears that the method of capping can influence the overall burst behaviour of the xPCL devices. For future osmotic burst testing, xPCL tubes sealed with resin were chosen as the preferred method of capping due to the greater extent of swelling and volume of water released at burst shown from mechanical burst testing. MicroCT measurement of the wall thicknesses of the tubular parts produced from dip coating methods of both PCL and xPCL tubes show that the PCL tubes are thinner but feature a more consistent wall thickness distribution

throughout their overall length than the xPCL tubes. Images taken of devices burst during osmotic methods indicate that devices burst via osmotic and mechanical methods show different burst site characteristics, and may suggest that use of mechanical techniques to predict osmotic burst behaviour may not be directly suitable. Stereolithography printing of tubes was successfully demonstrated.

6.5.2 Dip coating and wall thickness

Dip coating enabled relatively easy production of both thermoplastic and photo-cured tubes. As shown most clearly in Figure 6.7, the average tube wall thicknesses between the PCL and xPCL devices are quite substantially different. The target wall thickness for both types of devices was intended to be approximately 200 µm. There appears to be two separate issues, the first of which is that out of the 4 PCL tubes scanned, 2 show an average thickness of approximately 130 µm, while the remaining 2 are on the target of 200 µm. This is perhaps due to differences in polymer solution viscosity as the chloroform solvent evaporated slightly through the day causing differences in the deposited polymer layer thickness on the rod. It was not intended for the xPCL tubes to be up to 2.6x thicker. It is expected that the issue arose from improper care while measuring prototype tubes produced during the basic exploratory phase, where calipers were used to measure wall thicknesses. It is likely that too much force was applied while closing the calipers around the specimen, returning a smaller thickness value that led to underestimation of the sample wall thicknesses. Based on previous work that showed that there was a strong correlation between wall thickness and burst pressure strength, it is highly likely that the difference in wall thicknesses between material types may have contributed to some of the differences observed from mechanical burst pressure testing. Future work should ensure that when comparing tubes of different materials that the wall thickness is kept similar between groups, to allow determination of material specific behaviour from other aspects. The dip coating sequences were not fully optimised, which is most evident from the variance in average wall thicknesses between tubes of the same material type, and even from different regions of the same tube. The dip coating methodologies for the PCL and xPCL materials result in the xPCL tubes featuring approximately 2.6x thicker walls on average, as determined from the full tube microCT scans. The full tube scans also indicate that the PCL tube wall thicknesses are more homogenous than the xPCL tube. When considering the regional scans, the opposite appears true, particularly when comparing the thicknesses at different positions of the same tube. In comparison to previous wall thickness measurements of a PCL tube, the particular method used here

appears to generate tubes with a similar level of wall thickness variance (171 ± 21 μm) [21], [232]. Recent investigations conducted after the work detailed in this chapter was complete identified the withdrawal speed of the rod as a critical controlling factor for wall thickness variation when using the PCL material [233]. Ideally, the dip coating cycle should be investigated and optimised for each different polymer solution/resin with particular considerations regarding the withdrawal speed, rotation speed, and evaporation/cure time. The main drawback to the dip coating curing method specifically was the non-automated nature of the UV source. This then required the user to be present at all times, and concentrating on setting timers to alert the user to turn the light on or off as required. A disadvantage of that particular dip coating machine was that it was only able to dip coat a single rod, which limited throughput and overall efficiency. Both drawbacks were addressed when constructing the new variant of the dip coater as detailed in Chapter 7.

6.5.3 Effect of sealing method on mechanical bursts

Mechanical burst testing of xPCL tubes suggest that the capping/sealing method can have a significant effect on the extent of deformation and ultimately burst behaviour of the tubes. xPCL tubes sealed by cyanoacrylate glue, plug and glue, or resin required different displaced volumes of water and displayed different internal hydrostatic pressures to yield and burst. Overall, the xPCL devices required a greater pressure and displaced volume to yield and burst, than the PCL devices. However, the PCL and xPCL - Glue devices burst after a similar volume displacement, which appears primarily due to the xPCL – Glue tubes bursting where other xPCL counterparts would typically only yield. The xPCL – Glue tubes were the only tubes to burst around the cap region, indicating that perhaps there is a poor interface between the cyanoacrylate glue plug and the inner-barrel walls of the xPCL tubular part, providing a suitable weakness to cause burst at the first instance of material yield/deformation. The rigidity of the capping method of the xPCL tubes appears to affect the ability of the tubular part to freely deform, as shown by the reduced displacement at burst and greater pressure required to yield by the xPCL- Plug + Glue devices versus the Resin sealed tubes. The xPCL – Resin device was capable of accommodating the greatest volume displacement prior to burst, and was shown to burst in the desired manner, visibly expelling the greatest volume of water immediately upon burst. The xPCL – Resin devices would require a 10x greater volume uptake than the PCL devices, and therefore suggests they would take longer to burst in an osmotic test environment. From the favourable observations regarding the nature of burst, use of

xPCL10k0.9k resin was chosen as the sealing method of choice for the xPCL devices. The xPCL – Resin sealed tubes possess a similar mechanical burst profile to the PDMS walled tubes tested by Dunker [232]. The xPCL tubes feature a more prominent yield peak due to being composed of a stiffer material than the soft PDMS tubes, but the PDMS tubes required displacement of approximately 800 μL of water to burst, which was more than double that of the xPCL - Resin tubes. The xPCL tubes offer an intermediate between the PCL and PDMS devices in terms of their swelling during mechanical testing, and still demonstrate an explosive-like release at burst while being fully degradable. Critical analysis of the mechanical testing methodology and relating mechanical bursts here to osmotic bursts in Chapter 8, will be evaluated in Chapter 9.

6.5.4 Burst sites

The mechanical burst sites of the xPCL – Resin, and Plug + Glue devices were similar, while the xPCL – Glue, and PCL devices displayed very different appearances. The overall size of the deformation zone and tear of the Resin sealed tubes were approximately twice are large as the Plug + Glue sealed tubes. This appears to relate back to the effect of more rigid Plug + Glue sealing method hindering yield and deformation of the tubular part, as discussed above. While the cyanoacrylate glue sealed xPCL tubes were witnessed to burst through the glue cap, it was not possible to identify the hole from which the contents were expelled from the microscope images. An added complication was that as the glue cured, it formed a concave crystalline structure requiring focusing at various depths to search for a crack or hole within the cap. It is possible that perhaps the xPCL material around the glue cap deformed under load to eject the material around a portion of the cap, which returned to its original shape after the reduction in pressure following burst, hindering identification of the burst site. It was shown that the PCL device burst sites released water from a pinhole around a superficial fissure, which provides the reason for the narrow jet of water expelled from the device at the moment of mechanical burst. This pinhole burst behaviour was described by Dunker from similar PCL devices [232]. The PCL device osmotic burst sites appear quite different, with no evidence of the fissure-like surface deformation, but displays multiple discreet pinhole bursts on the tubular part. While it was expected that osmotic bursts of the PCL material devices would still be in the form of a pinhole, it was not anticipated that there could be multiple simultaneously. It is not known if all the pinholes on a device occurred at the same instant, or staggered over time. It is perhaps possible for the device to burst at multiple points at the same time through similar defect areas, such as areas with thinner walls from defects introduced

during dip coating, or bubbles. Staggered pinhole development may be possible if the initial pinhole is very small and unable to support sufficient ejection of material and/or relieve internal pressure, where internal pressure then continues to rise. However, it does not seem probable considering some devices show up to 4 individual pinholes, which would require multiple instances of the behaviour. Referring to burst site images of the xPCL – Resin sealed devices tested in the osmotic studies of Chapter 8 (Figure 8.7 b), again some differences to the mechanical bursts are evident. Both osmotic and mechanical bursting of xPCL – Resin tubes result in similar longitudinal tears long the tubular part, however no evidence of the bulbous deformation around the tear remains in the osmotically burst devices. This would suggest that the deformation during the mechanical test is predominantly plastic in nature, while the osmotic bursts are mainly elastic in nature. This switch in dominant deformation from plastic to more elastic in nature is likely caused by the elevated temperature environment combined with the slow increase in applied strain during the osmotic studies.

6.5.5 Stereolithography printing of tubes

While stereolithography printing of the xPCL10k+4A resin produced defect free tubes, the printed parts were prone to being damaged during post-processing, such as rinsing of excess resin from the internal space, and removal of supporting material. The xPCL10k+4A resin was used instead of the xPCL10k0.9k resin due to previous printing successes reported in Chapter 4, where the xPCL10k+4A resin offered greater reactivity and survivability during printing. The post-processing damage here was in retrospect predominately due to poor methodology, but also partly due to the weak nature of the 'green' part during printing due to the resin composition (as discussed extensively in Chapter 4). Prior to post-curing, removal of the trapped resin within the inner space of the tube was performed by flushing the part with isopropanol using a syringe and needle, or by sucking the resin out also with a syringe and needle. A long blunt needle in a small enough gauge was not immediately available and therefore a sharp needle was used, making it easy to perforate the tube walls if proper care was not taken. Another source of preventable damage occurred during cutting of the tube from the supporting structures. Cutting of the supports was performed after rinsing, and post-curing, but without extraction and drying. Therefore, the material was still in the weaker solvated state rather than the tough crystalline state. Particularly with the 'X' shaped support structure it was challenging to remove the linking material at the extremities of the 'X' without tearing the tube wall. Such issues could likely be negated or at least reduced substantially by only

removing supports after extraction and drying of the entire structure prior to support removal.

For production of larger numbers of tubes, the vertically positioned layout offers greater scaling than the flatter angled layout. If utilising the full build area that the EMBER offers, an interconnected array of approximately 140+ tubes could be printed simultaneously (based on an outer diameter of 2.4 mm per tube and considering the spacing of the support structures). With the DLP projector of the EMBER, the print time for such a quantity of tubes would not increase from the demonstration print of 4 tubes, as the entire build area is illuminated at once, without requiring consideration of laser raster speeds. However, caution is advised due to the non-homogeneous irradiance over the entire buildable area.

6.5.6 Device sterilisation

Sterilisation is an essential process in the manufacture of medical devices to render them safe for patient use. Sterilisation itself is defined as the process by which all-living cells, viable spores, viri, and viroids are either destroyed or removed from an object [234]. Various sterilisation techniques can be utilised, such as more traditional methods of autoclaving, and gamma irradiation, or newer novel techniques such as microwaves or sound waves. The sterilisation process suitable for a medical device can be limited by compatibility with the construction materials, active compound, or the nature of the device. For example, metal medical devices and equipment are often sterilised using gamma irradiation due to its simplicity, speed, and efficiency. However, it is known that this type of sterilisation processing results in physical changes via chain scission or cross-linking, that ultimately affect mechanical properties and/or induce premature degradation [235]. Other considerations should include that the production of a medical device suitable for patient trials would have to be manufactured in accordance with ISO 13485 and under general good manufacturing practice (GMP) conditions.

Determining suitable sterilisation processes for our capsule requires consideration of the stage or stages that a sterilisation process would be used. One of the main advantages of our capsule is that it is manufactured separately from the payload, which allows methods of sterilisation during manufacture that may have otherwise damaged the active compound in an integrated system. For example, while Soxhlet extraction of the tubular part with hot IPA will provide a sterilisation effect during manufacturing, after the later filling process such an extraction process would result in penetration of solvent into the central compartment of the device. This could potentially denature the active compound due to the heat or solvent itself. In addition to the sterilisation provided by extraction, the

UV curing processes during manufacture will also exert a sterilisation effect on the surfaces that are illuminated.

It is envisioned that manufacture of this device would require sterilisation of the components as they are manufactured (as mentioned above), with assembly and filling under aseptic conditions, followed by one or more terminal sterilisation processes. Terminal sterilisation processes are generally preferred as it is considered to remove reliance on aseptic processing and therefore incorporates a safety margin [236]. For our device, typical terminal processes such as autoclaving, gamma radiation, dry heat, and ethylene oxide sterilisation are not suitable, due to destructive effects on the polymer or an active compound. In this regard, novel techniques using UV light or sound waves (non-contact ultrasound [NCU]) are likely to be more appropriate [234].

6.6 Conclusions

Devices composed of the xPCL10k0.9k photo-cured material were shown to accommodate up to 10x the volume of the PCL devices before burst via mechanical means. As the displaced volume increases, the xPCL devices were shown to swell more than those made from PCL and upon burst were observed to expel a greater volume of water. The xPCL mechanical bursts also demonstrate that the rigidity of the sealing mechanism affects the ability of the tube as a whole to swell and distribute stress, which in turn can affect the manner in which the device bursts. An xPCL tube sealed with resin featured significant swelling during displacement of 277 μL of water, prior to an immediate explosive burst through a 5 mm long tear at the site of swelling. Mechanical and osmotic bursting of PCL devices show little swelling in comparison, and result in small pinholes that limit content release. While dip coating was a simple and effective method for production of viable devices, better optimisation for each individual material type would help make the tubular part walls more homogeneous and less variable between dip cycles. Printing of tubular structures was performed using the xPCL10k+4A resin, and shows potential as an alternative tubular part production method. Further work should be performed characterising the water permeability, swelling, and burst behaviour of printed tubes and compare them to dip coated specimens of the same material. Overall, the xPCL material devices swell and burst in the desired manner while still being degradable.

Chapter 7– Development of a fully autonomous dip coat curing apparatus for the mass production of the tubular part

In this Chapter, the development of an improved custom-built dip coating machine is detailed.

7.1 Introduction

From earlier dip coating work performed in Chapter 6, the mark I machine worked well and was easy to operate but was relatively time consuming and inefficient. This was primarily due to only being able to coat one rod at a time, yielding one tubular part per 15/20 mins. Additionally, the machine had no ability to automate photo curing, requiring the user to operate the light source manually when coating with photo-crosslinkable materials, making the process even less efficient.

To improve the efficiency, and reduce user involvement in the process, an improved dip coating machine was devised. Use of a single motor and gear system to support rotation of up to 10 individual rod substrates will enable a 10x increased throughput in a simple manner. Building the electronic control system of the machine around an Arduino will provide a cheap and expandable system capable of controlling a UV lighting circuit in addition to the motors required for the dip coating movements.

7.2 Design overview

The updated variant of the dip coater expands upon the first-generation automatic dip coater shown in Chapter 6. The dip coater mark II consists of two separate structures; one is the dip coating system itself and the other is the UV lighting gantry. When using non-photo-crosslinkable materials the dip coater unit can be used without the light gantry. Alternatively, when using photo-crosslinkable materials, the gantry can be simply placed over the top of the dip coater unit and plugs in directly to the dip coater unit without any further need for cables. The dip coater unit contains the majority of the components, with the light gantry being simply a frame with the bulbs and ballast attached. Affixed to the main unit is the Arduino and RAMPS 1.4, LCD screen and integrated controls, ball-screw rail and stage for mounting the resin vats, stepper motors for the rail and rod rotation, and the relay required to operate the UV lights. An image of the both structures is shown in Figure 7.1.

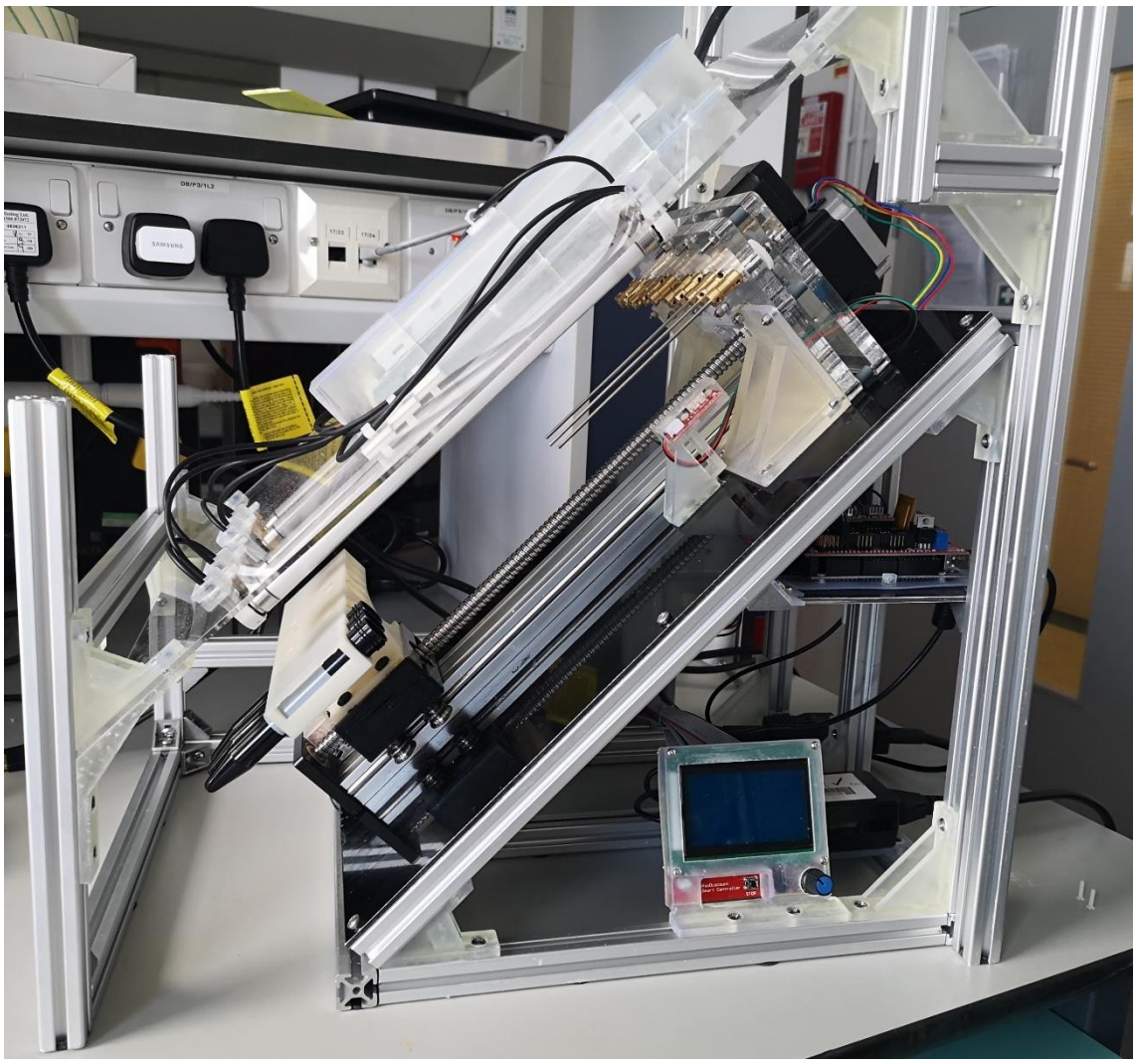

Figure 7.1:- The main dip coater unit shown with the UV light gantry placed over it.

The frames for both structures are composed of 20x20 mm extruded aluminium struts with 5 mm wide grooves for mounting of parts via t-slot nuts. The struts are connected by mainly 90^{o} brackets, with 45^{o} brackets used to produce the wedge shape. Most of the joint brackets were custom designed and printed using a Formlabs Form 2 SLA printer with the Clear v4 resin. All the mounts and housings for the electronics were also produced using this printer/resin.

7.2.1 The dip coater main body

The multi-rod capability was developed using a simple gear system. Spur gears were mounted on 5 mm diameter steel shafts and sandwiched between two 10 mm thick acrylic plates spaced using 9.5 mm tall chlorinated polyvinyl chloride (CPVC) spacers to provide support. The plates were designed in CAD and laser cut. A total of 11 gears were arranged horizontally, with the centre gear being mounted on the stepper motor shaft instead. Each shaft other than the drive gear itself was fitted with a brass “5 mm to 2 mm” shaft coupler

for attaching the substrate rods. The shaft couplers utilise grub screws to affix firmly to both shafts. The open central tunnel of the sandwich plate allows the linear ball-screw rail and its associated motor to fit snugly underneath. The rail is mounted directly down the centre of a 3 mm thick aluminium sheet. The sandwich plate assembly is positioned over the rail and fixed to the aluminium sheet through 3D printed 90^{o} mounts. 3D printed end stop towers were also mounted to the aluminium sheet at the lower-most point of the rail and just prior to the sandwich plate mounts to prevent collision of the stage. The aluminium sheet with the aforementioned parts fitted to it was fixed to the sloped edge of the wedge frame. A riser for mounting 10 15 mL falcon tubes was designed and printed on a Stratasys FDM printer and mounted on the stage. Mounts and cases for the LCD screen, Arduino/RAMPS 1.4, relay and 12 V power supply were designed and printed. All mounts affix directly to the aluminium struts of the wedge-shaped frame via t-slot nuts. Annotated images showing the overall layout and key components are shown in Figure 7.2 – Figure 7.5.

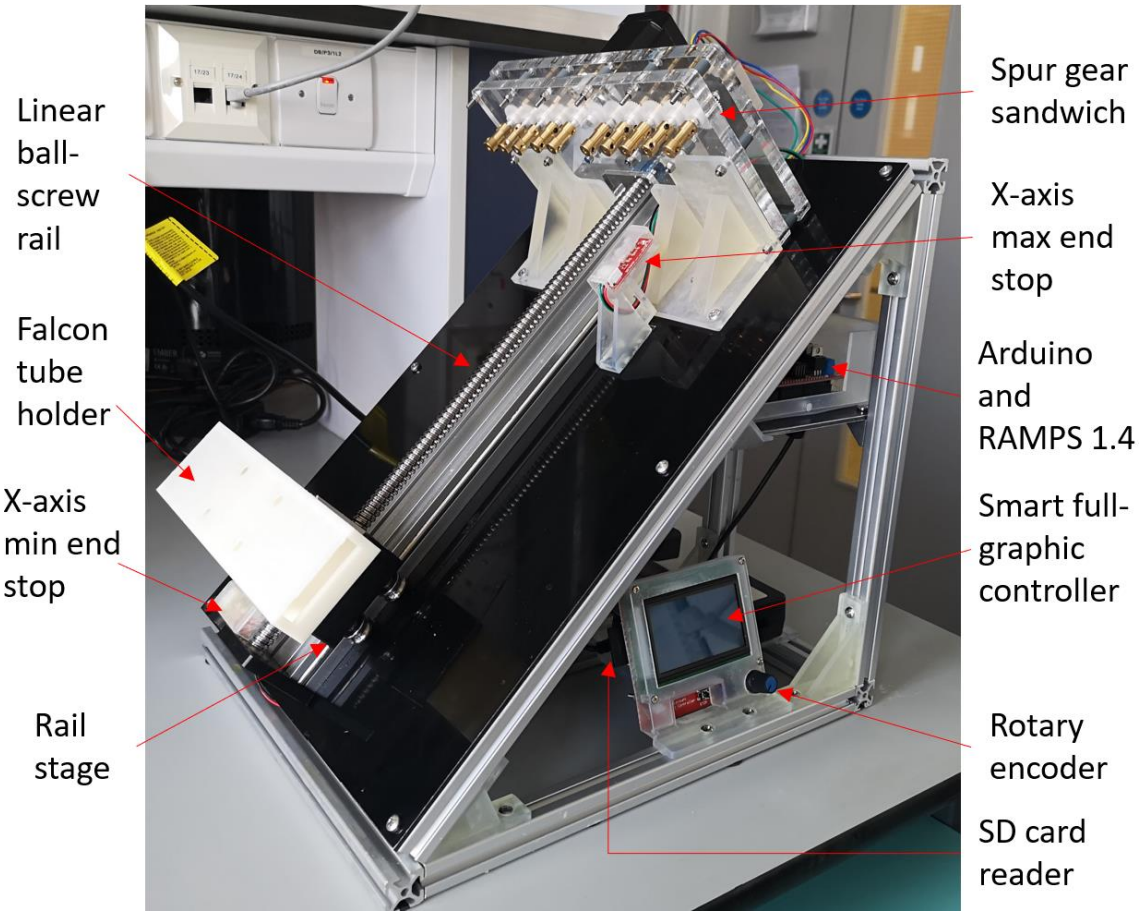

Figure 7.2:- Main dip coater unit side angle.

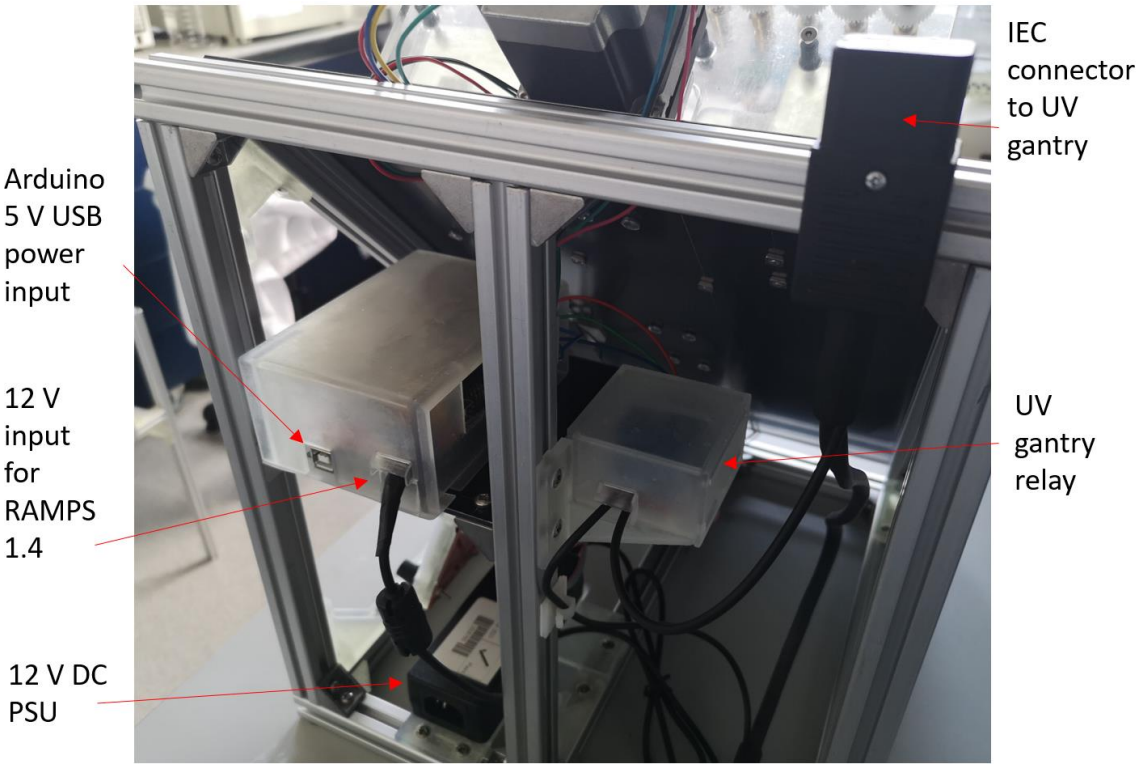

Figure 7.3:- Dip coater main unit rear view.

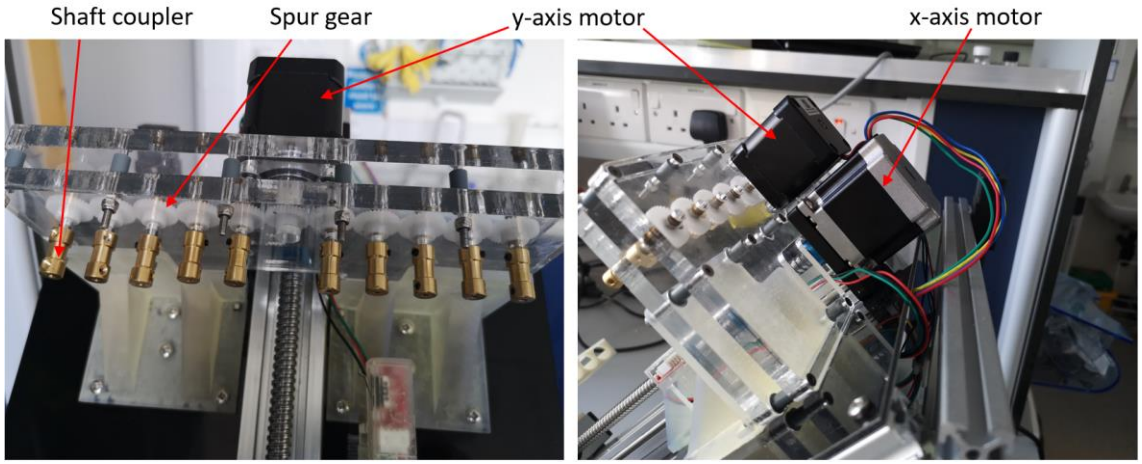

Figure 7.4:- (Left) Front view of spur gear layout. (Right) Side view.

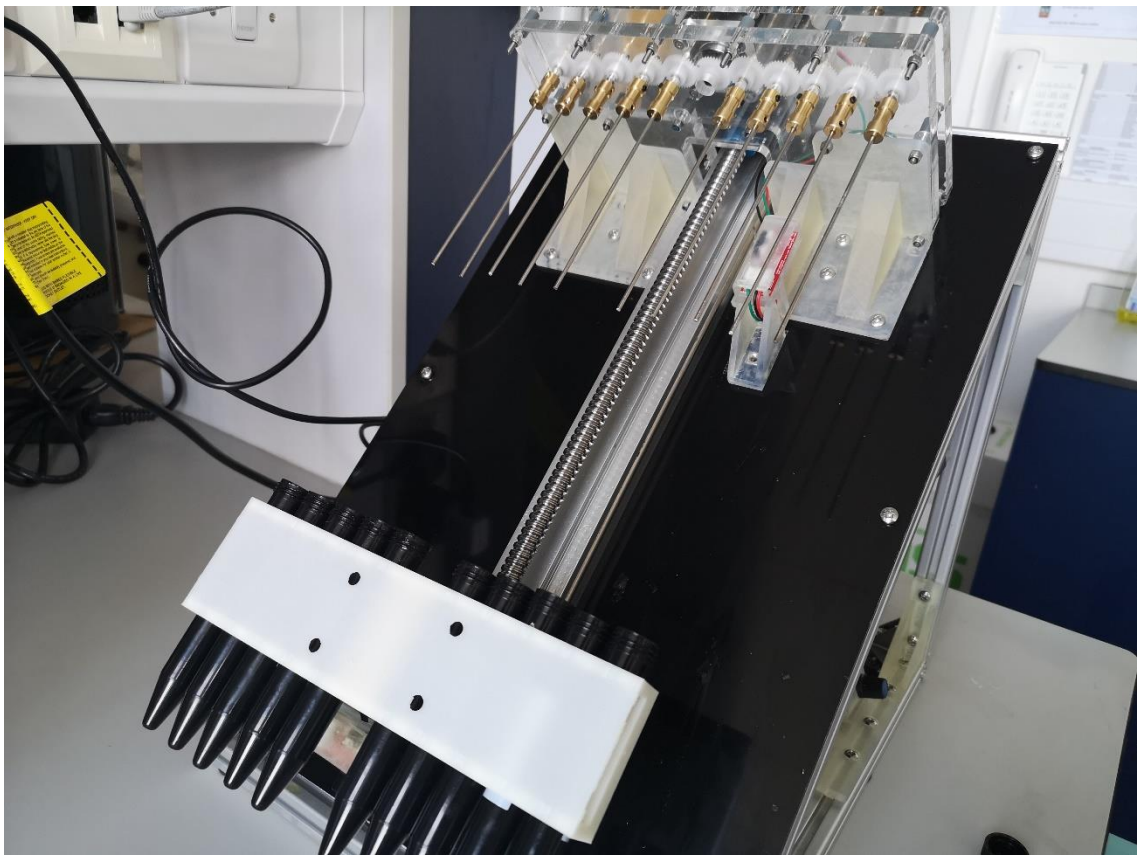

Figure 7.5:- Front view of fully loaded dip coater with 10 falcon tube polymer resin vats and 10 2mm steel shafts fitted.

7.2.2 The UV lighting gantry

A labelled diagram of the gantry is shown in Figure 7.6.

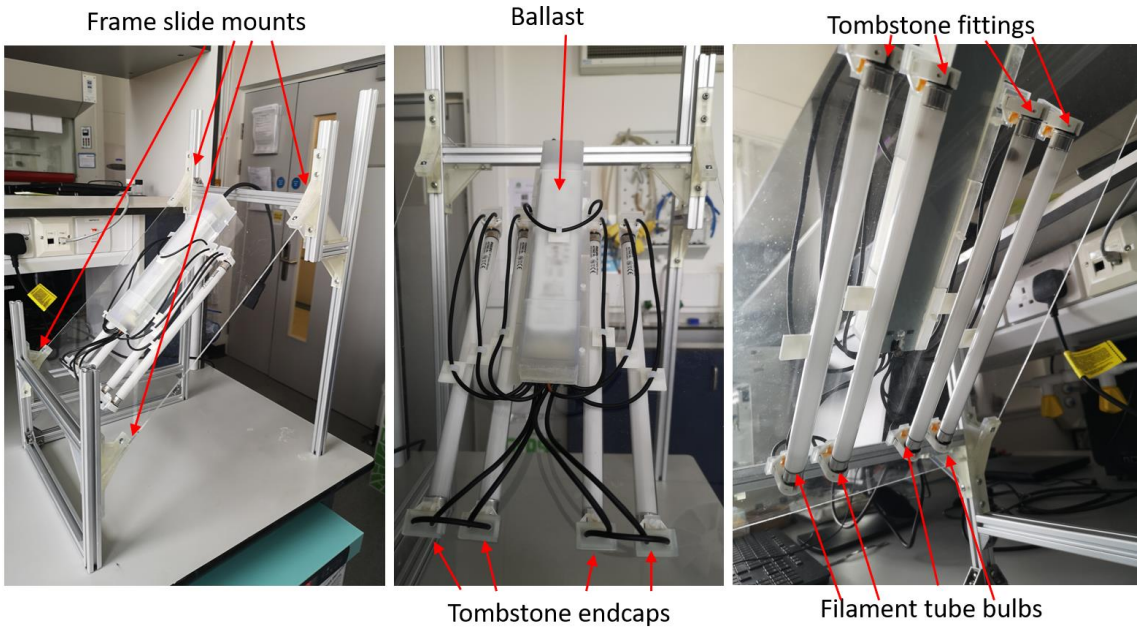

Figure 7.6:- UV lighting gantry side (left), front (centre) and underneath (right) views.

The gantry consists of the aluminium strut frame fitted with an acrylic sheet at a 45^{o} angle to which the bulbs and ballast are mounted. The UV-A lights are in the form of Philips 8 W T5 fluorescent bulbs with a peak emission wavelength at 365 nm. This type of bulb is

typically used to attract houseflies in insect killing equipment. These particular bulbs have no UV-B output, making them safer for general use than wide band UV emitting bulbs. The four bulbs are positioned evenly over the width of the acrylic sheet, and the height of the bulbs from the substrates can be controlled by sliding the mounting points up or down the vertical struts. The Philips HF-P 3/418 TL-D III ballast was chosen to power the bulbs and modulate power during the programmed start-up due to being marketed for this type of tube. The bulbs are held in place by T5 rotating tombstone fittings, which are un-shunted to match the wiring requirements of the ballast. The power cable to the ballast from the main body uses IEC plugs to allow separation of the gantry from the main body when not required for use.

7.3 Control electronics and g-code

7.3.1 Mega2560 and RAMPS 1.4 setup and wiring

The Arduino Mega2560 is a microcontroller board that is capable of controlling complex machines though a vast number of digital and analogue pins and expanded memory over smaller microcontrollers like the Arduino Uno. The Mega2560 is required for direct mounting of the RAMPS 1.4 adapter. The RAMPS 1.4 shield is specifically designed to fit over an Arduino Mega2560 unit and serve as the interface between the Arduino and the 3D printer hardware, such as the motors, sensors, and screens. The RAMPS 1.4 shield features connections for more hardware than required for the dip coater, but comes with the ease of compatibility, and capability for future expansion. With this machine, two bipolar 4-wire stepper motors with 1.8^{o} stepping angles were used. The motor for driving the linear rail was wired to the X-axis motor output on the RAMPS 1.4 board, while the rod rotating motor was wired to the Y-axis output. A4988 Polou stepper motor drivers are used (1 for each motor), each with 3 jumpers to enable the most accurate $1/16^{th}$ micro stepping. The motors are powered through a 12 V power connection wired directly to the 5 A power inputs on the RAMPS 1.4 board. The Arduino is powered separately through the USB 5 V connection to a PC or through a 5 V A/C to USB wall adapter. The full graphic smart controller features an LCD screen, push-button rotary encoder, and SD card reader grouped as one unit, and plug into the entirety of the AUX-3 and AUX-4 banks of pins on the RAMPS 1.4. Upper and lower limit end stops (MakerBot mechanical microswitch type) are fitted to prevent the stage crashing into the bottom of the rail or the gear system mounts, and also for setting of the zero-position of the x-axis. While risk of crashing is reduced by setting hard limits within the firmware, such a method only works

when operating the machine in absolute coordinate mode. Use of relative coordinates can be useful, especially for the y-axis rod rotation of long dip coating cycles, and so the end stops would serve as emergency stops if these limits were breached. The end stops are connected to their appropriate pins in bank S annotated on the RAMPS 1.4 board. The lighting circuit is controlled by the Arduino through a relay (SONGLE SLA-05VDC-SLC 30A 240VAC), which has a 5 V control side with low (2-4 mA) trigger current suitable for use with an Arduino. The load side is suitable for the mains voltage required for the ballast and bulbs. The control side of the relay has 3 inputs, a DC+, DC- and IN. The DC+ is wired to one of the 5 V VCC outputs adjacent to the D2 diode on the RAMPS 1.4. The DC- is connected to the ground (GND) pin on the AUX-2 bank. The IN or input signal is wired to pin 44 on the AUX-2 bank. A pinout diagram of the RAMPS 1.4 board detailing all the utilised connections is shown in Figure 7.7.

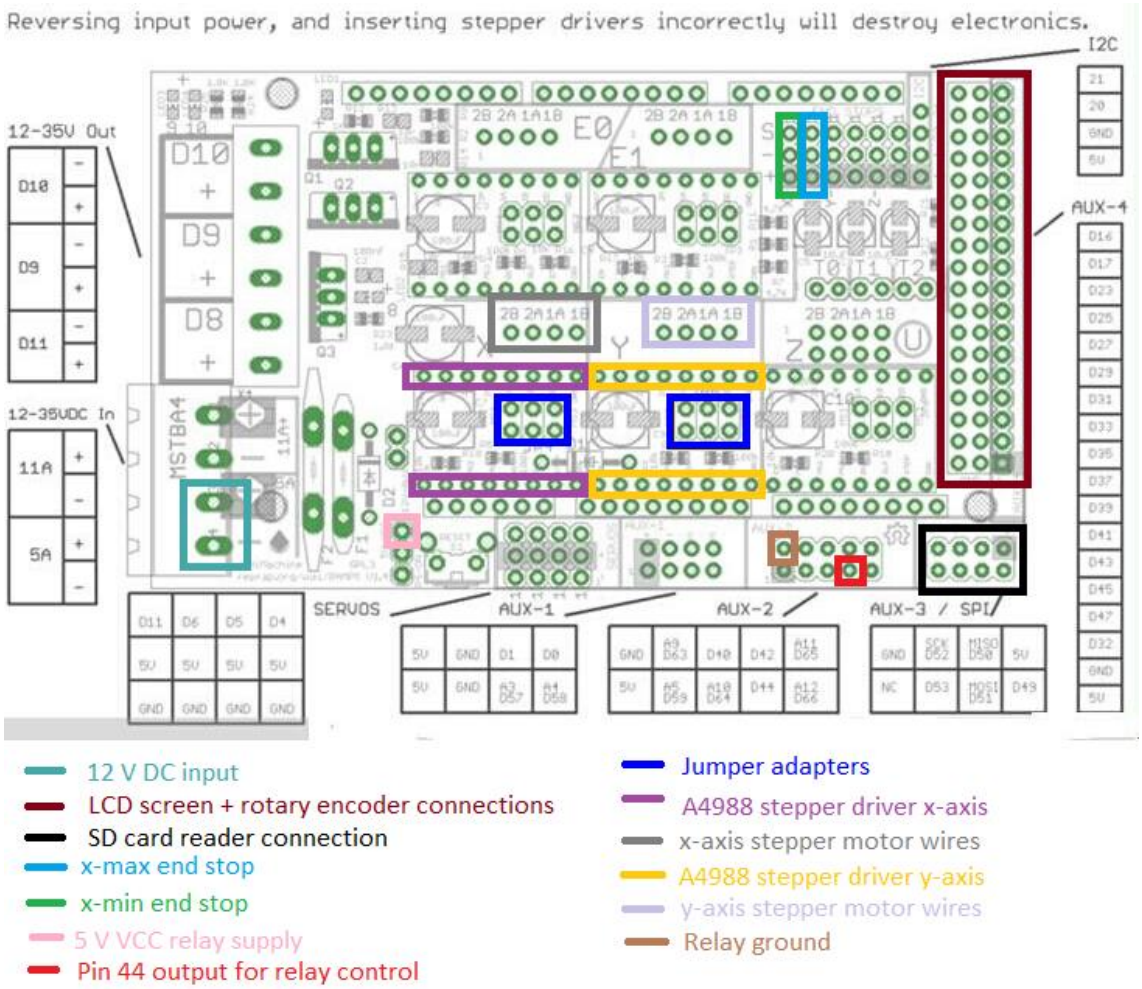

Figure 7.7:- Pinout diagram of RAMPS 1.4 board. Colour legend details what is associated with each pin(s) by matching to colour of box on the image. This is a modified pinout diagram of the original found at reprap.og/wiki/RAMPS1.4. The RAMPS 1.4 board is open source hardware under the General Public License v3.0.

When the input pin signal is low the relay remains open with the lights off. When the input pin signal is high the relay closes allowing current to flow to the ballast, turning the

lights on. Mains power to the relay is taken from a standard 3-pin UK plug to an IEC plug isolated but mounted on the main frame. At the output side of the mounted IEC plug, the neutral and ground wires travel up to a second IEC plug, while the live wire goes via the relay. The live input is connected to the COM relay terminal, and the output wire connected to the NO (normally open) terminal, which is then routed up to the second IEC plug. The live, neutral, and ground wires on the other side of the second IEC plug are connected directly to the appropriate terminals on the ballast. Use of two sets of IEC plugs makes the main body tidier by allowing complete disconnection of the lighting circuitry when not required. The ballast and bulbs are then powered by 230 V A/C when the relay input signal is high. This is the safest wiring option, keeping the live side as short as possible before interruption by the relay. On the output side of the ballast, the wiring to the bulbs follows the directed scheme for 4 bulbs as shown in Figure 7.8 below.

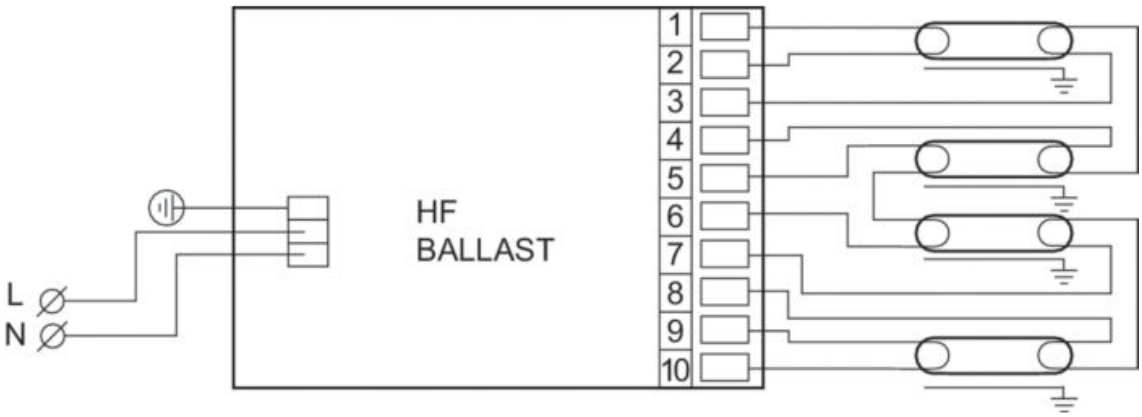

Figure 7.8:- Ballast wiring diagram for control of 4 bulbs. Used as shown from the manufacturers installation guidelines:https://www.lighting.philips.co.uk/prof/electronic-control-gear/fluorescent/fluorescent-fixed-output-gear/hf-performer-iii-for-tl-d-lamps/913713031466_EU/product#downloads.

7.3.2 Firmware

The Arduino runs on the highly popular open source Marlin 3D printer firmware. Marlin is a community driven printer driver specifically designed for use with Arduino Mega2560s and RAMPS 1.4 hardware (used here), but can be edited to accommodate other combinations of hardware if necessary. The main motivation for using Marlin is that it offers easy integration of an LCD screen and controls, alongside the ability to read g-code scripts directly from an SD card. The latest Marlin firmware can be found at https://marlinfw.org/meta/download/. The Marlin firmware code is extensive and therefore only the edited parts and changes will be discussed here.

Firstly, the Arduino integrated development environment (IDE) must be configured to communicate with the Arduino Mega 2560. This can be selected via Tools>Board>Arduino Mega or Mega 2560. Connect the Arduino via USB to the PC and

ensure the correct COM port is chosen. Most of the other changes are within the "configuration.h" sketch. The communication baudrate is set to the fastest speed of 250000 by #define BAUDRATE 250000. The RAMPS board version must be defined. The board used in this project should be defined as #define MOTHERBOARD BOARD_RAMPS_14_EFB. For homing the axis, due to only the x-axis having end stops those listed for the Y and Z axis should be commented out. The x-axis motor was determined to have 800 steps/mm, while the y-axis motor was 500 steps/mm, and were defined through the #define DEFAULT_AXIS_STEPS_PER_UNIT line. The max feedrates of the motors were also defined separately with the x-axis being capped at 10 mm/min and the y-axis at 1 mm/s (which is equivalent to approximately 9 rpm). As an extra safety feature for if the x-axis max end stop failed in absolute coordinate mode the max x-axis position was defined as 235 mm, which is just before the stage collides with the spur gear sandwich mounts.

Typically, printers are used in absolute coordinate mode and therefore typically use a single end stop per axis to home against during start-up, after which the end stop stops being polled by the CPU. This is also generally desirable as polling the end stop(s) constantly utilises CPU cycles and can cause printers to slow down. The dip coater is only operating a maximum of two motors and will therefore be operating at a relatively lower CPU load in comparison to an FDM printer running 3+ motors, extruders, and heated nozzles or beds all at once. Additionally, due to the potential use of relative coordinates preventing damage to motors or other parts is highly important. Enabling ENDSTOPS_ALWAYS_ON_DEFAULT within the 'Configuration_adv.h' sketch allows constant polling of the end stops, which will cut motor movement and end the script if triggered.

For calibration verification, or troubleshooting the Arduino was connected via USB to a PC running Pronterface, which is a graphical user interface (GUI) host used to manage 3D printers. Within Pronterface, commands to the motors can be given through the GUI or through a text window in which g-code commands can be given instead.

7.3.3 G-code commands

G-code exists in various flavours, with some firmware being able to interpret more G-code commands than others or interpret the same command in different ways. The extensive list of G-code commands compatible with Marlin is listed on the reprap wiki (https://reprap.org/wiki/G-code). The commands commonly utilised within this project are listed in Table 7.1.

Command	Format (example)	Purpose
G1	G1 Xnnn Ynnn (G1 X-120 Y40)	Linear move
G28	G28 n (G28 X)	Homes the listed axis. The example homes X axis only.
G90	G90	Set to absolute coordinates
G91	G91	Set to relative coordinates
M42	M42 Pnnn Snnn (M42 P1 S255)	Switches a general purpose I/O pin to a set value.
M400	M400	Wait for current move to finish

Table 7.1:- Table of key G-code commands used during typical dip coater operation. n represents an integer, a minimum of 1 integer must be used for such commands to function. Valid integers for the S component of the M42 command are either 0 or 255, where 0 is off(low), and 255 is on (high).

The rotation of the rods and movement on the resin vat attached to the stage is primarily dictated by the G1 command line. The speed upon which the axis move is defined by the feedrate set within the firmware. The feedrate can be overridden by introducing an Fnnnn parameter as part of the G1 command line (e.g. G1 X10 F10), providing it is within the min/max range defined within the firmware. Movement commands are interpreted by the Arduino on a line by line basis, but certain M commands including M42, are not synchronised with the movement commands and are executed immediately as they are read. The lighting circuit relay is operated by the M42 command raising the IN pin to high, which triggers the relay coil closing the AC circuit. The command used to turn on the circuit is M42 P44 S255, and off is M42 P44 S0. Due to M42 commands being executed immediately after being read, regardless of current and planned move orders listed prior to the M42 line, use of M400 before a M42 command is required. M400 waits for the movement command immediately above to be completed fully prior to proceeding, allowing control of the lights at the desired time.

7.4 Typical usage

7.4.1 File preparation

A text editor program such as notepad should be used to generate the script that the dip coater should follow. The file must be saved as a compatible g-code type file, with file extension suffixes such as .g, .gco or .gcode. The file is then loaded on to a SD card that supports SPI (serial peripheral interface) protocol and of a capacity no larger than 2 GB

(limit for a 16-bit computer), using FAT 16 formatting. Keep filenames short (< 8 characters) and ensure no more than 10 layers depth of sub-folders are present.

7.4.2 Example g-code script

A 3-dip cycle for a photo-curable resin is shown in Figure 7.9.

```
;Initial Test File for SD card automated dip-coat-curing
;No feedrate commands therefore Y axis rotating at ~9rpm during Y moves, x axis adjusts to suit
G28 X ;           Home X axis only
G1 X2 ;           move x axis 2 mm upwards just to lift it off endstop
G91 ;             switch to Relative Coordinate System
G1 X230 Y25.52 ;  1 - initial dip move, rod rotating during x move
G1 Y25.52 ;       1 - Dipping phase for circa 4 rotations
G1 X-230 Y63.8 ;  1 - Withdrawal, X speed slower than previous dip, slowed down by increasing y distance
M400 ;            1 - Forces wait for complete withdrawal prior to turning on relay
M42 P44 S255 ;    1 - Engages relay coil to activate lights. Digital Pin 44, constant digital signal given at Signal "S255"
G1 Y58 ;          1 - Curing stage, rotates Y while lights are on.
M400              1 - Forces wait for full previous Y movement before disengaging relay coil
M42 P44 S0 ;      1 - Turns off lights, Signal to Pin 44 is zero at "S0"
G1 X230 Y25.52 ;  2 - same as above, repeated. Dip 2
G1 Y25.52
G1 X-230 Y63.8
M400
M42 P44 S255
G1 Y58
M400
M42 P44 S0 ;      3 - same as above, repeated. Dip 3
G1 X230 Y25.52
G1 Y25.52
G1 X-230 Y63.8
M400
M42 P44 S255 ;    "Copy" ended: Final cure, give longer time for "post-cure" in next Y command
G1 Y290 ;         At this feedrate, 290 is approximately a 5 min cure cycle at ~9 rpm.
M400
M42 P44 S0 ;      Relay disengage, REMEMBER TO TURN OFF AT PLUG BEFORE TOUCHING!
G1 X2 ;           Raises stage off of the x-axis min end stop
G1 X2 ;           Repeated twice as this ver. of Marlin appears to ghost the last command.
```

Figure 7.9:- G-code file for the dip coat curing of a photo-curable resin. For more dips, the lines between the red lines can be copied multiple times to achieve however many dips desired. All commands used as listed in Table 7.1.

The first 3 lines prepare the dip coater to start the sequence, homing the x-axis and switching to relative coordinates after being zeroed. For a single complete dip coat cycle as described in Chapter 6, 8 lines of code are required, indicated in Figure 7.9 between the red lines. These lines of code involve keeping the rods constantly rotating while raising the stage/falcon tubes to dip the rods. Due to the firmware of the system being setup to control a 3-axis 3D space, where motors work in synergy to move a machine tool, or print head, here the x and y motors also remain linked. Therefore, the motors work together to trace a virtual hypotenuse of a length defined by Pythagorean theorem $c = \sqrt{(x^2 + y^2)}$, where c is the length of the virtual hypotenuse, and x and y are the distances in the g-code for the requested x and y motor movements. Due to the difference in max feedrates, providing the x distance is no more than 10x greater than the y distance, the movement will be limited by the slower y-axis maximum feedrate resulting in the rods spinning at a constant speed while the x-axis feedrate adjusts to suit. This is exploited in the code above to maintain a constant rotation of the rods of the max y-motor feedrate, equating to approximately 9 rpm. Alternatively, if the x distance is greater than 10x of

the y distance, then the x-motor operates at maximum feedrate while the y-motor will turn slower to accommodate, resulting in a variable rod rotation speed.

The rods stay immersed in the falcon tubes for approximately 4 full rotations before the tube are lowered, withdrawing the rods slowly from the polymer solution. An M400 command is issued to ensure the dip coater waits for the tubes to be fully lowered prior to activating the lights in the next line. While the lights are active, the rods are kept turning to cure them evenly all round. Another M400 command is issued to keep the coater waiting for the cure stage to be complete, after which the lights are deactivated. The cycle described above is then repeated a number of times to make the coating on the rod the desired thickness. The final dip cycle is similar but features a longer curing stage to post cure the rods *in situ*.

7.4.3 Dip coater setup

Mount the number of rods desired and fill the associated number of 15 mL falcon tubes with resin and place them within the holder. Plug in the 5V power for the Arduino and the 12V power for the motors. If using the lighting gantry, position it over the dip coater and plug the IEC connectors first, prior to turning on at the mains.

7.4.4 Start the print

Insert the SD card into the card reader on the back of the LCD screen. Upon insertion of the card, the screen should read “SD card inserted“. Use the rotary encoder to access the menu: print from SD card > select file name. Upon pushing the rotary encoder in while having the file name selected will initiate the dip coating cycle. The script will be performed until completion or an error occurs.

7.5 Proof of concept

While the author and builder of this machine has not been able to use the machine extensively yet, the new dip coater has been heavily used by the group postdoc and an undergraduate student. Both have been successful in producing photo-cured polymer tube networks from resins containing lactide-caprolactone (LA-CL) and trimethylene carbonate-caprolactone (TMC-CL) macromers. An image of the TMC-CL tubes produced using the dip coater by the undergraduate student are shown in Figure 7.10.

Figure 7.10:- TMC-CL tubes produced from a 5 dip cure cycle using the new dip coater. Tubes have been post-cured, extracted via Soxhlet apparatus and dried, as is reported in previous methods sections.

7.5.1 Dip coating of LA-CL photo-curable resins

Here I will present the work of Esmat Jalalvandi, who used the new dip coater to produce tubes of both TMC-CL and LA-CL networks, as a proof of concept/functionality of the new dip coater.

A series of TMC-CL tubes were produced using a 5 dip and cure cycle, and 5 tubes were selected at random. The outer diameters and wall thicknesses were measured at three positions along the tube, near the bottom (resin vat side), middle and top. The calculated averages and standard deviations of both outer diameter and wall thickness are presented in Figure 7.11 and detailed in Table 7.2

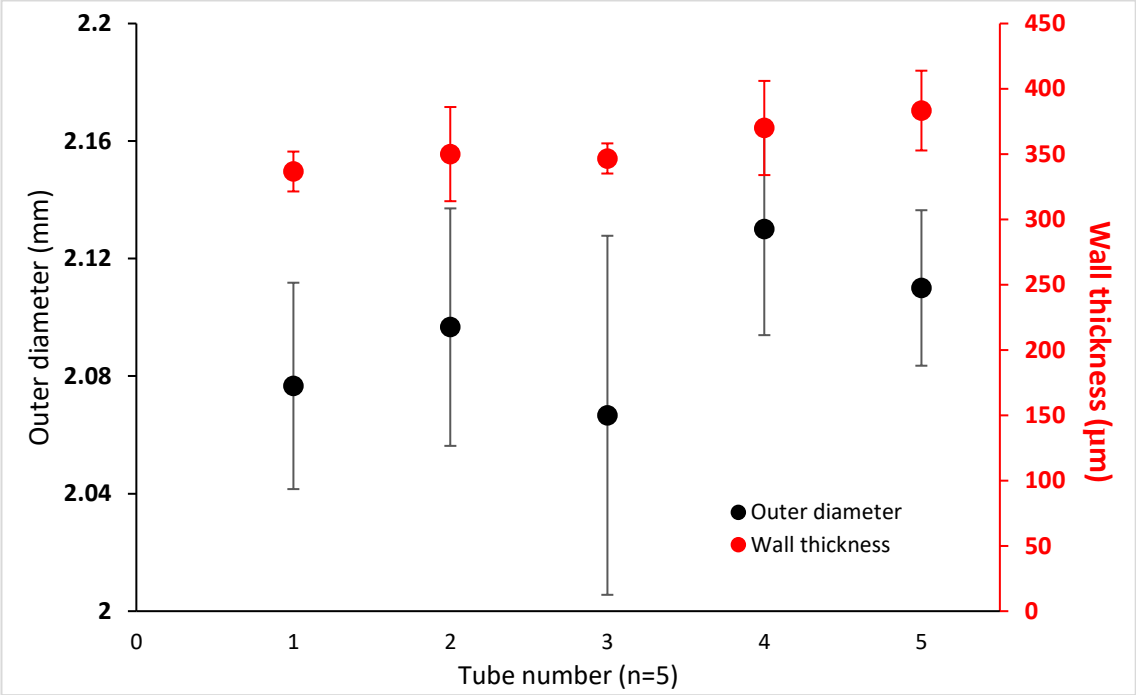

Figure 7.11:- TMC-CL tube average outer diameters and wall thicknesses. Error bars represent standard deviations. n=3

		Outer diameter (mm)	Wall thickness (µm)
Tube number	1	2.07 ± 0.04	336.7 ± 15.3
	2	2.09 ± 0.04	350.0 ± 36.1
	3	2.06 ± 0.07	346.7 ± 11.5
	4	2.13 ± 0.04	370.0 ± 36.1
	5	2.11 ± 0.03	383.3 ± 30.5

Table 7.2:- The average ± standard deviation of the TMC-CL tube outer diameters and wall thicknesses, n=3.

The tubes produced show consistent outer diameters and wall thicknesses with overall averages of 2.10 ± 0.04 mm and 357.3 ± 25.9 µm, respectively. While outer diameter measurements have not been made before, the variance in wall thickness is comparable to the xPCL tubes produced in Chapter 6 (335 ± 29 µm), and to tubes from Melchels *et al* [21] (171 ± 21 µm). Here the dip cycle takes approximately the same time to complete as the original dip coater, but dips 10 rods instead of 1, making it vastly more efficient. Similarly to what was discussed in Chapter 6, the TMC-CL tubes above were produced from the author's firmware settings and thus the consistency of the outer diameters and wall thicknesses may have the potential to be improved further following some optimisation work on that specific resin formulation. TMC-CL tubes that were produced using this dip coater were sealed and tested using mechanical and osmotic means. The devices were able to sustain and build pressure prior to burst via mechanical means and

demonstrated mass gain through the osmotic uptake of water during osmotic studies, which demonstrate that the tubes produced could be used to construct viable devices.

7.6 Closing remarks

7.6.1 Future improvements

While the dip coater works well in its current form, limiting the users' exposure to the UV-A light is the first priority for improvement. Concave reflective shrouds will be fitted to direct all the light down to the rods, combined with spraying the acrylic sheet with a thick layer of matt black paint to eliminate light penetration and prevent reflections.

It has been noticed that some incident light is curing resin near the open end of the falcon tubes. As a temporary fix a rectangular piece of cardboard was used to block direct entry of light into black/amber falcon tubes. The cardboard was mounted to the top of the falcon tube holder and acts similarly to the bill of a baseball cap. It's height and length are enough to provide a meaningful effect without touching the rods during dipping/retraction or blocking light from the coated resin during the curing phase. For future use a more permanent removable shroud that will provide a greater resin-protecting effect while not interfering with falcon tube loading/positioning, will be designed and 3D printed. Lastly, editing what is displayed on the screen prior to and during the print to be more relevant to the dip coater actions specifically rather than keeping the generic FDM printer display functionality would offer a more professional quality of life improvement for users. While this change does not affect safety or critical functionality, much of what is shown on screen is irrelevant such as FDM nozzle temperature, fan status, heated bed temperature, which all aren't in use on the dip coater. Ideally the initial home screen would just display the state of readiness of the dip coater, while during the cycle a countdown timer to completion as well as an indicator of what part of the cycle it is on would be useful to the user. Due to the linked nature of the motors, creating a g-code script that results in the movements the user wants can be hard to understand depending on their background. A MATLAB script could be made to assist with this, where the user inputs the desired outcomes, for example the rotation speed, vat raising/withdrawal speed, hold/exposure times, and number of dips. The script would then determine the required X and Y coordinates and feedrates to correspond to the real-world numbers desired and output a complete g-code file read for use. An alternative, but substantially more involved option is to completely rewrite the firmware so that the motors work independently. If such a route was taken it would be worthwhile to generate an equivalent to the MATLAB script

described above within the firmware, and have a GUI using the full graphic smart controller.

7.6.2 Conclusion

An improved dip coater with multi-rod dipping capability and autonomous UV light control was designed and built. The new dip coater was able to produce viable tubular parts with wall thickness variations similar to that of previous dip coating apparatus, but with up to 10x greater efficiency through the capacity to dip up to 10 rods. Additionally, the integrated UV light circuit will enable more consistent exposure times during the curing stages than the previous manually controlled systems. The Arduino-based system allows adjustments of essentially every function of the dip coater by any user, while use of g-code provides a simple format for customisation of the dip cycle. Further improvements have been highlighted and will be implemented prior to future work.

Chapter 8– Osmotic burst release study

In this Chapter, we describe *in-vitro* osmotic burst studies of tubular capsules manufactured from the techniques used and discussed in Chapter 6. The following work was conducted at the Institute of Health and Biomedical Innovation (IHBI) at Queensland University of Technology, Brisbane, Australia.

8.1 Introduction

We conducted *in-vitro* burst studies with the aim of determining device burst profiles in terms of the delay to burst, reliability, reproducibility, and the rate-of-release of payload after burst, that result from adjustment of particular critical variables, such as material type and osmogent concentration, as a prerequisite to future *in-vivo* device testing. Devices were immersed in PBS and incubated over 72 days, with periodic visual checking for dye release, sampling of the external PBS solution, and weighing.

This study was primarily setup to compare the difference in burst release delay between devices made from solvent-evaporation-formed 70,000 g/mol PCL (PCL) and dip-coat-UV-cured bimodal PCL resin (xPCL), as well as comparing the differences between osmogent loading concentrations and payload type. Experimental groups were firstly divided by material type (PCL, xPCL), then by payload type (dye, tetanus toxoid), and finally further sub-divided by osmogent concentration (3, 3.5, and 4 molar), as shown in Figure 8.1.

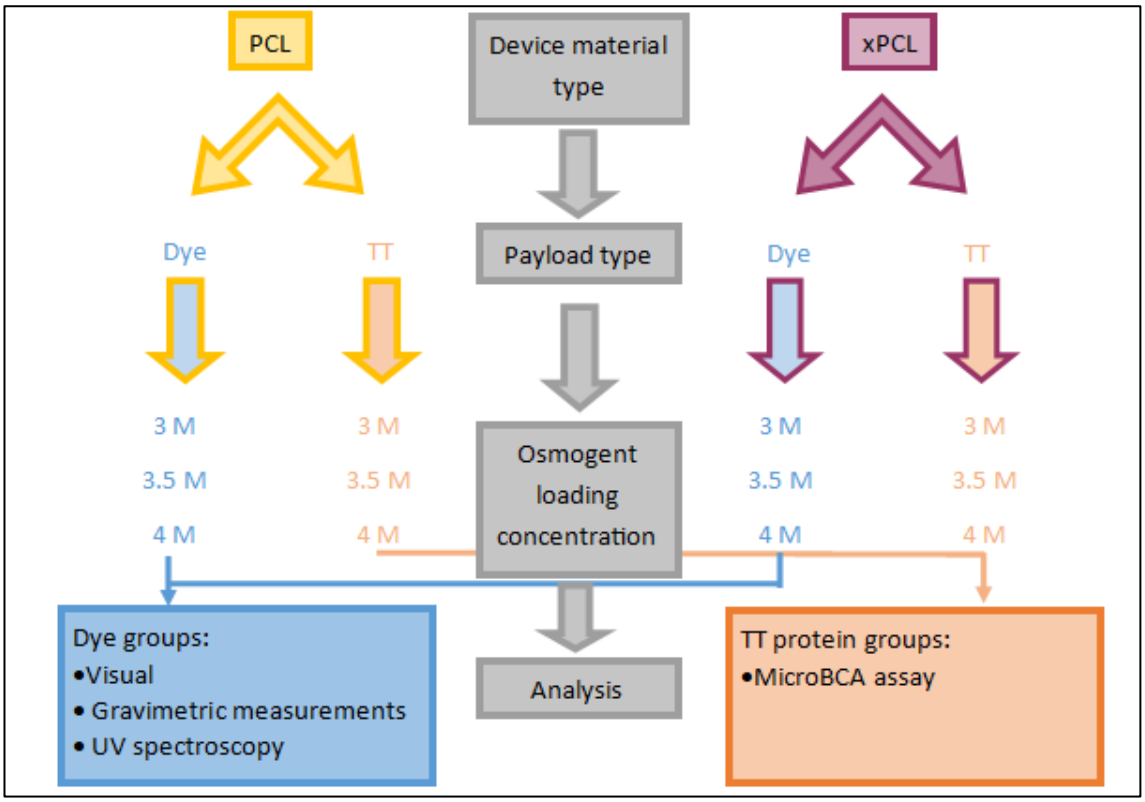

Figure 8.1:- Schematic displaying the breakdown of the experimental groups and subsets for the osmotic burst experiment. "TT" is shorthand for tetanus toxoid.

Detection and analysis of the rate of payload release was performed based on the payload type. The external PBS solutions that devices from both payload groups were immersed in were regularly sampled. Solution taken from the dye group and toxoid group devices were analysed using UV spectrophotometry and micro-bicinchoninic acid (BCA) assay, respectively. The BCA assay is a well-established method for protein quantification and has largely replaced other quantitative colourimetric methods, such as the modified Lowry, or Coomassie assays [237]. The micro-BCA assay has been optimised for dilute protein samples and features an improved limit of detection (2 µg/mL), which will enable early detection of device protein payload leaks or bursts. Quantification of dye release using UV spectroscopy is based on the principles of the Beer-Lambert law, shown in Equation 8-1.

$$A = \varepsilon l c \qquad \text{Equation 8-1}$$

Where A is the absorbance, ε is the molar absorptivity of the absorbing species, l is the path length of the light through the absorbing solution, and c is the concentration of the solution [238]. When samples are processed in the same manner (the same dye is used, within the same buffer solution, with the same path length) variance in dye concentration is the only cause for differences in absorbance. The dye-containing devices were also gravimetrically monitored throughout the experiment, with its main objective to

determine the profile and rate of water uptake during the initial stages following immersion. Evidence of payload leakage or device burst of the dye-containing devices could also be visually identified. Due to a series of problem such as glucose interference with the MicroBCA assay, the tetanus toxoid work is presented within Appendix A.

It is hypothesised that the xPCL devices will release more payload at the point of burst than their PCL counterparts. The flexibility of the xPCL material will enable a greater extent of swelling under loading, and its cross-linked nature will provide a greater degree of shape recovery than the non-crosslinked PCL material. Therefore, at the point of burst the swollen xPCL devices should return, at least partially, to their original shape, ejecting payload in the process. It is expected that the quantity of payload ejected from the xPCL devices will greatly exceed what is released at burst from the PCL devices. This hypothesis will be investigated by assessing the payload ejection at point of burst, which can be confirmed i) visually, ii) from detection and quantification of a loss of mass, and iii) by quantification of the payload release. Additionally, this hypothesis would be further supported by evidence of a visible increase in xPCL tube swelling during water uptake, combined with a larger burst site than shown from the PCL devices.

We hypothesise that tubes constructed out of the more flexible xPCL material will feature a longer delay to burst over their more rigid/tough PCL counterpart, due to their indicated ability to swell and accommodate a larger volume increase (from mechanical burst testing) prior to reaching the burst pressure. This hypothesis will be evaluated through the comparison of the delay to burst times between devices constructed from each type of material.

We hypothesise that the permeability of the xPCL network will be greater than that of PCL due to possessing a greater volume fraction of amorphous regions for water uptake to occur. However, we expect this to be partly counter-acted by the xPCL tubes featuring thicker walls over the PCL tubes. As a result, this factor may cause xPCL tubes of comparable osmolarity to uptake water faster than their PCL equivalents, and perhaps hinder burst delay extension gained from other material properties discussed below. This hypothesis will be tested through comparison of the water uptake rates during the initial stage after immersion.

It is hypothesised that the time to burst of a device, regardless of material type, can be tuned by adjustment of the initial osmogent loading concentration. Devices with a higher initial loading concentration of osmogent will feature a greater rate of water uptake as a

direct result of a greater osmotic driving force, and will therefore burst quicker than devices with lower osmogent loading concentrations. This hypothesis will be assessed by comparison of the water uptake gradients from first phase of mass monitoring data, and the comparison of visual, mass related, and payload detection indicators of burst.

8.2 Materials and methods

8.2.1 Material compositions and device production

The tubular part of the devices were produced using the dip coating methodologies presented and discussed in Chapter 6. PCL tubes were formed from Purasorb PC12 with a claimed M_n of 70,000 g/mol, using the solvent evaporation dip coating technique. Cross-linked xPCL tubes were produced using the UV curing dip coating technique, utilising a resin composed of 30 wt% PCL-2MA, 15 wt% PCL-3MA, 55 wt% BnOH, and 2 wt%* of TPO (*where the wt% of TPO is considering the total mass of the formerly mentioned components). Details of device manufacture and preparation can be found in Chapter 6.

8.2.2 Device loading

Tubes for osmotic release experiments were sealed on one end using the methods detailed in Chapter 6 6.3.4 and 6.3.5. For the xPCL tubes, only the xPCL10k0.9k resin sealing method was used. Stock solutions of 3, 3.5 and 4 M glucose, and either food dye or tetanus toxoid (TT) material (depending on the required payload type) were prepared. Concentration of each payload was kept equal between solutions of differing osmolality. The target TT protein concentration for the solutions was 8000 µg/mL. The raw undiluted food dye was assigned to be 2 arbitrary concentration units (AU), which was diluted down to the target concentration of 1 AU to form the glucose/dye solutions. Devices were loaded with 70 µl of the appropriate glucose/payload stock solution using a syringe fitted with a 22-gauge blunt needle. Due to capillary forces, care had to be taken to position the needle tip at the bottom of the tube to prevent trapping an air bubble at the base of the tube. After filling, the capping process was repeated on the remaining open end.

8.2.3 Device incubation and immersion

Filled and sealed devices were submerged within 15 mL falcon tubes containing 10 mL of PBS. The tubes were kept within an incubator set at 37 ^{o}C for the total duration of the experiment, and were only removed briefly for analysis.

8.2.4 Device evaluation and data acquisition

Device behaviour was monitored over 72 days by gravimetric (dye only), UV spectrometry (dye only), and microBCA assay (TT only) measurements. All measurements were taken every 2-3 days, and devices were inspected visually each time for signs of burst (dye groups only). Weight measurements were taken on an analytical balance (d = 0.0001 g). A wavelength sweep was performed to find the absorbance maximum of the food dye, which was determined to be at 630 nm. All future measurements of dye concentration were performed at 630 nm. At each time point, the entire volume of PBS that the device was immersed in was removed and replaced with fresh PBS. A quartz cuvette was filled with a sample of the removed solution. Each time point for every dye-containing device was performed in triplicate. Blank PBS absorbance readings were deducted from experimental sample absorbance values before being averaged for data analysis. The microBCA assay kit was purchased from ThermoFisher Australia, and was used as per kit instructions for the microplate format. Similarly to the dye groups, at each time point for analysis via microBCA the entire PBS solution the device was immersed in was taken and replaced with fresh PBS. 150 µL of the taken sample was then used per well of the microBCA assay for each device, with each device's solution being analysed in triplicate. Sample absorbance readings were blank-corrected prior to being averaged for data analysis.

8.3 Results

8.3.1 Overall gravimetric and UV profiles

Persistent logging of mass and UV absorbance data enabled construction of charts that depict the mass and dye profiles over the course of the entire experiment. Device mass profiles from both material groups appear split into 3 phases; an initial uptake phase, a post-burst stabilisation phase, and a final steady-state release phase. The transition between the uptake and post-burst phases occurs at the point in time upon which the device bursts. An annotated example highlighting these 4 important aspects in the mass and dye profiles of a xPCL 3.5 M device, is shown in Figure 8.2.

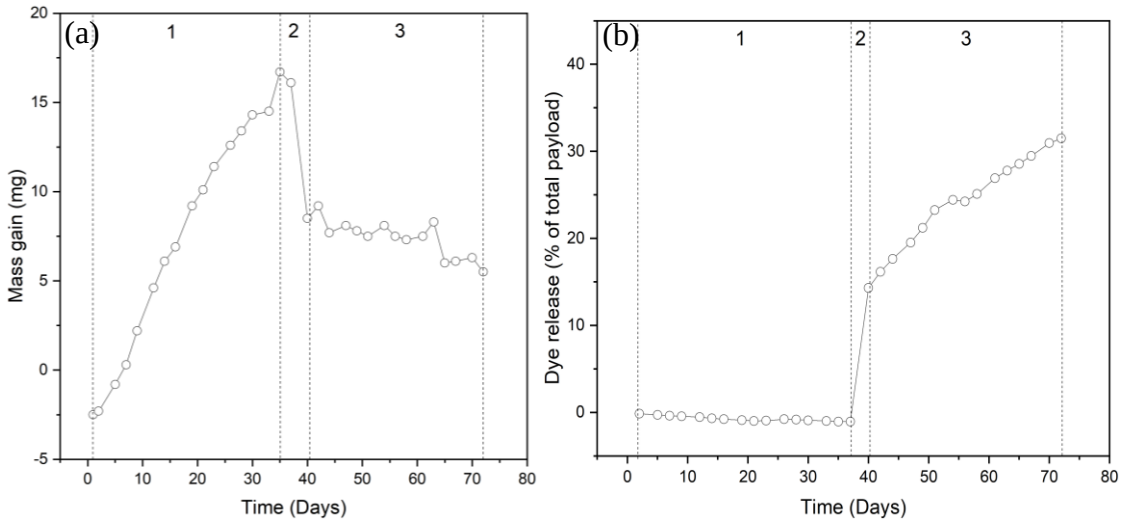

Figure 8.2:- Annotated mass (a) and dye (b) profiles of a xPCL 3.5 M device. Phases are shown as 1) water-uptake, 2) post-burst stabilisation, and 3) steady-state release. The point of burst is depicted by the dashed line that separates phase 1 and 2.

In this example, during the initial water uptake phase (1) a steady gain in mass can be noticed combined with the dye absorbance signal maintained at baseline. After the moment of burst, and into the post-burst phase (2) the device begins to lose mass, while the dye absorbance signal becomes positive and sharply increases. In the final steady-state release phase (3) the device releases dye and loses mass at a more constant rate.

Further insights into different mass and dye behaviours resulting from devices produced from the different materials, and different osmogent loading concentrations, can be seen from the representative mass and dye profiles as shown in Figure 8.3.

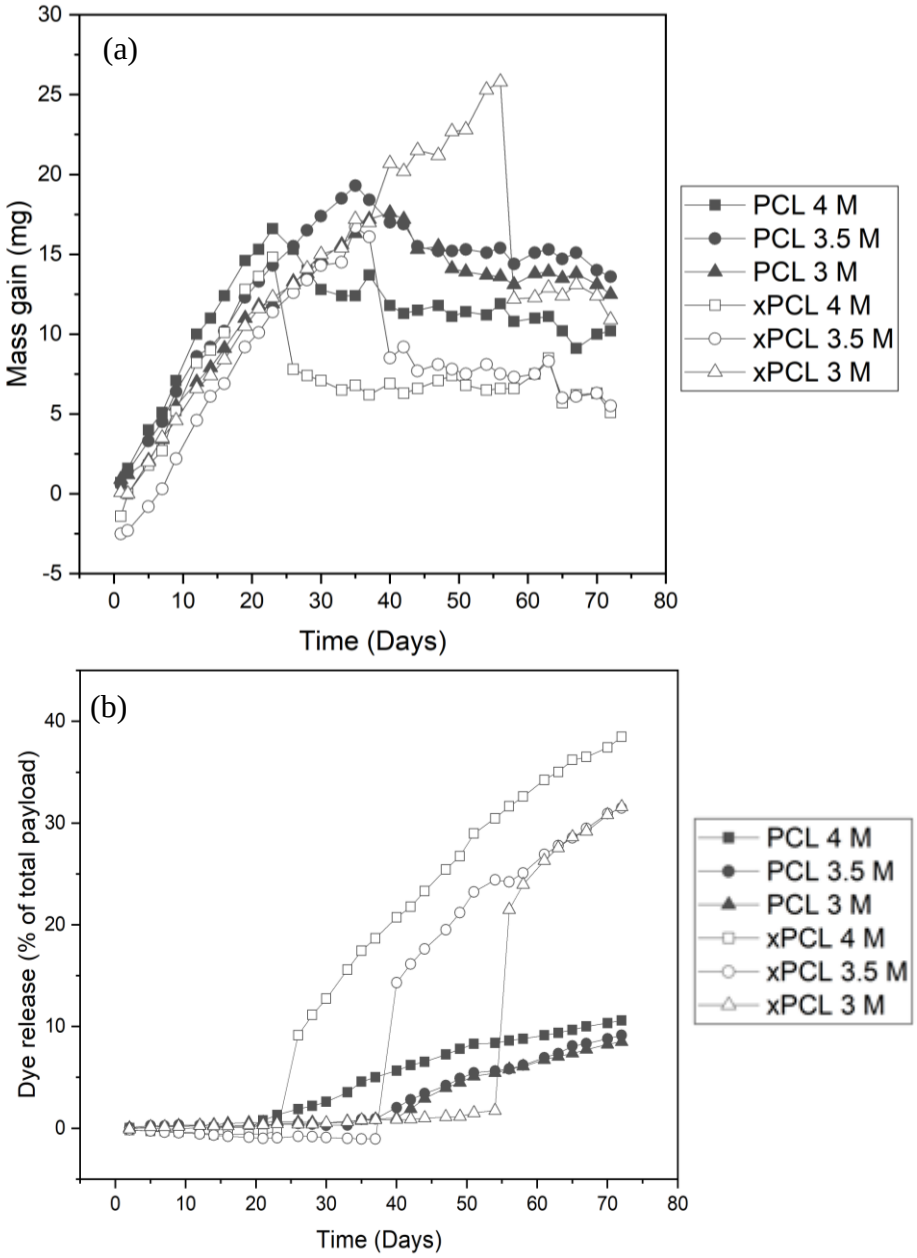

Figure 8.3:- Mass gain (a) and dye release (b) of representative devices from each experimental group.

Devices of all groups display a gradual gain in mass over the initial water uptake period after immersion. After reaching a peak mass gain, a loss of mass occurs, signifying burst of the device. The xPCL devices feature a steep loss in mass over a short period before stabilising, and transitioning into a more gradual mass decline. PCL tubes typically lose a lesser extent of mass over a shorter period before also developing into a more gradual mass loss profile. Dye release is maintained around baseline prior to devices bursting, with xPCL group devices showing a step-like increase in dye release upon burst followed by a gradual release profile, while the PCL devices only demonstrate a gradual release of dye after burst. The following sub-sections look more closely at each phase in turn.

8.3.2 The water uptake phase

Here, the data acquired from the gravimetric measurements during the water uptake phase are presented. As displayed in Figure 8.2, no payload release is taking occurring during this uptake stage for non-defective devices. The water uptake rate was determined from the gradient of the mass gain over the first 14 days after immersion for each tube within a group, where linearity was most clearly defined (mean R^2 = 0.986 ± 0.013, min R^2 = 0.948). The peak mass gain was determined from the highest mass value returned during the gravimetric measurements throughout the experiment, which corresponded with being the last data point taken prior to burst and followed by subsequent evidence of mass loss. The resulting data is displayed in Table 8.1 and Figure 8.4.

Device material	Osmolarity (Molar)	Water uptake rate (µg/day)	Peak mass (mg)
PCL	3	507.0 ± 44.7	15.5 ± 2.8
	3.5	692.1 ± 3.9	16.3 ± 3.4
	4	829.9 ± 33.8	15.3 ± 2.5
xPCL	3	589.7 ± 32.2	11.6 ± 10.4
	3.5	762.1 ± 58.9	13.8 ± 3.1
	4	893.2 ± 92.5	12.9 ± 1.7

Table 8.1:- Average water uptake rate and peak mass prior to burst of all device groups.

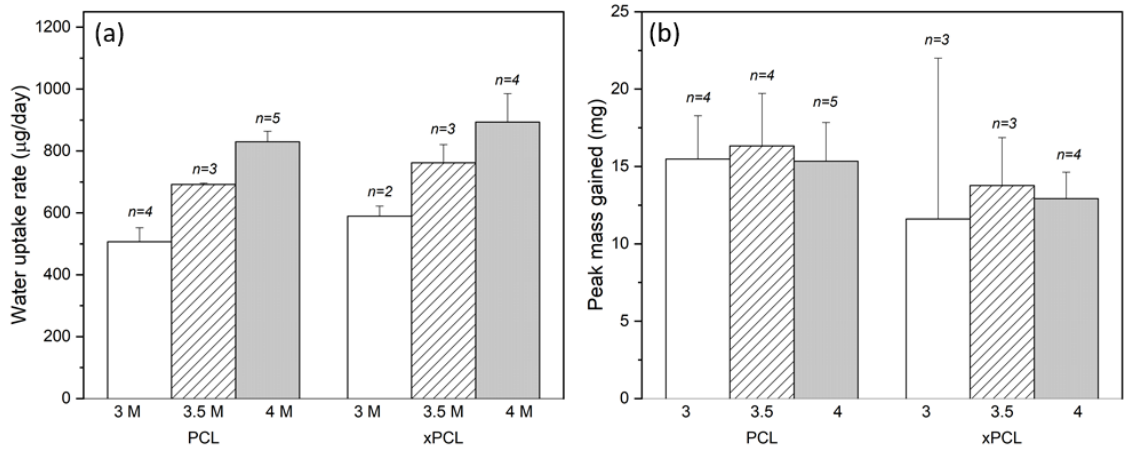

Figure 8.4:- Comparisons of the average water uptake rates (a) and peak masses (b) of devices from the three osmolarity groups and each material type. Error bar indicates standard deviation. Population values are indicated above each bar.

The water uptake rate increases with initial osmogent loading concentration, and appears to be similar between device material groups with the same osmolarity. The average peak mass is relatively similar and typically within standard deviation across all groups.

8.3.3 The delay to burst

The burst delay time of the devices was determined by performing visual, gravimetric, and UV detection methodologies on each device. The PCL group contained 5 individual devices for each osmogent loading concentration, while the 4 and 3.5 M xPCL group possessed 4 devices and the 3 M xPCL group featuring 3 devices. Figure 8.5 displays the burst times of the devices as determined from each type of detection methodology.

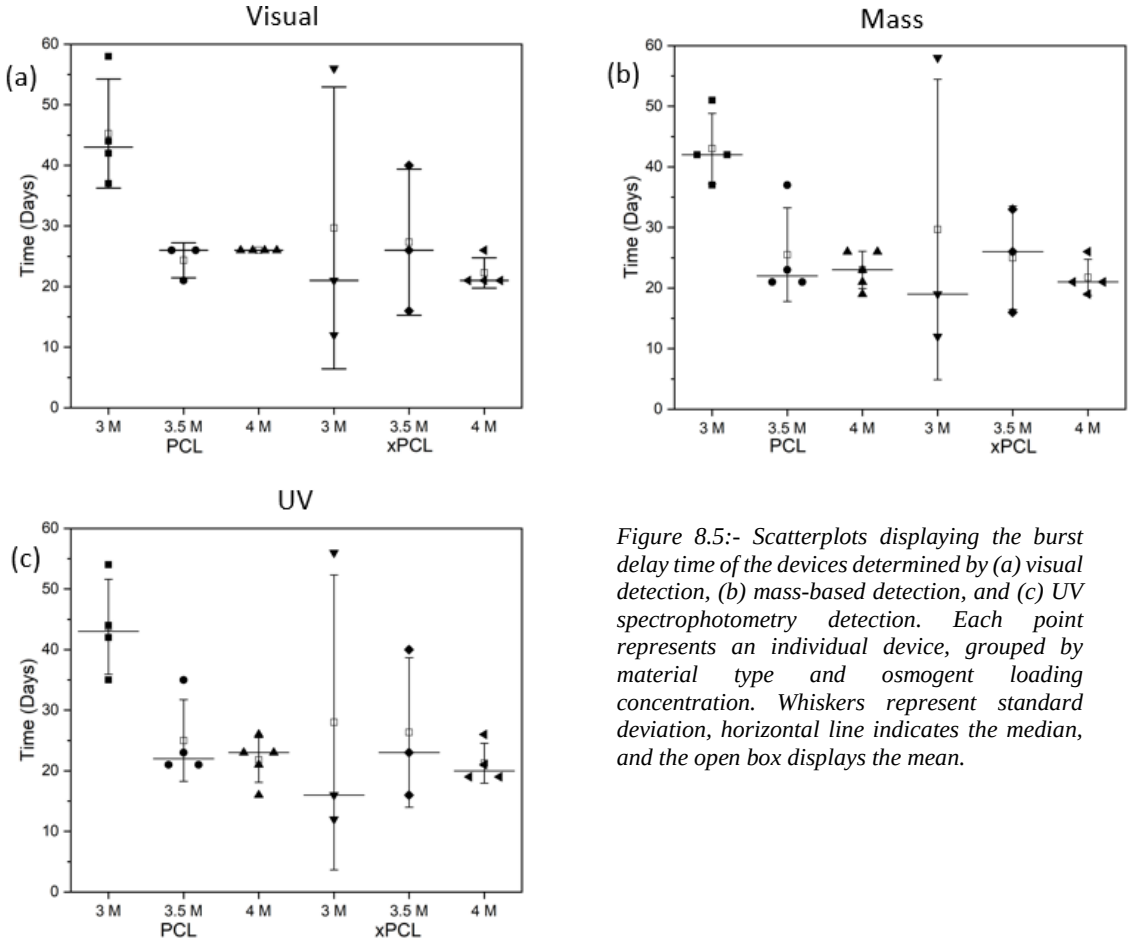

Figure 8.5:- Scatterplots displaying the burst delay time of the devices determined by (a) visual detection, (b) mass-based detection, and (c) UV spectrophotometry detection. Each point represents an individual device, grouped by material type and osmogent loading concentration. Whiskers represent standard deviation, horizontal line indicates the median, and the open box displays the mean.

The average burst delay of each subgroup is shown in Table 8.2.

		Average burst delay (days)		
Device material	Osmogent Conc. (Molar)	Visual detection	Gravimetric monitoring	UV Spectrophotometry
PCL	3	45.3 ± 7.8	43.0 ± 5.0	43.8 ± 6.8
	3.5	24.3 ± 2.4	25.5 ± 6.7	25.0 ± 5.8
	4	26.0 ± 0.0	23.0 ± 2.8	23.3 ± 1.8
xPCL	3	29.7 ± 19.0	29.7 ± 20.2	28.0 ± 19.9
	3.5	27.3 ± 9.8	25.0 ± 7.0	26.3 ± 10.1
	4	22.3 ± 2.2	21.8 ± 2.6	21.3 ± 2.9

Table 8.2:- Average burst delay times of each device subgroup from each detection methodology, and their associated standard deviations (n=3-5).

Devices demonstrated a burst range between 12-58 days. Devices with higher osmogent concentration generally burst after a shorter delay, with some 3.5 M concentration group devices bursting within similar times to the 4 M group. The variation within a group increases with lower initial loading osmolarity. Detection through mass-based or UV means typically identified device bursts earlier than by eye.

8.3.4 The moment of burst

The release of payload immediately after burst was extracted from the gravimetric and UV data. Referring back to Figure 8.3, we can define the burst event in terms of mass lost and dye released. The burst events occur between 2 points, where due to the sampling intervals, we have a range of 2-3 days between data points. For mass-based burst assessments, the burst occurs between the peak mass and the successive data point. The difference in mass between these points is defined as the mass lost at burst. Similarly, for dye-based detection of burst, we regard the burst to have occurred between the first point that displays a positive detection of dye above baseline and the preceding baseline data point. Therefore, the difference in detected dye between these points is regarded as the dye released at burst. The average mass released, and the average percentage of total loaded dye released upon burst is shown in Table 8.3, and depicted in Figure 8.6.

Device Material	Osmolarity (Molar)	Mass released at burst (mg)	Dye released at burst (%)
PCL	3	0.5 ± 0.2	1.3 ± 1.3
	3.5	1.2 ± 0.4	1.0 ± 0.2
	4	1.8 ± 0.7	0.8 ± 0.2
xPCL	3	13.6	21.5
	3.5	5.8 ± 2.5	13.0 ± 1.3
	4	6.1 ± 2.6	7.6 ± 1.6

Table 8.3:- Displays the average mass and dye released at burst from each experimental group.

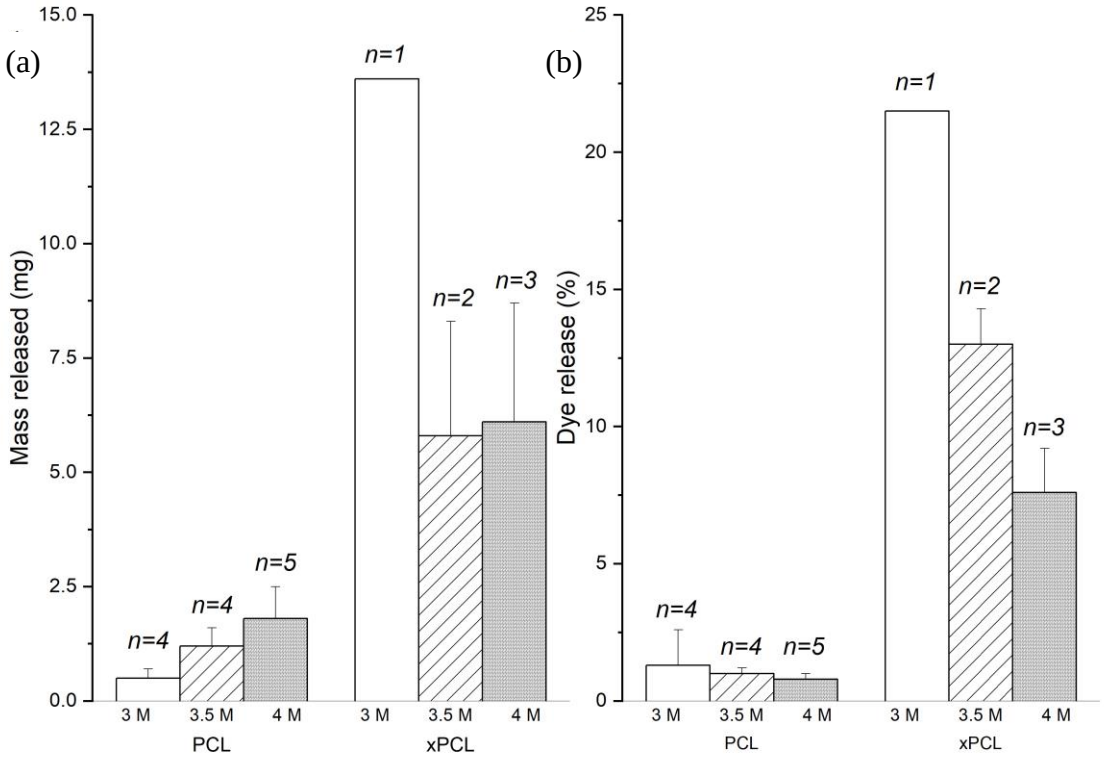

Figure 8.6:- (a) average mass, and (b) average perentage of loaded dye released upon burst of the devices. Error bars represent standard deviation. Population sizes are indicated above each bar.

We can notice that the xPCL groups typically lose more mass, and release a larger quantity of dye upon burst in comparison to their PCL counterparts. The PCL devices lost more mass as osmogent concentration increased. The xPCL 3 M group mass loss and dye release appear to suggest that increased mass loss may be linked to increased dye release. However, this is not evident from the release data from all the other groups irrespective of osmolarity or material type. The xPCL groups suggest an inverse relationship between loading osmolarity and dye release, but this is not shown in the PCL groups.

The burst sites of several tubes were imaged using a DinoLite^{TM} Basic AM2111 digital microscope. Representative images of burst sites belonging to both material groups are shown in Figure 8.7.

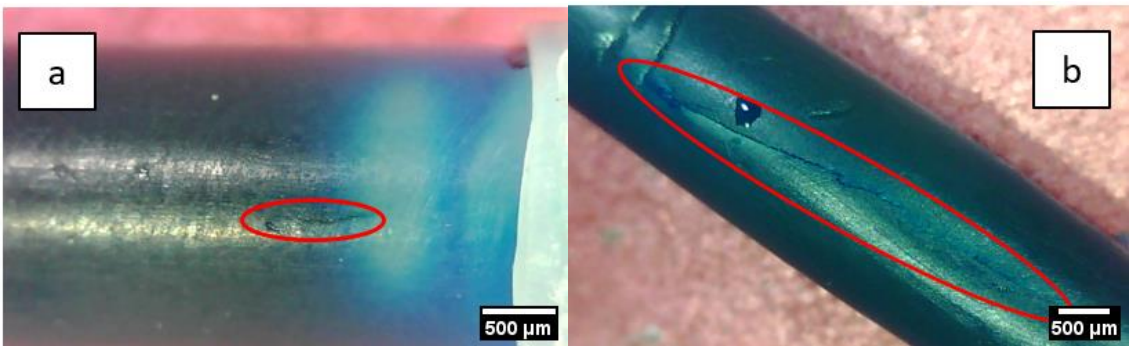

Figure 8.7:- Microscope images of representative burst sites of a PCL tube (a) and an xPCL tube (b). Red circles are to highlight the lengths of the burst areas. Fissure lengths circa 0.7 mm (a), and 5 mm (b).

PCL devices typically demonstrate pinhole bursts or a small fissure along the tubular part of the device, while xPCL devices display a fissure of longer length and with greater width than fissures noticed on PCL devices. On the assumption that devices of both material types would have partially deformed during the uptake phase, all appeared to have recovered their original shape.

8.3.5 The post-burst release phases

The rates of post-burst release were calculated from the gravimetric and UV data. The rate of mass loss was calculated for each device by determining the mass gradient after the initial burst and post-burst stabilisation phase until day 72. Due to the differences in burst and post-burst mass behaviour between each group, the time interval considered suitable for calculation of the gradient was assessed separately for each individual group. A time interval was chosen by considering the mass profiles of each tube within a group, and determining an interval where the majority of devices were deemed to have entered a steady state release phase. Samples that had not burst, or were still to establish a profile that resembled steady state release prior to this interval, were excluded. The dye release gradients were determined using the same criteria as for the mass loss gradients. PCL groups were assessed after day 51 (3 M), 45 (3.5 M), and 33 (4 M), while xPCL groups were assessed after day 21 (3 M), 40 (3.5 M), and 30 (4 M). The average mass and dye release rate after burst of each device group is shown in Table 8.4 and Figure 8.8.

Device material	Osmolarity (Molar)	Mass loss rate (µg/day)	Dye release rate (%/day)
PCL	3	72.0 ± 76.7	0.16 ± 0.03
	3.5	47.0 ± 9.3	0.20 ± 0.01
	4	68.5 ± 27.4	0.22 ± 0.04
xPCL	3	13.0 ± 11.3	0.56 ± 0.03
	3.5	69.0 ± 32.2	0.47 ± 0.03
	4	31 ± 25.4	0.48 ± 0.07

Table 8.4:- Displays the average mass loss rate, and dye release rate of each device group.

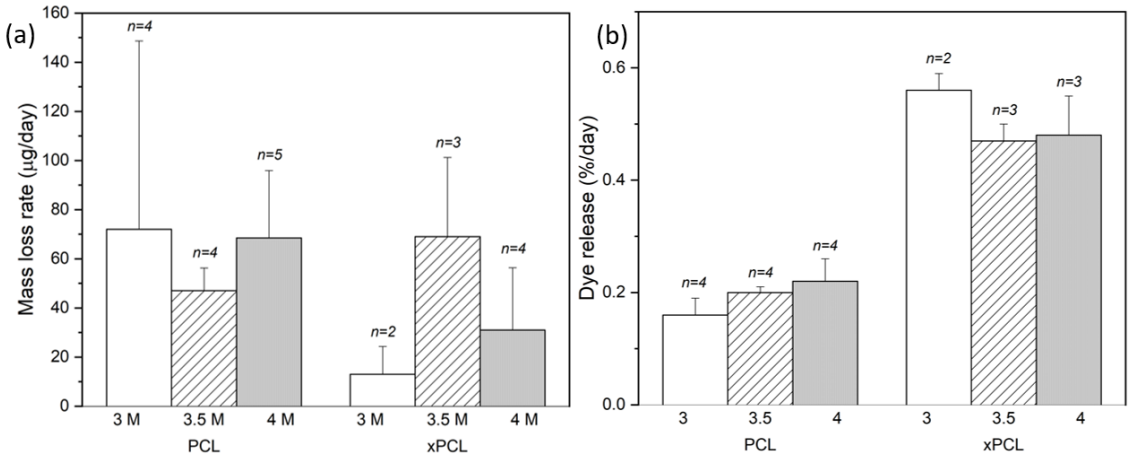

Figure 8.8:- Comparisons of the average post-burst release rates of mass (a) and dye (b) of devices from the three osmolarity groups and each material type. Error bar indicates standard deviation. Population values are indicated above each bar.

After the burst event, mass loss rates across all groups show high variability and offer no distinguishable trend. Post-burst dye release rates however, show that the xPCL devices were releasing dye approximately twice as fast as the PCL group devices. The dye release rates also suggest that osmolarity does not determine the extent of release after burst, with release rates within a material-type group being highly similar.

The total release of payload was evaluated by the mass lost and dye release after burst until day 72 (end) of the experiment. The total mass released was calculated by taking the peak mass prior to burst and subtracting the mass measured at day 72. The total dye released by day 72 was calculated from the summation of dye release from all data points

after burst detection. The average mass lost, and dye released by day 72 is shown in Table 8.5 and Figure 8.9.

Device material	Osmolarity (Molar)	Mass lost by day 72 (mg)	Dye released by day 72 (%)
PCL	3	4.4 ± 0.5	8.2 ± 1.6
	3.5	6.4 ± 1.3	13.7 ± 0.9
	4	6.6 ± 2.0	12.6 ± 1.5
xPCL	3	14.9	35.2 ± 2.6
	3.5	7.2 ± 3.2	35.5 ± 3.7
	4	8.4 ± 4.3	38.1 ± 1.9

Table 8.5:- Displays average mass lost and dye released by 72 at the end of the experiment for each group.

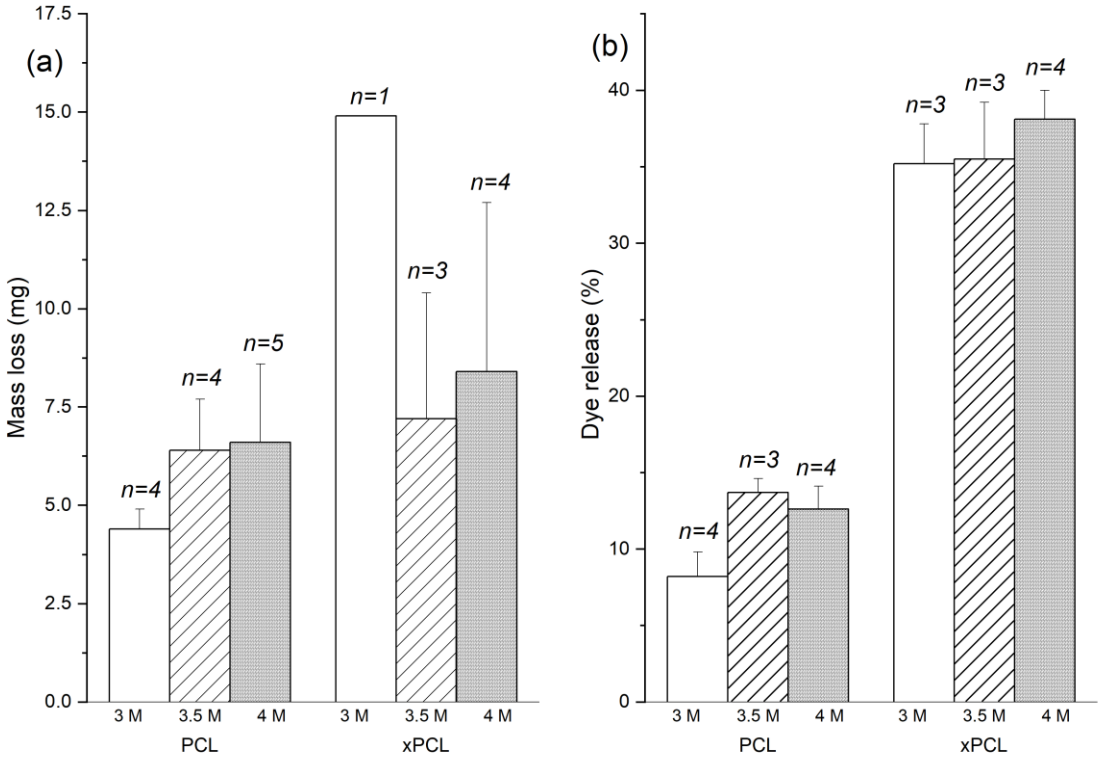

Figure 8.9:- (a) Average mass lost at day 72 in reference to peak mass prior to burst. (b) Average percentage of total loaded dye released by day 72. Error bars indicate standard deviation. Population sizes are indicated above each bar.

With the exception of the xPCL 3 M device, it can be noticed that the mass lost by day 72 across the other groups is relatively similar. The xPCL 3 M device lost approximately twice as much mass than the other groups. At day 72, the xPCL devices have released more than double the quantity of dye that the PCL devices released at the same stage.

8.3.6 Defective devices

There were 3 defective devices, which burst either immediately or overnight after initial immersion. The defective devices are not shown in Figure 8.5. The mass loss, and dye release profiles of each of the defective tubes is shown in Figure 8.10.

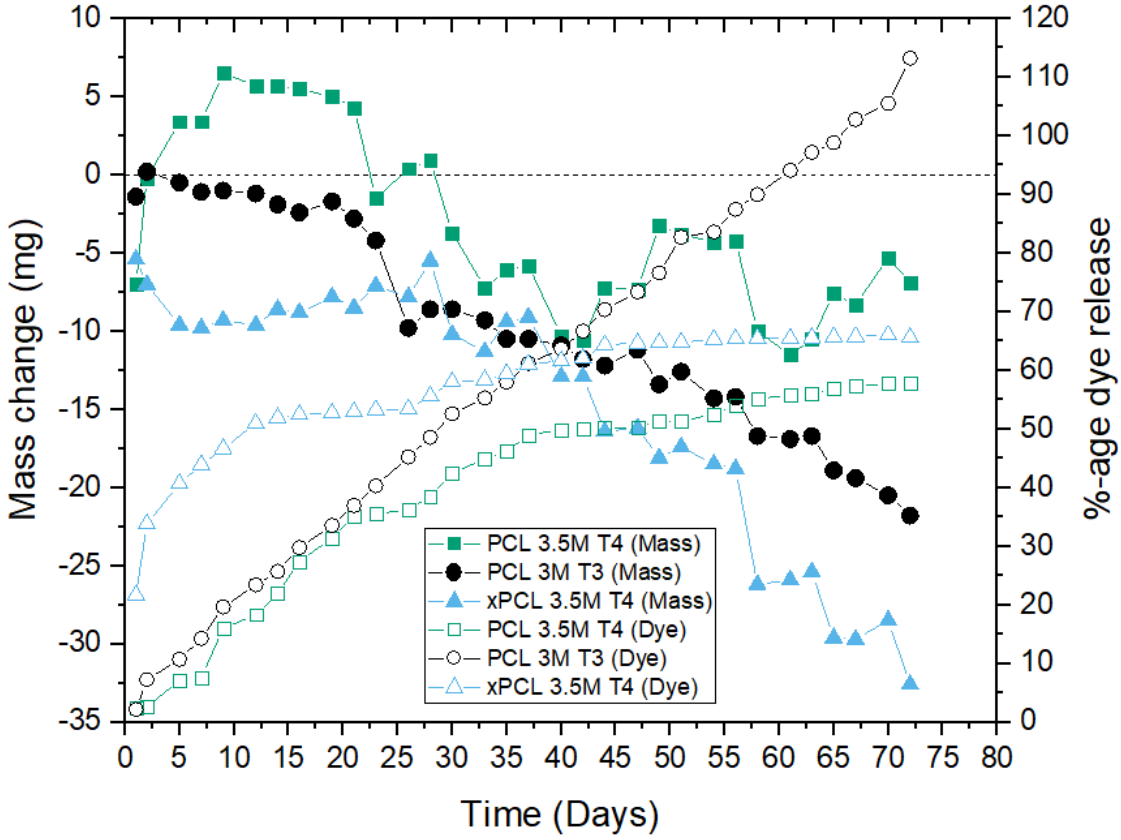

Figure 8.10:- Mass change (solid) and percentage of maximal dye release (open) of three defective tubes. Individual tube mass and dye release is paired by colour and shape. Legend identifies tubes by tube material, osmolarity and tube number, i.e. "PCL 3.5 M T4" refers to a non-crosslinked PCL device loaded with 3.5 M glucose and is tube number 4 from that specific subgroup.

The PCL 3.5 and 3 M groups and the xPCL 3 M group each contained one of the aforementioned defective tubes. Defective tubes typically lost mass during the early stages after immersion, combined with immediate release of large quantities of dye.

8.4 Discussion

8.4.1 Summary

Osmotically triggered delayed release of a dye has been successfully performed from our devices. Gravimetric and UV spectroscopy measurements show that all devices follow a multi-stage profile of water uptake, burst, initial mass loss and payload release, followed

by a gradual continuous loss of further mass and payload. The xPCL devices release up to 16.5x more dye upon burst, combined with essentially twice the steady-state rate of dye release, resulting in approximately 25 % greater total release by the end of the experiment, than their PCL equivalents. The devices of both material types uptake similar mass/volume of water prior to burst, with the difference in the extent of release at all post-burst phases appearing to be largely influenced by differences in shape recovery and size of the burst sites. The device delay to burst times were primarily dependent on the rate of water uptake determined by the osmogent loading concentration, with no noticeable effect from material type. Utilisation of lower osmogent loading concentrations (3.5 or 3 M) introduce greater variability in the delay time to burst of the devices of both material types.

8.4.2 Influence of material mechanical characteristics on the delay to burst and payload release

The xPCL tubes did not feature a longer delay to burst, as shown from the data displayed in Figure 8.5 and summarised by comparing the sub-group averages in Table 8.2. The mechanical burst tests (Chapter 6) indicated that the xPCL devices would require a greater volume increase than the PCL tubes to burst. In these osmotic tests, the peak mass uptake, shown in Figure 8.4 (b) and Table 8.1, and therefore the volume increase, was similar between materials and loading osmolarity groups, with the lower osmolarity groups taking a longer time to reach peak mass/volume uptake than higher osmolarity groups. It was not anticipated that the devices composed of the different materials would take up a similar volume at burst, which may be due to a combination of the significantly slower loading rate, 37 ^{o}C temperatures, and wet material state during the osmotic test, as opposed to the fast loading and dry room temperature conditions during mechanical testing. This behaviour may suggest that the form (elastic/plastic) and extent of material deformation is influenced by the rate of pressure loading, and therefore in osmotic studies, affected by the rate of water uptake. Material hydration may also have a plasticising effect, but this would need to be investigated further to determine its presence and magnitude.

The xPCL devices did eject more payload at burst than the PCL devices as shown in Figure 8.6 (b) and Table 8.3. The xPCL groups released approximately 16.5x (3 M), 13x (3.5 M), and 9.5x (4 M) more dye upon burst than their PCL counterparts of the same osmolarity. Release of dye was detectable for both material groups by eye and UV

methods, accompanied by a drop in mass. Comparing the mass lost at burst against the extent of dye release in Figure 8.6 (a) and Table 8.3, indicates that a greater extent of mass release did not necessarily imply a larger concentration of dye was released at burst. In the xPCL group, a device possessing larger peak mass was associated with greater dye release at burst. This observation was true to a lesser extent for the 4 M xPCL group, where 1 out of 4 devices did not conform. However, the PCL devices did not feature this behaviour. The lack of a consistent correlation between mass lost and dye released was unexpected. While the peak mass/volume uptake of devices constructed from both types of material were similar (overall average 15 ± 4 mg), the manner in which the material responds at burst appears responsible for this difference in release at burst. From previous *in-vitro* and mechanical burst assessments, PCL tubes feature a small degree of deformation leading to and at burst, which appears predominately as plastic deformation, along with a small pore or tear for payload flux to occur. The xPCL tubes in comparison during mechanical testing displayed an overall greater extent of deformation of which some is elastic, resulting in a degree of shape recovery after burst. From the images of the device osmotic burst sites in Figure 8.7, other than the burst pinholes and fissures, no evidence of deformation was present. Perhaps the elevated temperature combined with a plasticising effect from hydration has enabled both materials to behave in a more elastic manner, allowing them to return to their original shape. The xPCL material fissure shown in Figure 8.7 (b) is approximately 5x larger than the PCL burst site in Figure 8.7 (a), which may account for the greater level of release. The size of the burst sites appear to be the main influence regarding the rate of dye release during the steady-state release phases. The rates of dye release from the devices during this stage is shown in Figure 8.8 (b) and Table 8.4. The rates of dye release appear to be independent from the osmogent loading concentration, with release rates within a material group being similar. Again, it is interesting to note that there is a lack of a correlation between the rate of mass loss and the rate of dye release during this phase. The mass release rates shown in Figure 8.8 (a) and Table 8.4 are highly variable, with no particular trends apparent. This could perhaps be explained by the remaining glucose solution within the burst devices still exerting an osmotic pressure on its surrounding area, and therefore causing a continued uptake in mass, which would then hinder the usefulness of considering the behaviour of mass as a method of release analysis.

The different material behaviours also appear to play a role in overall payload release, shown in Figure 8.9 (summarised in Table 8.5) by the loss of mass, and release of dye at the end of the experiment. The xPCL devices have an advantage in both overall mass loss and dye release, due to the greater extent of dye released at burst providing a large head start over the PCL devices. The xPCL devices release significantly greater dye content by day 72 in comparison to the PCL devices. With decreasing osmolarity, the xPCL tubes released 3x, 2.6x, and 4.3x more dye at day 72 than the PCL groups. The xPCL devices lost more mass than the PCL devices by day 72, but the average difference between the material types is marginal, with the exception of the 3 M osmogent concentration groups. Similarly with the release profiles at the point of burst, it is anticipated that the xPCL devices again release more content overall due to the combination of deformation and shape recovery characteristics and more extensive burst site.

In future studies featuring flexible materials, it would be advantageous to monitor or image the devices periodically to determine the material behaviour during the water uptake phase, and to see any evidence of shape recovery upon burst. Due to dye release not correlating with mass loss, monitoring of dye or any other payload target directly should be preferred.

8.4.3 Effect of material permeability and device wall thickness on the water uptake rate

The rates of water uptake between material groups with the same osmogent loading concentration are highly similar, as shown in Figure 8.4 (a). We know from the microCT data (Chapter 6 6.4.1) that the xPCL tube wall thicknesses are ~2.6x larger than the PCL walls on average, therefore considering Equation 2-6, the permeability of the xPCL network must be essentially 2.6x greater than the PCL material to return such similar rates of water uptake for the same osmogent concentration (and therefore osmotic pressure). Referring back to our initial hypothesis, the data demonstrates that the xPCL material does indeed have a greater permeability than the PCL material. However, the effect of permeability on the rate of water uptake, and ultimately burst delay, is counteracted by the thick xPCL device walls.

8.4.4 Relationship between initial loading osmogent concentration and the rate of water uptake and its effect on the delay to burst

The water uptake rates of devices increase with rising osmogent concentration. Higher initial osmolarity was also associated with a quicker time-to-burst. Burst variability was negatively impacted by lower osmogent concentrations. The underlying spread of data within the "time to burst" averages shown in Figure 8.5 suggests an increased dispersion as osmolarity decreases, and/or potential consistency issues with tube production. Due to this variation, the experiment would also benefit from larger sample populations. It is reasonable to assume that tube consistency is evenly spread amongst all tube groups of the same material type due to being manufactured and assembled in the same way and being assigned to a specific osmolarity group at random. While the burst delay time averages display the expected trend, there are samples in the lower osmolarity groups that burst around the same time as, or even sooner than, the 4 M groups.

8.4.5 Burst delay methodology assessment

All three detection methods generally indicate a similar burst window for each group of the dye-loaded tubes. From Figure 8.5, UV spectrophotometry and gravimetric measurements generally detect device bursts earlier than visual means. Referring to the raw data, UV and gravimetric analysis on average detects bursts 3.5 ± 1.7 days earlier than visual identification. Out of 23 viable tube bursts, in 7 instances all burst detection methods agree on one day of burst, UV spectrophotometry detected bursts earliest 8 times, gravimetric analysis detected bursts earliest 3 times, while UV and gravimetric means agreed 5 times on a single day of burst. Visual identification did not detect a burst before UV or gravimetric methods. In terms of determining the burst delay, looking at a device-by-device basis like this reveals that UV spectrophotometry is typically the most sensitive methodology, closely followed by gravimetric analysis. Based on this assessment, the UV spectrophotometry burst estimates were regarded as the 'true' burst points for all tubes.

The UV and gravimetric data spread of all the tube groups, but especially the 4 M groups due to the relative size of their standard deviation over their entire delay to burst time, may be artificially high due to the relatively infrequent sampling times. For example, the standard deviation of the 4 M burst times across both material groups fall below 3 days, which was the upper sampling interval time. Therefore, it is possible that certain tubes burst on day 1 of that interval that were not detected until a further 2 days later. A demonstration of this is the PCL 4 M dye group, which were spotted to have burst on day

26, which was 3 days after the previous check (day 23). UV and gravimetric data suggest that the same devices burst approximately around day 23 instead, again demonstrating the weakness of long sampling intervals and the limits of visual identification of burst for the thermoplastic tubes. The more flexible xPCL tubes show on average much closer agreement between visual detection and UV detection, which is likely due to the burst behaviour causing a greater and more immediate colour change, in comparison to the PCL tubes which release more gradually and to a lesser overall extent.

Ideally, in future studies assessments would be made daily or more frequently by utilising automated means. Naturally, daily checking and sampling of approximately 80 tubes (or greater if using increased group *n* numbers) takes a significant portion of a researcher's time. In this instance, it was made more complicated due to me being required to leave Brisbane to return to Edinburgh to continue the rest of my PhD. Therefore, the group in Brisbane had to take on data collection duties on my behalf, while attending to their own research and deadlines (see acknowledgements).

For studies involving PCL or other thermoplastic devices that are expected to demonstrate the same "leaky" pinhole bursts, visual or time lapse imaging are likely to overestimate the burst delay while the dye colouring builds in the surrounding solution. For devices constructed from flexible or elastomeric materials that show a greater bolus release at the time of burst, time lapse imaging would be a less labour-intensive way to relatively accurately determine the burst delay times of large quantities of samples.

It should be noted however that gravimetric and UV analysis provide useful information such as the overall profiles of mass and dye shown in Figure 8.3, and subsequently the extraction of other "functional property" aspects like the water uptake rate (gravimetric), and payload release rate (UV) . Perhaps for larger future studies, burst delay assessment of the tubes could be handled by time lapse imaging, while a smaller or less frequently sampled subset of devices could be subjected to mass and UV spectrophotometry assessments to retain generation of these other useful data sets.

8.4.6 Defective devices

A defective tube was defined as a tube that was found to leak dye immediately after submersion. We were generally able to identify leaking tubes immediately due to the colour change of the PBS solution, but it could also be verified from the mass and UV data as shown in Figure 8.10, with extensive mass loss and dye release observed. Overall, the number of defective tubes were low, with only one in the xPCL group (n=11) and two

in the PCL group (n=15). This would suggest a manufacturing failure rate of 9% for xPCL tubes, and 13% for PCL tubes. This failure rate is essentially on par with what Melchels *et al* previously reported, where four out of twenty-seven tubes failed directly after immersion (circa 15%) [21]. These defective tubes were classed as outliers and not included in further analysis of their respective datasets.

8.5 Conclusions

We successfully demonstrated delayed burst release of a dye from manufactured devices. In this experiment, the material type did not generally influence the delay to burst time, but did affect the characteristics of the payload release after burst. The more flexible xPCL devices displayed up to 16.5x greater initial release immediately following burst by releasing up to 21.5 % of total loaded dye, compared with up 3.5 % from PCL devices. Additionally, by day 72 the xPCL devices had released up to 2.5x more payload than comparable PCL devices. These findings would suggest that a more flexible material could further improve the approximate bolus release profile that we wish to achieve. The delay to burst could be extended by reduction in the concentration of glucose that was loaded into the device during manufacture. This was attributed to the rate of water uptake into the device, with faster water uptake occurring when the device was loaded with higher concentrations of glucose. However, the delay to burst time was most reproducible when glucose-loading concentration was highest, demonstrated by comparing the burst delay time of 4 M xPCL device at 21.3 ± 2.9 days to 3 M xPCL devices at 28 ± 20 days. Due to the increase in burst variability at lower glucose concentrations, it may be advised to maintain a 4 Molar glucose loading concentration and use other variables such as material water permeability, and wall thickness to prolong/or tune the burst delay time.

Chapter 9 – Final discussion

9.1 Main findings

The overall aim of this work was to develop the next generation of monolithic osmotically triggered delayed-release vaccine delivery device as first conceptualised by Melchels *et al*. The main shortcoming of the 1st generation device was the non-bolus trickle-like release of payload upon burst. The 2nd generation monolithic delivery devices were constructed from a bimodal PCL photo-cured network, composed from long linear bi-functional 10 kg/mol and 0.9 kg/mol tri-functional macromers. Liquid photo-curable PCL resins were formulated using benzyl alcohol as a non-reactive diluent, with low-toxicity and low vapour pressure. It is recommended that benzyl alcohol should be considered to replace dioxane, the diluent typically used in the literature to formulate low-M_w PCL resins, which is significantly more toxic and has a higher vapour pressure. A series of photo-cured uni- and bimodal networks composed from a variety of bi- and trifunctional PCL macromers of various molecular weights were characterised. While networks composed of macromers with higher molecular weights demonstrated higher crystallinity and toughness, such networks possessed lower reactivity and poorer mechanical properties in the 'green state' than resins featuring lower M_w macromers. Bimodal networks of the 10 kg/mol PCL macromer and either 0.9kg/mol PCL or PTOL-4A demonstrated improved reactivity and maintained a portion of the toughness shown by the 10 kg/mol networks, while being vastly tougher than 2 kg/mol networks of similar crosslinking potential. A resin featuring the 10 kg/mol PCL macromer and pentaerythritol tetraacrylate (xPCL10k+4A) was shown to be suitable for stereolithography printing, and several intricate objects were successfully printed. All PCL-based (including xPCL10k+4A) networks were shown to be degradable via accelerated hydrolysis, with bimodal networks degrading faster than unimodal networks. During cytotoxicity experiments, the xPCL10k0.9k bimodal network was indicated to be of low toxicity, by performing similarly to non-crosslinked high M_w PCL. Prototype devices were manufactured using automated dip coating apparatus. A revised high-throughput dip coater system was designed and built to assist future work. While dip coating was a simple and effective method of producing the tubular part, greater optimisation of the dip coating cycles should be performed in order to improve the wall thickness homogeneity. Mechanical burst testing indicated that crosslinked-PCL devices would require a greater volume uptake to burst, than non-crosslinked-PCL devices. This was however shown not

to be the case in later *in vitro* osmotic burst testing. Caps with higher rigidity appear to affect the ability of the tubular part to freely deform. *In vitro* osmotic burst testing demonstrated that the crosslinked-PCL devices released up to 16.5x more payload than non-crosslinked-PCL devices at the point of burst. Analysis of the burst sites indicate that the xPCL devices burst through a larger tear as opposed to small pinholes or cracks shown from PCL devices. These findings suggest that a more flexible material could further improve the approximate bolus release profile that we wish to achieve. Due to increased burst delay variability at lower osmogent concentration, it is recommended to maintain a high osmogent concentration and use material water permeability and device geometry aspects (such as wall thickness) to adjust the burst delay timing.

9.2 Final discussion

9.2.1 Results in view of the proposed application

The 2nd generation crosslinked PCL devices offer a marked improvement in bolus release over 1st generation non-crosslinked PCL devices. Original devices were shown to release approximately 1 % of the payload immediately after burst, while xPCL devices were able to release up to 21.5 %. The xPCL material demonstrates a proof of concept of utilising a crosslinked material that swells under load and features elastic recovery upon burst to achieve a degree of bolus release. It is hoped that by using a more elastomeric material, a greater extent of immediate bolus release can be achieved.

During the initial stages of the project, consideration of the device *in vivo* degradation time was not a priority. The slow degradation rate of PCL was seen as a positive, as was then highly unlikely that any meaningful degree of degradation would occur prior to the device delivering the booster dose. However, following the more recent establishment of a collaboration with The Roslin Institute, where we aim to test the devices in cattle, degradation time becomes substantially more important. Particularly, where the cattle being immunised are destined for the meat industry, post-slaughter remnants of a polymer capsule are undesirable. While the accelerated degradation studies demonstrate that the photo-cured PCL networks should remain biodegradable, the conditions used make it difficult to relate the rate of degradation to *in vitro* studies under physiological conditions. In particular, the high temperatures will eliminate all crystallinity within the samples, making the samples completely amorphous and therefore much more susceptible to water uptake and hydrolytic cleavage. Ideally, a long-term degradation study should be performed using physiological conditions to determine whether the bimodal networks still

degrade faster than the unimodal or non-crosslinked materials when sample crystallinity is maintained.

One of the main potential issues of the new photo-cured devices is that the crosslinked nature of the tubular part limits the available options for capping. The current method uses injections of resin into the ends of the device, which enables the resin to crosslink to available reactive groups on the inside barrel of the tubular part, covalently bonding the plug to the tube. These plugs of resin are not subjected to an extraction procedure, meaning that uncured macromer, and left-over photo-initiator will remain. It is demonstrated in Chapter 5 that both such components can have toxic effects. While the amount of resin used to create these plugs/caps is small the residual content of photo-initiator in particular, may be enough to irritate surrounding tissue as it leaches out of the plug. Additionally, while it would be possible to re-extract the device after curing of the 1st plug/cap, after filling and curing of the 2nd cap extraction is no longer suitable due to fluid exchange between the extracting solvent and the glucose/payload solution within the device. At present, this has not been resolved in a satisfactory manner and will apply to any future radical-based crosslink-able network system developed. Changing the photopolymerisation chemistry of the system to a photo-initiator-less photoclick system may offer a less toxic solution [239], [240]. However, photo-curable resin formulations of such materials typically require irradiation with < 300 nm light, with commercially available DLP systems generally not featuring light sources with peak wavelengths that short. Another potential approach would be the use of thermoplastic elastomers (TPEs). TPEs are a class of copolymer that typically consist of hard crystalline blocks and comparatively soft elastic segments, which gives them the elasticity of a conventional thermoset rubber with the processability of plastics [241]. The hard block components of various polymer chains can self-agglomerate during cooling to assemble into crystalline domains with physical crosslinks that resist creep and viscous flow under load, while the soft portion remains amorphous and elastic [242]. Use of TPEs would allow use of thermal fusion capping techniques used in this thesis and the previous conceptual work [21], while improving the elasticity that appears useful in achieving immediate bolus release from the devices.

9.2.2 Mechanical burst testing as a prediction of osmotic burst behaviour

Despite the mechanical burst assessment predicting that the xPCL tubes would require the uptake of a greater volume to burst, the delay-to-burst, and peak mass/volume reached by tubes composed of the different materials were similar. The mechanical peak volumes

prior to burst overestimate the volume required to burst *in vitro*, particularly so for the xPCL material. The PCL device mechanical volume to burst was ~22 μL, while the osmotic volume uptaken prior to burst was ~15 μL. For the xPCL – Resin tubes, the peak mechanical volume was 277 μL and the osmotic peak volume ~13 μL. Such a huge disparity between the mechanical and osmotic volumes required to burst the xPCL tubes clearly indicates that the mechanical test methodology is unsuitable in its current form for evaluating the burst nature of the devices. Use of the particular mechanical test method in Chapter 6 to predict *in vitro* osmotic burst behaviour should be used as an indicative assessment only, due to a few key differences. The mechanical burst testing was performed at room temperature, with the devices being in the dry state, and with water being forced into the devices at a relatively fast rate (83.5 μL/min) in comparison to the rate of water translocation during an osmotic test. At 37 ^{o}C in the incubator during *in vitro* osmotic tests, the materials will be more flexible and less stiff than at room temperature, leading to changes in the yield and deformation behaviour [243] with magnitudes being difficult to predict without further testing. However, 37 ^{o}C is just within the onset of the melting peak of the xPCL10k0.9k networks (determined from DSC), therefore only a very minimal reduction in crystallinity is expected. Water saturation of the xPCL network walls is likely to exert a plasticising effect [244], which would potentially cause further changes in material yield/deformation. However, based on data shown by Melchels *et al*, the effect from the state of hydration is expected to be small [21]. During osmotic tests discussed in Chapter 8, typical osmotic water uptake rates into xPCL devices were shown to be approximately 893 μg/day (xPCL 4 M), equivalent to 0.6 nL per hour. This greatly reduced rate of volume gain of approximately 7 orders of magnitude will generate a slower strain rate on the device walls, which can influence the point of yield as well as strain hardening behaviour [243]. Considering the expected minimal effects of temperature and hydration discussed above, the effect of strain rate is anticipated to be the main cause of the differences between in vitro and mechanical testing burst behaviour. Tensile and burst testing of the xPCL material at physiological temperature and water saturation is required to develop a more complete methodology to predict *in vitro* behaviour from the mechanical tests. The mechanical test in its current form does not take into consideration of potential wall thickness differences between devices. It has been previously shown that there is a strong correlation between wall thickness and burst pressure strength [21]. Additionally, the mechanical test methodology does not consider that devices composed of the different materials may uptake water at different rates due

to differences in material water permeability. This is emphasised when considering the delay-to-burst times, and peak mass in Chapter 8 between the PCL and xPCL devices containing the same osmogent concentration. As discussed above, testing of the material at the appropriate temperature, and with a slower rate of loading are considered key aspects to better correlate the mechanical predictions to the osmotic outcomes.

For future mechanical testing, devices could be incubated at 37 ^{o}C while submerged in water for a few days prior to the experiment, to replicate the water-saturated state of the device during osmotic burst testing. During mechanical testing, a beaker of water kept at approximately 37 ^{o}C could be placed underneath the syringe mount for the tube to be submerged in throughout the test. This would maintain the tube at the most relevant temperature and state of hydration. To assess the effect on the manner of burst from the rate of loading, testing could be performed using a series of injection rates over a few orders of magnitude. Use of true elastomers in future work may minimise the influence of the strain rate, as the mechanical properties of such materials are not considered to be strongly dependent on strain rate.

9.2.3 xPCL10k+4A printed tubes

The xPCL10k+4A tubes manufactured by stereolithography may behave differently from their dip coated xPCL10k0.9k counterparts due to differences in their network structure and production technique. Most notably, the xPCL10k+4A networks contain a substantially lower degree of crystallinity (Table 4.3), with approximately 14 % of the xPCL10k0.9k network crystallinity. As previously discussed in Chapter 4 and Chapter 8, the degree of crystallinity plays an important role in determining both the mechanical properties and water permeability of the network. In an osmotic setting, the xPCL10k+4A network would likely offer greater diffusivity than the xPCL10k0.9k networks due to the greater extent of amorphous domains facilitating uptake. However, the permeability may be limited by the water uptake equilibrium within the polymer walls, and therefore the greater diffusivity may not necessarily result in a faster rate of water uptake or lead to a shorter delay to burst. The xPCL10k+4A networks are also less stiff and yield at a lower stress but after slightly longer elongation (1.20 ± 0.15 mm vs. 0.81 ± 0.03 mm) than the xPCL10k0.9k networks. This would result in a greater degree of elastic deformation at the same internal pressure, with elastic deformation occurring over a greater elongation/strain potentially leading to a greater elastic response at break, but the magnitude of the difference between the materials would be small. It is claimed that the elongation at break of the trifunctional crosslink-containing networks would be higher

than the tetrafunctional-containing networks, due to the trifunctional junctions imposing less drastic restrictions on chain motions [245]. However, the difference in elongation at break between the tri- and tetrafunctional crosslinkers appears negligible, based on the tensile testing data. There are also too many differences between the networks to isolate this effect here.

9.2.4 Comparison of manufacturing methods

Structures that are printed via stereolithography and subjected to post-curing are generally considered to possess no significant (< 1%) mechanical anisotropy [246], [247] This would imply that there should be no significant differences between tubular parts produced by STL or dip-coating when using the same resin formulation, providing dip-coating also results in an isotropic part. Verification of isotropy can be performed through a simple experiment, where tensile specimens are printed in different orientations and subjected to tensile tests. If the networks are isotropic they should all perform similarly, in terms of ultimate strength and Young's modulus for example, regardless of their build orientation. Continuing on the basis that both STL and dip-coated parts will offer the same mechanical properties, the quality of the parts made, the time required to manufacture them, and the associated costs should be considered. In terms of quality, the STL fabricated tubes should offer more consistent wall thicknesses throughout the length of the tubes and are likely to be more consistent within, and between batches. The dip-coating cycle would need significant optimisation to achieve the same wall thickness consistency. Slight variance in the dimensions, surface qualities, and mounting of the dip coating substrate rods will also introduce further variance, although variance from these sources is expected be relatively acute. The time and cost to fabricate the tubular parts requires consideration of the number of tubes being made at one particular time, and the curing times required. The DLP process increases in efficiency as the number of tubes built within a single print cycle increases, as the print time stays the same regardless of the number of tubes being printed at once. DLP requires consideration of operational costs due to replacement of consumables such as the resin vats. EMBER has the potential to print approximately 140 tubes at once based on the vertical arrangement with the 'X' shaped supporting structures, but other DLP printers with larger build areas would be able to fit many hundreds or thousands of tubes within a single print job. Other potentially useful features of DLP is that mini barcodes or other manufacturing tracking marks could be procedurally generated and integrated on to the printed parts directly. When considering production of a single tube geometry on an industrial scale, a well optimised

dip-coating procedure will have a time/cost advantage over DLP technology. However, industrial DLP machines would offer a versatile manufacturing platform for the production of various device geometries for different vaccination programme boost dose delay lengths, and therefore shouldn’t be disregarded. The main challenge that remains is to obtain the required material properties with this technique.

APPENDIX A: osmotically triggered delayed burst release of tetanus toxoid

Protein release and quantification issues

Introduction

This appendix will discuss the methodology used during the setup of the microBCA assay, the discovery of detection and quantification issues, how the issues were investigated and verified, and recommendations to rework the methodology to achieve the original objective.

As introduced in Chapter 8, osmotic release of vaccine material in the form of tetanus toxoid was one of the experimental objectives. During the very early stages of data analysis, it was noticed that protein concentrations from the microBCA assay appeared to be influenced by the presence of glucose. After further investigation, it was realised that glucose concentrations above 1 mM are known to have an interfering effect on the assay, and was listed within the kit's manual. Therefore, the absorbance values and calculated "protein" concentrations consisted of a protein component, and a glucose component, of which discerning the fraction attributed to each would be difficult and unreliable. Due to this oversight, further microBCA work was halted.

The sections below contain all the protein release work that was conducted as initially planned in the introduction to Chapter 8, and as such follow the same material group labels (PCL = non-cross-linked PCL devices, xPCL = UV cross-linked PCL devices).

Experimental setup

Protein release calibration

In order to quantify the protein as a concentration, a relationship between absorbance and protein concentration had to be established. The microBCA assay was initially calibrated against a series of BSA protein standards of known concentration provided with the kit. The assay was utilised in the microplate format, which provides a linear working range of 2-40 µg/mL for BSA containing solutions. BSA solutions of concentrations 0, 0.5, 1, 2.5, 5, 10, 20, 40 and 200 µg/mL were used to generate Figure A1 (a). For quantification purposes, only samples within the linear working range were used to generate the equation of the calibration curve shown in Figure A1 (b).

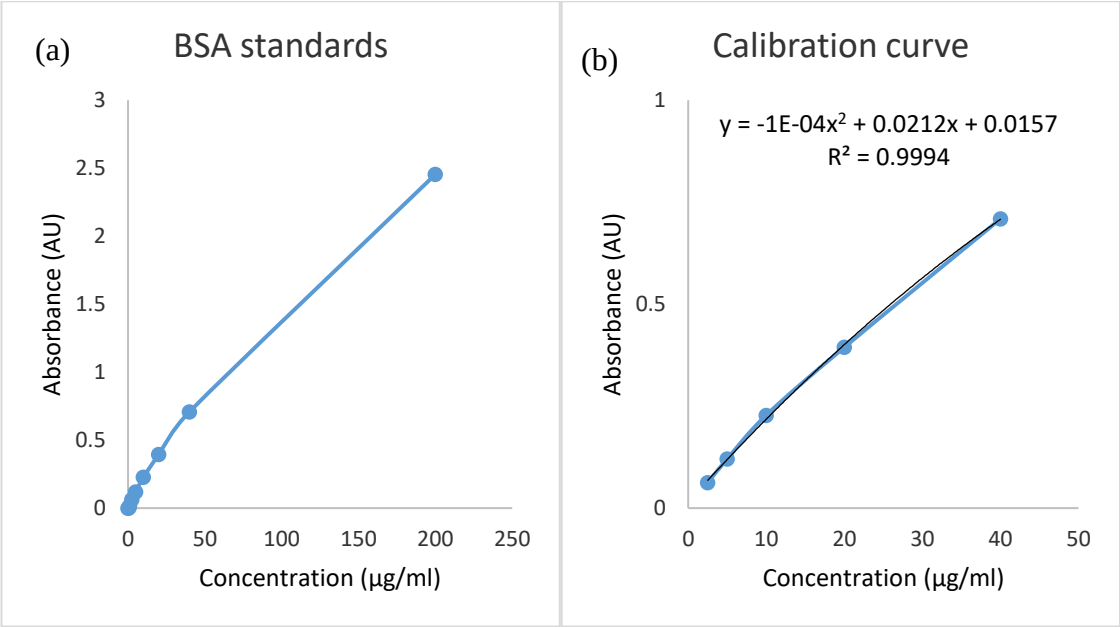

Figure A1:- BSA standard curve (a), and the linear working range calibration curve with fitted polynomial (2nd order) equation (b).

A series of dilutions of the TT stock were performed to prepare 8 TT samples which we could perform the microBCA on, and use to back calculate their respective concentrations as well as the overall concentration of the stock solution. The main assumption is a 1:1 assay colour response to TT as with BSA protein. The polynomial (recommended within assay manual) trendline equation from Figure A1 (b) was rearranged for x (concentration), and the sample absorbance values entered as y values. Five out of the 8 samples ended up below the quantifiable range, however the difference between the remaining 3 samples were in good agreement with what would be expected based on the dilutions. Further back-calculation estimated that the stock protein concentration was 15,105 µg/mL.

Results

Osmotic tetanus toxoid release

Release of the tetanus toxoid vaccine from the devices was performed as discussed in Chapter 8. Analysis was performed on the five tubes belonging to the PCL 3.5M group. The cumulative protein concentrations released into the PBS samples from 7, 14, 21, 28, 35, 42, and 49 days after immersion were determined from the microBCA assay, as shown in Figure A2. For clarity, where no protein was detected, no data point is shown.

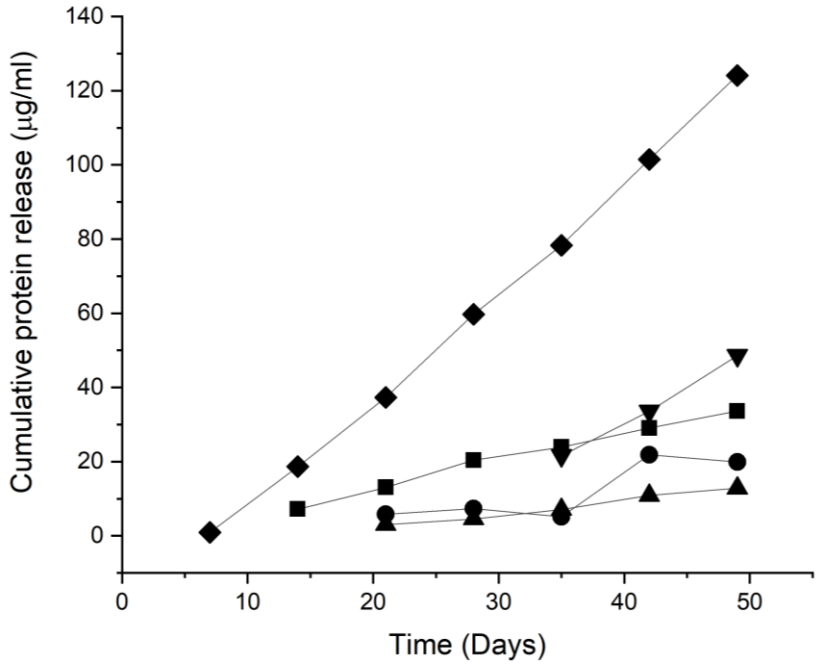

Figure A2:- Cumulative protein release from the PCL 3.5 M group devices. Each line represents the protein concentration profile for an individual device.

The devices gradually release protein after burst. Initial protein detection, and therefore device burst, occurred between 7-35 days (mean = 20 ± 9 days).

Example of glucose interference

Due to suspicions regarding glucose interference on the absorbance values returned by the microBCA assay, a small investigation was performed to determine whether these suspicions were well founded. The stock solutions of 3, 3.5 and 4 M glucose with TT that were used for the loading of the tubes were diluted to 2 different theoretical concentrations (8 and 18 µg/mL) that should be within the linear working range. Additionally, TT stock solution with no glucose was diluted down to the same concentrations. Therefore, in total there were 8 experimental samples. All 8 samples were tested using the microBCA assay, and their absorbances (a) and calculated protein concentrations (b) plotted against their predicted theoretical protein concentrations, as shown in Figure A3.

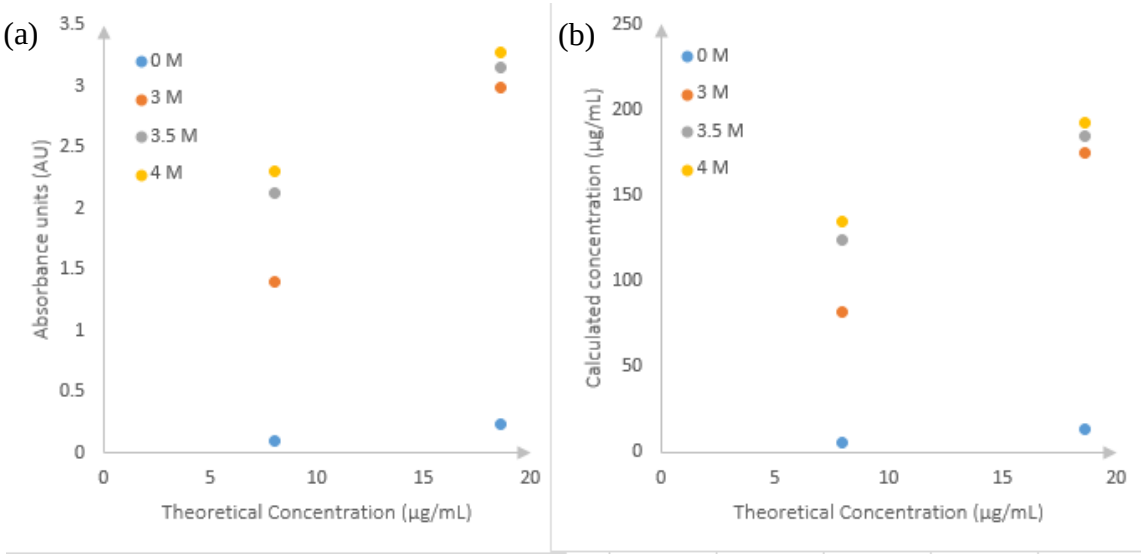

Figure A3:- Sample absorbance (a), and calculated protein concentrations (b) against predicted theoretical concentration based on previous TT stock concentration calculations.

The absorbance values for all the glucose-containing samples are significantly higher than their 0 M glucose counterparts, and therefore their calculated concentrations follow the same trend. The increase in absorbance within a theoretical concentration appear to be linked to the concentration of glucose, with higher glucose containing samples returning greater absorbance and concentration values.

Stock protein investigation

Sodium dodecyl sulphate-polyacrylamide gel electrophoresis (SDS-PAGE) was performed on samples taken from the stock solutions that the devices were loaded with prior to immersion. Additionally, a positive control with 10 µg of BSA and a sample of the TT stock with no glucose present were included. After separation, the gel was fixed and stained with coomassie blue to visualise the protein bands. The gel image is shown below in Figure A4.

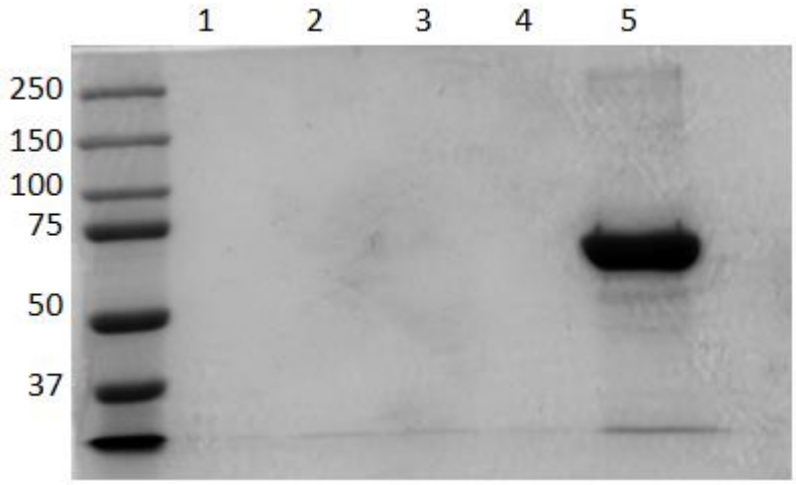

Figure A4:- Image of the gel after SDS-PAGE. Calibration ladder in leftmost column with units in kDa. Column contents are as follows: TT stock with no glucose (1); sample solutions from 3 M (2), 3.5 M (3), and 4 M glucose group (4); BSA positive control (5).

No bands are visible in columns 1-4 indicating the absence, or very low concentration below the limit of detection, of protein within these samples. The BSA positive control band is present between the 50 and 75 kDa molecular weight markers.

Discussion

Summary

The microBCA assay did return a positive absorbance signal after a delay period, indicating that the devices did demonstrate osmotically triggered delayed release of their contents. Mean device burst occurred after 20 ± 9 days of immersion. However, evidence of glucose interference with the microBCA assay was discovered, and its extent appears to be linked with glucose concentration. Protein sample solutions with glucose present returned absorbance values of up to 10x higher than the non-glucose containing equivalent. Further attempts at characterising the TT protein stock solution failed, with no-protein material being detected from SDS-PAGE. It was found in the microBCA assay kit manual, that the presence of glucose of concentrations over 1 mM in samples was known to have an interfering effect on the colourimetric mechanism of the assay. Technical bulletins from the supplier recommended a series of methods to remove or reduce the presence of interfering substances from samples, of which the protein precipitation methods appear most promising.

Osmotically triggered delayed release of tetanus toxoid

Delayed release of device contents was demonstrated from the PCL 3.5 M devices shown in Figure A2, which burst over a range of 7 – 35 days with a mean burst delay of 20 ± 9

days. In comparison to the PCL 3.5 M dye-containing devices, the TT-containing devices appear to burst sooner and with a greater variance. However, the mean burst delay times are within standard deviation of one another (PCL 3.5 M dye-containing device burst delay mean = 25 ± 5.8 days). The TT-containing device group features two device bursts at days 7 and 14, which are notably early when considering both payload groups of PCL 3.5 M devices together. Further analysis of the other (3 and 4 M) osmogent loading concentration groups would be necessary to draw any potential conclusions regarding any tendency of the protein-containing devices to burst earlier than their dye-containing equivalents. Considering the general trend witnessed from the dye-containing data, where greater variance could be associated to lower loading osmolarities, it is likely that these early bursts at days 7 and 14 are within the expected variance for the 3.5 M loading condition, rather than any influence by the payload. Comparing the rate of release of the contents of the protein- and dye-containing PCL 3.5 M devices in a qualitative manner shows the same gradual release characteristic, which appears typical for the PCL devices in general. Due to the glucose interference effect with the microBCA assay, which will be discussed in the next sub-section, it is not certain if the displayed protein concentrations in Figure A2 are valid. Instead, the y-axis values should be considered a semi-quantitative representation of content (both protein and glucose) release at best, or more conservatively as a qualitative indicator of device burst.

Glucose interference with the microBCA assay

From the brief investigation into the effect of various glucose concentrations on the microBCA assay results, it can be shown from Figure A3 that the presence of glucose leads to overestimation of the protein content of the sample solution in a glucose-concentration dependant manner. The presence of glucose at the concentrations used during device loading increased the absorbance produced by the colourimetic mechanisms of the assay to such an extent that all of the glucose-containing solutions tested greatly exceeded the linear working range of the assay. Considering that the glucose-containing samples are out with the linear working range, care should be taken to state that this experiment is conclusive proof of the glucose-concentration dependant effect. However, considering the data in at least a semi-quantitative manner, the assay does consistently associate higher glucose concentrations with higher absorbances. Further work would be required to quantify the extent that different glucose concentrations affect the assay. Ideally, a glucose-only control solution would have been tested, combined with solutions containing significantly lower concentrations of glucose

(so that the signal is within the linear quantifiable zone) to enable quantification of the effect of glucose concentration on the assay.

TT stock concerns

The tetanus toxoid stock solution was of unverified purity and concentration. In order to address this, SDS-PAGE was performed in an attempt to purify and quantify the stock solution. The experiment was performed with 4 sample columns, of which one was the TT stock solution, with the others containing solutions of TT and glucose of the three concentrations used to load the devices, and a BSA positive control column. SDS-PAGE was performed, but was unsuccessful in detecting any protein in the samples of interest (columns 1-4), as shown in Figure A4 by the lack of identifiable protein bands. Mature BSA protein has a molecular weight of approximately 66 kDa [248]. The BSA positive control displayed a clear protein band between 50 and 75 kDa, which validates that the assay was functioning and performed correctly. We would expect to detect protein bands in the other experimental columns at 150 kDa, or 100 and 50 kDa representing the separate heavy B-chains and light A-chains of the tetanus toxin, respectively. Additionally, further analysis by A280 and BCA (non-micro) assays were also unsuccessful in detecting protein.

Methodology oversight and limitations

While the microBCA assay was able to get positive absorbance signals from sample solutions, as shown in Figure A2, it was discovered that the maximum compatible concentration of glucose with the kit was 1 mM [249]. Glucose was listed as a known interfering agent at the back of the assay manual, which section was overlooked at the time of purchasing and conducting the microBCA assay. Beyond 1 mM, the error in protein concentration determination may exceed 10 %. With our minimum initial osmogent concentration being 3 M, it would be reasonable to anticipate that it would exceed the 1 mM limit rapidly after device burst. This expectation is likely to be especially relevant for the xPCL tubes that release a greater extent of inner contents at burst and therefore as part of that, glucose. Unfortunately, this ultimately means that this method of protein quantification is not suitable for the sample material in its current state.

Future work improvements

For future protein-release experiments, if utilising the same TT material, further in-depth confirmation/characterisation of the stock would be important to ensure that the protein is in its expected state, and not denatured/degraded. Otherwise, use of a different already

characterised protein material of a known initial concentration would be recommended. The issues regarding the potential glucose concentrations surpassing the microBCA kit limitations would remain regardless of protein stock used. A method of eliminating interfering substances, which would include glucose, from samples for BCA protein assays are suggested in the tech tip series from Thermo Scientific [250]. The procedure involves precipitation of the protein material in -20 ^{o}C acetone, centrifugation, removal of supernatant, and resuspension of the protein pellet in a known volume of ultrapure water. The microBCA reagents are then added, and the assay performed as normal. Another method suggested involves a highly similar procedure with trichloroacetic acid and sodium deoxycholate instead of acetone. Lastly, dialysis of the sample would separate the 150 kDa protein from the 0.18 kDa glucose, but would require determination of the extent of dilution of the TT in the glucose-free solution, and is likely to also be more time intensive.

Another aspect to consider regarding true quantification is that the protein colour response from the microBCA assay will show differences depending on the protein it is being used to detect and quantify. The microBCA assay is centred on bovine serum albumin (BSA), and has known adjustment ratios for 13 commonly tested proteins (which does not include tetanus toxoid material). For protein material that is not already standardised for this kit, it is encouraged to generate a calibration curve from purified target protein of a known starting concentration. As mentioned previously, the TT stock used was of unverified purity and concentration. The stock protein concentration was estimated (15,105 µg/mL) by preparing a dilution series and performing the microBCA assay on those samples as mentioned in section "protein release calibration" and shown in Figure A1 (b), assuming a 1:1 protein colour response of the TT with the BSA standards included in the kit. It is quite likely that in reality a 1:1 colour response is not the case for TT, and that this estimation contains a substantial degree of error. If a stock of known concentration was used, it would have been possible to determine a correction factor (correction ratio), as noted within the assay kit manual.

Conclusions

Osmotically triggered delayed release of tetanus toxoid was demonstrated from the delivery devices, with a mean delay to burst of 20 ± 9 days. Due to glucose interference with the colourimetric aspect of the microBCA assay, it was not possible to quantify the protein released from the devices with any degree of confidence. However, a future attempt at releasing protein from such devices may benefit from methodology

adjustments, such as use of a protein stock of known concentration and purity, and utilising one of the strategies to eliminate or minimise the interfering effects of high (> 1 mM) glucose concentrations, such as the acetone precipitation method.

APPENDIX B: mark I dip coater g-code and ImageJ wall thickness calculation script

Dip coating g-code

The dip coating g-code for production of PCL and xPCL tubes via the mark I dip coating apparatus is shown below. The code should be copied into a notepad file and saved with an appropriate g-code file extension suffix, such as .gcode.

The non-crosslinked PCL dip cycle g-code is shown below:

```
G17 G21 G40 G49 G54 G80 G91 G94 F1200          %G91 is relative coordinates!

F100 G1 y10              % slow rotation to check things are aligned
F1200 G1 x-115 y10       % speed is 1200 for both x and y and move the tube up 115 mm whilst rotating y for 6 seconds (or 1 rotation)
F100 G1 Y10              % F = rotate y at a speed of 100 ; Y = for 6 seconds (or 1 rotation)
F1200 G1 x115 y10        % F = speed is 1200 for both x and y and move the tube down 115 mm whilst rotating y for 6 seconds (or 1 rotation)
F100 G1 Y300             % F = rotate y at a speed of 100; Y = for 3 mins (or 30 rotations)

F1200 G1 x-115 y10       % speed is 1200 for both x and y and move the tube up 115 mm whilst rotating y for 6 seconds (or 1 rotation)
F100 G1 Y6               % F = rotate y at a speed of 100 ; Y = for 3.5 seconds (or 2/3 rotation)
F1200 G1 x115 y10        % F = speed is 1200 for both x and y and move the tube down 115 mm whilst rotating y for 6 seconds (or 1 rotation)
F100 G1 Y300             % F = rotate y at a speed of 100; Y = for 3 mins (or 30 rotations)

F1200 G1 x-115 y10       % speed is 1200 for both x and y and move the tube up 115 mm whilst rotating y for 6 seconds (or 1 rotation)
F100 G1 Y4               % F = rotate y at a speed of 100 ; Y = for 2.5 seconds (or 2/5 rotation)
F1200 G1 x115 y10        % F = speed is 1200 for both x and y and move the tube down 115 mm whilst rotating y for 6 seconds (or 1 rotation)
F100 G1 Y300             % F = rotate y at a speed of 100; Y = for 3 mins (or 30 rotations)
```

```
F1200 G1 x-115 y10      % speed is 1200 for both x and y and move the tube up 115 mm whilst rotating y for 6 seconds (or 1 rotation)
F100 G1 Y3              % F = rotate y at a speed of 100 ; Y = for 2 seconds (or 1/3 rotation)
F1200 G1 x115 y10       % F = speed is 1200 for both x and y and move the tube down 115 mm whilst rotating y for 6 seconds (or 1 rotation)
F100 G1 Y300            % F = rotate y at a speed of 100; Y = for 3 mins (or 30 rotations)
F100 G1 y10             % slow rotation to check things are aligned at the end
```

The photo-curable xPCL dip cycle g-code is shown below:

```
G17 G21 G40 G49 G54 G80 G91 G94 F1200          %G91 is relative coordinates!
%initial dip
F100 G1 Y10            %Initial turns to check for collisions 6 seconds of rotation
F1000 G1 X-120 Y6      %Moves tube upwards for dip with slow y rotation of rod
F40 G1 Y10             %rotates at 4rpm for 15 seconds
F1000 G1 X120 Y6       %moves tube back down
F60 G1 Y420            %rotates at 6 rpm for 7 mins - cure stage

%2nd dip
F1000 G1 X-120 Y6      %Moves tube upwards for dip with slow y rotation of rod
F40 G1 Y10             %rotates at 2rpm for 1 mins
F1000 G1 X120 Y6       %moves tube back down
F60 G1 Y420            %rotates at 6 rpm for 7 mins - cure stage

%3rd dip
F1000 G1 X-120 Y6      %Moves tube upwards for dip with slow y rotation of rod
F40 G1 Y10             %rotates at 2rpm for 1 mins
F1000 G1 X120 Y6       %moves tube back down
F60 G1 Y420            %rotates at 6 rpm for 7 mins - cure stage
F60 G1 Y420            %rotates at 6 rpm for 7 mins - post cure stage
```

ImageJ script code

Below is the ImageJ script code for batch-processed calculation of wall thicknesses of tubular parts. Note that this script requires ImageJ version of 1.52k or newer to run correctly. The text below should be arranged as a .txt file and selected through the "process>batch>macro…" processing window. Input folder of images to be measured

must be selected as the input. The script assumes all images will have the sample holder and the sample itself present. After processing, the measurements will be listed within a table in ImageJ, and can be saved in multiple file formats (.csv was chosen here). Note that the variable “pel” that determines the ‘pixels per mm’ of the image can be set to whatever known scale for the images. In this instance pel was kept at 1, and the measurements were converted afterwards.

```
// imagej-macro "batch pipe wall thickness (CoC)"
requires( "1.52k" );
nme = "Polar_Transformer.class";
if ( !File.exists( getDirectory( "plugins" ) + nme ) ) exit( "Macro requires PlugIn \"" +
nme + "\" !" );
setBackgroundColor(0, 0, 0);
setOption("BlackBackground", true);
pel = 1; // pixels per millimeter
inc = 1; // angular increment in degrees
dir=getDirectory("");
list=getFileList(dir);
setBatchMode( true );
for ( i=0; i<list.length; i++ ) {
  open(dir+list[i]);
  wallThickness( inc, pel, File.nameWithoutExtension  );
  close();
}
setBatchMode( false );
exit();
function wallThickness( deg, scale, fileName ) {
  run("Set Scale...", "distance=0 known=0 pixel=1 unit=pixel");
  run( "8-bit" );
  setAutoThreshold( "Default dark" );
  run( "Convert to Mask" );
  doWand( 90, getHeight() * 0.48 );
  run("Clear Outside");
  List.setMeasurements;
```

```
  x = List.getValue( "XM" );
  y = List.getValue( "YM" );
  nMax = round( List.getValue( "Perim." ) );
  run( "Select None" );
  outer = newArray( 0, y );
  inner = newArray( x, y );
  fitCircle( outer );
  fitCircle( inner );
  run( "Select None" );
  x = ( outer[0] + inner[0] ) * 0.5;
  y = ( outer[1] + inner[1] ) * 0.5;
  n = round( 360 / deg );
  if ( n > nMax ) { n = nMax; deg = 360 / nMax; }
  run( "Polar Transformer", "method=Polar degrees=360 number=[n] center_x=[x]
center_y=[y]" );
  run( "Make Binary" );
  wMax = 0;
  wMin = getWidth();
  wMean = 0;
  for ( i=0; i<n; i++ ) {
    w = calcWidth( i );
    wMean += w;
    if ( w > wMax ) wMax = w;
    if ( w < wMin ) wMin = w;
  }
  wMean /= n;
  setResult( "Label", nResults, fileName );
  setResult( "#Angles", nResults-1, n );
  setResult( "Mean/mm", nResults-1, wMean/scale );
  setResult( "Min/mm", nResults-1, wMin/scale );
  setResult( "Max/mm", nResults-1, wMax/scale );
  close();
}
function fitCircle( a ) {
```

```
  doWand( a[0], a[1] );
  run( "Fit Circle" );
  getSelectionBounds( x, y, w, h );
  a[0] = x + w * 0.5;
  a[1] = y + h * 0.5;
}
function calcWidth( idx ) {
  makeRectangle( 0, idx, getWidth(), 1 );
  p = getProfile();
  s = 0;
  for ( i=0; i<p.length; i++ ) { if ( p[i] > 0 ) s++; }
  return s;
}
// imagej-macro "batch pipe wall thickness (CoC)"
Originally from Herbie G., 04./06. Feb. 2019
With edits from Kerr S
```

Thanks to user: Herbie G. on forum.image.sc for assistance in the construction of the above script.

References

[1] WHO - World Health Organization, “Key components of a well functioning health system,” *Geneva WHO Heal. Syst.*, p. 2, 2010.

[2] WHO - World Health Organization, “Global Vaccine Action Plan 2011-2020,” pp. 1–77, 2013.

[3] S. De Koker *et al.*, “Designing polymeric particles for antigen delivery.,” *Chem. Soc. Rev.*, vol. 40, no. 1, pp. 320–339, 2011.

[4] D. Tago, B. Sall, R. Lancelot, and J. Pradel, “VacciCost – A tool to estimate the resource requirements for implementing livestock vaccination campaigns. Application to peste des petits ruminants (PPR) vaccination in Senegal,” *Prev. Vet. Med.*, vol. 144, pp. 13–19, 2017.

[5] L. Peidro-Garces, R. Otero-Fernandez, and L. Lozano-Lizarraga, “Adherence to and satisfaction with oral outpatient thromboembolism prophylaxis compared to parenteral: SALTO study,” *Rev Esp Cir Ortop Traumatol*, vol. 57, no. 1, pp. 53–60, 2013.

[6] J. F. Correia-Pinto, N. Csaba, and M. J. Alonso, “Vaccine delivery carriers: Insights and future perspectives,” *Int. J. Pharm.*, vol. 440, no. 1, pp. 27–38, 2013.

[7] J. Jorba *et al.*, “Update on vaccine-derived polioviruses – worldwide, January 2018-June 2019,” *Wkly. Epidemiol. Rec.*, no. 46, pp. 532–540, 2019.

[8] M. O’Ryan and A. C. Linhares, “Update on Rotarix^{TM}: An oral human rotavirus vaccine,” *Expert Rev. Vaccines*, vol. 8, no. 12, pp. 1627–1641, 2009.

[9] N. J. Carter and M. P. Curran, “Live Attenuated Influenza Vaccine (FluMist®; Fluenz^{TM}),” *Drugs*, vol. 71, no. 12, pp. 1591–1622, 2011.

[10] G. Birrenbach and P. P. Speiser, “Polymerized micelles and their use as adjuvants in immunology,” *J. Pharm. Sci.*, vol. 65, no. 12, pp. 1763–1766, 1976.

[11] I. Preis and R. S. Langer, “A single-step immunization by sustained antigen release,” *J. Immunol. Methods*, vol. 28, no. 1–2, pp. 193–197, 1979.

[12] K. J. McHugh, R. Guarecuco, R. Langer, and A. Jaklenec, “Single-injection vaccines: Progress, challenges, and opportunities,” *J. Control. Release*, vol. 219, pp. 596–609, 2015.

[13] M. T. Aguado, “Future approaches to vaccine development: Single-dose vaccines using controlled-release delivery systems,” *Vaccine*, vol. 11, no. 5, pp. 596–597, 1993.

[14] Y. Nir, A. Paz, E. Sabo, and I. Potasman, “Fear of injections in young adults:

Prevalence and associations," *Am. J. Trop. Med. Hyg.*, vol. 68, no. 3, pp. 341–344, 2003.

[15] J. Wallis, D. P. Shenton, and R. C. Carlisle, "Novel approaches for the design, delivery and administration of vaccine technologies," *Clin. Exp. Immunol.*, vol. 196, no. 2, pp. 189–204, 2019.

[16] R. A. Schwendener, "Liposomes as vaccine delivery systems: A review of the recent advances," *Ther. Adv. Vaccines*, vol. 2, no. 6, pp. 159–182, 2014.

[17] I. D. SPIERS, J. E. EYLES, L. W. J. BAILLIE, E. D. WILLIAMSON, and H. O. ALPAR, "Biodegradable Microparticles with Different Release Profiles: Effect on the Immune Response After a Single Administration via Intranasal and Intramuscular Routes," *J. Pharm. Pharmacol.*, vol. 52, no. 10, pp. 1195–1201, 2000.

[18] L. Zhao *et al.*, "Nanoparticle vaccines," *Vaccine*, vol. 32, no. 3, pp. 327–337, 2014.

[19] R. Pati, M. Shevtsov, and A. Sonawane, "Nanoparticle vaccines against infectious diseases," *Front. Immunol.*, vol. 9, no. OCT, 2018.

[20] B. G. De Geest, S. De Koker, J. Demeester, S. C. De Smedt, and W. E. Hennink, "Self-exploding capsules," *Polym. Chem.*, vol. 1, no. 2, pp. 137–148, 2010.

[21] F. P. W. Melchels *et al.*, "Initial design and physical characterization of a polymeric device for osmosis-driven delayed burst delivery of vaccines," *Biotechnol. Bioeng.*, vol. 112, no. 9, pp. 1927–1935, 2015.

[22] S. Rose and J. Nelson, "A CONTINUOUS LONG-TERM INJECTOR," *Aust. J. Exp. Biol. Med. Sci.*, vol. 33, no. 4, pp. 415–420, Aug. 1955.

[23] R. Conley, S. K. Gupta, and G. Sathyan, "Clinical spectrum of the osmotic-controlled release oral delivery system (OROS*), an advanced oral delivery form," *Curr. Med. Res. Opin.*, vol. 22, no. 10, pp. 1879–1892, 2006.

[24] V. Malaterre, J. Ogorka, N. Loggia, and R. Gurny, "Oral osmotically driven systems: 30 years of development and clinical use," *Eur. J. Pharm. Biopharm.*, vol. 73, no. 3, pp. 311–323, 2009.

[25] R. A. Nief, N. T. Sulaimann, and S. A. Jabir, "Pulsatile drug delivery system - A review article," *J. Pharm. Res.*, vol. 12, no. 5, pp. 764–770, 2018.

[26] B. G. Stubbe, S. C. De Smedt, and J. Demeester, "'Programmed polymeric devices' for pulsed drug delivery," *Pharm. Res.*, vol. 21, no. 10, pp. 1732–1740, 2004.

[27] I. G. Barr and W. J. Thiel, "A single dose vaccination system," International Patent

No.: WO 92/17165, 1992.

[28] K. Adams and M. W. Beal, “Implanon: A Review of the Literature With Recommendations for Clinical Management,” *J. Midwifery Women’s Heal.*, vol. 54, no. 2, pp. 142–149, 2009.

[29] K. Matsuo, S. Hirobe, N. Okada, and S. Nakagawa, “Frontiers of transcutaneous vaccination systems: Novel technologies and devices for vaccine delivery,” *Vaccine*, vol. 31, no. 19, pp. 2403–2415, 2013.

[30] A. A. Walters, C. Krastev, A. V. S. Hill, and A. Milicic, “Next generation vaccines: Single-dose encapsulated vaccines for improved global immunisation coverage and efficacy,” *J. Pharm. Pharmacol.*, vol. 67, no. 3, pp. 400–408, 2015.

[31] J. Cleland, “Single-administration vaccines: controlled-release technology to mimic repeated immunizations,” *Trends Biotechnol.*, vol. 17, no. 1, pp. 25–29, Jan. 1999.

[32] R. J. Nevagi, M. Skwarczynski, and I. Toth, “Polymers for subunit vaccine delivery,” *Eur. Polym. J.*, vol. 114, no. March, pp. 397–410, 2019.

[33] P. M. H. Heegaard *et al.*, “Adjuvants and delivery systems in veterinary vaccinology: Current state and future developments,” *Arch. Virol.*, vol. 156, no. 2, pp. 183–202, 2011.

[34] N. Chen, M. M. Johnson, M. A. Collier, M. D. Gallovic, E. M. Bachelder, and K. M. Ainslie, “Tunable degradation of acetalated dextran microparticles enables controlled vaccine adjuvant and antigen delivery to modulate adaptive immune responses,” *J. Control. Release*, vol. 273, no. September 2017, pp. 147–159, 2018.

[35] L. J. Cruz, P. J. Tacken, C. Eich, F. Rueda, R. Torensma, and C. G. Figdor, “Controlled release of antigen and Toll-like receptor ligands from PLGA nanoparticles enhances immunogenicity,” *Nanomedicine*, vol. 12, no. 5, pp. 491–510, 2017.

[36] S. Shi and A. J. Hickey, “PLGA microparticles in respirable sizes enhance an in vitro T cell response to recombinant mycobacterium tuberculosis antigen TB10.4-Ag85B,” *Pharm. Res.*, vol. 27, no. 2, pp. 350–360, 2010.

[37] J. L. Cleland, A. Lim, L. Barrón, E. T. Duenas, and M. F. Powell, “Development of a single-shot subunit vaccine for HIV-I: Part 4. Optimizing microencapsulation and pulsatile release of MN rgp120 from biodegradable microspheres,” *J. Control. Release*, vol. 47, no. 2, pp. 135–150, 1997.

[38] R. Guarecuco *et al.*, “Immunogenicity of pulsatile-release PLGA microspheres for

single-injection vaccination," *Vaccine*, vol. 36, no. 22, pp. 3161–3168, 2018.

[39] R. A. Jain, C. T. Rhodes, A. M. Railkar, A. W. Malick, and N. H. Shah, "Controlled delivery of drugs from a novel injectable in situ formed biodegradable PLGA microsphere system," *J. Microencapsul.*, vol. 17, no. 3, pp. 343–362, Jan. 2000.

[40] A. C. Allison and G. Gregoriadis, "Liposomes as immunological adjuvants," *Nature*, vol. 252, no. 5480. p. 252, 1974.

[41] P. A. Bovier, "Epaxal®: A virosomal vaccine to prevent hepatitis A infection," *Expert Rev. Vaccines*, vol. 7, no. 8, pp. 1141–1150, 2008.

[42] C. Herzog *et al.*, "Eleven years of Inflexal® V-a virosomal adjuvanted influenza vaccine," *Vaccine*, vol. 27, no. 33, pp. 4381–4387, 2009.

[43] N. Wang, M. Chen, and T. Wang, "Liposomes used as a vaccine adjuvant-delivery system: From basics to clinical immunization," *J. Control. Release*, vol. 303, no. April, pp. 130–150, 2019.

[44] C. G. Begley and L. M. Ellis, "Preclinical cancer research highlights," *Nature*, vol. 483, no. 7391, pp. 531–533, Jul. 2012.

[45] B. G. De Geest, C. Déjugnat, M. Prevot, G. B. Sukhorukov, J. Demeester, and S. C. De Smedt, "Self-rupturing and hollow microcapsules prepared from bio-polyelectrolyte- coated microgels," *Adv. Funct. Mater.*, vol. 17, no. 4, pp. 531–537, 2007.

[46] B. G. De Geest, C. Déjugnat, G. B. Sukhorukov, K. Braeckmans, S. C. De Smedt, and J. Demeester, "Self-rupturing microcapsules," *Adv. Mater.*, vol. 17, no. 19, pp. 2357–2361, 2005.

[47] P. F. Kiser, G. Wilson, and D. Needham, "A synthetic mimic of the secretory granule for drug delivery," *Nature*, vol. 394, no. 6692, pp. 459–462, 1998.

[48] A. G. Skirtach, A. A. Antipov, D. G. Shchukin, and G. B. Sukhorukov, "Remote activation of capsules containing Ag nanoparticles and IR dye by laser light," *Langmuir*, vol. 20, no. 17, pp. 6988–6992, 2004.

[49] C. Déjugnat and G. B. Sukhorukov, "pH-Responsive Properties of Hollow Polyelectrolyte Microcapsules Templated on Various Cores," *Langmuir*, vol. 20, no. 17, pp. 7265–7269, Aug. 2004.

[50] B. G. De Geest, S. De Koker, J. Demeester, S. C. De Smedt, and W. E. Hennink, "Pulsed in vitro release and in vivo behavior of exploding microcapsules," *J. Control. Release*, vol. 135, no. 3, pp. 268–273, 2009.

[51] B. G. De Geest *et al.*, "Polymeric multilayer capsule-mediated vaccination induces

protective immunity against cancer and viral infection," *ACS Nano*, vol. 6, no. 3, pp. 2136–2149, 2012.

[52] S. De Koker *et al.*, "Polyelectrolyte microcapsules as antigen delivery vehicles to dendritic cells: Uptake, processing, and cross-presentation of encapsulated antigens," *Angew. Chemie - Int. Ed.*, vol. 48, no. 45, pp. 8485–8489, 2009.

[53] B. Sun *et al.*, "Engineering an effective immune adjuvant by designed control of shape and crystallinity of aluminum oxyhydroxide nanoparticles," *ACS Nano*, vol. 7, no. 12, pp. 10834–10849, 2013.

[54] K. Niikura *et al.*, "Gold nanoparticles as a vaccine platform: Influence of size and shape on immunological responses in vitro and in vivo," *ACS Nano*, vol. 7, no. 5, pp. 3926–3938, 2013.

[55] A. E. Gregory *et al.*, "A gold nanoparticle-linked glycoconjugate vaccine against Burkholderia mallei," *Nanomedicine Nanotechnology, Biol. Med.*, vol. 11, no. 2, pp. 447–456, 2015.

[56] Y. S. Chen, Y. C. Hung, W. H. Lin, and G. S. Huang, "Assessment of gold nanoparticles as a size-dependent vaccine carrier for enhancing the antibody response against synthetic foot-and-mouth disease virus peptide," *Nanotechnology*, vol. 21, no. 19, 2010.

[57] M. G. Kim, J. Y. Park, Y. Shon, G. Kim, G. Shim, and Y. K. Oh, "Nanotechnology and vaccine development," *Asian J. Pharm. Sci.*, vol. 9, no. 5, pp. 227–235, 2014.

[58] T. Wang, M. Zou, H. Jiang, Z. Ji, P. Gao, and G. Cheng, "Synthesis of a novel kind of carbon nanoparticle with large mesopores and macropores and its application as an oral vaccine adjuvant," *Eur. J. Pharm. Sci.*, vol. 44, no. 5, pp. 653–659, 2011.

[59] Y. Lin, X. Wang, X. Huang, J. Zhang, N. Xia, and Q. Zhao, "Calcium phosphate nanoparticles as a new generation vaccine adjuvant," *Expert Rev. Vaccines*, vol. 16, no. 9, pp. 895–906, 2017.

[60] J. D. Masson, M. Thibaudon, L. Bélec, and G. Crépeaux, "Calcium phosphate: a substitute for aluminum adjuvants?," *Expert Rev. Vaccines*, vol. 16, no. 3, pp. 289–299, 2017.

[61] H. Jain, Krutika, "BIODEGRADABLE, LIQUID-FILLED, SPHERICAL CAPSULES WITH PRE-DETERMINED BURST TIMES," The University of Minnesota, 2017.

[62] M. J. H. Gerritzen, D. E. Martens, R. H. Wijffels, L. van der Pol, and M. Stork, "Bioengineering bacterial outer membrane vesicles as vaccine platform,"

Biotechnol. Adv., vol. 35, no. 5, pp. 565–574, 2017.

[63] A. Kulp and M. J. Kuehn, "Biological Functions and Biogenesis of Secreted Bacterial Outer Membrane Vesicles," *Annu. Rev. Microbiol.*, vol. 64, no. 1, pp. 163–184, 2010.

[64] N. J. Carter, "Multicomponent meningococcal serogroup B vaccine (4CMenB; Bexsero®): A review of its use in primary and booster vaccination," *BioDrugs*, vol. 27, no. 3, pp. 263–274, 2013.

[65] M. Shirley and S. Dhillon, "Bivalent rLP2086 Vaccine (Trumenba®): A Review in Active Immunization Against Invasive Meningococcal Group B Disease in Individuals Aged 10-25 Years," *BioDrugs*, vol. 29, no. 5, pp. 353–361, 2015.

[66] E. A. Specht and S. P. Mayfield, "Algae-based oral recombinant vaccines," *Front. Microbiol.*, vol. 5, no. FEB, pp. 1–7, 2014.

[67] K. C. Kwon, D. Verma, N. D. Singh, R. Herzog, and H. Daniell, "Oral delivery of human biopharmaceuticals, autoantigens and vaccine antigens bioencapsulated in plant cells," *Adv. Drug Deliv. Rev.*, vol. 65, no. 6, pp. 782–799, 2013.

[68] T. H. Roulston and J. H. Cane, "Pollen nutritional content and digestibility for animals," *Plant Syst. Evol.*, vol. 222, no. 1–4, pp. 187–209, 2000.

[69] S. U. Atwe, Y. Ma, and H. S. Gill, "Pollen grains for oral vaccination," *J. Control. Release*, vol. 194, pp. 45–52, 2014.

[70] M. J. Uddin and H. S. Gill, "Ragweed pollen as an oral vaccine delivery system: Mechanistic insights," *J. Control. Release*, vol. 268, pp. 416–426, 2017.

[71] N. Peyraud, D. Zehrung, C. Jarrahian, C. Frivold, T. Orubu, and B. Giersing, "Potential use of microarray patches for vaccine delivery in low- and middle-income countries," *Vaccine*, vol. 37, no. 32, pp. 4427–4434, 2019.

[72] M. Isley, "Implanon: the subdermal contraceptive implant.," *J. Pediatr. Adolesc. Gynecol.*, vol. 23, no. 6, pp. 364–367, 2010.

[73] F. Lakha and A. F. Glasier, "Continuation rates of Implanon® in the UK: data from an observational study in a clinical setting," *Contraception*, vol. 74, no. 4, pp. 287–289, 2006.

[74] S. Funk *et al.*, "Safety and efficacy of Implanon™, a single-rod implantable contraceptive containing etonogestrel," *Contraception*, vol. 71, no. 5, pp. 319–326, 2005.

[75] J. Le and C. Tsourounis, "Implanon: A critical review," *Ann. Pharmacother.*, vol. 35, no. 3, pp. 329–336, 2001.

[76] A. V. Tobolsky and H. F. Mark, *Polymer Science and Materials*. New York: John Wiley & Sons, Inc, 1971.

[77] A. Grattoni, M. Merlo, and M. Ferrari, "Osmotic pressure beyond concentration restrictions," *J. Phys. Chem. B*, vol. 111, no. 40, pp. 11770–11775, 2007.

[78] P. BARLOW, "ON THE FORCE EXCITED BY HYDRAULIC PRESSURE IN A BRAMAH PRESS; THE RESISTING POWER OF THE CYLINDER, AND RULES FOR COMPUTING THE THICKNESS OF METAL FOR PRESSES OF VARIOUS POWERS AND DIMENSIONS.," *Trans. Inst. Civ. Eng.*, vol. 1, no. 1836, pp. 133–139, Jan. 1836.

[79] M. A. Woodruff and D. W. Hutmacher, "The return of a forgotten polymer - Polycaprolactone in the 21st century," *Prog. Polym. Sci.*, vol. 35, no. 10, pp. 1217–1256, 2010.

[80] J. C. Middleton and A. J. Tipton, "Synthetic biodegradable polymers as orthopedic devices," *Biomaterials*, vol. 21, no. 23, pp. 2335–2346, 2000.

[81] D. H. Ha *et al.*, "Development of a radiopaque, long-term drug eluting bioresorbable stent for the femoral-iliac artery," *RSC Adv.*, vol. 9, no. 59, pp. 34636–34641, 2019.

[82] S. Borhani, S. Hassanajili, S. H. Ahmadi Tafti, and S. Rabbani, *Cardiovascular stents: overview, evolution, and next generation*, vol. 7, no. 3. Springer Berlin Heidelberg, 2018.

[83] S. A. Park *et al.*, "In vivo evaluation of 3D-printed polycaprolactone scaffold implantation combined with β-TCP powder for alveolar bone augmentation in a beagle defect model," *Materials (Basel).*, vol. 11, no. 2, 2018.

[84] S. Kehoe, X. F. Zhang, and D. Boyd, "FDA approved guidance conduits and wraps for peripheral nerve injury: A review of materials and efficacy," *Injury*, vol. 43, no. 5, pp. 553–572, 2012.

[85] M. D. Dhanaraju, D. Gopinath, M. R. Ahmed, R. Jayakumar, and C. Vamsadhara, "Characterization of polymeric poly(ε-caprolactone) injectable implant delivery system for the controlled delivery of contraceptive steroids," *J. Biomed. Mater. Res. - Part A*, vol. 76, no. 1, pp. 63–72, 2006.

[86] M. Lotfi, N. Ghasemi, S. Rahimi, S. Vosoughhosseini, M. A. Saghiri, and A. Shahidi, "Resilon: a comprehensive literature review.," *J. Dent. Res. Dent. Clin. Dent. Prospects*, vol. 7, no. 3, pp. 119–11930, 2013.

[87] M. R. Miner, D. W. Berzins, and J. K. Bahcall, "A Comparison of Thermal

Properties Between Gutta-Percha and a Synthetic Polymer Based Root Canal Filling Material (Resilon)," *J. Endod.*, vol. 32, no. 7, pp. 683–686, 2006.

[88] B. J. Green *et al.*, "Effect of Molecular Weight and Functionality on Acrylated Poly(caprolactone) for Stereolithography and Biomedical Applications," *Biomacromolecules*, vol. 19, no. 9, pp. 3682–3692, 2018.

[89] L. Cai and S. Wang, "Poly(ε-caprolactone) acrylates synthesized using a facile method for fabricating networks to achieve controllable physicochemical properties and tunable cell responses," *Polymer (Guildf).*, vol. 51, no. 1, pp. 164–177, 2010.

[90] H. Kweon, "A novel degradable polycaprolactone networks for tissue engineering," *Biomaterials*, vol. 24, no. 5, pp. 801–808, Feb. 2003.

[91] L. Elomaa, S. Teixeira, R. Hakala, H. Korhonen, D. W. Grijpma, and J. V. Seppälä, "Preparation of poly(ε-caprolactone)-based tissue engineering scaffolds by stereolithography," *Acta Biomater.*, vol. 7, no. 11, pp. 3850–3856, 2011.

[92] S. Wang, L. Lu, J. A. Gruetzmacher, B. L. Currier, and M. J. Yaszemski, "Synthesis and characterizations of biodegradable and crosslinkable poly(ε-caprolactone fumarate), poly(ethylene glycol fumarate), and their amphiphilic copolymer," *Biomaterials*, vol. 27, no. 6, pp. 832–841, 2006.

[93] S. Wang, M. Yaszemski, J. Gruetzmacher, and L. Lu, "Photo-Crosslinked Poly(ε-caprolactone fumarate) Networks: Roles of Crystallinity and Crosslinking Density in Determining Mechanical Properties," *Polymer (Guildf).*, vol. 49, no. 26, pp. 5692–5699, 2008.

[94] S. C. Woodward, P. S. Brewer, F. Moatamed, A. Schindler, and C. G. Pitt, "The intracellular degradation of poly(ε-caprolactone)," *J. Biomed. Mater. Res.*, vol. 19, no. 4, pp. 437–444, 1985.

[95] M. Bartnikowski, T. R. Dargaville, S. Ivanovski, and D. W. Hutmacher, "Degradation Mechanisms of Polycaprolactone in the Context of Chemistry, Geometry and Environment," *Prog. Polym. Sci.*, vol. 96, pp. 1–20, 2019.

[96] L. M. Lam, C, S. H. Teoh, and D. W. Hutmacher, "Comparison of the degradation of polycaprolactone and polycaprolactone– (β-tricalcium phosphate) scaffolds in alkaline medium," *Polym. Int.*, vol. 56, pp. 718–728, 2008.

[97] J. M. Meseguer-Dueñas, J. Más-Estellés, I. Castilla-Cortázar, J. L. Escobar Ivirico, and A. Vidaurre, "Alkaline degradation study of linear and network poly(ε-caprolactone)," *J. Mater. Sci. Mater. Med.*, vol. 22, no. 1, pp. 11–18, 2011.

[98] J. Jansen, M. J. Boerakker, J. Heuts, J. Feijen, and D. W. Grijpma, “Rapid photo-crosslinking of fumaric acid monoethyl ester-functionalized poly(trimethylene carbonate) oligomers for drug delivery applications,” *J. Control. Release*, vol. 147, no. 1, pp. 54–61, 2010.

[99] International Organization for Standardization, “ISO 10993-1:2018 - Biological evaluation of medical devices -- Part 1: Evaluation and testing within a risk management process,” p. 41, 2018.

[100] R. F. Wallin and E. F. Arscott, “A practical guide to ISO 10993-5: cytotoxicity,” *Med. Device Diagnostic Ind.*, vol. 20, no. 4, pp. 10–13, 1998.

[101] W. Li, J. Zhou, and Y. Xu, “Study of the in vitro cytotoxicity testing of medical devices,” *Biomed. Reports*, vol. 3, no. 5, pp. 617–620, 2015.

[102] C. S. A. (CSA), “ISO 10993-5 in vitro cytotox,” *Int. Organ.*, vol. 2007, pp. 1–11, 2009.

[103] O. S. Aslanturk, “In Vitro Cytotoxicity and Cell Viability Assays: Principles, Advantages, and Disadvantages,” in *Genotoxicity: A Predictable Risk to Our Actual World*, 1st ed., M. L. Larramendy and S. Soloneski, Eds. London: IntechOpen, 2018, p. 18.

[104] T. L. Riss, R. A. Moravec, A. L. Niles, H. A. Benink, T. J. Worzlla, and L. Minor, “Cell Viability Assays,” in *Assay Guidance Manual*, EBook., G. S. Sittamplalam, Ed. Bethesda: The National Centre for Advancing Translational Sciences (NCATS), 2016, pp. 1–30.

[105] J. O’Brien, I. Wilson, T. Orton, and F. Pognan, “Investigation of the Alamar Blue (resazurin) fluorescent dye for the assessment of mammalian cell cytotoxicity,” *Eur. J. Biochem.*, vol. 267, no. 17, pp. 5421–5426, 2000.

[106] M. S. Crosley and W. T. Yip, “Kinetically Doped Silica Sol-Gel Optical Biosensors: Expanding Potential Through Dip-Coating,” *ACS Omega*, vol. 3, no. 7, pp. 7971–7978, 2018.

[107] M. Schneider, C. Günter, and A. Taubert, “Co-deposition of a hydrogel/calcium phosphate hybrid layer on 3D printed poly(lactic acid) scaffolds via dip coating: Towards automated biomaterials fabrication,” *Polymers (Basel).*, vol. 10, no. 3, 2018.

[108] C. J. Brinker, “Chapter 10: Dip Coating,” in *Chemical Solution Deposition of Functional Oxide Thin Films*, 1st ed., vol. 9783211993, T. Schneller, R. Waser, M. Kosec, and D. Payne, Eds. Wien: Springer-Verlag Wien, 2013, pp. 1–796.

[109] C. W. Hull, “APPARATUS FOR PRODUCTION OF THREE-DMENSONAL OBJECTS BY STEREOLITHOGRAPHY,” US Pat. 4675330, 1984.

[110] K. V. Wong and A. Hernandez, “A Review of Additive Manufacturing,” *ISRN Mech. Eng.*, vol. 2012, pp. 1–10, 2012.

[111] P. F. Jacobs, *Rapid Prototyping and Manufacturing: Fundamentals of Stereolithography*. Mcgraw-Hill, 1992.

[112] J. Partanen, M. Kaivola, J. Seppälä, H. Korhonen, and P. Lehtinen, “Producing parts with multiple layer thicknesses by projection stereolithography,” *Int. J. Rapid Manuf.*, vol. 6, no. 4, p. 235, 2017.

[113] S. C. Ligon, R. Liska, J. Stampfl, M. Gurr, and R. Mülhaupt, “Polymers for 3D Printing and Customized Additive Manufacturing,” *Chem. Rev.*, vol. 117, no. 15, pp. 10212–10290, 2017.

[114] J. H. Lee, R. K. Prud’homme, and I. A. Aksay, “Cure depth in photopolymerization: Experiments and theory,” *J. Mater. Res.*, vol. 16, no. 12, pp. 3536–3544, 2001.

[115] E. Andrzejewska, “Photopolymerization kinetics of multifunctional monomers,” *Prog. Polym. Sci.*, vol. 26, no. 4, pp. 605–665, 2001.

[116] T. M. Shick, A. Z. Abdul Kadir, N. H. A. Ngadiman, and A. Ma’aram, “A review of biomaterials scaffold fabrication in additive manufacturing for tissue engineering,” *J. Bioact. Compat. Polym.*, vol. 34, no. 6, pp. 415–435, 2019.

[117] H. N. Chia and B. M. Wu, “Recent advances in 3D printing of biomaterials,” *J. Biol. Eng.*, vol. 9, no. 1, pp. 1–14, 2015.

[118] A. Di Bartolo, “LOW TEMPERATURE SHAPE MEMORY RECOVERY OF 3D PRINTED POLY (D , L-LACTIDE) NETWORKS : INVESTIGATING THE POTENTIAL FOR LONG TIME SCALE APPLICATIONS,” Heriot-Watt University, 2019.

[119] F. P. W. Melchels, K. Bertoldi, R. Gabbrielli, A. H. Velders, J. Feijen, and D. W. Grijpma, “Mathematically defined tissue engineering scaffold architectures prepared by stereolithography,” *Biomaterials*, vol. 31, no. 27, pp. 6909–6916, 2010.

[120] F. P. W. Melchels, J. Feijen, and D. W. Grijpma, “A poly(d,l-lactide) resin for the preparation of tissue engineering scaffolds by stereolithography,” *Biomaterials*, vol. 30, no. 23–24, pp. 3801–3809, 2009.

[121] O. Guillaume *et al.*, “Poly(trimethylene carbonate) and nano-hydroxyapatite

porous scaffolds manufactured by stereolithography," *Polym. Adv. Technol.*, vol. 28, no. 10, pp. 1219–1225, 2017.

[122] S. Schüller-Ravoo, E. Zant, J. Feijen, and D. W. Grijpma, "Preparation of a Designed Poly(trimethylene carbonate) Microvascular Network by Stereolithography," *Adv. Healthc. Mater.*, vol. 3, no. 12, pp. 2004–2011, 2014.

[123] O. Guillaume *et al.*, "Orbital floor repair using patient specific osteoinductive implant made by stereolithography," *Biomaterials*, vol. 233, no. July 2019, 2020.

[124] T. M. Seck, F. P. W. Melchels, J. Feijen, and D. W. Grijpma, "Designed biodegradable hydrogel structures prepared by stereolithography using poly(ethylene glycol)/poly(d,l-lactide)-based resins," *J. Control. Release*, vol. 148, no. 1, pp. 34–41, 2010.

[125] J. W. Lee, K. S. Kang, S. H. Lee, J. Y. Kim, B. K. Lee, and D. W. Cho, "Bone regeneration using a microstereolithography-produced customized poly(propylene fumarate)/diethyl fumarate photopolymer 3D scaffold incorporating BMP-2 loaded PLGA microspheres," *Biomaterials*, vol. 32, no. 3, pp. 744–752, 2011.

[126] UMC-Utrecht, "3D-printed skull implanted in patient," 2014. [Online]. Available: https://www.umcutrecht.nl/en/about-us/news/research/3d-printed-skull-implanted-in-patient. [Accessed: 07-Apr-2020].

[127] S. Sudesh Dandekeri, M. K. Sowmya, and S. Bhandary, "Stereolithographic surgical template: A review," *J. Clin. Diagnostic Res.*, vol. 7, no. 9, pp. 2093–2095, 2013.

[128] C. Bordes *et al.*, "Determination of poly(ε-caprolactone) solubility parameters: Application to solvent substitution in a microencapsulation process," *Int. J. Pharm.*, vol. 383, no. 1–2, pp. 236–243, 2010.

[129] K. S. Lee, D. S. Kim, and B. S. Kim, "Biodegradable molecularly imprinted polymers based on poly(ε-caprolactone)," *Biotechnol. Bioprocess Eng.*, vol. 12, no. 2, pp. 152–156, 2007.

[130] European Medicines Agency, "Questions and Answers on benzyl alcohol in the context of the revision of the guideline on ' Excipients in the label and package leaflet of medicinal products for human use,'" 2014.

[131] European Commission, "Opinion of the Scientific Committee on Food on Benzyl alcohol," 2002.

[132] Y. S. Chang, C. L. Wu, S. H. Tseng, P. Y. Kuo, and S. Y. Tseng, "In vitro benzyl alcohol cytotoxicity: Implications for intravitreal use of triamcinolone acetonide,"

Exp. Eye Res., vol. 86, no. 6, pp. 942–950, 2008.

[133] Y. S. Chang *et al.*, "Mechanisms underlying Benzyl alcohol cytotoxicity (triamcinolone acetonide preservative) in human retinal pigment epithelial cells," *Investig. Ophthalmol. Vis. Sci.*, vol. 52, no. 7, pp. 4214–4222, 2011.

[134] J. L. E. Ivirico, M. S. Sánchez, R. Sabater i Serra, J. M. M. Dueñas, J. L. G. Ribelles, and M. M. Pradas, "Structure and properties of poly(ε-caprolactone) networks with modulated water uptake," *Macromol. Chem. Phys.*, vol. 207, no. 23, pp. 2195–2205, 2006.

[135] H. A. Zaharin, A. M. Abdul Rani, T. L. Ginta, and F. I. Azam, "Additive Manufacturing Technology for Biomedical Components: A review," *IOP Conf. Ser. Mater. Sci. Eng.*, vol. 328, p. 012003, 2018.

[136] F. Calignano, M. Galati, L. Iuliano, and P. Minetola, "Design of Additively Manufactured Structures for Biomedical Applications: A Review of the Additive Manufacturing Processes Applied to the Biomedical Sector," *J. Healthc. Eng.*, vol. 2019, 2019.

[137] F. P. W. Melchels, J. Feijen, and D. W. Grijpma, "A review on stereolithography and its applications in biomedical engineering," *Biomaterials*, vol. 31, no. 24, pp. 6121–6130, 2010.

[138] K. Ikuta and K. Hirowatari, "Real three dimensional micro fabrication using stereo lithography and metal molding," *Proc. IEEE Micro Electro Mech. Syst. Conf.*, pp. 42–47, 1993.

[139] M. Miwa, S. Juodkazis, T. Kawakami, S. Matsuo, and H. Misawa, "Femtosecond two-photon stereo-lithography," vol. 566, pp. 561–566, 2001.

[140] T. Kuhnt *et al.*, "Biomaterials Science of bioresorbable tissue engineering implants †," *Biomater. Sci.*, vol. 7, no. Scheme 1, 2019.

[141] K. Arcaute, B. Mann, and R. Wicker, "Stereolithography of spatially controlled multi-material bioactive poly(ethylene glycol) scaffolds," *Acta Biomater.*, vol. 6, no. 3, pp. 1047–1054, 2010.

[142] N. A. Chartrain, C. B. Williams, and A. R. Whittington, "A review on fabricating tissue scaffolds using vat photopolymerization," *Acta Biomater.*, vol. 74, pp. 90–111, 2018.

[143] S. F. Abdellah Ali, "Mechanical and thermal properties of promising polymer composites for food packaging applications," *IOP Conf. Ser. Mater. Sci. Eng.*, vol. 137, no. 1, 2016.

[144] A. Mazzoli, C. Ferretti, A. Gigante, E. Salvolini, and M. Mattioli-Belmonte, "Selective laser sintering manufacturing of polycaprolactone bone scaffolds for applications in bone tissue engineering," *Rapid Prototyp. J.*, vol. 21, no. 4, pp. 386–392, 2015.

[145] W. Kempin *et al.*, "Assessment of different polymers and drug loads for fused deposition modeling of drug loaded implants," *Eur. J. Pharm. Biopharm.*, vol. 115, pp. 84–93, 2017.

[146] S. Schüller-Ravoo, J. Feijen, and D. W. Grijpma, "Flexible, elastic and tear-resistant networks prepared by photo-crosslinking poly(trimethylene carbonate) macromers," *Acta Biomater.*, vol. 8, no. 10, pp. 3576–3585, 2012.

[147] B. van Bochove, G. Hannink, P. Buma, and D. W. Grijpma, "Preparation of Designed Poly(trimethylene carbonate) Meniscus Implants by Stereolithography: Challenges in Stereolithography," *Macromol. Biosci.*, vol. 16, no. 12, pp. 1853–1863, 2016.

[148] Z. Zhang and J. E. Mark, "Birefringence Measurements on the Bimodal Networks at Very Low Temperatures *," *J. Polym. Sci. Polym. Phys. Ed.*, vol. 20, pp. 473–480, 1982.

[149] P. Xu and J. E. Mark, "Elasticity networks networks undiluted measurements on bimodal crosslinked in solution and studied and networks crosslinked in the state and studied swollen," vol. 33, no. 9, pp. 1843–1848, 1992.

[150] J. E. Mark, "Elastomeric Networks with Bimodal Chain-Length Distributions," *Acc. Chem. Res.*, vol. 27, no. 9, pp. 271–278, 1994.

[151] J. E. Mark, "Improved elastomers through control of network chain-length distributions," *Rubber Chem. Technol.*, vol. 72, no. 3, pp. 465–483, 1999.

[152] J. E. Mark, "Elastomers with multimodal distributions of network chain lengths," *Macromol. Symp.*, vol. 191, pp. 121–130, 2003.

[153] B. Van Bochove, S. Schüller-ravoo, and D. W. Grijpma, "Photo-Crosslinked Elastomeric Bimodal Poly (trimethylene carbonate) Networks," *Macromol. Mater. Eng.*, vol. 1800623, pp. 1–5, 2019.

[154] K. Balani, V. Verma, A. Agarwal, and R. Narayan, "Physical, Thermal and Mechanical Properties of Polymers," in *Biosurfaces: A Materials Science and Engineering Perspective*, 1st ed., K. Balani, V. Verma, A. Agarwal, and R. Narayan, Eds. Hoboken: John Wiley & Sons, Inc, 2015, pp. 329–344.

[155] E. Malikmammadov, T. E. Tanir, A. Kiziltay, V. Hasirci, and N. Hasirci, "PCL

and PCL-based materials in biomedical applications," *J. Biomater. Sci. Polym. Ed.*, vol. 29, no. 7–9, pp. 863–893, 2018.

[156] X. Feng, C. Song, and W. Chen, "Synthesis and evaluation of biodegradable block copolymers of e-caprolactone and D,L-lactide," *J.Polym. Sci. Polym. Lett.*, vol. 21, no. 3, pp. 593–600, 1983.

[157] I. Engelberg and J. Kohn, "Physico-mechanical properties of degradable polymers used in medical applications: A comparative study," *Biomaterials*, vol. 12, no. 3, pp. 292–304, 1991.

[158] T. F. Vandamme and R. Legras, "Physico-mechanical properties of poly(ε-caprolactone) for the construction of rumino-reticulum devices for grazing animals," *Biomaterials*, vol. 16, no. 18, pp. 1395–1400, 1995.

[159] H. H. Winter, "Can the Gel Point of a Cross-linking Polymer Be Detected by the G' - G" Crossover?," *Polym. Eng. Sci.*, vol. 27, no. 22, pp. 1698–1702, 1987.

[160] H. H. Winter and F. Chambon, "Analysis of Linear Viscoelasticity of a Crosslinking Polymer at the Gel Point," *J. Rheol. (N. Y. N. Y).*, vol. 30, no. 2, pp. 367–382, 1986.

[161] C. M. Tung and P. J. Dynes, "Relationship between viscoelastic properties and gelation in thermosetting systems," *J. Appl. Polym. Sci.*, vol. 27, no. 2, pp. 569–574, 1982.

[162] L. Weng, X. Chen, and W. Chen, "Rheological Characterization of in situ Crosslinkable Hydrogels Formulated form Oxidized Dextran and N-Carboxyethyl Chitosan," *Biomacromolecules*, vol. 8, no. 4, pp. 1109–1115, 2007.

[163] M. M. R. Nayini, S. Bastani, S. Moradian, C. Croutxé-Barghorn, and X. Allonas, "Rheological investigation of the gel time and shrinkage in hybrid organic/inorganic UV curable films," *J. Photopolym. Sci. Technol.*, vol. 29, no. 1, pp. 105–110, 2016.

[164] S. A. Khan, I. M. Plitz, and R. A. Frantz, "In situ technique for monitoring the gelation of UV curable polymers," *Communications*, vol. 160, no. 31, pp. 151–160, 1992.

[165] C. Hofstetter, S. Orman, S. Baudis, and J. Stampfl, "Combining cure depth and cure degree, a new way to fully characterize novel photopolymers," *Addit. Manuf.*, vol. 24, pp. 166–172, 2018.

[166] C. A. Bonino, J. E. Samorezov, O. Jeon, E. Alsberg, and S. A. Khan, "Real-time in situ rheology of alginate hydrogel photocrosslinking," *Soft Matter*, vol. 7, no.

24, pp. 11510–11517, 2011.

[167] J. M. Duliei-Barton and M. C. Fulton, “Mechanical Properties of a Typical Stereolithography Resin,” *Strain*, vol. 36, no. 2, pp. 81–87, 2000.

[168] A. Bens *et al.*, “Non-toxic flexible photopolymers for medical stereolithography technology,” *Rapid Prototyp. J.*, vol. 13, no. 1, pp. 38–47, 2007.

[169] Y. Yang, L. Li, and J. Zhao, “Mechanical property modeling of photosensitive liquid resin in stereolithography additive manufacturing: Bridging degree of cure with tensile strength and hardness,” *Mater. Des.*, vol. 162, pp. 418–428, 2019.

[170] A. Höglund, M. Hakkarainen, and A. C. Albertsson, “Degradation profile of poly(ε;-caprolactone)-the influence of macroscopic and macromolecular biomaterial design,” *J. Macromol. Sci. Part A Pure Appl. Chem.*, vol. 44, no. 9, pp. 1041–1046, 2007.

[171] G.-Z. Yin, X. Yang, Z. Zhou, and Q. Li, “A green pathway to adjust the mechanical properties and degradation rate of PCL by blending bio-sourced poly(glycerol-succinate) oligoesters,” *Mater. Chem. Front.*, vol. 2, pp. 544–553, 2018.

[172] S. Schüller-Ravoo, J. Feijen, and D. W. Grijpma, “Preparation of flexible and elastic poly(trimethylene carbonate) structures by stereolithography,” *Macromol. Biosci.*, vol. 11, no. 12, pp. 1662–1671, 2011.

[173] Autodesk, “Autodesk Standard Clear Prototyping Resin (PR48).” p. 1, 2015.

[174] C. X. F. Lam, D. W. Hutmacher, J. T. Schantz, M. A. Woodruff, and S. H. Teoh, “Evaluation of polycaprolactone scaffold degradation for 6 months in vitro and in vivo.,” *J. Biomed. Mater. Res. A*, vol. 90, no. 3, pp. 906–919, 2009.

[175] C. X. F. Lam, S. H. Teoh, and D. W. Hutmacher, “Comparison of the degradation of polycaprolactone and polycaprolactone– (β-tricalcium phosphate) scaffolds in alkaline medium,” *Polym Int*, vol. 56, pp. 718–728, 2007.

[176] A. A. Sawyer *et al.*, “The stimulation of healing within a rat calvarial defect by mPCL-TCP/collagen scaffolds loaded with rhBMP-2,” *Biomaterials*, vol. 30, no. 13, pp. 2479–2488, 2009.

[177] J. Schantz *et al.*, “Repair of Calvarial Defects with Customised Tissue-Engineered Bone Grafts II. Evaluation of Cellular Efficiency and Efficacy in Vivo,” *Tissue Eng.*, vol. 9, p. S-127-S-139, 2003.

[178] L. Ghasemi-Mobarakeh, D. Kolahreez, S. Ramakrishna, and D. Williams, “Key terminology in biomaterials and biocompatibility,” *Curr. Opin. Biomed. Eng.*, vol. 10, pp. 45–50, 2019.

[179] L. Elomaa, Y. Kang, J. V. Seppälä, and Y. Yang, “Biodegradable photocrosslinkable poly(depsipeptide-co-caprolactone) for tissue engineering: Synthesis, characterization, and in vitro evaluation,” *J. Polym. Sci. Part A Polym. Chem.*, vol. 52, no. 23, pp. 3307–3315, 2014.

[180] W. H. De Jong, J. W. Carraway, and R. E. Geertsma, “In vivo and in vitro testing for the biological safety evaluation of biomaterials and medical devices,” in *Biocompatibility and Performance of Medical Devices*, 1st ed., J.-P. Boutrand, Ed. Cambridge: Woodhead Publishing Limited, 2012, pp. 120–158.

[181] M. V. Berridge and A. S. Tan, “Trans-plasma membrane electron transport: A cellular assay for NADH- and NADPH-oxidase based on extracellular, superoxide-mediated reduction of the sulfonated tetrazolium salt WST-1,” *Protoplasma*, vol. 205, no. 1–4, pp. 74–82, 1998.

[182] E. Kennett, “Transmembrane Electron Transport Systems in Erythrocyte Plasma Membranes,” The University of Sydney, 2004.

[183] M. V. Berridge, P. M. Herst, and A. S. Tan, “Tetrazolium dyes as tools in cell biology: New insights into their cellular reduction,” *Biotechnol. Annu. Rev.*, vol. 11, no. SUPPL., pp. 127–152, 2005.

[184] A. Ferro, T. Mestre, P. Carneiro, I. Sahumbaiev, R. Seruca, and J. M. Sanches, “Blue intensity matters for cell cycle profiling in fluorescence DAPI-stained images,” *Lab. Investig.*, vol. 97, no. 5, pp. 615–625, 2017.

[185] M. L. Cano, L. Cassimeris, M. Joyce, and S. H. Zigmond, “Characterization of tetramethylrhodaminyl-phalloidin binding to cellular F-actin,” *Cell Motil. Cytoskeleton*, vol. 21, no. 2, pp. 147–158, 1992.

[186] T. Oda, K. Namba, and Y. Maéda, “Position and orientation of phalloidin in F-actin determined by x-ray fiber diffraction analysis,” *Biophys. J.*, vol. 88, no. 4, pp. 2727–2736, 2005.

[187] H. Frickmann, E. Schröpfer, and G. Dobler, “Actin assessment in addition to specific immuno-fluorescence staining to demonstrate rickettsial growth in cell culture,” *Eur. J. Microbiol. Immunol.*, vol. 3, no. 3, pp. 198–203, 2013.

[188] H. Vindin, L. Bischof, P. Gunning, and J. Stehn, “Validation of an algorithm to quantify changes in actin cytoskeletal organization,” *J. Biomol. Screen.*, vol. 19, no. 3, pp. 354–368, 2014.

[189] K. Kapat, P. P. Maity, A. P. Rameshbabu, P. K. Srivas, P. Majumdar, and S. Dhara, “Simultaneous hydrothermal bioactivation with nano-topographic modulation of

porous titanium alloys towards enhanced osteogenic and antimicrobial responses," *J. Mater. Chem. B*, vol. 6, no. 18, pp. 2877–2893, 2018.

[190] M. Popal, J. Volk, G. Leyhausen, and W. Geurtsen, "Cytotoxic and genotoxic potential of the type I photoinitiators BAPO and TPO on human oral keratinocytes and V79 fibroblasts," *Dent. Mater.*, vol. 34, no. 12, pp. 1783–1796, 2018.

[191] E. Yoshii, "Cytotoxic effects of acrylates and methacrylates: Relationships of monomer structures and cytotoxicity," *J. Biomed. Mater. Res.*, vol. 37, no. 4, pp. 517–524, 1997.

[192] L. Klouda, M. C. Hacker, J. D. Kretlow, and A. G. Mikos, "Cytocompatibility evaluation of amphiphilic, thermally responsive and chemically crosslinkable macromers for in situ forming hydrogels," *Biomaterials*, vol. 30, no. 27, pp. 4558–4566, Sep. 2009.

[193] Y. Xie *et al.*, "Development of a three-dimensional human skin equivalent wound model for investigating novel wound healing therapies," *Tissue Eng. - Part C Methods*, vol. 16, no. 5, pp. 1111–1123, 2010.

[194] R. Rezgui, K. Blumer, G. Yeoh-Tan, A. J. Trexler, and M. Magzoub, "Precise quantification of cellular uptake of cell-penetrating peptides using fluorescence-activated cell sorting and fluorescence correlation spectroscopy," *Biochim. Biophys. Acta - Biomembr.*, vol. 1858, no. 7, pp. 1499–1506, 2016.

[195] K. M. Hakkinen, J. S. Harunaga, A. D. Doyle, and K. M. Yamada, "Direct comparisons of the morphology, migration, cell adhesions, and actin cytoskeleton of fibroblasts in four different three-dimensional extracellular matrices," *Tissue Eng. - Part A*, vol. 17, no. 5–6, pp. 713–724, 2011.

[196] P. Adtani, M. Narasimhan, K. Ranganathan, A. Punnoose, P. Prasad, and P. M. Natarajan, "Characterization of oral fibroblasts: An in vitro model for oral fibrosis," *J Oral Maxillofac Pathol*, vol. 23, pp. 198–202, 2019.

[197] T. R. Elsdale, "Parallel orientation of fibroblasts in vitro," *Exp. Cell Res.*, vol. 51, no. 2–3, pp. 439–450, 1968.

[198] X. Li, R. Balagam, T. F. He, P. P. Lee, O. A. Igoshin, and H. Levine, "On the mechanism of long-range orientational order of fibroblasts," *Proc. Natl. Acad. Sci. U. S. A.*, vol. 114, no. 34, pp. 8974–8979, 2017.

[199] A. G. Foote, Z. Wang, C. Kendziorski, and S. L. Thibeault, "Tissue specific human fibroblast differential expression based on RNAsequencing analysis," *BMC Genomics*, vol. 20, no. 1, pp. 1–19, 2019.

[200] R. Augustine, A. Saha, V. P. Jayachandran, S. Thomas, and N. Kalarikkal, “Dose-dependent effects of gamma irradiation on the materials properties and cell proliferation of electrospun polycaprolactone tissue engineering scaffolds,” *Int. J. Polym. Mater. Polym. Biomater.*, vol. 64, no. 10, pp. 526–533, 2015.

[201] P. Ferreira, P. Alves, P. Coimbra, and M. H. Gil, “Improving polymeric surfaces for biomedical applications: a review,” *J. Coatings Technol. Res.*, vol. 12, no. 3, pp. 463–475, 2015.

[202] G. Kaur *et al.*, “Selective cell adhesion on peptide-polymer electrospun fiber mats,” *ACS Omega*, vol. 4, no. 2, pp. 4376–4383, 2019.

[203] W. Wang *et al.*, “Enhancing the hydrophilicity and cell attachment of 3D printed PCL/graphene scaffolds for bone tissue engineering,” *Materials (Basel).*, vol. 9, no. 12, 2016.

[204] N. Recek *et al.*, “Cell Adhesion on Polycaprolactone Modified by Plasma Treatment,” *Int. J. Polym. Sci.*, vol. 2016, 2016.

[205] C. Y. C. Hsieh, F.-W. Hu, W.-S. Chen, and W.-B. Tsai, “Reducing the Foreign Body Reaction by Surface Modification with Collagen/Hyaluronic Acid Multilayered Films,” *ISRN Biomater.*, vol. 2014, pp. 1–8, 2014.

[206] E. G. Hayman and M. D. Pierschbacher, “Vitronectin-A Major Cell Attachment-promoting Protein in Fetal Bovine Serum Sera and Serum Proteins Isolation of Vitronectin Antisera and Zmmunoassays,” *Exp. Cell Res.*, vol. 160, pp. 245–258, 1985.

[207] J. G. Steele, G. Johnson, and P. A. Underwood, “Role of serum vitronectin and fibronectin in adhesion of fibroblasts following seeding onto tissue culture polystyrene,” *J. Biomed. Mater. Res.*, vol. 26, no. 7, pp. 861–884, 1992.

[208] J. M. Anderson, A. Rodriguez, and D. T. Chang, “Foreign body reaction to biomaterials,” *Semin. Immunol.*, vol. 20, no. 2, pp. 86–100, 2008.

[209] Y. Chandorkar, K. Ravikumar, and B. Basu, “The Foreign Body Response Demystified,” *ACS Biomater. Sci. Eng.*, vol. 5, no. 1, pp. 19–44, 2019.

[210] O. Veiseh *et al.*, “Size- and shape-dependent foreign body immune response to materials implanted in rodents and non-human primates,” *Nat. Mater.*, vol. 14, no. 6, pp. 643–651, 2015.

[211] B. Basu, *Biomaterials for Musculoskeletal Regeneration*. Singapore: Springer Singapore, 2017.

[212] T. R. Kyriakides *et al.*, “The CC chemokine ligand, CCL2/MCP1, participates in

macrophage fusion and foreign body giant cell formation," *Am. J. Pathol.*, vol. 165, no. 6, pp. 2157–2166, 2004.

[213] B. D. Ratner, "Reducing capsular thickness and enhancing angiogenesis around implant drug release systems," *J. Control. Release*, vol. 78, no. 1–3, pp. 211–218, 2002.

[214] J. M. Anderson, "Biological Responses to Materials," *Annu. Rev. Mater. Res.*, vol. 31, pp. 81–110, 2001.

[215] A. A. Sharkawy, B. Klitzman, G. A. Truskey, and W. M. Reichert, "Engineering the tissue which encapsulates subcutaneous implants. II. Plasma-tissue exchange properties," *J. Biomed. Mater. Res.*, vol. 40, no. 4, pp. 586–597, 1997.

[216] S. C. Woodward, "How fibroblasts and giant cell encapsulate implants: Considerations in design of glucose sensors," *Diabetes Care*, vol. 5, no. 3, pp. 278–281, 1982.

[217] D. G. Hackam and D. A. Redelmeier, "Translation of Research Evidence From Animals to Humans," *JAMA*, vol. 296, no. 14, p. 1727, Oct. 2006.

[218] H. Pan, H. Jiang, and W. Chen, "The biodegradability of electrospun Dextran/PLGA scaffold in a fibroblast/macrophage co-culture," *Biomaterials*, vol. 29, no. 11, pp. 1583–1592, 2008.

[219] M. Enayati *et al.*, "Biocompatibility Assessment of a New Biodegradable Vascular Graft via In Vitro Co-culture Approaches and In Vivo Model," *Ann. Biomed. Eng.*, vol. 44, no. 11, pp. 3319–3334, 2016.

[220] C. A. Feghali-Bostwick, H. Yasuoka, A. T. Larregina, and Y. Yamaguchi, "Human Skin Culture as an Ex Vivo Model for Assessing the Fibrotic Effects of Insulin-Like Growth Factor Binding Proteins," *Open Rheumatol. J.*, vol. 2, no. 1, pp. 17–22, 2008.

[221] D. E. Corzo-León, C. A. Munro, and D. M. MacCallum, "An ex vivo human skin model to study superficial fungal infections," *Front. Microbiol.*, vol. 10, no. JUN, pp. 1–17, 2019.

[222] J. Shepherd, I. Douglas, S. Rimmer, L. Swanson, and S. MacNeil, "Development of three-dimensional tissue-engineered models of bacterial infected human skin wounds.," *Tissue Eng. Part C. Methods*, vol. 15, no. 3, pp. 475–484, 2009.

[223] W. M. Ross, A. C. Martens, and D. W. va. Bekkum, "Polymethacrylic Acid: Induction of Lymphocytosis and Tissue Distribution," *Cell Tissue Kinet*, vol. 8, pp. 467–477, 1975.

[224] Y. Murakami, Y. Tabata, and Y. Ikada, “Effect of the Molecular Weight of Water-Soluble Polymers on Accumulation at an Inflammatory Site Following Intravenous Injection,” *Drug Deliv*, vol. 3, pp. 231–238, 1996.

[225] A. K. Burkoth and K. S. Anseth, “MALDI-TOF Characterization of Highly Cross-Linked , Degradable Polymer Networks,” pp. 1438–1444, 1999.

[226] J. A. Burdick, T. M. Lovestead, and K. S. Anseth, “Kinetic chain lengths in highly cross-linked networks formed by the photoinitiated polymerization of divinyl monomers: A gel permeation chromatography investigation,” *Biomacromolecules*, vol. 4, no. 1, pp. 149–156, 2003.

[227] F. P. W. Melchels, A. H. Velders, J. Feijen, and D. W. Grijpma, “Photo-cross-linked poly(dl -lactide)-based networks. structural characterization by HR-MAS NMR spectroscopy and hydrolytic degradation behavior,” *Macromolecules*, vol. 43, no. 20, pp. 8570–8579, 2010.

[228] J. Jansen *et al.*, “Controlling the kinetic chain length of the crosslinks in photo-polymerized biodegradable networks,” *J. Mater. Sci. Mater. Med.*, vol. 24, no. 4, pp. 877–888, 2013.

[229] M. Wang, J. Etheridge, J. Thompson, C. Vorwald, D. Dean, and J. Fisher, “Evaluation of the In Vitro Cytotoxicity of Crosslinked Biomaterials,” *Biomacromolecules*, vol. 14, no. 5, pp. 1321–1329, 2013.

[230] M. D. Timmer, H. Shin, R. A. Horch, C. G. Ambrose, and A. G. Mikos, “In vitro cytotoxicity of injectable and biodegradable poly(propylene fumarate)-based networks: Unreacted macromers, cross-linked networks, and degradation products,” *Biomacromolecules*, vol. 4, no. 4, pp. 1026–1033, 2003.

[231] I. Fehr, “Melt electrospun capsules of PCL-PEG Triblockcopolymers as delayed burst drug delivery device in the purpose of vaccination of Koala,” University of Aachen and Queensland University of Technology, 2014.

[232] U. Dunker, “Construction of Dip-Coated Polymer Capsules as Delayed Burst Delivery Systems as a New Vaccination Method in Koalas,” Aachen University and Queensland University of Technology, 2014.

[233] M. Y. L. Torres, “Optimisation of manufacturing parameters for dip-coating of polymer,” The University of Queensland, Queensland University of Technology, 2019.

[234] N. P. Tipnis and D. J. Burgess, “Sterilization of implantable polymer-based medical devices: A review,” *Int. J. Pharm.*, vol. 544, no. 2, pp. 455–460, 2018.

[235] A. Simmons, “Future trends for the sterilisation of biomaterials and medical devices,” in *Sterilisation of Biomaterials and Medical Devices*, Elsevier, 2012, pp. 310–320.

[236] European Medicines Agency (EMA), “Guideline on the sterilisation of the medicinal product, active substance, excipient and primary container,” *Guidelines*, pp. 1–25, 2019.

[237] S. Chang and Y. Zhang, *Food Analysis: Protein Analysis*, Fifth., vol. 44, no. October. Cham: Springer Nature, 2017.

[238] D. F. Swinehart, “The Beer-Lambert law,” *J. Chem. Educ.*, vol. 39, no. 7, pp. 333–335, 1962.

[239] H. Leonards *et al.*, “Advantages and drawbacks of Thiol-ene based resins for 3D-printing,” in *Laser 3D Manufacturing II*, 2015, vol. 9353, p. 93530F.

[240] N. B. Cramer, J. P. Scott, and C. N. Bowman, “Photopolymerizations of thiol-ene polymers without photoinitiators,” *Macromolecules*, vol. 35, no. 14, pp. 5361–5365, 2002.

[241] R. J. Spontak and N. P. Patel, “Thermoplastic elastomers: Fundamentals and applications,” *Curr. Opin. Colloid Interface Sci.*, vol. 5, no. 5–6, pp. 333–340, 2000.

[242] W. Wang *et al.*, “Recent advances in thermoplastic elastomers from living polymerizations: Macromolecular architectures and supramolecular chemistry,” *Prog. Polym. Sci.*, vol. 95, pp. 1–31, 2019.

[243] J. Richeton, S. Ahzi, K. S. Vecchio, F. C. Jiang, and R. R. Adharapurapu, “Influence of temperature and strain rate on the mechanical behavior of three amorphous polymers: Characterization and modeling of the compressive yield stress,” *Int. J. Solids Struct.*, vol. 43, no. 7–8, pp. 2318–2335, 2006.

[244] H. Levine and L. Slade, “Water as a plasticizer: physico-chemical aspects of low-moisture polymeric systems,” in *Water Science Reviews 3: Water Dynamics, Vol. 3*, F. Franks, Ed. Cambridge: Cambridge University Press, 1988, pp. 79–185.

[245] L. E. Nielsen, *Mechanical Properties of Polymers and Composites - Volume 2*. New York: Marcel Dekker, Inc., 1974.

[246] J. R. C. Dizon, A. H. Espera, Q. Chen, and R. C. Advincula, “Mechanical characterization of 3D-printed polymers,” *Addit. Manuf.*, vol. 20, pp. 44–67, 2018.

[247] R. Hague, S. Mansour, N. Saleh, and R. Harris, “Materials analysis of stereolithography resins for use in Rapid Manufacturing,” *J. Mater. Sci.*, vol. 39,

no. 7, pp. 2457–2464, 2004.

[248] K. A. Majorek *et al.*, “Structural and immunologic characterization of bovine, horse, and rabbit serum albumins,” *Mol. Immunol.*, vol. 52, no. 3–4, pp. 174–182, 2012.

[249] Pierce Biotechnology, “Micro BCA Protein Assay Kit Manual; Product No.: 23235,” *Thermo Sci. PDF*, vol. 0412.6, pp. 1–6, 2010.

[250] Pierce Biotechnology, “Tech Tip #8; Eliminate interfering substances from samples for BCA protein assays,” *Thermo Sci. PDF*, vol. TR0008.3, pp. 1–3, 2010.